Two-dimensional electron systems in functional oxides studied by photoemission spectroscopy

Tobias Rödel

To cite this version:

Tobias Rödel. Two-dimensional electron systems in functional oxides studied by photoemission spectroscopy. Materials Science [cond-mat.mtrl-sci]. Université Paris Saclay (COmUE), 2016. English. ⟨NNT : 2016SACLS197⟩. ⟨tel-01722152v2⟩

HAL Id: tel-01722152
https://hal.science/tel-01722152v2

Submitted on 9 Mar 2018

NNT : 2016SACLS197

THESE DE DOCTORAT
DE
L'UNIVERSITE PARIS-SACLAY
PREPAREE A
UNIVERSITE PARIS-SUD

ECOLE DOCTORALE N° 564
Physique de l'Ile-de-France

Spécialité de doctorat: Physique

Par

Mr Tobias RÖDEL

Two-dimensional electron systems in functional oxides studied by photoemission spectroscopy

Thèse présentée et soutenue à Orsay, le 08/09/2016 :

Composition du Jury :

- M, CLAESSEN, Ralph (Rapporteur)
  Professeur, Universität Würzburg
- M, FINOCCHI, Fabio (Rapporteur)
  Directeur de recherche, Université Pierre et Marie Curie
- M, FAGOT-REVURAT, Yannick (Président du Jury)
  Professeur, Université de Lorraine
- M, LECOEUR, Philippe (Examinateur)
  Professeur, Université Paris-Sud
- M, SANTANDER-SYRO, Andres (Directeur de thèse)
  Maître de Conférence, Université Paris-Sud
- M, LE FÈVRE, Patrick (Co-encadrant de thèse)
  Chargé de Recherche, Synchrotron Soleil

Université Paris-Saclay
Espace Technologique / Immeuble Discovery
Route de l’Orme aux Merisiers RD 128 / 91190 Saint-Aubin, France

Titre : Gaz bidimensionnels d’électrons dans les oxydes fonctionnels étudiés par spectroscopie de photoémission

Mots clés : 2DEG, ARPES, métaux de transition, $SrTiO_3$, lacunes en oxygène, TiO_2

Résumé : De nombreux oxydes de métaux de transition (TMOs) possèdent des propriétés physiques complexes (ferroélectricité, magnétisme, supraconductivité à haute Tc ou magnétorésistance colossale). Les différents degrés de liberté (le réseau, la charge, le spin ou l'ordre orbitalaire) interagissent pour donner des phases différentes, très proches en énergie, qui vont former une grande variété d'états fondamentaux accessibles. La possibilité de fabriquer des hétérostructures de TMOs a encore accru la complexité de ces systèmes, de nouveaux phénomènes apparaissant aux interfaces. Un exemple typique est le gaz d'électrons bidimensionnel (2DEG) créé à l'interface entre deux oxydes isolants, $LaAlO_3$ et $SrTiO_3$, qui montre une transition métal-isolant, du magnétisme ou de la supraconductivité (contrôlée par une tension de grille). Le point de départ de cette thèse a été la découverte d'un 2DEG similaire à la surface nue de $SrTiO_3$ fracturée sous vide, rendant possible l'étude de sa structure électronique par photoémission angulaire.

Dans cette thèse, l'étude de surfaces préparées, plutôt que de petites facettes fracturées, a permis l'obtention de données spectroscopiques possédant des largeurs de raie proches des valeurs intrinsèques. Il est alors possible d'étudier les effets à N corps comme la renormalisation de la self-énergie due à l'interaction électron-phonon.

Ces recherches sur la structure électronique du 2DEG à la surface de $SrTiO_3$ ont pris un tour nouveau lorsqu'une texture de spin complexe y a été mesurée par photoémission résolue en spin. Nous présentons des résultats qui contredisent ces conclusions et nous discutons des raisons pouvant expliquer ce désaccord.

Une des motivations de cette thèse était de savoir si la structure électronique et les propriétés du 2DEG pouvaient être contrôlées. L'étude du 2DEG sur des surfaces (110) et (111) de SrTiO3 révèle que sa structure de bandes (ordre orbitalaire, symétrie de la surface de Fermi, masses effectives) peut être ajustée en confinant les électrons sur des surfaces de différentes orientations du même matériau.

Un succès majeure est la mise en évidence de 2DEGs à la surface de nombreux autres TMOs (TiO_2-anatase, $CaTiO_3$, $BaTiO_3$) ou d'oxydes plus simples utilisés dans les applications (ZnO). Dans tous ces oxydes, nous avons identifié les lacunes en oxygène comme étant à l'origine de la création des 2DEGs.

Dans l'anatase, ou d'autres TMOs en configuration électronique initiale d^0, les lacunes en oxygène produisent à la fois des électrons localisés ou itinérants (le 2DEG). Il peut être subtile de prévoir quel est le cas est le plus favorable énergétiquement comme le démontre l'étude de deux polymorphes de TiO_2, anatase et rutile. Dans $CaTiO_3$, l’octaèdre formé par les atomes d'oxygène autour du Ti est incliné. Cette rupture de symétrie provoque un mélange des orbitales *d* et modifie le 2DEG. Dans $BaTiO_3$, la création d'un 2DEG entraîne la coexistence de deux phénomènes normalement incompatibles, la ferroélectricité et la métallicité, dans deux zones spatialement distinctes du même matériau. Ce travail démontre qu'un 2DEG existe aussi à la surface de ZnO qui est, contrairement aux oxydes à base de Ti, plutôt un semiconducteur conventionnel, le caractère des orbitales pour les électrons itinérants étant alors de type *s* et non de type *d*.

Le principal résultat est la mise au point d'une méthode simple et versatile pour la création de 2DEGs en évaporant de l'aluminium sur des surfaces d'oxydes. Une réaction d'oxydo-réduction entre le métal et l'oxyde permet de créer un 2DEG à l'interface entre le métal oxydé et l'oxyde réduit. Dans cette thèse, les 2DEGs ont été étudiés uniquement par photoémission sous ultravide. Cette méthode ouvre la possibilité d'étudier ces 2DEGs dans des conditions de pression ambiante en utilisant, par exemple, des techniques de transport, un pas important vers la production de masse et à bas coûts de 2DEGs dans les oxydes pour de futures applications.

Title : Two-dimensional electron systems in functional oxides studied by photoemission spectroscopy

Keywords : 2DES, ARPES, transition metal oxides, $SrTiO_3$, oxygen vacancy , TiO_2

Abstract : Many transition metal oxides (TMOs) show complex physics, ranging from ferroelectricity to magnetism, high-T_c superconductivity and colossal magnetoresistance. The existence of a variety of ground states often occurs as different degrees of freedom (*e.g.* lattice, charge, spin, orbital) interact to form different competing phases which are quite similar in energy. The capability to epitaxially grow heterostructures of TMOs increased the complexity even more as new phenomena can emerge at the interface. One typical example is the two-dimensional electron system (2DES) at the interface of two insulating oxides, namely $LaAlO_3/SrTiO_3$, which shows metal-to-insulator transitions, magnetism or gate-tunable superconductivity. The origin of this thesis was the discovery of a similar 2DES at the bare surface of $SrTiO_3$ fractured in vacuum, making it possible to study its electronic structure by angle-resolved photoemission spectroscopy (ARPES).

In this thesis, the study of well-prepared surfaces, instead of small fractured facets, results in spectroscopic data showing line widths approaching the intrinsic value. This approach allows a detailed analysis of many-body phenomena like the renormalization of the self-energy due to electron-phonon interaction.

Additionally, the understanding of the electronic structure of the 2DES at the surface of $SrTiO_3$ (001) was given an additional turn by the surprising discovery of a complex spin texture measured by spin-ARPES. In this thesis data is presented which contradicts these conclusions and discusses possible reasons for the discrepancy.

One major motivation of this thesis was the question if and how the electronic structure and the properties of the 2DES can be changed or controlled. In this context, the study of 2DESs at (110) and (111) surface revealed that the electronic band structure of the 2DES (orbital ordering, symmetry of the Fermi surface, effective masses) can be tuned by confining the electrons at different surface orientations of the same material, namely $SrTiO_3$.

A major achievement of this thesis is the generalization of the existence of a 2DES in $SrTiO_3$ to many other surfaces and interfaces of TMOs (TiO_2 anatase, $CaTiO_3$, $BaTiO_3$) and even simpler oxides already used in modern applications (ZnO). In all these oxides, we identify oxygen vacancies as the origin for the creation of the 2DESs.

In anatase and other doped d^0 TMOs, both localized and itinerant electrons (2DES) can exist due to oxygen vacancies. Which of the two cases is energetically favorable depends on subtle differences as demonstrated by studying two polymorphs of the same material (anatase and rutile).

In $CaTiO_3$, the oxygen octahedron around the Ti ion is slightly tilted. This symmetry breaking results in the mixing of different *d*-orbitals demonstrating again why and how the electronic structure of the 2DES can be altered.

In $BaTiO_3$, the creation of a 2DES results in the coexistence of the two, usually mutual exclusive, phenomena of ferroelectricity and metallicity in the same material by spatially separating the two. Moreover, this work demonstrates that the 2DES also exists in ZnO which is - compared to the Ti-based oxides - rather a conventional semiconductor as the orbital character of the itinerant electrons is of *s* and not *d*-type.

The main result of this thesis is the demonstration of a simple and versatile technique for the creation of 2DESs by evaporating Al on oxide surfaces. A redox reaction between metal and oxide results in a 2DES at the interface of the oxidized metal and the reduced oxide. In this thesis the study of such interfacial 2DESs was limited to photoemission studies in ultra high vacuum. However, this technique opens up the possibility to study 2DESs in functional oxides in ambient conditions by *e.g.* transport techniques, and might be an important step towards cost-efficient mass production of 2DESs in oxides for future applications.

Science cannot solve the ultimate mystery of nature. And that is because, in the last analysis, we ourselves are part of nature and therefore part of the mystery that we are trying to solve.

Max Planck (1932)

Université Paris-Saclay
Espace Technologique / Immeuble Discovery
Route de l’Orme aux Merisiers RD 128 / 91190 Saint-Aubin, France

Acknowledgements

My first thanks go to my family, especially my parents and my brother who made me the person I am today and supported me throughout my studies. Next, I want to thank my girlfriend who made the transition to the French culture & lifestyle much easier and reminds me everyday of things that are more important in life than pursuing my career. I also want to thank my friends who made the often frustrating process of learning physics much more fun and bearable.

I am very grateful for the time I spent as a student researcher at the Lawrence Berkeley National Laboratory in California. Mary Gilles and Ryan Moffet introduced me to the daily routines of the life of a researcher and thereby motivated me to pursue an academic career.

Special thanks go to my thesis advisers Andrés Felipe Santander-Syro (CSNSM, University of Paris Sud) and Patrick Le Fèvre (Cassiopé beamline, Synchrotron Soleil) who granted me the opportunity to conduct the research for my PhD thesis in Paris.

The discussions with and help of my coworkers, especially Franck Fortuna (CSNSM), Cédric Bareille (ISSP Tokyo), Thomas Maroutian (IEF), François Bertran (Synchrotron Soleil), Valérie Pillard (IEF), Philippe LeCoeur (IEF), Emmanouil Frantzeskakis (CSNSM), Marc Gabay (LPS), Marcelo Rozenberg (LPS) and my fellow PhD students Monika Güttler (University of Dresden), Dzung-Han Tsai (CSNSM), Oliver Hijano Cubelos (LPS) & Manali Vivek (LPS), made it much easier to advance my understanding in physics and material science. I am also indebted to all the beamline scientists and their support which made sure that our photoemission experiments at synchrotron facilities could be conducted without major complications. In this context, I am grateful to the Synchrotron Soleil (Gif-sur-Yvette, France), Synchrotron Radiation Center (Stoughton, USA), BESSY (Berlin, Germany), Swiss Light Source (Villingen, Switzerland), HiSOR (Hiroshima, Japn), Photon Factory (Tsukuba, Japan), Elettra (Trieste, Italy) and the The Institute for Solid State Physics (Tokyo, Japan) to provide the infrastructure to conduct photoemission experiments. I am grateful for the access to the ultra high vacuum chambers for thin film growth & surface preparation and the atomic force microscope at the Cassiopée beamline and the IEF as well as the surface preparation conducted by Valérie Pillard and Thomas Maroutian in the clean room of IEF. I also thank the administrative stuff of all the involved institutes who ensured that I could focus on my research project.

Finally, I am thankful for the financial support for my thesis given by Synchrotron Soleil & the Triangle de la Physique as well as for support by the Centre de Sciences Nucléaires et de Sciences de la Matière (CSNSM), the Institut d'Electronique Fondamentale (IEF), the Centre de la recherche scientifique (CNRS) and the Université de Paris Sud & Université Paris-Saclay.

Contents

Motivation and overview of thesis

Framework of this thesis

In the framework of this thesis, I worked in the team of “Strongly Correlated Systems and New Electronic States of Matter” at CSNSM in Orsay, in the team of “Oxide growth, magnetism and transport” at IEF in Orsay and in the team of the Cassiopée beamline at Synchrotron Soleil. I studied the two dimensional electron systems (2DESs) at the surface of transition metal oxides (TMOs), mainly band insulating titanates, by locally doping the surface region with oxygen vacancies and characterizing their microscopic electronic structure by angle-resolved photoemission spectroscopy (ARPES). Since the discovery of the 2DES at the surface of $SrTiO_3$ in 2011 [1, 2], there have been 17 ARPES works on 2DESs at the surface of transition metal oxides (TMOs): [3–19]

Towards a microscopic knowledge of electronic band structure

The research on 2DESs in systems based on transition metal oxides surged after the discovery of a metallic channel at the interface between two insulating oxides: $LaAlO_3$ and $SrTiO_3$. [20] The rich physics in this system ranging from field controlled insulator-to-superconductor transitions [21], magnetism [22] or the coexistence of superconductivity & magnetism [23–25] together with different possible origins for the existence of the 2DES (electronic reconstruction due to polar catastrophe [26], oxygen vacancies [27] or cation intermixing [28]) lead to intense research efforts over the last decade.

A large fraction of the studies on $LaAlO_3/SrTiO_3$ are transport studies. To better understand these macroscopic measurements, the knowledge of the microscopic electronic band structure is essential. The discovery and study of the 2DES at the surface of $SrTiO_3$ contributed to this field by determining the electronic band structure of the electrons confined at the interface or respectively the surface. [1, 2] Using ARPES, the t_{2g} orbital manifold composing the 2DES can be characterized and the electronic microscopic properties (band masses, ordering, splitting as well as Fermi surface and charge carrier density) directly measured. Moreover, by the study of related materials (*e.g.* TiO_2 or $CaTiO_3$) or other surface orientations, the influence of different lattice configurations (*e.g.* stacking order or tilt of oxygen octahedra) on the electronic structure can be directly accessed and will be discussed in this thesis.

Study of surfaces: a bottom-up approach to interface physics in transition metal oxides

More generally, the physics of transition metal oxides coupled with interface effects in oxide heterostructures result in various interface properties not necessarily observed in the bulk. [29] In this context, one can see oxide heterostructures as an evolved version of semiconductor based heterostructures which are known *e.g.* for the discovery of the fractional Quantum Hall effects [30] or the omnipresent field effect transistors [31]. TMOs have rich physics, one of the reasons being the d character of the valence orbitals instead of p character in conventional semiconductors. Various different ground states (ferroelectricity, ferromagnetism and superconductivity,...) not common in semiconductors together with an often strong coupling between various degrees of freedom (lattice, spin, charge, orbital) yield an immense playground for material scientists and physicists. [32–34]

In this context, the study of the surface can be seen as a bottom-up approach to the complex problems at oxide interfaces. After all, the vacuum/ surface interface is a comparably simpler interface. One can wonder if the exotic properties of the $LaAlO_3/SrTiO_3$ mentioned above are exclusive to this particular interface or a general property of electron doped $SrTiO_3$ interfaces. Thus, the knowledge about the physics of the simpler vacuum/surface interface can help to better understand related interfaces in oxide heterostructures and to disentangle the origin of different emerging properties at the interface of more complicated systems.

Role and engineering of oxygen vacancies

Another way to motivate this work is based on the control of defects, namely oxygen vacancies. The oxygen vacancy is a common/ omnipresent point defect in oxides. [35] The properties of TMOs often change dramatically due to the presence or ordering (homogeneously/ randomly distributed point defect, cluster, layered) of oxygen vacancies. Usually, the oxygen vacancy is an electron donor and can induce an insulator-to-metal transition in insulating TMOs (*e.g.* $SrTiO_3$). The engineering of oxygen vacancies can result in local insulator-metal transitions [15, 36], the electric-field induced diffusion of vacancies influences the resistive switching behavior of possible memristor devices [37–39], ferromagnetism has been related to oxygen vacancies [40, 41] as well and the (photo)chemistry or (photo)catalytic properties also depend on the vacancy distribution [42–45].

The local creation of oxygen vacancies at the surface or interface of oxides and the control of their concentration are essential to study and to control the properties of 2DESs in transition metal oxides.

Overview of thesis

1. Physics of TMOs

We use angle-resolved photoemission spectroscopy (ARPES) at synchrotron radiation facilities to probe the electronic structure of doped band insulating transition metal oxides. I will motivate the study of transition metal oxides in chapter 1 and briefly discuss the variety of their properties which are enhanced by combining the properties of different parent compounds in oxide heterostructures. The focus is on ternary perovskite oxides (*e.g.* $SrTiO_3$, $CaTiO_3$, $BaTiO_3$) as well as common binary oxides (TiO_2 and ZnO). The origin of this thesis was the discovery of the two-dimensional electron system (2DES) at the oxygen-deficient surface of $SrTiO_3$(001) which will be introduced in section 1.2.

2. ARPES

Most of the experimental results presented in thesis were obtained using photoemission techniques at synchrotron radiation facilities (see section 2.1). As all spectroscopic techniques, ARPES never probes the ground state of the system but an excited state: the spectral function (see section 2.2).

The creation of the intense UV light in synchrotron facilities used to conduct photoemission experiments is introduced in section 2.3 together with the Cassiopée beamline at which a large fraction of the experimental data was obtained.

As UV-ARPES is a very surface sensitive technique (inelastic mean free path of electrons: 5-10 Å), the structure and quality of the surface is essential to obtain high-quality data and to understand the data. Hence, the characteristics of surfaces of single crystalline oxides and different ways to control the surface structure of transition metal oxides are discussed in 2.4.

For some of the materials we studied, the excitation of the electronic structure by intense UV synchrotron light results in a change of the stoichiometry of the sample and even the lattice structure in extreme cases. Thus, in our case the irradiation to conduct ARPES experiments is more than a mere probe of the electronic structure but can significantly alter the properties of the material as will be discussed in chapter 3.

3. Oxygen vacancies

For the creation of the two dimensional electron system, the formation of oxygen vacancies is the dominating process for the local electron doping of the surface region as discussed in section 3.1. A direct experimental proof is that the charge carrier density can be controlled by exposing the surface of the samples to oxygen. [14, 16] The creation of oxygen vacancies by oxygen desorption due to light irradiation occurs for photon energies larger than the binding energy of certain core levels of the transition metal. This desorption induced by electron transition will be discussed in section 3.1. Experimental results demonstrating oxygen desorption as a function of photon dose and energy are presented in section 3.2.

The photoemission results in sections 3.3 and 3.4 show the electronic core levels and the band structure of the 2DES at the surface of anatase(001) and (101). These results helped to gain further insights about the behavior of excess electrons due to oxygen vacancies. The question whether these electrons will become delocalized in the conduction band or localized within the band gap of doped insulators is far from trivial (see discussion in section 3.1). Experimentally, this is demonstrated by the different behavior of electrons in two polymorphs of TiO_2: anatase and rutile.

4. Metal-oxide interface

As outlined above, chapter 3 discusses the mechanism responsible for the creation of the 2DES under intense UV irradiation. However, there are different means to locally dope the surface region with electrons. One route is the growth of ultra-thin metal layers on the surface of transition metal oxides (see section 4.1). Depending on the metal and the oxide, electron doping can occur due to different chemical potentials in the oxide and the metal. Alternatively, redox reactions can occur based on the oxidation of the metal and the reduction of the oxide. In both cases, the surface region is doped with electrons, either directly by the electrons of the metal, or indirectly by the metal-induced creation of oxygen vacancies.

In section 4.2, I will present the creation of 2DESs after deposition of an ultrathin Al layer. Compared to other 2DESs at the interface of heterostructures (*e.g.* $LaAlO_3/SrTiO_3$), this method is much simpler and versatile. The existence of 2DESs can be generalized to many different oxides using this method. As an example, the electronic structure of the 2DES at the interface of AlO_x and $ZnO(000\bar{1})$ will be characterized by ARPES in section 4.3. Another major advantage of this method is that - compared to 2DESs at the surface of oxides in UHV - it enables to characterize 2DESs in ambient conditions using *e.g.* transport measurements.

Finally, the electron doping of the surface using metals with low work functions is explored in section 4.4.

5. 2DES in $SrTiO_3$: orientational tuning

Chapters 3 and 4 explain the formation mechanism of the 2DES and give an example of the band structure of a 2DES at the surface or interface of a transition metal oxide (*e.g.* $SrTiO_3(001)$ and anatase). A major question of this thesis is if and how the properties of the 2DES can be tuned or altered. In chapter 5, the tuning of the properties is explored by confining the 2DES at different surface orientations of the *same material*, namely $SrTiO_3$. The geometry of the surface lattice depends on the surface orientation and alters the orbital ordering, the symmetry of the Fermi surface as well as the effective mass along a specific crystallographic direction of the 2DES. This is demonstrated by using a simple tight-binding model (section 5.1) and by ARPES measurements (section 5.2).

6. 2DESs in ATiO$_3$ (A=Ba,Ca)

Another way to obtain 2DESs with different properties is changing the lattice geometry by *e.g.* replacing the A-site cation in ATiO$_3$ perovskites. The 2DES at the (001) surface of SrTiO$_3$ is a reference system to understand the changes induced in the 2DES at the surface of CaTiO$_3$ and BaTiO$_3$ as discussed in chapter 6. The lattice geometry does not only influence the properties of the 2DES but also determines the dielectric properties of the ATiO$_3$ perovskites. Hence, quantum paraelectricity (*e.g.* SrTiO$_3$, CaTiO$_3$) and ferroelectricity (*e.g.* BaTiO$_3$) are briefly discussed in section 6.1.

The central building block of ATiO$_3$ perovskites is the octahedral configuration of the oxygen anions around the Ti cation. In cubic SrTiO$_3$, the octahedra are neither deformed nor rotated. However, in tetragonal BaTiO$_3$, the off-center movement of the Ti cation results in ferroelectricity. Normally, ferroelectricity and metallicity are two exclusive phenomena as mobile carriers screen the long-range Coulomb interaction of electric dipoles. However, by locally doping the surface region and thus, creating a 2DES, the two phenomena coexist spatially separated in the *same material* (see section 6.2). In orthorhombic CaTiO$_3$, the octahedra are rotated. This breaking of symmetry results in the mixing of different d orbitals which is not observed in SrTiO$_3$ (see section 6.3).

7. Spin polarization in SrTiO$_3$

As will be discussed in chapter 3, oxygen vacancies are responsible for the creation of 2DESs at the surface of certain insulating transition metal oxides. But oxygen vacancies are also related to d^0 magnetism, *i.e.* the presence of ferromagnetism in slightly doped band insulators with d valence orbitals. d^0 magnetism and diluted magnetic oxides will be reviewed in section 7.1. Recent photoemission experiments sensitive to the spin polarization, gave insights into the complex spin structure of the 2DES created by UV irradiation at the bare, oxygen-deficient surface of SrTiO$_3$(001) [12] as reviewed in section 7.2 together with the technique of spin-resolved ARPES (SARPES). In this thesis, the spin polarization of the 2DEG created by our new Al-capping technique at the AlO$_x$/SrTiO$_3$ interface (section 4.2) is also explored by SARPES. The data do not show any large spin polarization, contrary to the aforementioned measurements at the bare SrTiO$_3$ surface. A discussion of these contradictory results in presented.

8. e-ph coupling

The characterization of the 2DESs in the previous chapters of this thesis focuses on the band structure measured by ARPES. However, ARPES measures the spectral function and hence, yields information on many-body phenomena beyond the band structure, *e.g.* electron-phonon (e-ph) coupling. The topic of e-ph interaction and more specifically the coupling between electrons and Einstein phonons is introduced in section 8.1. To gain quantitative information on the e-ph coupling, the analysis of the self-energy is necessary as also discussed in section 8.1. Finally, I will discuss polaron formation in SrTiO$_3$ and analyze the spectral function of the 2DES data at the surfaces of SrTiO$_3$, Anatase and ZnO in section 8.2. Many recent photoemission papers deal with e-ph coupling in $SrTiO_3$ and anatase [14, 17, 18, 46–48], one motivation being to better understand the transport properties of the $LAlO_3$/$SrTiO_3$ interface.

Chapter 1

Physics of transition metal oxides

1.1 Introduction: correlated electrons and spin, charge, lattice and orbital interactions

Many transition metal oxides (TMOs) show complex physics, often because different degrees of freedom (*e.g.* lattice, charge, spin, orbital) interact to form different competing phases/ states which are quite similar in energy. Thus, phase diagrams of TMOs can be complex and a (small) external perturbation can create a dramatic response of the system due to a phase transition between the competing phases. [33] The control of these transitions is necessary to embed new functionalities in devices. [49]

The focus of this thesis is on the electronic structure of transition metal oxides. The electronic structure of a material is determined among others by the orbital character of its conduction band. The rather localized d orbitals of the transition metals result in correlation effects of electrons [32, 34] which can give rise to spectacular phenomena such as high-temperature superconductivity or colossal magnetoresistance. In correlated materials the ratio between on-site Coulomb repulsion U and hopping amplitude t or respectively band width W describe the competition between the localization or delocalization of an electron. [50]

1.1.1 ABO_3 Perovskites

The perovskite lattice hosts a variety of different properties ranging from insulators, metals to superconductors as well as ferroelectrics and ferromagnets.

In the following paragraphs, I will briefly review how different degrees of freedom can alter the properties of the perovskite materials. Firstly, I will discuss the perovskite lattice structure and common lattice distortions and secondly, their electronic structure.

Lattice structure

Many of the transition metal oxides in this thesis share a common lattice, the perovskite lattice. The perovskite lattice has the elemental formula ABO_3, where A is often an alkali metal or an

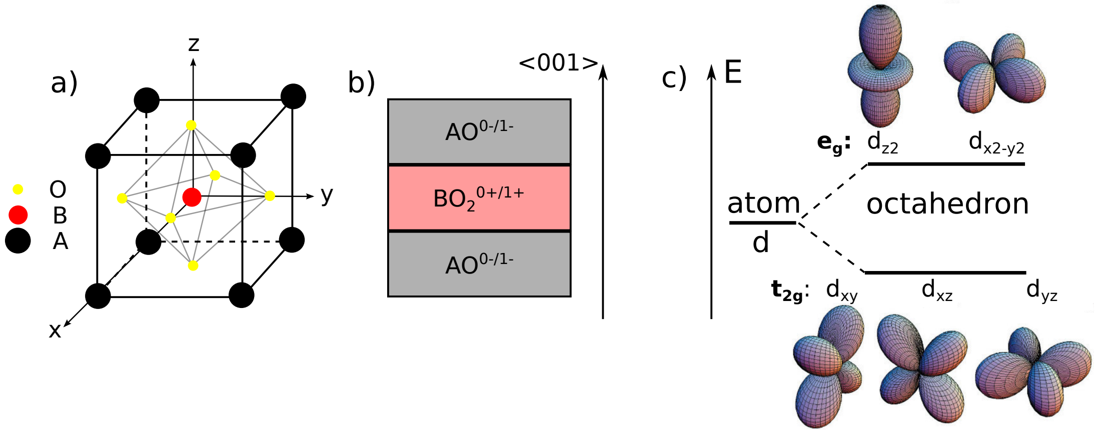

Figure 1.1: Cubic perovskite unit cell. The oxygen anions (yellow spheres) form an octahedron (gray lines) around the transition metal cation (red sphere). The alkali metal/earth alkaline metal cations (black spheres) are situated in the corners of the unit cell. Along the <001> direction, the perovskite structure can be represented by the alternating stacking of AO and BO_2 planes. Depending on the oxidation state of the metal cations, the planes can be either charge neutral or single charged. (c) Lifting of the degeneracy of d orbitals in an atom due to a crystal field of octahedral symmetry in a solid as shown in (a). The eigenenergies of the d states split in t_{2g} and e_g states. The probability amplitude of the d wave functions shown in (c) was taken from reference [32].

alkaline earth metal, B a transition metal and O oxygen. In this case, the oxidation states are: -II for oxygen, +I/+II for A and +IV/+V for B. A cubic perovskite lattice is shown in figure 1.1(a) on page 8. The lattice is ionic and thus consists out of O^{2-} anions, $B^{4+/5+}$ cations and $A^{+/2+}$ cations. Not only the oxidation state of the individual ions is of importance for the properties of perovskites, but also the charge state of alternating planes. As shown in figure 1.1(a), the lattice consists of alternating planes of AO and BO_2 along the <001> direction which can be either electrically neutral or charged based on the oxidation state of the ions. This potential polarity influences the lattice structure and the electronic structure at the surface and interface of oxides. [26, 51]

There are three common lattice distortions of the cubic perovskite lattice described above: the first one is an off-center displacement of the B cation in the oxygen octahedron (ferroelectric distortion). The second one consists of opposite rotations of the oxygen octahedra (antiferrodistortive distortions). The third one which will not be discussed here is a deformation of the oxygen octahedron (Jahn-Teller distortions). Which one of the first two distortions is present depends on the ratio between the ionic radii of the A and B site cations and can be estimated by Goldschmidt's tolerance factor t [52]:

$$t = \frac{r_A + r_O}{\sqrt{2}(r_B + r_O)}.$$

A tolerance factor equal to one means that the ionic radii r_A, r_B and r_O have values so that all the anions barely touch the cations and hence, that the cubic phase is stable. An instructive example are the titanates ($ATiO_3$) which show either ferroelectric distortions, rotations of the

Material	$CaTiO_3$	$SrTiO_3$	$BaTiO_3$
tolerance factor	0.97	1.01	1.08

Table 1.1: Tolerance factor of some perovskite materials using ionic radii from reference [54].

oxygen octahedra or none of the two depending on the size of the A site cation. For $BaTiO_3$, the Ti^{4+} cation is too small to fit well in the oxygen octahedron ($t > 1$) and hence, tends to move off center. This off-center movement is responsible for the ferroelectricity in $BaTiO_3$. For $SrTiO_3$, the tolerance factor is close to one ($t \approx 1$) and consequently, the lattice is perfectly cubic at room temperature. In $CaTiO_3$, an antiferrodistortive ordering is observed as the oxygen octahedra are tilted and form a orthorhombic lattice ($t < 1$) (see short discussion in review by Zubko *et al.* [53]).

Other examples for phase transitions depending on the size of the A site cation are the rare earth nickelates ($RNiO_3$) and manganites ($RMnO_3$) as shown in figure 1.2(a) on page 10. In both materials, the ionic radii of the rare earth (r_R) alters the rotation of the oxygen octahedra and hence, the Ni-O-Ni or Mn-O-Mn bonding angle. The alteration of the bonding angle results in a insulator-to-metal transition and a change of the Néel temperature in nickelates [55] as well as the orbital and spin ordering temperatures in manganites [56].

In principal, the tolerance factor can be tuned continuously by doping the A-site. The complex phase diagram due to this fine tuning plus electron doping can be observed for $La_{1-x}Sr_xMnO_3$ [57] as displayed in figure 1.2(b).

Another possibility to alter the lattice distortions is stress or pressure. This is of course true for any material, but the stress or pressure induced alterations can result in dramatic phase transitions due to the competing phases in perovskites (one highly cited example is the coexistence of metallic and insulating phases in a strained manganite [58]).

Electronic structure

Next, I will discuss the electronic structure of perovskite materials. The valence band is formed mainly by the $2p$ orbitals of the oxygen anions and the conduction band by the d orbitals of the transition metal. The covalent bonding between the transition metal and oxygen results in a hybridization of the d orbitals of the transition metal and the $2p$ orbitals of the oxygen (as demonstrated *e.g.* in the case of TiO_2 anatase in figure 7 in reference [61]). Consequently, a fraction of the valence band is made out of d orbitals of the transition metal and a fraction of the conduction band out of $2p$ orbitals of oxygen. The octahedral symmetry of the oxygen ions around the transition metal results in a crystal field which will lift the degeneracy of the d states and split them in a lower t_{2g} triplet and an higher e_g doublet as shown in figure 1.1(c) on page 8.

While discussing the possible lattice distortions in perovskites, the interaction between the lattice and electronic structure became already evident. Depending on the bonding angle between the

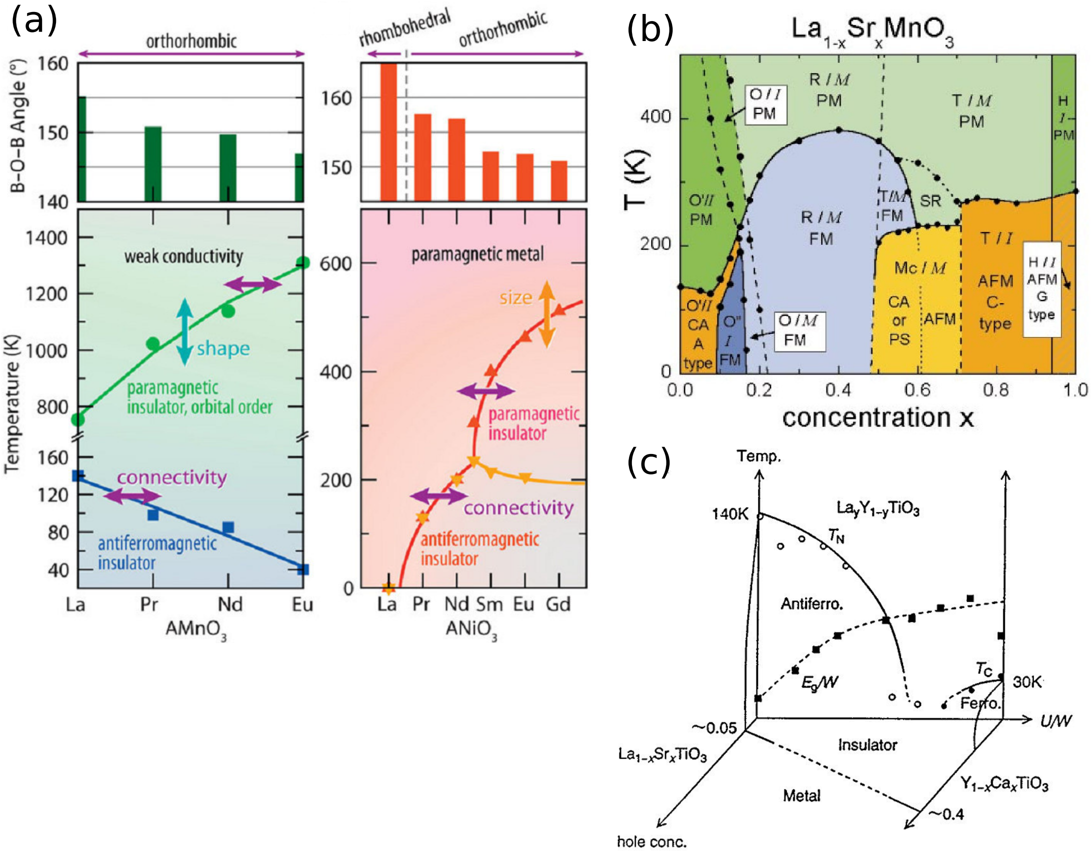

Figure 1.2: Phase diagram of nickelates, manganites and titanates. (a) The electronic properties as well as the temperature of phase transitions depend on the tolerance factor or respectively the bonding angle between transition metal and oxygen. Taken from reference [59]. (b) The interplay of the change in tolerance factor as well as electron doping results in a highly complex phase diagram in $La_{1-x}Sr_xMnO_3$. Taken from reference [57]. (c) Adding electron correlation as another parameter yields a phase diagram as the one shown *e.g.* for the rare earth titanates. Taken from reference [60].

transition metal and oxygen, insulator to metal transitions and changes in the spin/ magnetic as well as the orbital order can occur. Thus, in perovskites the electronic structure depends strongly on the lattice structure and vice versa. One of the most prominent examples is the colossal magnetoresistance in manganites. [62] Another prime example which is a very active field in solid state research today are multiferroics. Multiferroics are both ferroelectric and ferromagnetic, and one of the focuses of the research community is on the perovskite $BiFeO_3$. [63] An example of a striking phenomenon believed to be entirely due to correlated electrons is the high T_C superconductivity in cuprates, like $YBa_2Cu_3O_{7-x}$, which have a structure closely related to the one of the perovskites. And of course, the Mott insulating state (found *e.g.* in the $RTiO_3$ family, R=rare earth) is a prime example of a novel state of matter directly emerging from strong electron interactions in a material. [60]. The interplay of structure, doping and electron correlations is demonstrated in the phase diagram of the rare earth titanates in figure 1.2(c).

Interfaces

As already mentioned several times, the complex physics in the bulk of single crystals of transition metal oxides can be altered dramatically due to perturbations. Another possible perturbation is the breaking of the translational symmetry of the lattice structure, like *e.g.* at the surface or at domain/ twin boundaries of the crystal or at the interface of a perovskite heterostructure. Over the last 20 years the progress in epitaxially grown transition metal oxides has been continuous and today, perovskite heterostructures can be grown with atomic sharp interfaces. [64, 65] The interest in oxide heterostructures is huge and is ranging from novel transport, magnetism, ferroelectric to quantum confinement phenomena as reviewed in the December issue of the MRS Bulletin in 2013 [66–70] or in the review of Zubko *et al.* [53]. Of the many phenomena, the discovery [20] of a metallic, two dimensional electron system at the interface of two insulating oxides ($LaAlO_3$ grown on $SrTiO_3$) is of special importance for this thesis. Several reviews discuss the particularity of this 2DES from both a fundamental as well as device oriented point of view. [71–73] Its electronic properties range from field-effect induced insulator-to-superconductor transitions [21] and magnetism [22] to the coexistence of magnetism and superconductivity [23–25].

In this context, the discoveries that 2DESs can also be created at the bare (001) surfaces of $SrTiO_3$ and $KTaO_3$ opened new roads in the fabrication and study of different types of 2DESs in transition metal oxides. [1–4]

$SrTiO_3$

The 2DESs at the various surfaces of the perovskite $SrTiO_3$ is one of the major topics of this thesis. At first glance, stoichiometric bulk $SrTiO_3$ at room-temperature does not seem to bear interesting physics as it is a paralectric, paramagnetic band-insulator with a indirect band-gap of ca 3.2 eV. But $SrTiO_3$ shows non-trivial properties at very low temperatures (*e.g.* superconductivity [74, 75] in electron-doped crystals and quantum critical behavior towards ferroelectricity[76, 77] at $T < 1$ K), due to doping with oxygen vacancies (*e.g.* magnetism [78] and electron confinement

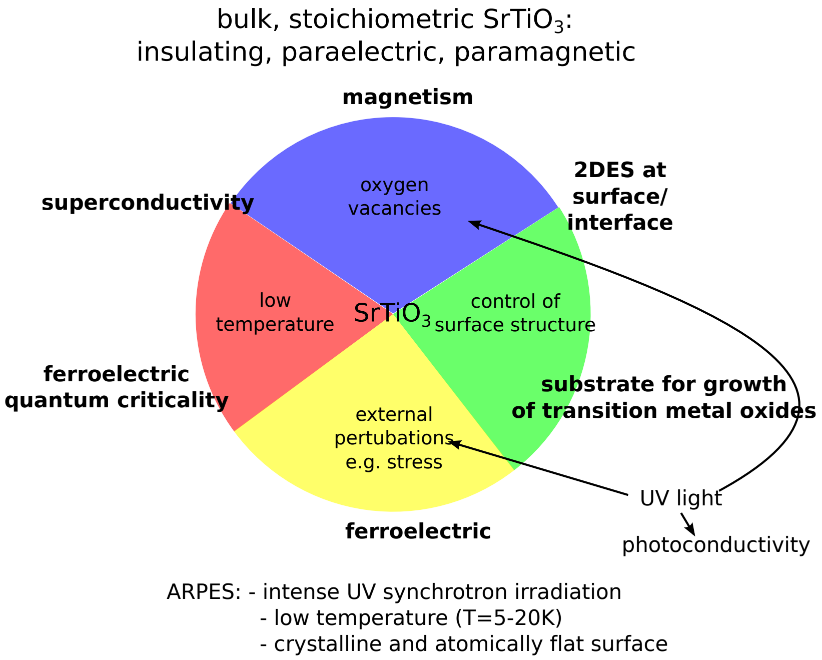

Figure 1.3: Properties of $SrTiO_3$ depending on presence of oxygen vacancies, temperature, perturbations and the control of the surface structure. Although $SrTiO_3$ is a paramagnetic, paraelectric and band insulating material in its stoichiometric form, various different properties emerge by slightly disturbing the system. Oxygen vacancies can lead to a 2DES confined at the surface, magnetism and superconductivity at low temperatures. The incipient ferroelectric state can be tuned to a real ferroelectric state by *e.g.* A-site doping or strain in thin films of $SrTiO_3$. UV-light which we used as an experimental probe can create oxygen vacancies or influence the polar order of $SrTiO_3$.

at the surface [1]) and due to perturbations (*e.g* ferroelectricity [79]). This is summarized in figure 1.3 on page 12. The discovery of 2DESs at the interface with/ the surface of $SrTiO_3$ resulted in a renewed interest in this perovskite and an abundance of literature is published on the properties of $SrTiO_3$ - some of them will be discussed later on in more detail. To sum up, the variety of properties in $SrTiO_3$ ranging from superconductivity, (ferro)magnetism, (incipient) ferroelectricity, ferroelasticity, electron confinement and interface physics make it possible to study a large fraction of properties and phenomena occurring in solid state physics in one material.

1.1.2 Binary oxides: TiO_2 and ZnO

Rutile and anatase

In its pure stoichiometric form, TiO_2 is a transparent insulator that crystallizes mainly in two different phases: rutile and anatase.

Similar to the perovskite lattice, the oxygen anions form octahedra around the transition metal cation (Ti^{4+}). The difference between the two phases is in the stacking order of the distorted octahedra as shown in figure 1.4 on page 13. The unit cell is body-centered tetragonal in both

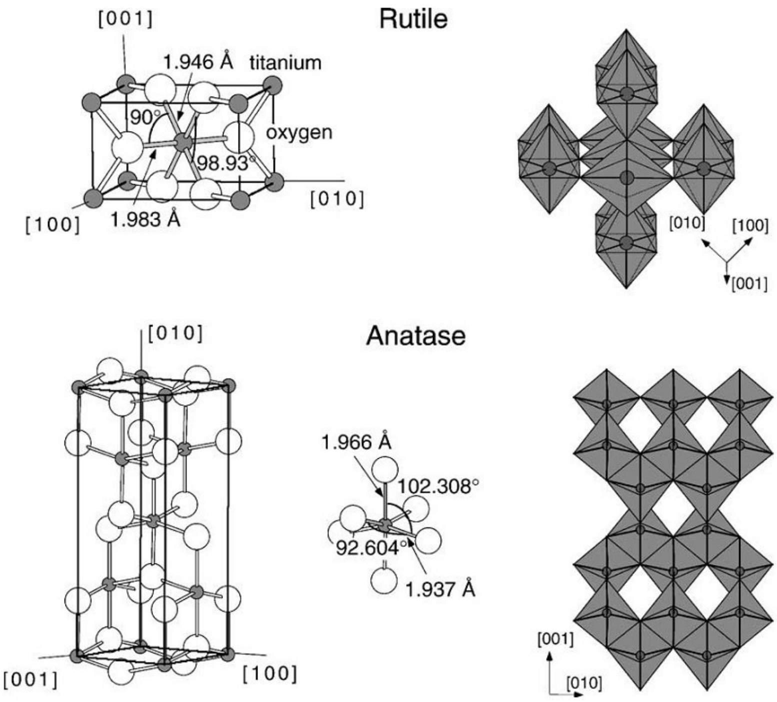

Figure 1.4: Taken from reference [80]: Tetragonal unit cell of anatase and rutile. The oxygen anions (black circles) form distorted octahedra around the Ti cation (gray spheres). The stacking order of the octahedra is different in anatase and rutile.

phases in contrast to the cubic (or close to cubic) unit cell of a perovskite lattice.

Both phases have been studied extensively over the last decades, mainly due to their photocatalytic properties discussed in several reviews [43, 80–82].

Recently, a strong interest in the anatase phase of TiO_2 also surged in other research fields. For instance, networks of anatase nanoparticles are found in dye-synthesized solar cells [83, 84], anatase thin films can be used as transparent conducting oxides [85], and devices based on anatase can function as memristors [38, 86] or can be envisioned in spintronics [87, 88].

To harness such a wide range of functionalities and guide potential applications using anatase, it is important to understand its microscopic electronic structure, which will be ultimately responsible for the remarkable properties of this material. Moreover, as most applications in microelectronics or heterogeneous catalysis involve essentially the electronic states at the material's surface/interface, it is crucial to directly measure and characterize such states as described in section 3.3.

Wurtzite ZnO

ZnO is a wide band-gap insulator which crystallizes in the wurtzite form with lattice constants a=3.25 Å and c=5.2 Å as shown in figure 1.5 on page 14. In contrast to the transition metal oxides discussed above, the lattice of ZnO is of hexagonal symmetry and the oxygen anions are forming a tetrahedron around the Zn cation. The crystal field related to this tetragonal oxygen

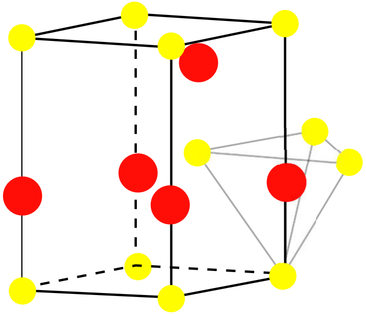

Figure 1.5: Wurtzite unit cell. The oxygen anions (yellow spheres) form an tetrahedron (gray lines) around the transition metal cation (red sphere).

configuration results in orbital ordering different to the octahedral configuration. The electronic configuration of the Zn^{2+} is a full d^{10} shell which is again in contrast to the empty d^0 shell of the Ti^{4+}-based systems. Due the full d shell, ZnO is often not considered as a transition metal oxide but rather as an oxide semiconductor.

Several reviews [89, 90] and books [91, 92] discuss properties and (potential) applications of ZnO-based systems.

From a fundamental point of view, the 2DES in a $Mg_xZn_{1-x}O$/ZnO based heterostructure is of interest as it was the first oxide system in which the integer and fractional Quantum Hall effects were measured. [93, 94] Until these discoveries, the Quantum Hall effects were reserved to classical semiconductor heterostructures as a high electron mobility is necessary to observe it. These observations evidence the improvements in oxide thin film growth over the last two decades.

1.2 Discovery: 2DES at the surface of fractured $SrTiO_3$(001)

After the general discussion of the physics and properties of transition metal oxides, we will start to focus on the main topic of this thesis. As already outlined above, 2DESs at the surfaces and interfaces of $SrTiO_3$ are an active field of research in the oxide community. In general, systems of low dimensionality are of interest because their properties can vary significantly from their 3D counterpart.

Photoemission results on $SrTiO_3$(001)

The main motivation of this thesis was the discovery of the two-dimensional electron system (2DES) at the surface of fractured $SrTiO_3$. [1, 2] The results are briefly summarized in figure 1.6 on page 15. This discovery was quite surprising as $SrTiO_3$ is an insulating oxide and the presence of a confined metallic state at the surface of this insulator is far from intuitive.

The technique used to observe the 2DES was photoemission spectroscopy. In photoemission experiments, photoelectrons are excited by UV-photons and their energies and emission angles are analyzed to obtain the electronic band structure (see chapter 2). As shown in figure 1.6(d), three parabolic bands corresponding to the t_{2g} were observed and assigned to 2D states confined in a potential well.

Different mechanism responsible for the creation of 2DESs in $SrTiO_3$ are discussed below.

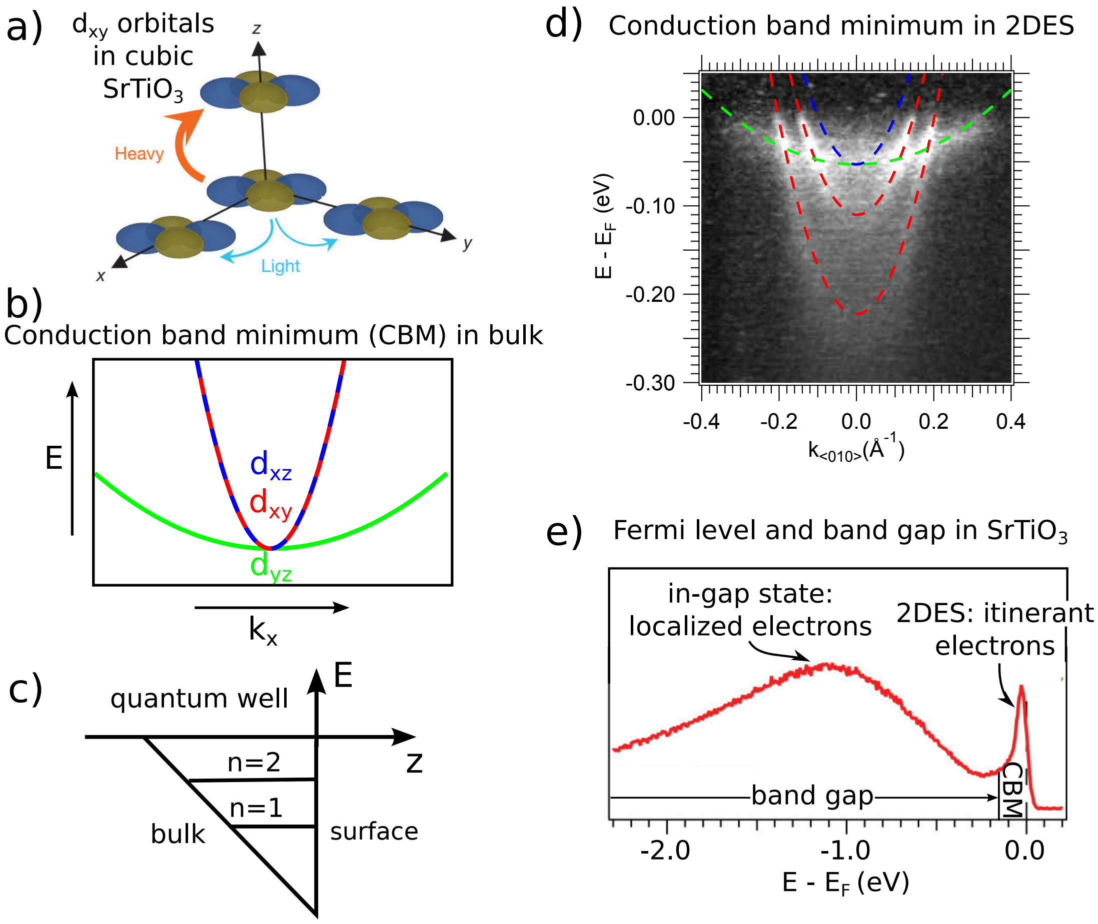

Figure 1.6: (a) d_{xy} orbitals in cubic SrTiO$_3$. The overlap of the orbital is large in x or y direction but small in z direction. Taken from reference [1]. (b) As a consequence, the conduction band minimum (CBM) in the bulk consists of light and heavy bands. (c) The confinement of the electrons in a triangular potential well results in the quantization of the eigenenergies. (d) The combination of bulk electronic structure and confinement leads to orbital ordering and the presence of two d_{xy} subbands in the 2DES at the surface of SrTiO$_3$. The color map shows the measured ARPES intensity where white corresponds to a high intensity and black to a low one. The dashed lines correspond to parabolic fits of the measured bands. Note that the shown intensity map is a superposition of two measurements which are shown and discussed in figure 4.4 on page 75. (e) The metallic behavior at the surface of insulating SrTiO$_3$ is related to electron doping due to oxygen vacancies. The electron released by the oxygen vacancy can either form itinerant electrons at the Fermi level E_F (2DES) or localized electrons in the band gap (in-gap states). These different states are shown by the red curve representing the electronic density of states measured by photoemission.

Creation of 2DESs in $SrTiO_3$

In $SrTiO_3$ there are two main mechanisms to create 2DESs:

1. local chemical doping
   (a) by growing $SrTiO_3$ thin films doped with an electron donor (*e.g.* Nb [95] or La [96])
   (b) by creating oxygen vacancies (double electron donor) close to the surface/ interface
      i. by growing a metal/ metal oxide which acts as an oxygen sink (*e.g.* Al oxides [97] and section 4.2)
      ii. by desorption induced by electronic transition (see section 3.1)
2. electrostatic doping
   (a) by the field effect at the interface of $SrTiO_3$ or $KTaO_3$ and an electrolyte [98, 99]
   (b) by the polar catastrophe of crystalline oxide heterostructures (*e.g.* $LaAlO_3/SrTiO_3$ [26])

In all cases the electrons are confined in a quantum well. A more detailed review of band bending mechanism at the surface of semiconductors/ insulators is given by Zhang *et al.* [81]. The band bending can also be affected by the surface structure, especially surface reconstructions and/or the crystallographic surface orientation.

Potential well at the surface of $SrTiO_3$

First, let us assume that a given concentration of positively charged oxygen vacancies N_{V_o} creates an electric field $F(z)$ confining electrons. [1–4, 9] Note that I assume that the oxygen vacancy is a double donor, resulting in two electrons per vacancy. A simple model usually applied in semiconductor physics (Schottky approximation) is that the charge concentration ρ is homogenous in a layer of thickness d and abruptly drops to zero beyond that layer:

$$\rho = \begin{cases} 2eN_{V_o}, & \text{for } 0 \leq z \leq d, \\ 0, & \text{for } z > d \end{cases}$$

where e is the elementary charge and $z = 0$ corresponds to the surface. In the case of the distribution of oxygen vacancies at the surface of $SrTiO_3$, this is a crude approximation. As the vacancies are created by desorption of oxygen (see section 3.1) one could assume that the concentration of vacancies is the highest in the surface layer and declines continually towards the bulk. For reasons of simplicity of the model and lack of experimental studies yielding the exact distribution of oxygen vacancies , we will continue to use the Schottky approximation.

The confining potential $V_{conf}(z)$ can be obtained by using the one-dimensional Poisson's equation

$$\frac{\partial^2 V_{conf}(z)}{\partial z^2} = -\frac{\rho}{\epsilon_r \epsilon_0} \tag{1.1}$$

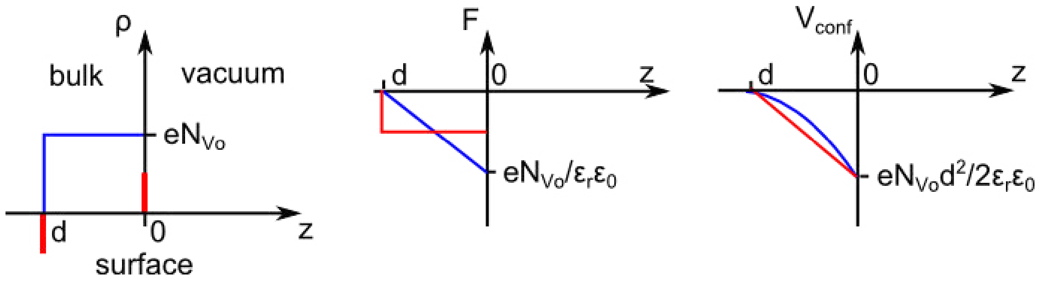

Figure 1.7: The charge concentration ρ, the electric field $F(z)$ and the confining potential $V_{conf}(z)$ of the Schottky model (blue curves) and its approximation (red).

where ϵ_0 is the vacuum permittivity and ϵ_r the relative permittivity. This equation yields

$$F(z) = \frac{2eN_{V_o}}{\epsilon_r \epsilon_0}(z-d), \quad \text{for } 0 \le z \le d \tag{1.2}$$

for the confining field $F(z)$ and

$$V_{conf}(z) = -\frac{eN_{V_o}}{\epsilon_r \epsilon_0}(z-d)^2, \quad \text{for } 0 \le z \le d \tag{1.3}$$

for the confining potential $V_{conf}(z)$. d is the elongation of the confining field $F(d) = 0$ and potential $V(d) = 0$. The band offset at the surface is $V_{conf}(0) = -(eN_{V_o}d^2)/(\epsilon_r\epsilon_0)$.
The 1D Hamiltonian of non-interacting electrons in this potential well is:

$$H(z)\Phi(z) = \frac{p_z^2}{2m_z^*}\Phi(z) + V_{conf}(z)\Phi(z) = E_n\Phi(z).$$

where m_z^* is the effective mass along the confinement direction which also depends on the symmetry (*i.e.* the azimuthal quantum number) of the concerned d orbitals. An approximation which facilitates the analytical solution of the Hamiltonian H is to consider that the confining potential is linear in z (*i.e.* a triangular potential well)

$$V_{conf}(z) \approx (z-d)F$$

with a constant electric field $F = (eN_{V_o}d)/(\epsilon_r\epsilon_0)$ which physically corresponds to a parallel plate capacitor with plate separation d and surface charge carrier densities of $eN_{V_o}/2$. The charge concentration ρ, the electric field $F(z)$ and the confining potential $V_{conf}(z)$ of the Schottky model and its approximation are shown in figure 1.7.

Using the variable transformation $z - d = \left(\frac{\hbar^2 e^2 F^2}{2m_z^*}\right)^{\frac{1}{3}}/(eF - E_n)\zeta$, the Hamiltonian yields the Airy equation:

$$\frac{d^2}{d\zeta^2}\Phi(\zeta) - \zeta\Phi(\zeta) = 0.$$

with Airy functions as eigenfunctions $\Phi(\zeta)$. The corresponding eigenvalues E_n are: [100]

$$E_n = V_{conf}(0) + \left(\frac{\hbar^2}{2m_z^*}\right)^{\frac{1}{3}} \left[\left(\frac{3\pi}{2}\right)\left(n - \frac{1}{4}\right) eF\right]^{\frac{2}{3}} \tag{1.4}$$

We will use the eigenvalues E_n later on, to estimate the extension of the electronic states confined at the surface. Note that differences in effective mass m_z^* due to a different orbital character will results in a splitting of the eigenenergies E_n of the bulk-degenerate t_{2g} manifold as shown in figure 1.6 on page 15.

The energy splitting of two subbands $\Delta E \equiv E_2 - E_1$ of same orbital character can be used to obtain the confining electric field:

$$F = \left(\frac{\hbar^2}{2m_z^*}\right)^{-\frac{1}{3}} \left(\frac{3\pi}{2}e\right)^{-\frac{2}{3}} \left[\left(\frac{7}{4}\right)^{\frac{2}{3}} - \left(\frac{3}{4}\right)^{\frac{2}{3}}\right]^{-1} \Delta E. \tag{1.5}$$

The confining field F and equation (1.4) yield the potential well depth $V_{conf}(0)$ and the spatial extension $d = -V_{conf}(0)/F$.

The model of the triangular potential well model discussed above captures the main features of electron confinement at the surface of $SrTiO_3$ based on analytical solutions of the 1D Hamiltonian. However, three approximations are necessary to justify this model: 1. the homogenous distribution of positively charged defects confining the electrons (Schottky approximation); 2. the linear approximation of the confining potential $V_{conf}(z)$; 3. the spatial independence of the relative permittivity ϵ_r(z) which is only justified in a constant electric field F (*i.e.* linear potential) as ϵ_r exhibits a large field-dependence $F(z)$ in $SrTiO_3$ as shown in figure 6.1(b) on page 106. Meesevana *et al.* overcame the 2. and 3. approximation by using coupled Poisson-Schrödinger calculations including the field-dependence of the relative permittivity to model the band bending at the surface of $SrTiO_3$. [2] In this approach [101], a z-dependent electron density $n(z)$ is added next to the homogenous density of positively charged donors in the Poisson equation 1.1 on page 16. This electron density $n(z)$ is calculated based on the density of states $D_{CB}(E)$ of the confined conduction band states and the z-dependent factor $g(z)$ based on the modified Thomas-Fermi approximation which models the potential barrier at the surface: [101]

$$n(z) = \int_{E_C}^{\infty} D_{CB}(E) f(E,T) g(z) dE \tag{1.6}$$

where E_C is the energy of the conduction band minimum and $f(E,T)$ is the Fermi-Dirac distribution defined in equation 2.17 on page 32. Next, the confining potential V_{conf} is obtained from the Poisson equation and used to numerically solve the 1D Hamiltonian yielding the wave function and energy eigenvalues E_n of the confined states.

Next to the scenario based on electron confinement due to oxygen vacancies confined close to the surface, Plumb *et al.* proposed that the band bending occurs because of ferroelectric distortions of the lattice [7, 102]. The distortions/ relaxations are most pronounced at the surface layer and damped in the subsequent layers. Hence, there is a gradient in the polarization density $P(z)$

and consequently in the electric displacement field D(z). The first Maxwell's equation (Gauss's law):

$$\frac{dD(z)}{dz} = n(z)$$

relates this gradient to the free charge carrier density $n(z)$ (electrons in the conduction band). It is important to understand that the two described mechanism cannot be considered exclusively. One one hand, an oxygen vacancy can influence the lattice dynamics (*e.g.* polarons in TiO_2 [103]), on the other hand can lattice distortions and the resulting charge transfer from oxygen to titanium facilitate the creation of oxygen vacancies. Another mechanism whose role and influence on the above mentioned mechanisms is not clear at present is the photovoltaic effect, *i.e.* the excitation of electrons from the valence to the conduction band. For example, the luminescence properties of $SrTiO_3$ have been discussed controversially [104–106].

The triangular potential well model discussed in this section helps to understand the ARPES results on the 2DES at the surface of $SrTiO_3(001)$ shown in figure 1.6 on page 15. Using the splitting of different subbands, equation (1.4) can be used to characterize the triangular potential well: electric field $F \approx 220$ MV/m; well depth $V_{conf}(0) \approx -370$ meV; spatial extension $d = 17$ Å (calculation based on data presented in figure 4.4 on page 75).

These values can be used to approximate the oxygen vacancy concentration $N_{V_o} = (\epsilon_r \epsilon_0 F)/(ed)$. However, one needs to approximate the relative permittivity ϵ_r which depends on the electron density in $SrTiO_3$ (see discussion in chapter 6) and the confining electric field [107, 108]. At an electric field of about $F \approx 220$ MV/m, the relative permittivity is $\epsilon_r \approx 70$ and is nearly temperature independent [107]. This yields a fraction of oxygen vacancies of $N_{V_o}/N_o \approx 1\%$ where N_o is the concentration of oxygen anions in $SrTiO_3$.

This discovery motivated many subsequent studies and raised many questions:

- Does the 2DES only exist at fractured surfaces (used in the original studies) or are other surface preparations possible?
- Details of doping mechanism? How are oxygen vacancies created?
- Control of level of electron doping?
- Are 2DESs a general phenomena at the surface of oxygen-deficient d^0 transition metal oxides?
- How can one alter the properties of the 2DES?
- Why are there localized as well as delocalized/ itinerant electronic states due to electron doping?
- Details of electronic structure? Spin structure? Many body effects?
- Is it possible to transform the 2DES in UHV into an inert 2DES that can be measured at ambient conditions?

As already mentioned, the discovery of this 2DES was made by using angle-resolved photoemission spectroscopy. Moreover, most of the experimental results presented in this thesis are based on ARPES measurements. Consequently, I will introduce the technique in the next chapter.

Chapter 2

Experimental - ARPES

This section is mainly based on the reviews of A. Damascelli and F. Reinert & S. Hüfner [109, 110], the slides of a presentation given by R. Claessen at the SUCCESS-2014 summer school and some of the following paragraphs are taken from my master thesis [111].

2.1 Photoemission basics

In the 19th century, it was experimentally observed by H. Hertz that charged particles are emitted from a solid when illuminated with UV light. His former assistants (W. Hallwachs and P. Lenard) continued his work and in 1899, P. Lenard identified the charged particles as electrons using a vacuum setup. In 1905, A. Einstein explained the photoelectric effect by assuming that radiation is made out of quanta - the photons. He predicted that the emitted electrons have a maximal kinetic energy of $E_{\text{kin, max}} = h\nu - \Phi$. ν is the frequency of the radiation and Φ is the work function - a characteristic constant of the sample surface [112].

The maximum kinetic energy is the one of electrons at the Fermi level. If an electron with a binding energy E_B with respect to the Fermi energy E_F is emitted, its kinetic energy is [109]:

$$E_{kin} = h\nu - \Phi - |E_B|. \tag{2.1}$$

in accordance with energy conservation. In the remaining of this chapter, the index B of E_B will not be explicitly written and E will refer to the binding energy.

In an photoemission experiment the kinetic energy E_{kin} can be measured by an electrostatic analyzer. A schematic of the setup of the experiment is shown in figure 2.1 on page 23. Monochromatic photons with energy $h\nu$ are emitted from a light source, *e.g.* a helium discharge lamp or a synchrotron (see section 2.3). The photons hit the sample and thereby, electrons are emitted from the surface at an angle θ_e and with the kinetic energy E_{kin} from equation (2.1). The electrostatic analyzer uses a more or less sophisticated retarding electric field to obtain the intensities of electrons with different kinetic energies. Then, a detector (multi-channel plate + fluorescent screen + CCD camera) counts the intensity of emitted electrons with a given kinetic energy.

With equation 2.1, the obtained kinetic energy is used to calculate the binding energy of the electrons in the solid. The work function Φ is constant and can be determined by photoemission experiments, but for determining the binding energy it is usually easier to use the measured Fermi level E_F as a reference: $|E_B| = E_{kin,F} - E_{kin}$ where $E_{kin,F}$ is the kinetic energy of electrons at the Fermi level.

The number of electrons detected at a certain kinetic energy is proportional to the density of states $D(E)$ at the corresponding binding energy of the electron in the solid. A schematic of a spectrum obtained in a photoemission experiment and its relation to the energy levels in a solid are shown in figure 2.2 on page 24. The figure is also used to define various energies which will be used in the following.

The measured intensity related to core electrons can be used for the chemical analysis of the surface region or to detect the local chemistry/ bonding environment of a given element. In this thesis, core-level analysis is used to determine the oxygen stoichiometry in transition metal oxide surfaces, the band bending at the surface of TMOs as well as the oxidation state of metal thin films grown on top of the oxide.

Angular distribution of photoelectrons

But the major part of this thesis focuses on the analysis of the angular distribution of the photoelectrons which correspond to the valence electrons of the solid. Using modern hemispherical analyzers the angular distribution of the photoelectrons at the entrance slit can be imaged at the detector plane.

As shown schematically in figure 2.1(b) on page 23 the electrostatic lens focuses all electrons emitted at the same angle η on one point in the image plane (entrance slit). The angular range of η can be chosen by adapting the electrostatic lens. However, in practice the voltages of the electrostatic lens are optimized for one or two angular ranges. In this thesis, almost all data was measured using an angular range of $\eta = [-15°, +15°]$. To measure a large range of kinetic energies of photoelectrons E_{kin} a retarding potential U_r is varied in the electrostatic lens to adapt the kinetic energy to the pass energy of the hemispherical analyzer: $PE = E_{kin} + U_r$ (see figure 2.1(b)).

The voltage bias between the two hemispheres of the analyzer is usually constant and thus, only electrons whose energy is equal to the pass energy ($\pm 10\%$) arrive at the detector. The major advantage of using a constant voltage bias is that the energy resolution is fixed independent of the kinetic energy of the emitted photoelectrons.

Finally, a multi-channel plate (MCP) increases the electron signal and the CCD camera images a fluorescent screen showing a two-dimensional intensity map composed of different angles and kinetic energies of the photoelectrons as shown in figure 2.1(c).

Using such a setup the band structure $E(\vec{k})$, the microscopic base to understand the macroscopic electronic properties of a solid can be measured. $\vec{k} = (k_x, k_y, k_z)$ is the momentum vector of the electron in the solid with k_z being the component perpendicular to the surface and k_x & k_y the

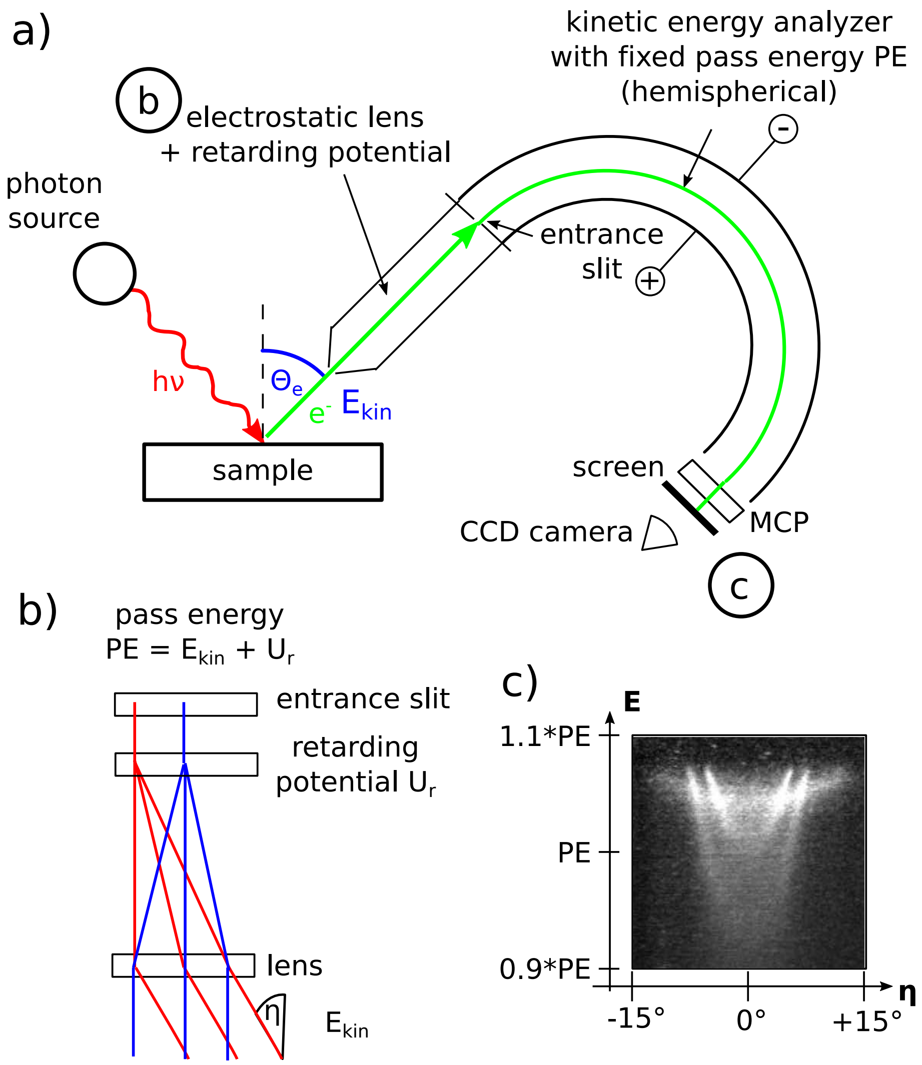

Figure 2.1: a) Schematic of the setup of a photoemission experiment. Monochromatic photons with energy $h\nu$ are emitted from a light source, *e.g.* a helium discharge lamp or a synchrotron. The photons hit the sample and thereby, electrons are emitted from the surface in an emission angle of θ_e and with the kinetic energy E_{kin} from equation (2.1) on page 21. After passing an electrostatic lens, an electrostatic hemispherical analyzer selects a small range of kinetic energies of the electrons: ±10% around the so called pass energy PE. To detect different ranges of kinetic energies, a retarding field in the electrostatic lens adapts the kinetic energy to the pass energy as shown in (b). The detector is composed out of a multi-channel plate, a fluorescent screen and a CCD camera. Adapted from Reinert & Hüfner [110]. b) To measure the angular distribution of photoelectrons, the electrostatic lens images electrons of identical emission angle η on the same point in the entrance slit and thus, on the same line of the 2D detector as shown in (c). c) The 2D detector measures the energetic and angular distribution of the photoelectrons yielding the band structure of solids.

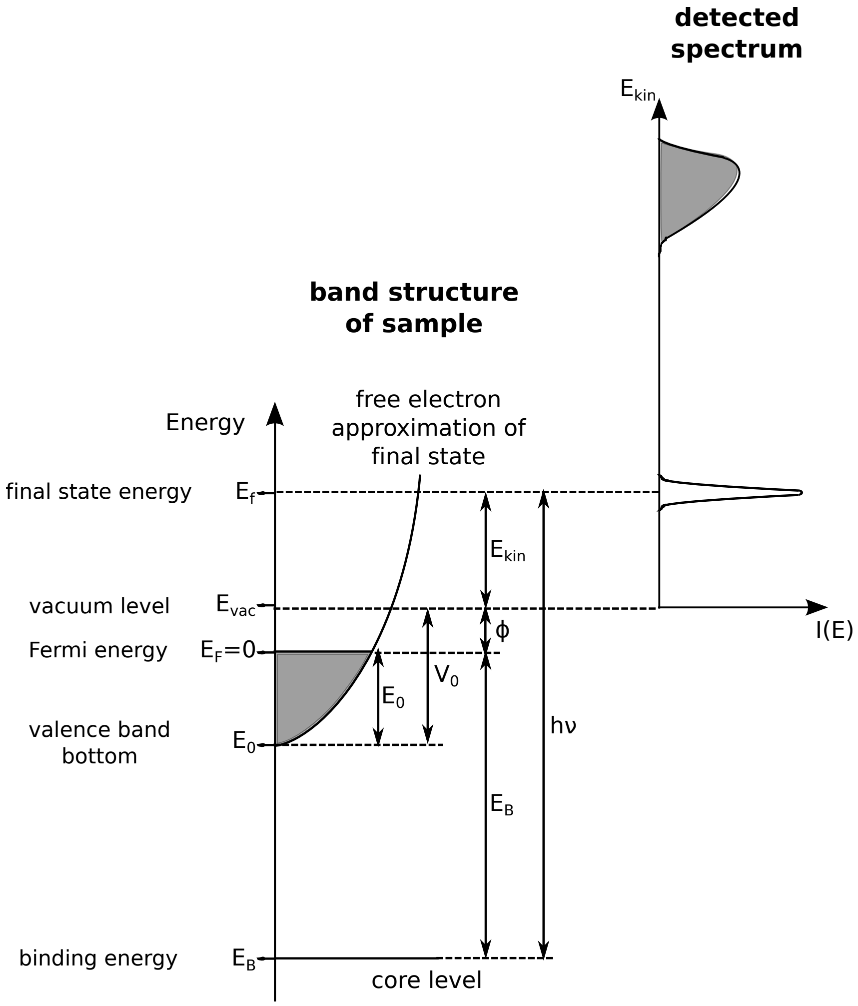

Figure 2.2: Schematic view of the photoemission process. On the left side a strongly simplified band structure of a sample is shown. It consists only of one core level and the valence band. The electron states are occupied up to the Fermi energy E_F which is defined as the energy zero $E_F = 0$. Electrons with the binding energy E_B are excited by photons with energy $h\nu$ to a final state with energy E_f. The kinetic energy E_{kin} of those electrons in vacuum is determined by equation (2.1) on page 21. The work function Φ is the energy between the Fermi energy E_F and the vacuum level E_{vac}. The final state of the photoexcited electron is modeled as a band of a free electron. The energy of the valence band bottom E_0 corresponds to the bottom of the free-electron parabola of the final state. Together with the vacuum level E_{vac}, E_0 defines the inner potential V_0. On the right side the detected spectrum of the band structure is shown. Taken from Reinert & Hüfner [110].

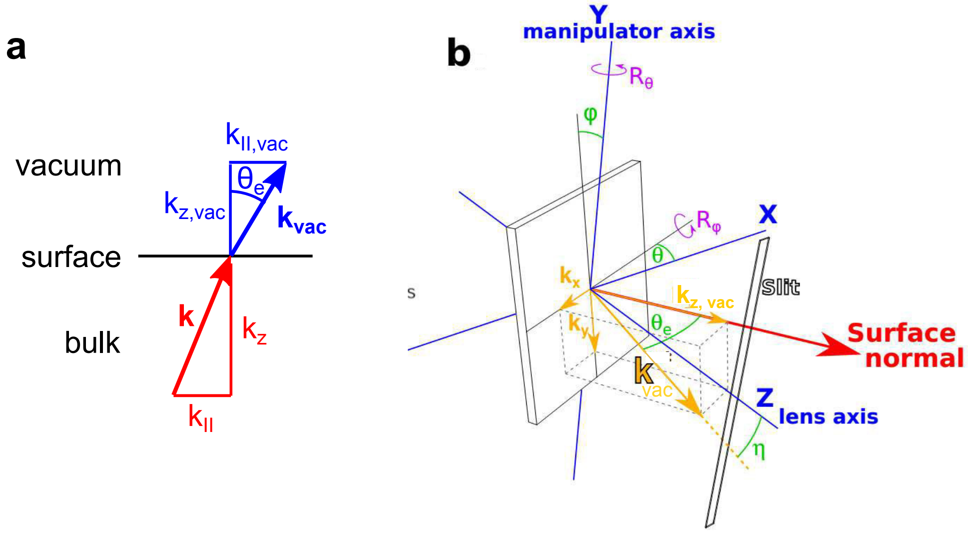

Figure 2.3: (a) Momentum of a photoelectron in the solid and in vacuum after overcoming the potential barrier at the surface. (b) Measurement geometry of sample and slit of the hemispherical analyzer in an ARPES experiment. Definition of angles θ_e, η, θ and ϕ as well as their rotation axis. Taken from C. Bareille [113].

components in the surface plane.

For a given measured kinetic energy E_{kin} and emission angle θ_e, the momentum of the electron in vacuum parallel $k_{||,vac}$ and perpendicular $k_{z,vac}$ to the surface can be calculated:

$$k_{||,vac} = \frac{\sqrt{2mE_{kin}}}{\hbar}\sin\theta_e \tag{2.2}$$

$$k_{z,vac} = \frac{\sqrt{2mE_{kin}}}{\hbar}\cos\theta_e \tag{2.3}$$

as illustrated in figure 2.3a. As the translational symmetry of the solid is conserved parallel to the surface, the momentum parallel to the surface is conserved. Thus, the parallel component of the momentum in vacuum can be directly converted to the one in the solid $k_{||} = k_{||,vac} = \sqrt{k_x^2 + k_y^2}$. To calculate the momentum perpendicular to the surface k_z, one has to take into account the energy loss of the electron due to the potential barrier at the surface of the solid.

$$k_{||} = \frac{\sqrt{2mE_{kin}}}{\hbar}\sin\theta_e \tag{2.4}$$

$$k_z = \frac{\sqrt{2m}}{\hbar}\sqrt{E_{kin}\cos^2\theta_e + V_0} \tag{2.5}$$

where V_0=$E_0 + \Phi$ is the so-called inner potential (see figure 2.2 on page 24). Note that under the assumption of nearly-free electrons as final states of the photoelectron in the solid in the three-step model (see next section), the kinetic energy of a photoexcited nearly-free electron *in* the solid is given with reference to the bottom of the valence band E_0 and not the Fermi level E_F. Hence, part of the valence electrons's binding energy E_B-E_0 is converted to kinetic energy and the energy loss of the electron at the surface is characterized by the inner potential V_0 and not the work function Φ. In practice, the inner potential V_0 is determined by measuring the periodicity of the electronic structure along k_z. Based on this measurement, V_0 is adjusted so that the k_z values of high symmetry points of the measured electronic structure correspond to the momenta of high symmetry points of the reciprocal lattice.

Experimentally, the emission angle is composed out of the three angles which are accessible/ changeable depending on the specific experimental setup. The angle η selected by the slit of the analyzer and measured by the CCD camera, θ due to rotation of the sample manipulator along the y-axis in the lab frame and ϕ due to a tilt of the sample along the axis defined by the vector $(\cos\theta, 0, \sin\theta)$, *i.e.* the x-axis in sample frame (see figure 2.3(b) for definition of angles and rotation axes). The k_x, k_y and k_z values of the electron can be obtained by rotating the k-vector

$$\vec{k}_{slit} = (0, \sin\eta, \cos\eta) \quad \text{(vertical slit)} \quad or \quad (\sin\eta, 0, \cos\eta) \quad \text{(horizontal slit)} \tag{2.6}$$

in the reference system of the analyzer's slit using two rotation matrices: $\vec{k_{vac}} = R_{\phi,x} R_{\theta,y} \vec{k}_{slit}$ Hence, to probe the reciprocal space (different k values of the electron in the solid), one needs to change η, θ or ϕ. Moreover, a change in the photon energy $h\nu$ changes the E_{kin} and consequently, also the probed position in reciprocal space.

2.2 ARPES: three-step-model

The preceding paragraphs gave a first idea of the photoemission process. However, photoemission is a more complex process. There are several assumptions and models to simplify the problem. The process of the excitation of an electron by a photon to the propagation of the electron in vacuum is modeled by the so-called three-step-model. The three steps in the solid: [109]

1. optical excitation of the initial electron (Bloch) state to the final state inside the solid
2. propagation of the electron in the solid to the surface
3. electron's crossing of the surface into vacuum by overcoming a potential barrier

are assumed to be independent from each other. A more accurate and complicated description is the one-step model which will not be discussed here.

1. step: optical excitation

In the first step the electron is excited due to the presence of an electromagnetic field. To describe the process mathematically, the electromagnetic field must be added to the Hamiltonian $\hat{H}$ of electrons in a solid. The perturbation Hamiltonian $\hat{H}_{int}$ is given by [110]:

$$\hat{H}_{int} = \frac{e}{2mc}\left(\vec{A}\hat{\vec{p}} + \hat{\vec{p}}\vec{A}\right) + \frac{e^2}{2mc^2}\vec{A}^2 \approx \frac{e}{mc}\vec{A}\hat{\vec{p}} \tag{2.7}$$

where c is speed of light in vacuum, $\vec{A}$ is the vector potential of the electromagnetic field and $\hat{\vec{p}}$ the electronic momentum operator. The vector potential $\vec{A}$ can be written as $\vec{A}(\vec{r},t) = A_0\vec{\epsilon}e^{i(\vec{q}\vec{r}-\omega t)}$ with A_0 being the amplitude, the vector $\vec{\epsilon}$ defines the light polarization, $\vec{q}$ the wave vector and ω the frequency of the electromagnetic wave. As the photons correspond to a weak perturbation of the total energy of the system, the electromagnetic field can be treated in first-order time-dependent perturbation theory. Thus, the eigenstates of the Hamiltonian are still Bloch waves. In UV-ARPES, photon energies lower than $h\nu < 100$ eV are usually used. As the corresponding wave length is much larger than the interatomic distance and hence the wave lengths of the Bloch functions, the factor $e^{i(\vec{q}\vec{r})}$ of the photon field can be approximated to one (dipole appoximation). Perturbation theory yields the probability w_{fi} that the electromagnetic field excites the electron from its initial state Ψ_i to its final state Ψ_f (Fermi's golden rule) [110]:

$$w_{fi} \propto \frac{2\pi}{\hbar} | < \Psi_f | H_{int} | \Psi_i > |^2 \delta(E_f - E_i - h\nu) \quad . \tag{2.8}$$

E_i is the energy of the initial state, E_f the one of the final state. The initial state Ψ_i is an eigenstate of the Hamiltonian $\hat{H}$ of the system consisting of N electrons. The final state Ψ_f is eigenstate of the $N-1$ electron system and the state of the photoelectron propagating in vacuum. The removal of one electron makes the final state Ψ_f substantially different from the initial state Ψ_i. To further simplify the process of the optical excitation, the so called sudden approximation is made. This approximation results in the factorization of the final state Ψ_f in two independent factors corresponding to the $N-1$ electron system and the photoelectron. Hence, the photoelectron is decoupled from the $N-1$ electron system and no interactions between the two occur.

2. step: propagation to the surface

During the second step the electron can be inelastically scattered. The scattering leads to a continuous background in the spectra recorded in an experiment. It is described by the mean free path of an electron in a solid which is the average distance an electron can propagate without being inelastically scattered. In figure 2.4 on page 28 the mean free path is shown as a function of the kinetic energy of the electrons. This dependence is called universal curve as it is approximately valid for many different materials. For UV-ARPES measurements the energy of the photons is around 20-100 eV corresponding to a mean free path of approximately 5 Å. Thus, ARPES is a surface sensitive technique.

3. step: emission into vacuum

In the third step (the escape of the electron from the solid) the electron needs a minimum energy to overcome the potential barrier of the surface (see previous section).

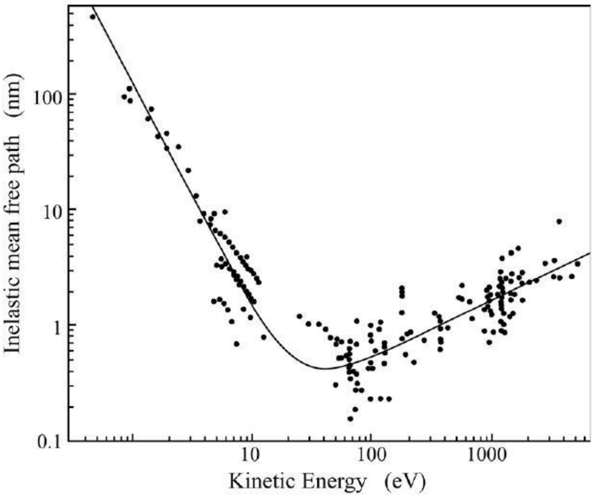

Figure 2.4: The universal curve [114] describes the dependence of the mean free path of an electron in a solid to the kinetic energy of the electrons. At a kinetic energy of 100 eV the mean free path is approximately 5 Å.

Photocurrent

The total measured intensity depends on all three steps. The photocurrent $I(E, h\nu)$ from a crystalline solid can be written as [115]:

$$I(E, h\nu) \propto |M_{fi}|^2 A(\vec{k}, E) f(E, T) \tag{2.9}$$

where $|M_{fi}|^2$ is a matrix element describing the optical transition of the photoelectron, $A(\vec{k}, E)$ the so-called spectral function (see below) and $f(E, T)$ the Fermi-Dirac function. The product $|M_{fi}|^2 A(\vec{k}, E)$ results from Fermi's golden rule in equation (2.8). In equation (2.9), multi-electronic effects contained in the spectral function $A(\vec{k}, E)$ are separated from a one-electron excitation described by the matrix element $|M_{fi}|^2$. The matrix element $|M_{fi}|^2$ describes the optical transition of the photoelectron using one electron wave functions and is proportional to [115]

$$|M_{fi}|^2 \propto | < \Phi_f | \hat{H}_{int} | \Phi_i > |^2 \tag{2.10}$$

with Φ_i the initial one-electron wave function of the electron before the optical excitation and Φ_f the final one-electron wave function of the electron in the solid after the optical excitation. All the interactions beyond the one electron/ independent particle picture are included in the spectral function $A(\vec{k}, E)$ which corresponds to the overlap between the wave functions of the remaining N-1 electron system of the initial and final state.

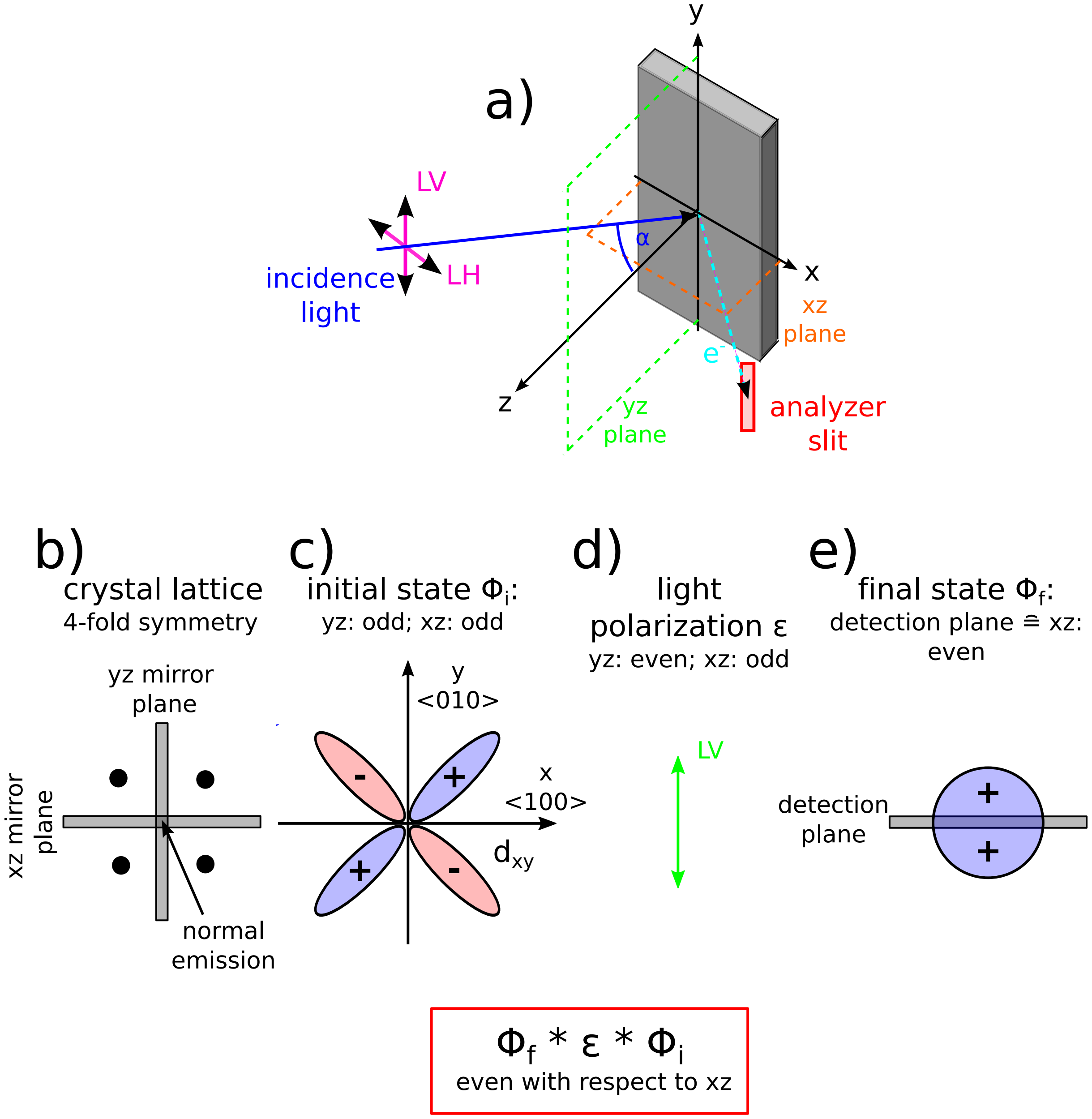

Figure 2.5: a) Sketch showing the ARPES setup including sample, incidence photon & photoelectron beam, analyzer slit, the xz & yz plane and the direction of linear horizontal and vertical polarization. Adapted from Yukawa *et al.* [6]. b) Cubic lattice of $SrTiO_3$ in the (001) plane and definition of mirror planes. (c) Parity of the initial state Φ_i (d_{xy}) and (d) light polarization ϵ with respect to the mirror planes (d). (e) Parity of the final state with respect to the detection plane corresponding to a mirror plane. For the given configuration, the matrix element $|M_{fi}|^2$ is non-zero as the product of $\Phi_f(\vec{r})$,$\Phi_i(\vec{r})$ and $\vec{\epsilon}\,\vec{r}$ is even (see equation (2.11)).

Matrix element

A quantitative analysis of the matrix element is complicated. But by considering the parity of the electron orbitals and the experimental geometry, qualitative conclusion can be drawn. Using the quantum-mechanical identity $< \Phi_f|\hat{\vec{p}}|\Phi_i > \propto < \Phi_f|\vec{r}|\Phi_i >$ (from the commutation relation between $\hat{\vec{p}}$ and $\vec{r}$) one can rewrite the matrix element $|M_{fi}|^2$ as:

$$|M_{fi}|^2 \propto \int dr^3 \Phi_f(\vec{r})\vec{\epsilon}\,\vec{r}\,\Phi_i(\vec{r}). \tag{2.11}$$

For a non-zero matrix element, the integrand (product of $\Phi_f(\vec{r})$,$\Phi_i(\vec{r})$ and $\vec{\epsilon}\,\vec{r}$) needs to be an even function with respect to mirror planes defined by the crystal lattice of the sample and the geometry of the measurement. The experimental setup shown in figure 2.5 on page 29 helps to determine the parity (even or odd) of the three factors.

To illustrate the parity, we consider *e.g.* the cubic crystal lattice of $SrTiO_3$ and assume that the <100> and <010> axes of the crystal are aligned along the x and y axes defined in figure 2.5(a). The xz and yz planes are mirror planes of the crystal as shown in figure 2.5(b) and thus, the probability amplitude of the initial and final state is of the same symmetry: $|\Phi_{i,f}(\vec{r})|^2 = |\Phi_{i,f}(-\vec{r})|^2$. Hence, the wave functions of the initial and final state need to be even or odd with respect to these planes: $\Phi_{i,f}(\vec{r}) = \pm\Phi_{i,f}(-\vec{r})$ as shown in the case of the d_{xy} orbital in figure 2.5(c) and a unspecific final state in figure 2.5(e). Additionally, if one detects electrons emitted in the planes defined by the mirror planes, the final state needs to be even as an odd function would be zero in that plane $\Phi_f(\vec{r}) = -\Phi_f(-\vec{r}) \;\Rightarrow\; \Phi_f(0) = 0$. Consequently, if the initial state has the same parity as the polarization with respect to the mirror plane, its band dispersion can be detected. Note that these arguments on the parity of the states are only of relevance if the emitted photoelectron propagates within a plane defined by the mirror planes of the crystal.

The parity of the light polarization

$$\vec{\epsilon} = (\underbrace{A_0^H \sin\alpha}_{LH_x}, \underbrace{A_0^V}_{LV}, \underbrace{A_0^H \cos\alpha}_{LH_z}) \tag{2.12}$$

where α is the incidence angle of the photons (see figure 2.5(a)) with respect to the xy and yz mirror planes are given in the left column of table 2.1 on page 31 and an example is given in figure 2.5(d). Note that in an experiment one can choose between linear vertical and linear horizontal polarization. Usually measurements are conducted close to normal emission *i.e.* at angles much smaller than the incidence angle of the light α. Consequently, the LH polarization is not aligned along one of the high-symmetry crystallographic directions and one measures a mixture of LH_x and LH_z contributions.

Taking all parity arguments into account, detectable orbitals based on light polarization and electron detection in one of the mirror planes are shown in table 2.1. The polarization dependence will be used later to confirm the orbital character of TiO_2 anatase and $CaTiO_3$.

Table 2.1: Detectable *s*,*p* and *d* orbitals under given light polarization (LV or LH) and detection of the photoelectrons in the planes defined by the mirror planes of the crystal lattice. At normal emission, *e.g.* the <001> direction in cubic $SrTiO_3$, both the xz and yz planes are mirror planes. The odd-even character of the orbitals and the light polarization with respect to a specific mirror plane is written in brackets. Taken from Yukawa *et al.* [6].

		xz mirror plane	yz mirror plane	normal emission
LH:	LH_x (xz: even, yz: odd)	s, p_x, d_{xz} (even)	p_x, d_{xy}, d_{xz} (odd)	p_x, d_{xz}
	LH_z (xz: even, yz: even)	s, p_z, d_{xz} (even)	s, p_z, d_{yz} (even)	s, p_z
	LV (xz: odd, yz: even)	p_y, d_{xy}, d_{yz} (odd)	s, p_y, d_{yz} (even)	p_y, d_{yz}

Spectral function

The spectral function $A(\vec{k}, E)$ describes the probability with which an electron can be added or removed from an electron system in its ground state. In an interacting electron system the energy eigenvalues $E(\vec{k})$ are renormalized relative to the ones of the non-interacting system $E^0(\vec{k})$. The lifetime of the photoelectron in a free-electron system is infinite, finite in an interacting one. This is expressed by the spectral function $A(\vec{k}, E)$ [115]:

$$A(\vec{k}, E) = \frac{1}{\pi} \frac{\Sigma_2(\vec{k}, E)}{(E - E^0(\vec{k}) - \Sigma_1(\vec{k}, E))^2 + (\Sigma_2(\vec{k}, E))^2}. \tag{2.13}$$

The complex function $\Sigma = \Sigma_1 + i\Sigma_2$ is the self-energy. The real part of the self-energy describes the renormalization of the energy and the imaginary part the finite life time τ.

The inverse of the life time Γ of an electron in a solid is proportional to Σ_2 and is given by:

$$\Gamma = \frac{\hbar}{\tau} = \Gamma_0 + \Gamma_{e-e} + \Gamma_{e-ph} + \ldots \quad = \quad 2\Sigma_2 \tag{2.14}$$

where Γ_0 represents the scattering due to defects in the solid, Γ_{e-e} the electron-electron interaction and Γ_{e-ph} the electron-phonon interaction. Other possible mechanisms of electron scattering are other many-body interactions, *e.g.* plasmons, magnons, spinons, ...

Later on, we will discuss the interaction of electrons with optical phonons in $SrTiO_3$, TiO_2 and ZnO (see chapter 8). To correlate the width and peak positions of the measured momentum (MDCs) and energy distribution curves (EDCs) with the self-energies of the spectral function (see discussion in section 8.1), the experimental resolution discussed in the next paragraphs must be sufficiently good.

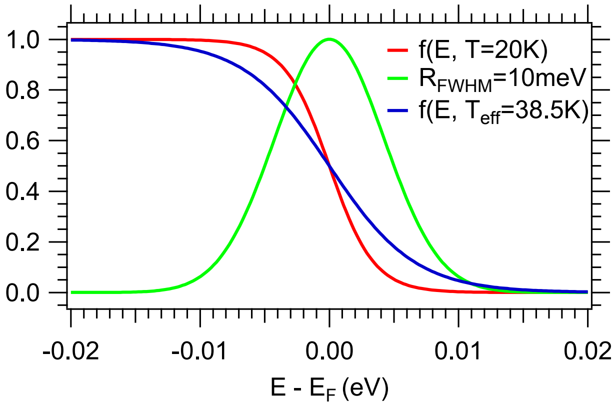

Figure 2.6: Fermi-Dirac distribution at a temperature $T = 20$ K (red curve). Due to the experimental resolution represented by a Gaussian of $FWHM = 10$ meV (green curve), the measured Fermi-Dirac distribution corresponds to an effective temperature of $T_{eff} = 38.5$ K.

Experimental resolution

To relate the intensity measured by the electron analyzer with the spectral function one has to consider that the actual measured intensity I_{mes} is a convolution of the photocurrent $I(E, h\nu)$ with the response function R of the experimental setup:

$$I_{mes} \propto I(E, h\nu) * R \tag{2.15}$$

We model the response function R by a Gaussian with full width half maximum ($FWHM$) corresponding to the resolution R_{tot} of the experiment. The energy resolution of the experiment is determined by the monochromacity of the incident photons R_{BL} (beamline resolution) and the resolution of the analyzer R_A. For a hemispherical electron analyzer, its resolution depends on the pass energy PE, the slit size W, the diameter of the hemisphere D and the acceptance angle α:

$$R_A = E_p \left(\frac{W}{D} + \frac{\alpha^2}{2} \right) \tag{2.16}$$

The total resolution R_{tot} is given by $R_{tot} = \sqrt{R_A^2 + R_{BL}^2}$.

To experimentally determine the energy width of the response function we fit the Fermi-Dirac distribution:

$$f(E,T) = \left(\exp\left(\frac{E - E_F}{k_B T} \right) + 1 \right)^{-1} \tag{2.17}$$

at the Fermi level and momenta $\vec{k}$ at which the spectral function is approximately constant close to the Fermi edge (no dispersing bands). The width of the Fermi-Dirac distribution is determined by the temperature T (for $T = 0$, $f(E,T)$ is the Heaviside step function). We will use the assumption of a constant spectral function away from band transitions. Kroger *et al.* discussed the limits of this assumption. [116]

In this case of a constant background *const* the measured intensity I_{mes} close to the Fermi level can be written as:

$$I_{mes} \propto const \cdot f(E,T) * R \;\equiv\; const \cdot f(E,T_{eff}) \qquad (2.18)$$

Hence, the measured intensity I_{mes} corresponds to a Fermi-Dirac distribution with a width given by an effective temperature T_{eff}. The width is determined by the convolution of the Fermi-Dirac distribution at the temperature of the sample T and the resolution R_{tot}. The Fermi-Dirac distributions $f(E,t)$ and $f(E,T_{eff})$ as well as the resolution function R are shown in figure 2.6. Assuming a Gaussian profile for the resolution function R_{tot}, the FWHM is given by [117]:

$$FWHM \approx 3.53\ k_B\sqrt{T_{eff}^2 - T^2}. \qquad (2.19)$$

Hence, if the temperature of the sample is measured and one can fit the measured Fermi cutoff in the ARPES spectra, an approximation of the resolution of the experiment can be determined.

2.3 Synchroton light source and Cassiopée beamline

After describing the photoemission process, we will focus in this section on the light source used to excite the electrons in the solid.

We conducted all of our ARPES measurements using synchrotron radiation as light source. The major advantage of synchrotron radiation is the tunability of the photon energy which allows to probe the 3D reciprocal space and to choose photon energies corresponding to an electronic resonance or to a high cross section for the photoexcitation process. In a conventional laboratory source, contrary to a synchrotron, the photon energy is fixed by the energy difference of the electronic states involved in the radiative decay in excited rare gases (*e.g.* He I_α=21.2 eV or Xe I_α=8.4 eV) or metals (*e.g.* Al K_α=1486.6 eV or Mg K_α=1253.6 eV).

The emission of light in a synchrotron is based on the radiation of accelerated relativistic charged particles. Generally, electrons are produced using *e.g.* a thermo-ionic gun, accelerated to relativistic speeds using a linear accelerator & a booster and then kept at constant energy in a storage ring. The storage ring is composed of magnetic elements altering the trajectory of the stored electrons and of radio-frequency cavities compensating the energy loss (*i.e.* radiation) of the electrons. Several beam lines with their endstations to conduct experiments are placed around the storage ring. The energy of the electrons in the storage ring is characterized by the normalized beam energy $\gamma = E/mc^2$, where E is electron beam energy, m the electron mass and c the speed of light. For example, in the synchrotron Soleil in France the beam energy is $E = 2.75$ GeV and the normalized energy $\gamma = 5382$.

The radiation to conduct experiments is produced by insertion devices (wigglers or undulators) while bending magnets bend the electron trajectory on a curved path. Wigglers and undulators are a periodic array of magnets forcing the electrons on a periodic trajectory. The difference between wiggler and undulator is in the amplitude of the periodic electron trajectory as shown

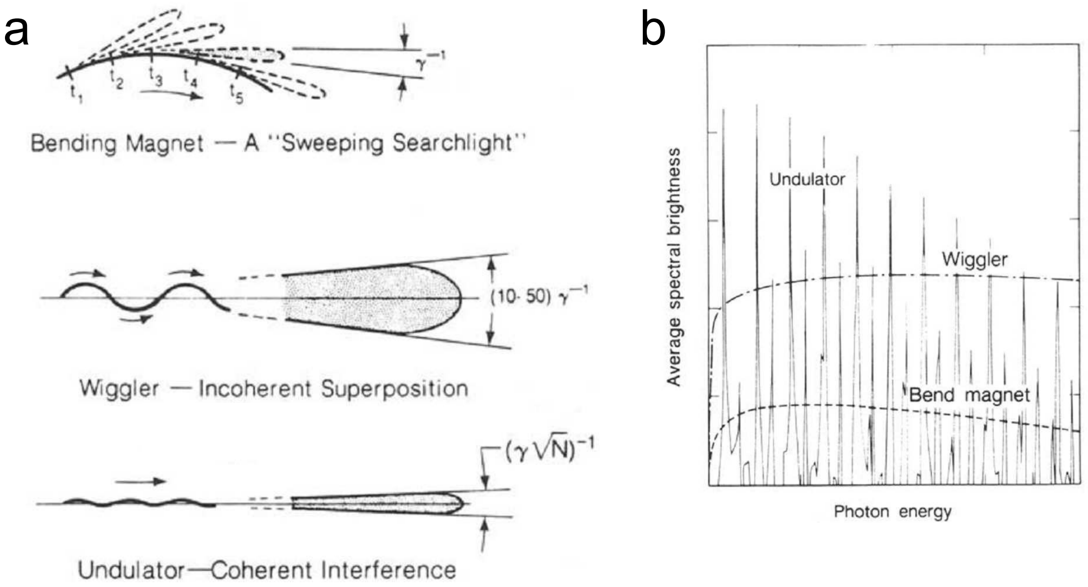

Figure 2.7: (a) Electron trajectory and spatial radiation profile depending on the insertion devices used to create synchrotron radiation. Bending magnet (top), wiggler (center), undulator (bottom). The spatial divergence of the radiation cone is determined by the inverse of the normalized beam energy γ^{-1} and in the case of the undulator by the number of magnetic periods N. (b) Spectral radiation profile of the three different insertion devices. The spectral profiles of bending magnet and wiggler are continuous whereas the undulator radiation is characterized by discrete emission peaks. Taken from reference [118].

in figure 2.7(a) on page 34.

Photon energy

Most of the ARPES results shown in thesis where mainly measured at two different synchrotron facilities: the Synchrotron Radiation Center in Madison, USA and the Soleil Synchrotron close to Paris, France. At both facilities, we used beam lines using undulators to produce the photons. The on-axis wavelength λ (and its n^{th} higher harmonics) emitted by an electron in a sinusoidal magnetic field of an undulator is given by [119]:

$$n\lambda = \frac{\lambda_u}{2\gamma^2}\left(1+\frac{K_u^2}{2}\right) \tag{2.20}$$

with λ_u being the undulator period, *i.e.* period of the magnetic elements and $K_u = eB_u\lambda_u/2\pi mc$ being the deflection parameter. One sees that the wavelength can be tuned by changing the strength of the magnetic field of the undulator B_u or the undulator period λ_u. Practically, the undulator period λ_u is fixed and the magnetic field B_u altered by varying the current in an electromagnet or the distance between permanent magnets.
At the Cassiopée beamline two undulators are used for different photon energy ranges. One is based on two series of electromagnets creating periodic magnetic fields orthogonal to the electron

trajectory and operates at photon energies between 7.5 eV and 120 eV ($\lambda_u = 0.256$ m, N=27). The other operates between $h\nu = 100$ eV and $h\nu = 1500$ eV ($\lambda_u = 0.6$ m, N=30) and is based on permanent magnets forming two rows below and above the electron trajectory. To give an example, equation (2.20) yields a photon energy for the fundamental line ($n = 1$) of 73 eV for the undulator composed out of electromagnets assuming a magnetic field of B_u=0.1 T.

The spectral width of the radiation emitted by an undulator is given by $\Delta\lambda = \lambda/nN_u$ which is much larger than the energy resolution (≈5-30 meV) needed to conduct UV-ARPES measurements. Thus, a monochromator consisting of a plane grating and a plane mirror is used to decrease the spectral width of the photon beam. The spectral width can be controlled by changing the size of the exit slit of the monochromator.

The possibility to change the photon energy due to undulator and monochromator allows to probe the dispersion of the band structure in the direction normal to the surface (see equation 2.5 on page 25). The existence or non-existence of dispersive bands in the k_z-direction gives direct information about the dimensionality of the electronic states. As we study confined electronic states at the surface, we often use k_z dispersion to demonstrate the 2D nature of the states (see *e.g.* figure 5.4 on page 100). The choice of the photon energy depends on the details of the reciprocal lattice of the studied crystal. Usually, high symmetry points (*e.g.* center or corner of Brillouin zone) and directions contain the essential information of the band structure. Finally, photon energies corresponding to electronic resonances allow to significantly increase the measured photocurrent. For example, as we measured different titanate compounds, we often choose the photon energy $hv = 47$ eV which corresponds to the Ti $3p \rightarrow 3d$ transition.

Photon flux

Next to the photon energy, the photon flux density is of somewhat special importance for this thesis. As will be discussed in section 3.2, there is a threshold in photon flux as well as in photon energy to change the stoichiometry of some transition metal oxides studied in the framework of this thesis. This change in stoichiometry can create itinerant electrons confined at the surface. Interestingly, the photon flux in some synchrotrons/ beamlines (*e.g.* at HiSOR) is too low to influence the stoichiometry while in others (*e.g.* Cassiopée beamline at synchrotron Soleil) it is sufficient too drastically alter the composition of the sample.

The photon flux is defined by the brilliance of the synchrotron light source & the insertion device (*e.g.* about 2×10^{18} Photons s^{-1}mm^{-2}mrad^{-2} in 0.1% in bandwidth for the current-controlled undulator at Cassiopée) and the optics of the specific beamline (spot size of photon probe on sample). As can be seen in figure 2.7 on page 34, the photon flux created by an undulator is orders of magnitudes higher than the other insertion devices and scales with N^2. At the ARPES endstation of the Cassiopée beamline the focusing optics consists of two spherical and toroidal mirrors yielding a beam size of approximately 40 × 20 µm for 100 eV (typical photon energy which we used). This spot size is roughly a factor of 250 smaller compared to the one at the 9B beamline at HiSOR (2 × 0.2 mm).

Processes occurring at the surface of TMOs under synchrotron irradiation

As already mentioned, the emission of an electron due to the photoelectric effect (see figure 2.8(a) on page 37) which can be characterized by ARPES is not the only process occurring during our synchrotron measurements. The multitude of processes occurring at the surface of transition metal oxides under intense synchrotron irradiation at low temperatures make it quite difficult to disentangle which process is responsible for which property. I will outline the processes in this section and will discuss them in more detail in later sections. The following processes (displayed in figure 2.8) occur in a typical photoemission measurement which we conducted at synchrotron beamlines:

- emission of photoelectron: electronic structure by ARPES (see chapters 3 - 8)
- UV irradiation: oxygen desorption/ photoconductivity/ formation of polar clusters (see sections 3.1 and 6.1)
- creation of oxygen vacancies: localized or delocalized behavior of excess e^- (see chapter 3)
- bluish luminescence

After describing the Cassiopée beamline as well as synchrotron irradiation in general (together with its effect on the surface of TMOs), I will briefly discuss the Cassiopée endstation.

Cassiopée endstation

The Cassiopée endstation is composed of a high-resolution ARPES endstation, a spin-resolved ARPES (SARPES) endstation and a Molecular Beam Epitaxy (MBE) chamber used for thin film growth or sample preparation. All three ultra-high vacuum chambers are connected via a small central chamber on top of which the load-lock is mounted to introduce samples in the UHV system. Depending on the sample preparation (see following section) the samples are either mounted on Ta or Mb Omicron plate (for UHV annealing) or on a copper Omicron plate (for cleaving/ fracturing samples in vacuum). To enable sample preparation as outlined in the next section and thin film deposition, the MBE chamber is equipped amongst other with:

- heating stage using electron bombardement up to approximately 1000°C (determination of temperature using thermocouple close to sample or pyrometer)
- electron diffraction (ED) techniques: low energy ED (LEED) and reflective high energy ED (RHEED)
- Auger spectroscopy setup
- ion gun for Ar^+ sputtering
- leak valve to increase partial pressure of specific gas species (*e.g.* O_2)
- various ports to mount evaporators (*e.g.* Al in Knudsen cell or alkali metals dispensers)

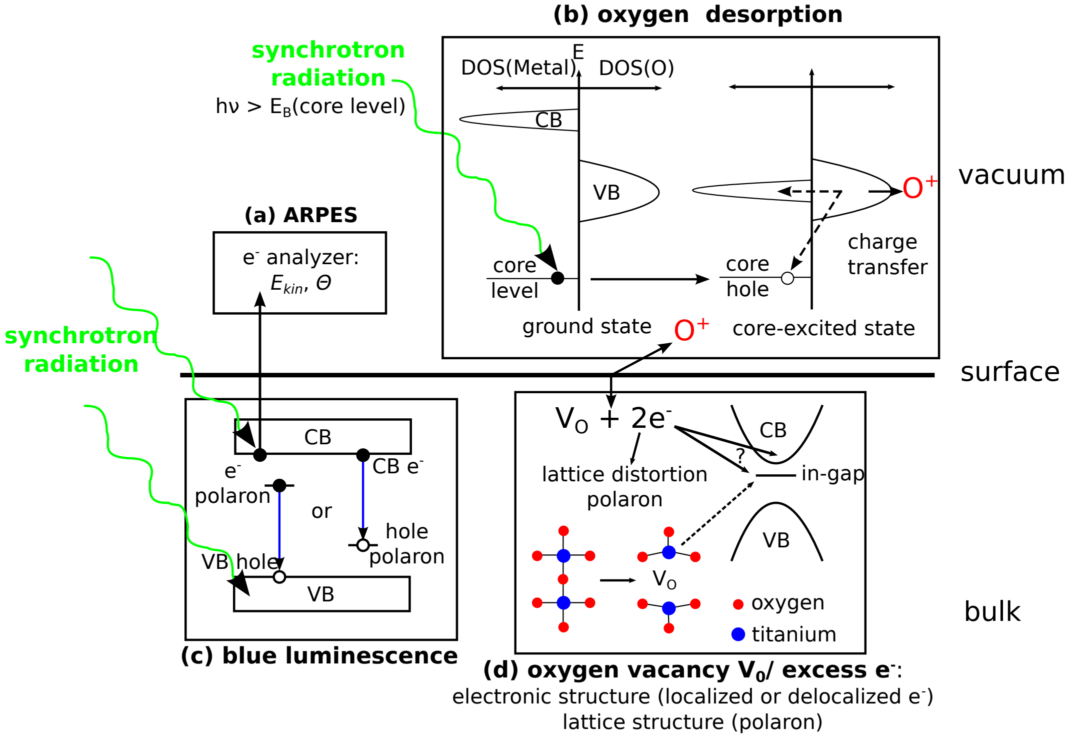

Figure 2.8: Processes occurring due to the excitation of electrons at different energy levels in a typical ARPES measurement conducted in the framework of this thesis. CB or VB is an abbreviation for conduction or respectively valence band, V_0 for oxygen vacancy and e^- for electron. (a) Emission of an electron due to the photoelectric effect and measurement of its kinetic energy E_{kin} and emission angle Θ_e using an hemispherical analyzer. (b) Partial density of states (DOS) of the transition metal and oxygen before and after the excitation of core-electrons. The relaxation of the system due to the presence of the core-hole results in a charge transfer of electrons from oxygen to the transition metal. The change in oxidation state of oxygen leads to the desorption of an oxygen ion. Model proposed by Tanaka *et al.* [120] (c) The emission of an electron from the valence band results in the creation of valence band holes. The radiative relaxation process of an electron from a defect-induced in-gap state or from the conduction band lead to a bluish luminescence. The relaxations shown in the figure are based on the model of Janotti *et al.* [121] (d) The creation of an oxygen vacancy results in doping the surface region with two excess electrons. Whether an excess electron is localized (in-gap state) or delocalized (CB) depends on the lattice geometry and the vacancy distribution (see discussions in sections 3.1 and 3.3). The missing oxygen anion results in a relaxation of the local lattice structure.

- a 10-crucible electron gun for material evaporation
- quartz microbalances to calibrate the growth rate of deposited matter

2.4 Preparation of oxide surfaces for ARPES

ARPES measurements are conducted to obtain the band structure of solids. As demonstrated by the universal curve in figure 2.4 on page 28, this technique is very surface sensitive as electrons escape within approximately the first 5 Å from the surface of the solid at a photon energy of the order of 100 eV. Thus, the surface needs to be very clean and free from any contaminants, *e.g.* due to exposure to air.

Another consequence of the shallow probing depth is that only the first few layers of the lattice of the solid contribute to the signal measured during an ARPES measurement. To probe the band structure, the surface region needs to be crystalline (otherwise there are no dispersing bands) and the majority of the probed surface oriented along a defined crystallographic plane (as momentum conservation is only valid parallel to the surface, a surface of mixed orientations is equivalent to an amorphous crystal).

Generally, there are two different ways to prepare the surface for photoemission experiments:

- cleaving/ fracturing in ultra high vacuum
- *ex situ* (polishing, chemical etching and annealing) and *in situ* treatments (sputtering and annealing)

The feasibility of cleaving a crystal to obtain a well-ordered surface depends on the lattice structure. Some crystals have natural cleaving planes, *e.g.* the (101) plane of the tetragonal body-centered lattice of anatase, whereas other crystals do not have any cleaving planes and can only be fractured, *e.g.* cubic $SrTiO_3$. Nevertheless, locally well-ordered surfaces can also be obtained on the surface of fractured $SrTiO_3$. [122] The observation of 2DESs with dispersing bands at the surfaces of fractured $SrTiO_3$, $KTaO_3$ as well as $CaTiO_3$ demonstrates that crystalline order in the surface region exists.

Single crystals of oxides were fractured by mounting samples as shown in figure 2.9 on page 39. To provide electrical grounding to the exposed surface, the crystals were glued with a conducting silver epoxy to the sample holder and (after gluing the top-post) wholly covered with graphite paint. The cleaves/ fractures were conducted at low temperatures T=7-25 K and at pressure ranging between $p=5 \times 10^{-11} - 5 \times 10^{-10}$ mbar using either a wobble stick or a transfer arm to apply mechanical stress on the top post (figure 2.9(a)) or sample (figure 2.9(b)).

But the crystalline order as well as the homogeneity of the surface can be improved/ controlled by preparing the surface in a different way. As $SrTiO_3$ is a wide spread substrate for the growth of transition metal oxides with perovskite lattice structure, the surface preparation has been studied extensively. The preparation we used is based on previous works and detailed below. Similarly, the surface preparation of TiO_2 anatase and rutile crystals is very well-known due the

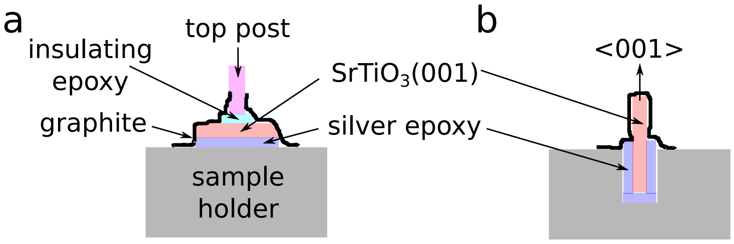

Figure 2.9: Schematic of mounting the sample to obtain clean and well-ordered surfaces by fracturing using (a) a top post and (b) a trench in the sample holder.

interest in the photocatalytic properties of their surfaces.
Regardless of the preparation technique, one has to consider certain characteristics of the surface:

- surface cleaniness
- surface crystallinity
- surface stoichiometry
- surface reconstruction/ relaxation
- surface termination

In our studies, the major concern regarding the stoichiometry of the surface region is the presence of oxygen vacancies. Fracturing the crystal or annealing the oxides in ultra high vacuum can create oxygen vacancies. As oxygen vacancies can be electron donors, they can dramatically change the electronic properties as will be discussed in the next chapter.

$SrTiO_3$(001)

The reconstructions for the different low index surfaces of $SrTiO_3$ have been well studied and are summarized for the (001) surface in the review of Fu and Wagner [123]. In general, the reconstruction of the surface of an oxide can be driven by oxygen vacancies [124] or in ionic crystals often occurs to compensate the polar instability due to a macroscopic dipole moment perpendicular to the surface [51, 125].
The relaxation of the surface (changes in internal layer distances) as well as the surface rumpling (the relative displacement of oxygen with respect to the metal cation in the surface layer) at the surface of $SrTiO_3$(001) have been investigated theoretically as well as experimentally in various studies and are summarized in table I in the study of Pancotti *et al.* [126]. Note that the surface rumpling can introduce a dipole moment at the surface, *i.e.* surface ferroelectricity [126–128].
In the case of $SrTiO_3$ the surface termination can be controlled by chemical etching [129] as described below. Cleaving or fracturing the crystal results in a mixed terminated surface.
Next, I will describe how to obtain clean and ordered $SrTiO_3$ surfaces using a chemical etch and annealing treatments.

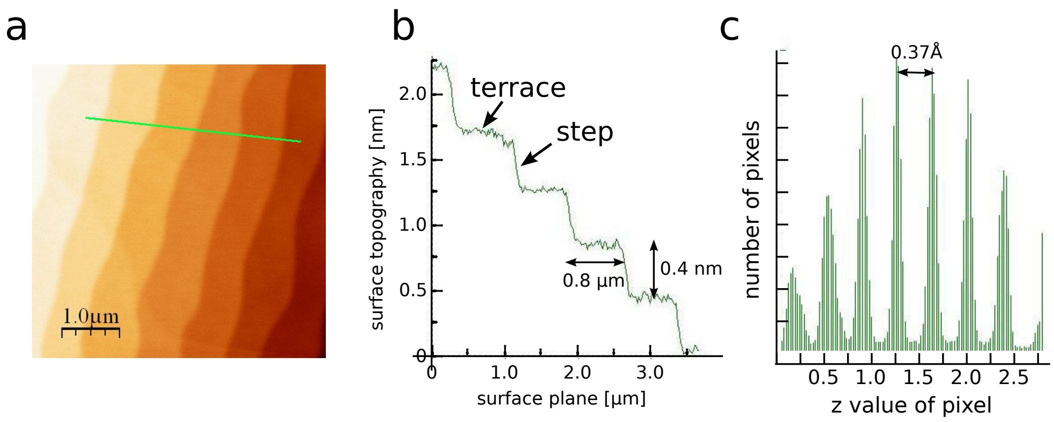

Figure 2.10: (a) Atomic force microscopy (AFM) image of a chemically and thermally prepared $SrTiO_3(001)$ surface. A step-and-terrace structured surface is visible. (b) The profile of the surface along the green line in (a). The numbers indicate the width of one terrace and respectively, the step height. (c) The histogram of the AFM image helps to approximate the step height.

***Ex situ*: Chemical etching and annealing**

The commercially available $SrTiO_3(001)$ substrates are already polished (*e.g.* mechanochemically). The polishing process decreases the roughness of a surface to values around half or one unit cell and also results in a miscut angle between the real surface and the (001) planes. This miscut angle can be minimized to angles smaller than 0.1° and determines the width of the terraces shown on the atomic force microscopy (AFM) image in figure 2.10(a).

As already mentioned previously, the stacking order of atomic planes along the <001> direction is alternating planes of TiO_2 and SrO. To create a TiO_2 single-terminated surface and to further reduce surface roughness, a chemical etch in buffered HF (NH_4F-HF) and a subsequent annealing in O_2 flow are conducted. The chemical etch is selective as the TiO_2 plane is basically chemically inert . [129] Better reproducibility, greater pH and etch time variability can be achieved by soaking $SrTiO_3$ in water before the etch [130]. At room temperatures SrO reacts with water to form $Sr(OH)_2$, whereas TiO_2 is inert to water. Strontium hydroxide dissolves in acidic solution and consequently facilitates the etching in BHF.

The subsequent annealing heals the surface of any etch holes and results in a step-and-terrace structure (see figure 2.10(a,b)) to minimize the overall surface free energy [131]. The surface energies of high-symmetry surface planes (like *e.g.* (001), (110), (111)) are low as the atomic density per unit area is high and thus, the low-index surfaces are relatively stable. The ideal annealing temperature is approximately 1000°C [132] and the annealing time depends on the miscut angle as the migration time of a surface atom to a step edge depends on the width of a terrace. Typical terrace widths range between 100 nm and 1 µm whereas the step height of the single terminated surface is one unit cell, i.e approximately 3.9 Å(see figure 2.10(b,c)). To obtain surfaces like the one shown in figure 2.10(a), we used the following procedure:

- cleaning in an ultrasonic bath of deionized H_2O for 30 min

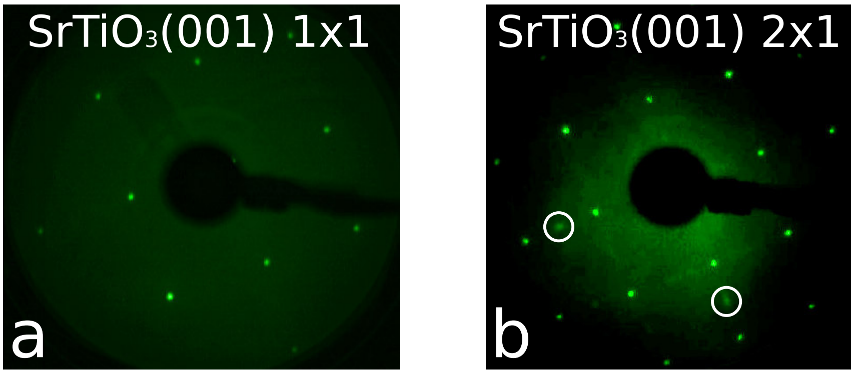

Figure 2.11: (a) LEED image of a unreconstructed $SrTiO_3(001)$ surface annealed at T=550°C in UHV. Annealing at higher temperatures can result in a surface reconstruction as the 2×1 reconstruction shown in (b). (b) LEED image of a $SrTiO_3(001)$ sample annealed at T=700° for approximately 1h. The diffraction spots corresponding to the two domain (2×1) reconstruction are highlighted by the white circles.

- etching in buffered HF (NH_4F:HF=7:1; pH=5.5) for 1 min
- rinsing in deionized H_2O for 10 min
- annealing in oxygen-flow furnace at 950°C for 3-10 h

The variable time of the annealing does not only change the morphology of the step-and-terrace structure (*e.g.* edge shape) but also the surface reconstruction. In the case of $SrTiO_3(001)$, a 3 h annealing results in a unreconstructed 1×1 surface, whereas 10 h result in a $(\sqrt{13} \times \sqrt{13})R33.7^\circ$ surface reconstruction.

In situ: vacuum annealing

The *ex situ* treatment described in the previous section creates a crystalline, single-terminated and step-and-terrace structured surface. In order to conduct ARPES experiments, one has to clean the surface from organic contamination present due to exposure of the samples to air. Hence, once introduced into the ultra high vacuum system, one needs either to conduct an Ar^+ sputtering or an annealing in UHV or a combination of both. Both procedures, affect not only the organic contamination but also the surface stoichiometry mainly due to the creation of oxygen vacancies. [133, 134]

The carbon contamination on the etched surface can be removed by annealing in UHV at 550-600°C or higher temperatures. [135, 136] At temperatures above 600°C several surface reconstructions can occur. The first one (lowest temperature) is a (2×1) reconstruction which consists of two domains oriented by an angle of 90°. [137]

Figure 2.11 shows the low-energy electron diffraction (LEED) images of two $SrTiO_3$ samples. One was annealed at approximately T=550°C, the other at approximately T=700°C for 1-2 h. As shown in figure 2.11(a,b) the first one is unreconstructed 1×1 while the other is reconstructed 2×1.

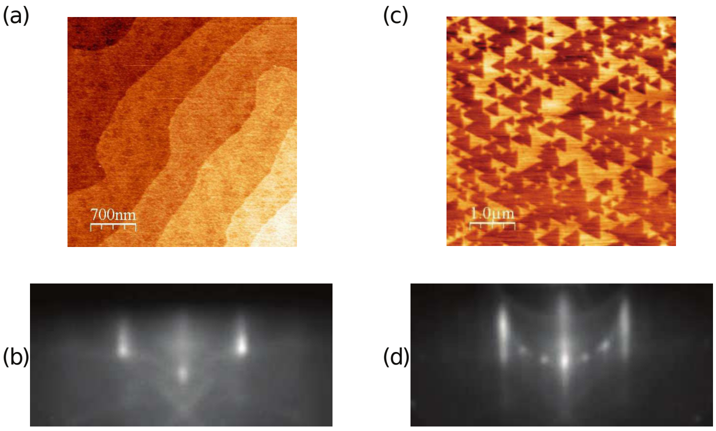

Figure 2.12: (a) Atomic force microscope (AFM) image of an etched and annealed $SrTiO_3$ (111) surface. The surface is single terminated and unreconstructed, as shown in the RHEED image in (b). Longer annealing times result in a mixed terminated surface, as demonstrated in the AFM friction image (c) measured in contact mode. A 3×3 reconstruction of the surface can be deduced from the corresponding RHEED image in (d). Figure published in reference [10].

$SrTiO_3$(111)

An identical treatment as the one discussed for the (001) surface can be used for the (110) and (111) surface of $SrTiO_3$. [132, 138]. Figure 2.12(a) on page 42 shows the AFM image of a $SrTiO_3$(111) surface of a sample annealed for 3h. This treatment produces a (1×1) unreconstructed surface, shown by the reflective high-energy electron diffraction (RHEED) image in figure 2.12(b). Longer annealing (10h) results in a mixed-terminated surface [139], as shown in the AFM friction image in figure 2.12(c), measured in contact mode. The surface prepared in such a way is (3×3) reconstructed, as displayed in the RHEED image in figure 2.12(d).

$CaTiO_3$

There is no literature on the preparation of the surfaces of $CaTiO_3$. The polished crystals were obtained from the SurfaceNet GmbH in Germany. Hence, to clean the surface from contamination, an approach similar to $SrTiO_3$ was used, *i.e.* annealing at approximately 600°C for one hour. This results in the LEED image shown in figure 2.13(a) on page 43. Note that no systematic study was conducted to optimize the parameters of the surface preparation.

Thin films of $BaTiO_3$

The $BaTiO_3$ 300Å-thick films were prepared by laser-MBE using a sintered $BaTiO_3$ target. A KrF excimer laser was used for the deposition. The $SrTiO_3$ substrate, which was etched prior to the deposition to obtain a TiO_2 terminating layer, was glued on the sample holder with silver paste. The growth of the film, monitored by RHEED, was carried out at 650 °C in 5×10^{-4}

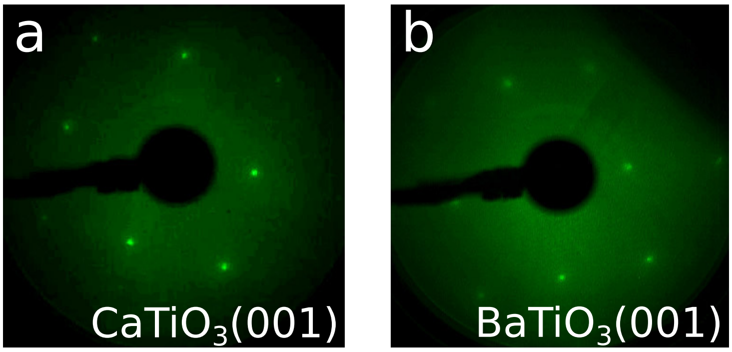

Figure 2.13: LEED image of (a) a polished CaTiO$_3$(001) surface and (b) the (001) surface of a thin film of BaTiO$_3$, both annealed at approximately T=600°C in UHV.

mbar oxygen pressure with 0.1 % ozone. RHEED oscillations were used to monitor the deposited thickness. At the end of the deposition, the films were cooled down in 6×10^{-3} mbar oxygen pressure, always with 0.1% ozone.

Ideally, the photoemission measurements are conducted right after the thin film growth without breaking vacuum. However, at synchrotron facilities only few ARPES setups have a laser-MBE/PLD connected to the photoemission chamber. Hence, the thin films exposed to air are cleaned by annealing in UHV. There is no literature on the best practice of cleaning BaTiO$_3$ thin films. Based on the experience on SrTiO$_3$, the surface of the BaTiO$_3$ thin films was cleaned by annealing the samples at temperatures of approximately $T = 550°$ C for $5 - 30$ min (see LEED image in figure 2.13(b)). One of the samples was Ar$^+$ sputtered ($U = 500$ V, $t = 10$ min) prior to the UHV annealing, without noticeable changes in the ARPES data. Note that extensive electron doping of BaTiO$_3$ due to oxygen vacancies created by UHV annealing results in a metallic state screening the long-range Coulomb interaction of electric dipoles and thus, destroy the ferroelectricity. [140]

The preparation of single crystal surfaces of BaTiO$_3$ is discussed by Rault *et al.*[141]

TiO$_2$ anatase(001) and (101)

The body-centered tetragonal structure of anatase discussed in section 1.1 results in the existence of natural cleaving planes. Thus, the preparation of well-ordered surfaces can be achieved by cleaving single-crystals. However, the preparation of single crystal surfaces by Ar$^+$ sputtering and UHV annealing is well documented. [142] Note that the crystal growth of large (approximately $5 \times 5 \times 0.5$ mm^3) single crystals is complicated. Hence, the studies on anatase were conducted on natural grown single crystals whose major impurities are Si, Fe and Mn.

We used a procedure based on the results of Setvin *et al.* [142] to prepare the surfaces:

1. Ar$^+$ sputtering at U=1kV for 10 min
2. annealing for approximately 15 min at approximately T=600-700°C in UHV
3. cycling of 1. and 2. depending on results of LEED image

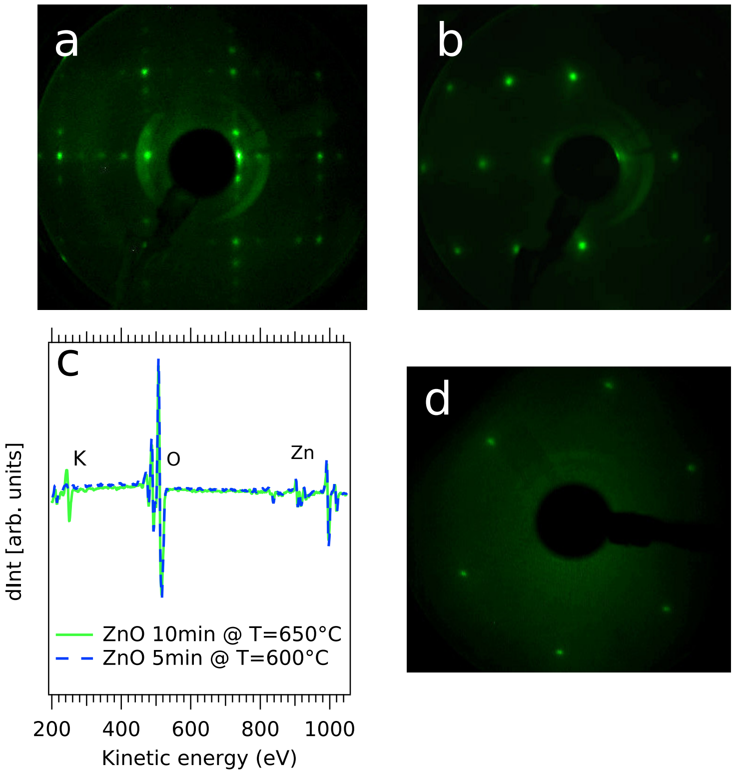

Figure 2.14: (a) LEED image of a 4 × 1 reconstructed Anatase(001) surface after Ar^+ sputtering and annealing at T=650°C in UHV. (b) LEED image of unreconstructed Anatase(101) surface using similar parameters as in (a). (c) Auger spectra of the oxygen-terminated ZnO(0001) surface. Depending on the chosen preparation routine, potassium diffuses from the bulk to the surface of ZnO as evidenced by the peak at a kinetic energy of $E_{kin} = 250$ eV. (d) LEED image of oxygen-terminated ZnO(0001) surface after sputtering and annealing at T=650°C.

This preparation results in the LEED images shown figure in 2.14(a,b) on page 44 measured at the anatase(001) and anatase(101) surface. Note that temperatures higher than T=750°C should be avoided as a phase transition to the rutile phase can occur. Rutile is the most stable phase of TiO_2 and artificially single crystals of rutile are commercially available. The surface sciences (including surface preparation) of the rutile surfaces are discussed in the review by U. Diebold. [80]

ZnO(0001)

There are two possible termination of the polar (0001) surface: Zn and O. [143] Commercially available single crystals with the two terminations at opposing faces can be purchased. The surfaces of ZnO were prepared based on the study of Dulub *et al.* [144] The existence of potassium impurities in single crystals of ZnO is possible as potassium hydroxide is an educt in the hydrothermal synthesis of single crystals. Long annealing at elevated temperatures resulted in the migration of potassium impurities from the bulk to the surface as evidenced by the Auger spectra in figure 2.14(c). There are two possible procedures to reduce the presence of potassium at the surface:

1. Ar^+ sputtering at U=1kV for 10 min
2. short annealing for 5 min at approximately T=600-700°C in UHV

or alternatively:

1. Ar^+ sputtering at U=1kV for 10 min at T=600-700°C
2. stop annealing approximately 5 min after sputtering

These procedures result in a LEED image similar to the one shown in figure 2.14(d).

This section serves as a reference for the sample preparation of the oxides studied by photoemission in the next chapters. After introducing ARPES and sample preparation in this chapter, I will focus on different topics which are essential to better understand and control the properties of 2DESs at the surface of TMOs. The next chapter focuses on the origin for the creation of 2DESs at oxide surfaces: oxygen vacancies.

Chapter 3

Oxygen vacancies: creation, electronic structure, 2DEGs and case study in TiO_2

Many of the ARPES results which I will present in this thesis have been published in scientific journals. [10, 15, 19] I use many paragraphs from these publications in this thesis.

3.1 Creation of oxygen vacancies and predicted electronic structure

Defects are decisive in determining the physical properties of a material. In transition metal oxides, an omnipresent defect type is the oxygen vacancy. To microscopically understand many properties of TMOs, it is vital to know the concentration of oxygen vacancies, if and how they diffuse and/or cluster, their energetically most stable sites in the lattice (*e.g.* domain boundaries, surface or subsurface layers) and the behavior of the two electrons left in the solid (one review discussing oxygen vacancies at the surface being [35]). Tremendous efforts have been made to understand the location of the lattice site of oxygen vacancies at the surface of TiO_2 rutile as its photocatalytic properties strongly depend on it. [80] The role of oxygen vacancies in the creation of the 2DES (as well as its properties) at the interfaces of TMOs heterostructure is still under debate. In this thesis, the focus is on 2DESs at the surfaces of TMOs for which the decisive role of oxygen vacancies will be demonstrated.

For this work, oxygen vacancies were created in three different ways: by annealing in ultra high vacuum, by irradiating the samples in UHV with UV synchrotron light and by a redox reaction with a metal thin film (see section 4.1).

Annealing in UHV

The creation of oxygen vacancies by annealing in UHV is a well known phenomena for transition metal oxides. Pal *et al.* used core-level photoemission spectroscopy to quantify the loss of oxygen in $SrTiO_3$ induced by annealing in UHV - in temperature and pressure ranges similar to the ones used for the experimental work in this thesis. [134] We annealed samples in UHV to make the bulk of $SrTiO_3$ slightly conductive so that there are no charging effects during the photoemission experiments at low temperature as well as to clean the surface of adsorbed contamination.

If we assume that oxygen vacancies alone are responsible for the confinement of the electrons in the 2DES at the surface, the concentration of the vacancies in the surface region (only several nm) would have to be much higher than in the bulk. To create such a scenario by annealing in UHV might be possible but very complicated. One would have to find the correct parameters of temperature and pressure to control oxygen desorption from the surface and oxygen diffusion from the bulk to the surface to have the correct depth profile for the concentration of oxygen vacancies. So far, there is only one study claiming that a 2DES can be produced at the surface by annealing in UHV. [145] However, the results of the ARPES measurements show that the observed confined states are identical for various different annealing parameters and similar to the ones at surfaces prepared by fracturing. [7] This indicates that another mechanism is responsible for the creation of the majority of oxygen vacancies at the surface, such as desorption induced by electronic transitions.

Desorption induced by electronic transition

Desorption induced by electronic transitions [146] can be stimulated by irradiating the surface of a solid by electrons, photons or other high-energy irradiation (*e.g.* positron-stimulated desorption of oxygen ions from a $TiO_2(110)$ surface [147]). The electron stimulated desorption [148] of oxygen was experimentally observed on the (110) and (011) surfaces of TiO_2 rutile [149–151] and $SrTiO_3$ (001) [152, 153]. The photon stimulated desorption of oxygen was experimentally observed in synchrotron facilities on the TiO_2 rutile surface [120, 154]. Electrons or photons with sufficient energy create holes at the core levels of the electronic structure of the irradiated material. The interaction of the core hole with the electrons can result in a charge transfer and create an O^+ like state as shown in figure 2.8(b) on page 37. The repulsive Coulomb interaction between O^+ and the surrounding transition metal cations lead to the desorption of O^+. The mechanism of the charge transfer is still under debate [120, 149].

Other results indicate that irradiation of a TiO_2 rutile surface with an energy larger than the band gap is sufficient to create the oxygen vacancies [155] and hence, no core level excitation is necessary to induce the desorption of oxygen.

Electronic structure of 2DES in $SrTiO_3$(001): insights from theory

The discovery of a 2DES at surface of $SrTiO_3$ sparked many theoretical investigations of the role of oxygen vacancies at the surface in the formation of the confined states. In this paragraph, I will quickly review recent publications:

- Shen *et al.* used density functional theory calculations to study different-sized supercells (to vary the concentration of neutral oxygen vacancies) of $SrTiO_3$. [156] They examined the change in electronic structure by introducing one oxygen vacancy in the TiO_2 or SrO-terminated surface. They draw several conclusions: firstly, a metallic state is only formed by including an oxygen vacancy in the surface layer; the relaxed stoichiometric surface is insulating. Secondly, the relaxation of the surfaces changes the electronic structure significantly. Thirdly, the charge carriers are strongly localized at the surface independent of the concentration of oxygen vacancies. Fourthly, Fermi surfaces, effective masses and charge carrier densities agree well with experimental results on the 2DESs.

- In a more recent study of the same group, Jeschke *et al.* characterized the electronic structure and behavior of multiple neutral oxygen vacancies (two or three) in a 3x3x4 supercells of $SrTiO_3$. [157] One of the vacancies is always on the TiO_2 surface layer. The vacancies tend to cluster vertically and weakly tend to distribute equally in-plane. Non-clustered oxygen vacancies in the TiO_2 surface layer donate itinerant electrons to the t_{2g} conduction band. Clustered vacancies in the surface layer or a second vacancy in subsurface layers create a localized in-gap state which is stabilized by the hybridization of Ti $3d$ e_g and O $4p$ states and elastic lattice deformations.

- Silva *et al.* found that the stoichiometric surface is insulating and a neutral oxygen vacancy induces a metallic state at TiO_2 or SrO-terminated surface using DFT calculations. [158] They also calculated the formation energy of an oxygen vacancy in different layers: the lowest formation energy (2.9eV) is at the TiO_2 surface layer.

- Zhuang *et al.* studied the atomic and electronic structure of two neutral oxygen vacancies in the topmost layer of TiO_2 and SrO-terminated surface in 4x4x9 symmetric supercell using DFT calculations. [159] They observe: firstly, the formation energy of oxygen vacancies at the TiO_2-terminated surface is lower than at the SrO-terminated surface or in the bulk. Secondly, the repulsion between oxygen vacancies is much larger at the TiO_2-terminated surface compared to the SrO-terminated surface. Thirdly, the by far most stable oxygen vacancy configuration of the TiO_2-terminated surface is the one with the fourth-nearest neighbor being the second vacancy. This configuration results in significant lattice distortions leading to octahedral tilts. Fourthly, the two vacancies induce a metallic state at the surface of both surface terminations. Fifthly, electrons in the SrO layer are much more localized at the SrO-terminated surface compared to the TiO_2-terminated surface.

Several other recent studies analyze oxygen vacancies at the bulk of $SrTiO_3$ or the interface of $LaAlO_3/SrTiO_3$.[160–163]
To sum up, DFT calculations confirm the presence of a 2DES at the oxygen-deficient surface of $SrTiO_3$. The introduction of multiple vacancies in a supercell give insights in the dual character of excess electrons (localized or delocalized) discussed in section 3.3. Note that the exact configuration of multiple oxygen vacancies is very difficult to access experimentally. While photoemission measurements can be used to obtain averaged vacancy concentrations, the microscopic configuration of the vacancies is often unknown. One exception are the surfaces of TiO_2 anatase and rutile [164, 165] (and references therein). Hence, DFT calculations are essential to

better understand which microscopic vacancy configurations can best explain the experimental photoemission results (*e.g.* localized states in the band gap) presented in the next sections.

3.2 Evolution of electronic structure of oxide surfaces under synchrotron irradiation

The influence of light irradiation at the surface of transition metal oxides was partly discussed in previous sections and can be categorized in three effects: photovoltaic effect, polar distortions of the lattice and the creation of oxygen vacancies induced by electronic transitions. We argued previously that the creation of oxygen vacancies is the driving factor for the creation of the 2DES and thus, we will focus on this effect. Note, that the photovoltaic effect strongly influences the conductivity at $LaAlO_3/SrTiO_3$ interfaces. [166] (and references therein) A detailed understanding of the synchrotron light influence at the surfaces in vacuum is still elusive as it depends on various parameters: surface preparation (cleaved or *in situ* prepared), bulk doping (*e.g.* Nb), temperature (influencing oxygen diffusion, see Supplement Material of [9]) as well as photon flux on the surface [photons s^{-1} m^{-2}] and photon energy.

Core levels, valence band, in-gap state

Regardless of the material or surface orientation we studied, the light irradiation (in a photon energy range from hv=40 to 110 eV in synchrotron radiation facilities with sufficient photon flux) always induces qualitatively similar changes in the photoemission spectra as shown in figure 3.1 on page 50 for the surfaces of anatase(001) and (101), $CaTiO_3(111)$ as well as $SrTiO_3(111)$. The dark-colored curves correspond to curves measured right after the first UV exposure of the sample and the light-curves were measured later (tens of minutes to several hours). Note that all photoemission measurements presented in this thesis were conducted at low temperatures $T = 7 - 20$ K if not specified otherwise.

Several changes can be observed,

1. an in-gap state approximately 1eV below the Fermi level is created in the band gap of the doped insulator which was attributed to oxygen vacancies [153, 167, 168].

2. a shoulder at the lower binding energy side of the Ti 3p peak appears due to the formation of Ti ions with lower valencies (*e.g.* 4+ to 3+) corresponding to the electron doping of the Ti ions. Note that the amplitude of the shoulder compared to the amplitude of the main peak of 4+ valency can vary significantly depending on photon dose and material.

3. the decrease in intensity of the O 2p valence band especially of the part close to the valence band maximum which consists mainly of O p_π states showing either almost negligible hybridization with d-orbitals [61].

4. the disappearance of the low intensity features 1 eV to 3 eV below the valence band minimum. These features are more distinct for surfaces prepared *in situ* (*e.g.* $SrTiO_3(111)$)

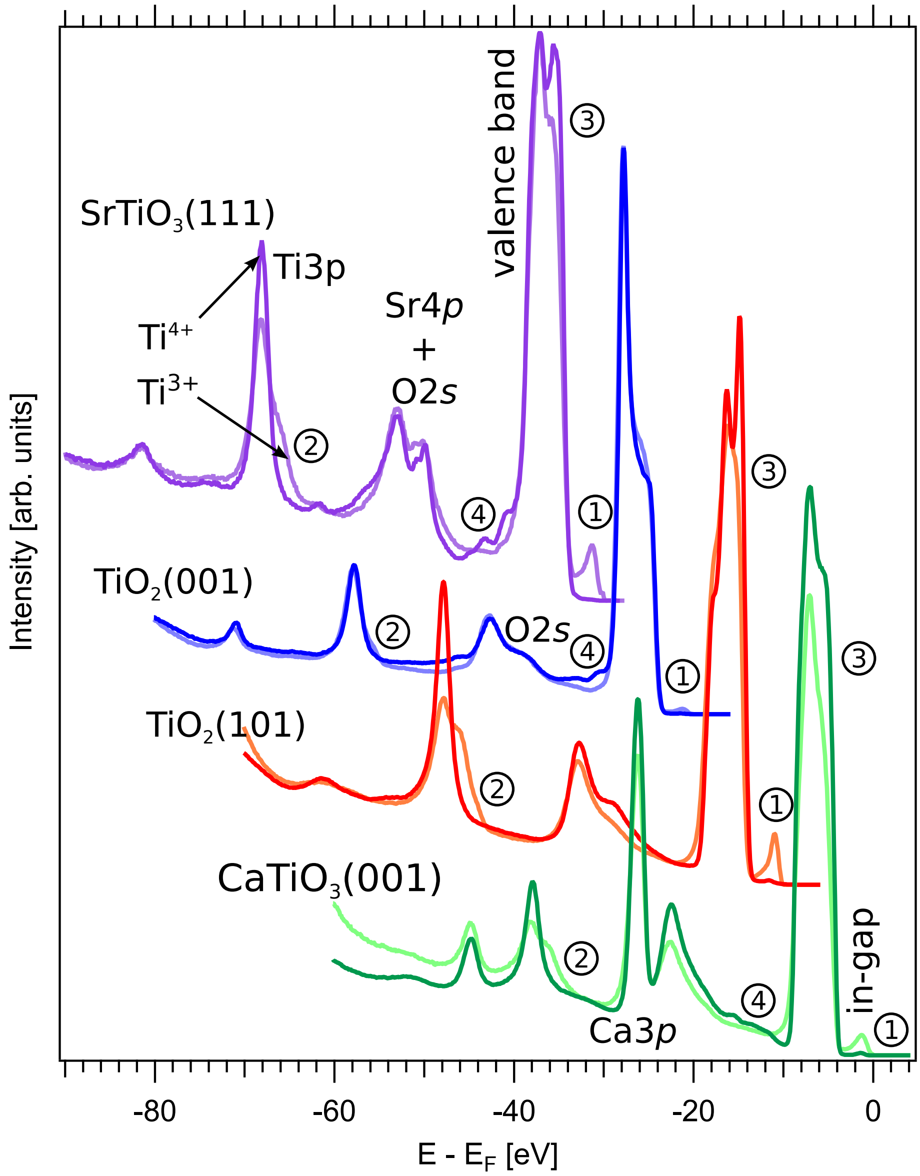

Figure 3.1: Angle-integrated spectra measured at a photon energy of $h\nu$ =100 eV at the surfaces of anatase (001) & (101) and CaTiO$_3$(001) or at $h\nu$ = 110 eV at the SrTiO$_3$(111) surface. The samples were cleaved in UHV except the SrTiO$_3$(111) sample which was prepared *in situ* as described in section 2.4. The dark-colored curves are measured shortly after the first beam exposure while the light-curves were measured later (tens of minutes to several hours). The light induced changes in the spectra are similar for all surfaces: 1. the creation of an in-gap state (at 1 to 1.5eV), 2. a shoulder at the Ti 3p peak and 3. decrease in intensity of the O2p valence band especially close to the valence band maximum as well as 4. the disappearance of the low intensity features 1 eV to 3 eV below the valence band minimum (marked by the black disks in the case of SrTiO$_3$(111)). For a better visibility, the three upper spectra are offset in binding energy by 10 eV with respect to the subjacent spectrum.

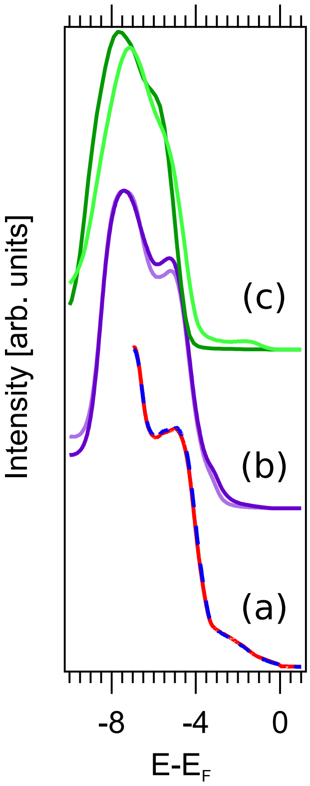

Figure 3.2: Angle-integrated spectra measured at a photon energy of $h\nu$ =21.2 eV (a) or 100 eV (b,c) at fractured or *in situ* prepared surfaces of $SrTiO_3$(001). (a) No spectral changes are induced by the irradiation because the photon flux or photon energy of He lamp are too low to desorb oxygen from the surface. The blue curve was measured 12 hours after measuring the red curve. (b) The photon flux at the beamline 9B in the HiSOR synchrotron is too low to induce significant changes (no in-gap state). (c) The in-gap state can be created using the much more intense irradiation of 0^{th} order of the monochromator grating (reflected, polychromatic beam).

and thus, could be related either to not removed carbonic contamination or to contamination due to the surface preparation (*e.g.* fluor [169] due to a chemical etch). Hatch *et al.* calculated that the substitution of oxygen at the surface with fluor or the (partial) hydrogenation of the surface results in features in this energy range. [170] In any case, the light irradiation reduces the contamination. In principle, no contamination should be present at the cleaved surfaces, but the aforementioned low intensity features are still present in the first minutes of the light irradiation.

Contrary to these observations, no (significant) spectral changes can be induced if the photon flux or photon energy is too low. A conventional lab source (He lamp with photon energy of 21.2eV) does not induce changes in the electronic structure even after an UV irradiation of 12 hours as shown in figure 3.2(a). Similarly, the photon flux on the sample at the 9B beamline in the HiSOR synchrotron is too low (about two orders of magnitude compared to Cassiopée) to induce significant changes (*e.g.* no in-gap state) as displayed in figure 3.2(b). However, figure 3.2(c) demonstrates that the in-gap state can be created by using the much more intense irradiation of the 0^{th} order of the monochromator grating (reflected, polychromatic beam). This indicates that there is a threshold of photon flux determining if the surface can be reduced sufficiently to create the 2DES.

In the previous paragraph, we discussed the influence of photon flux on the evolution of the electronic structure. There is also experimental evidence that the photon energy influences the desorption. A first indication is that we failed to observe the 2DES at the surface of fractured undoped $SrTiO_3$ crystals using a 7 eV laser at the ISSP in Tokyo. Additionally, using the same laser-ARPES setup, Ishida and coworkers measured the Fermi surface (*i.e.* charge carrier density) for *in situ* prepared Nb:$SrTiO_3$ samples. [171] The size of the Fermi surface was determined by the temperature and duration of the annealing in UHV. This is in contrast to the synchrotron based measurements as the UV irradiation will desorb oxygen to saturation value and hence, the Fermi surface size also saturates. At high photon flux synchrotron facilities, the Fermi surface size is independent of the parameters of the UHV annealing process. [7] Walker *et al.* demonstrated the existence of a photon energy threshold at the surface of $SrTiO_3$ using synchrotron irradiation and related it to oxygen desorption induced by electronic transitions as discussed in section 3.1. [16]

To sum up, the thresholds in photon flux as well as in photon energy show that the main mechanism for the creation of oxygen vacancies in synchrotron-based experiments is desorption induced by electronic transition.

Evolution of the electronic structure of the 2DES under light irradiation

The influence of the light irradiation on the 2DES has been discussed controversially. Santander-Syro *et al.* and Plumb *et al.* argued that only the intensity of the 2DES is increased (possibly due to an increased area of the sample surface hosting the 2DES) but the charge carrier density changes only slightly (ca 20%). [1, 7] In contrast, Meesevana and coworkers argued that the light irradiation dopes the 2DES at the surface of fractured $SrTiO_3$ from zero to its saturation value. [2, 4].

More recent work at surfaces prepared *in situ* support the dominating effect of the light irradiation. [14, 16, 17] We conducted a detailed study of the light influence at the surfaces of TiO_2 anatase which will be presented in the next section. However, before discussing the results on the anatase surfaces, I will briefly discuss the role of the temperature in the the concentration of oxygen vacancies.

Temperature dependence on vacancy diffusion

In the previous paragraphs, I discussed the influence of the photon beam on the creation of oxygen vacancies. The total concentration of oxygen vacancies also depends on the temperature of the sample. To demonstrate this temperature dependence, we first used the intense 0^{th}-order polychromatic beam at the TEMPO beamline (synchrotron Soleil) to create a high concentration of vacancies at the surface of $SrTiO_3(001)$. Subsequently, the fraction of Ti^{3+} in the Ti $3p$ peak was probed every 53 seconds using a low intensity monochromatic beam at $h\nu$=100 eV. At room temperature, all the vacancies created by the 0^{th} order beam are filled up again (*i.e.* no Ti^{3+} signal) within ≈ 2 h as shown by the blue markers in figure 3.3 on page 53. However, changing the temperature to $T = 80$ K results in an exponential decay of the Ti^{3+} signal reaching a stable value of $\approx 28\%$ (red markers in figure 3.3).

The disappearance of the Ti^{3+} signal or respectively, the filling up of oxygen vacancies can be related either to the diffusion or the healing of oxygen vacancies by the residual gas. As the experiments were conducted in UHV (pressure $p \approx 10^{-11}$ mbar) the role of the residual gas is

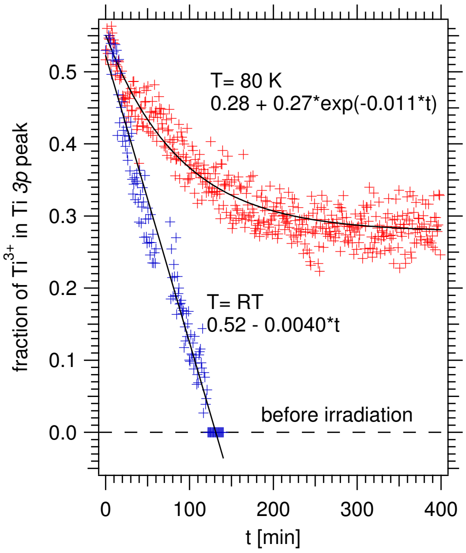

Figure 3.3: Evolution of the fraction of Ti^{3+} signal in the Ti $3p$ peak with time after irradiating the $SrTiO_3(001)$ surface using the intense 0^{th} order beam. At room temperature (blue markers), the Ti^{3+} signal drops back to zero, its initial value before irradiation as shown by the dashed black line. This indicates that all oxygen vacancies created by the intense beam are filled up again within ≈ 2 h. However, at $T = 80$ K (red markers), a quasi-stable concentration of oxygen vacancies is established after ≈ 5 h. The black lines are fits to red or respectively blue markers.

negligible. There are two possible mechanisms for the diffusion of oxygen. As the creation of the vacancies by the photon beam is local, oxygen ions can migrate on the surface to fill up the vacancies. Alternatively, as suggested by Wang *et al.*, the vacancies migrate to subsurface layer towards the bulk. [9] Note that one cannot distinguish between the two scenarios based on the data presented in figure 3.3.

3.3 TiO_2: insights on excess electrons created by oxygen vacancies

It is well established that the TiO_2 atomic planes, and their ability to accommodate chemical doping by oxygen vacancies at the surface region, play a key role in the formation of the 2DES at the surface of $SrTiO_3$ (001). In the case of the $LaAlO_3/SrTiO_3$ interface, only the $AlO_2/LaO/TiO_2$ interface and not the $AlO_2/SrO/TiO_2$ interface is conducting. [26] Thus, as a step forward to understand the formation of 2DESs in TMOs, it is natural to focus on pure TiO_2 crystals such as rutile or anatase.

In fact, it is known that, for both rutile and anatase crystal surfaces, UV or electron irradiation creates oxygen vacancies [120, 149, 155]. Although oxygen vacancies at the surfaces of rutile and anatase have been studied extensively, the presence of a 2DES at the surface of TiO_2 was not reported until our study. [15] As will be shown in section 3.4, 2DESs can be readily obtained at various anatase surfaces, whereas we failed to observe 2DESs on the cleaved or *in-situ* prepared surfaces of *rutile* TiO_2 (110). This indicates that oxygen vacancies at the surface of oxides do not necessarily create 2DESs and that other factors are equally important. In fact, excess electrons in TiO_2, due to oxygen vacancies at the surface, form polarons which behave quite differently for the rutile and anatase phases [14, 103]. This demonstrates that structural factors, such as surface lattice distortions, can determine the fate of those electrons. Thus, to elucidate the origin and realization of 2DESs in different oxides, it is essential to probe the surface electronic structure arising in different lattice configurations.

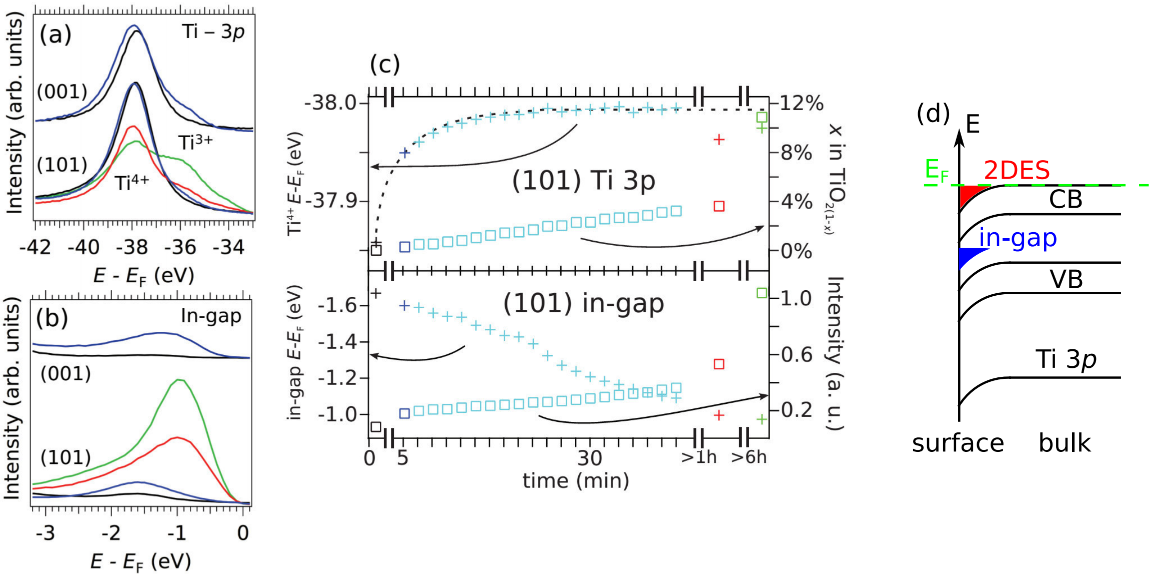

Figure 3.4: Angle integrated spectra of (a) the Ti-3p peak, and (b) the in-gap state of the anatase TiO_2 (001) and (101) surfaces (upper and lower curves, respectively) measured at $h\nu =$ 100 eV. The black curve was measured shortly after the first light exposure, and the blue, red and green curves at sequentially increasing times. (c) Binding energy of the Ti^{4+} peak and concentration of oxygen vacancies (ratio between the Ti^{3+} and total Ti-3p peak area) for different durations of irradiation exposure of the (101) surface (upper panel), and binding energy and intensity of the in-gap state (lower panel). (d) Schematic band alignment along the confinement direction showing the band bending at the surface which confines the 2DES. (a-c) Published in reference [15].

Light evolution of the electronic structure at the anatase surfaces

As shown in figures 3.4(a,b) on page 54, the presence of oxygen vacancies in the surface region of anatase can be identified in the photoemission spectra by the formation of a shoulder in the Ti-3p peak related to a lower valence of the Ti cation, and the appearance of an in-gap state [168] around 1 eV below the Fermi level (E_F), corresponding to electrons trapped near oxygen vacancies [103], The black curves were measured shortly after the first exposure of the sample to the synchrotron radiation, while the blue, red and green curves were recorded at later subsequent times specified respectively by the abscissas of the blue, red and green open squares in Fig. 3.4(c).

Core level Ti 3p

As seen in figures 3.4(a) on page 54, the peak position of the Ti-3p peak shifts to higher binding energies upon UV irradiation, demonstrating the band bending (bb) at the surface. The band bending at the surface is proportional to the concentration of oxygen vacancies as seen in equation (1.3) in section 1.2. All bands (conduction band, valence band and core levels) are effected by the band bending as schematically shown in figure 3.4(d). Hence, the measurement of the binding energy $E - E_F$ of a core level (*e.g.* Ti 3p) using surface-sensitive photoemission spectroscopy

gives an idea of the band bending.
We fit the Ti 3*p* peak by one or two Voigt functions plus a Shirley background to determine the contribution of Ti^{4+} and Ti^{3+} states to the line shape. This yields a shift of Ti^{4+} peak of $E_{bb}^{(001)} = 110$ meV for the (001) surface, and $E_{bb}^{(101)} = 150$ meV for the (101) surface, which corresponds to the *minimal* band bending at the surfaces averaged over the photoemission probing depth at the used photon energy. The actual band bending might be larger, as oxygen vacancies might be already induced at the surface by the cleaving process or by the short beam exposure before the first measurement.

The red and green curves in figures 3.4(a,b), show that many more oxygen vacancies can be induced at the TiO_2 (101) surface than at the (001) surface, in agreement with previous studies [172]. The band bending (peak position of the Ti^{4+} peak) and concentration of oxygen vacancies for the blue, green, and red curves as well as for intermediate measurements are plotted in figure 3.4(c) for the specific case of the anatase (101) surface. The concentration of oxygen vacancies averaged over the escape depth of the electrons is the ratio between the Ti^{3+} and total Ti-3*p* peak area divided by four (two electrons per vacancy and two oxygen anions per Ti cation in TiO_2). This shows that the band bending saturates at rather low concentration of vacancies (about 2%) at the surface. In fact, recent theoretical studies on the electronic structure of $SrTiO_3$ [157, 173] suggest that, for a high concentration of oxygen vacancies, excess electrons do not fill up the conduction band any longer, but form only localized (in-gap) states, and thus do not contribute to the rigid band shift. Thus, as shown in figure 3.4(c) an increase of the oxygen vacancy concentration by a factor of 6 (from 2% to 12%) does not increase the band bending but enhances the intensity of the in-gap state.

In-gap state

Similarly, as shown in figures 3.4(b) and (c) (lower panel), the intensity and binding energy of the in-gap state evolve significantly upon UV irradiation, both for the (001) and (101) surfaces. In contrast to the Ti 3*p* core level, the binding energy of the maximal peak intensity of the in-gap state increases with time (compare upper and lower panel in figure 3.4(c)) Possible explanations for the different binding energies are that the oxygen vacancies are located at different lattice sites and/or forming clusters [157], or the existence of different types of defects [174, 175].
The intensity of the in-gap state increases from the beginning ($t = 0$) even though the band bending is not yet saturated. This indicates that the excess electrons due oxygen vacancies form localized and delocalized states at low ($< 1\%$) concentrations and only localized states at higher concentrations ($> 2\%$).

Oxygen vacancy distribution at the Al(2Å)/anatase interface

To gain further insight in the oxygen vacancy distribution, the Ti core levels were probed after saturation of the vacancy concentration. To create a homogeneously reduced surface we deposited an ultrathin (2Å) film of aluminum on the (001) surface of anatase prepared *in-situ* as described in section 2.4. A redox reaction between Al and oxides creates oxygen vacancies at

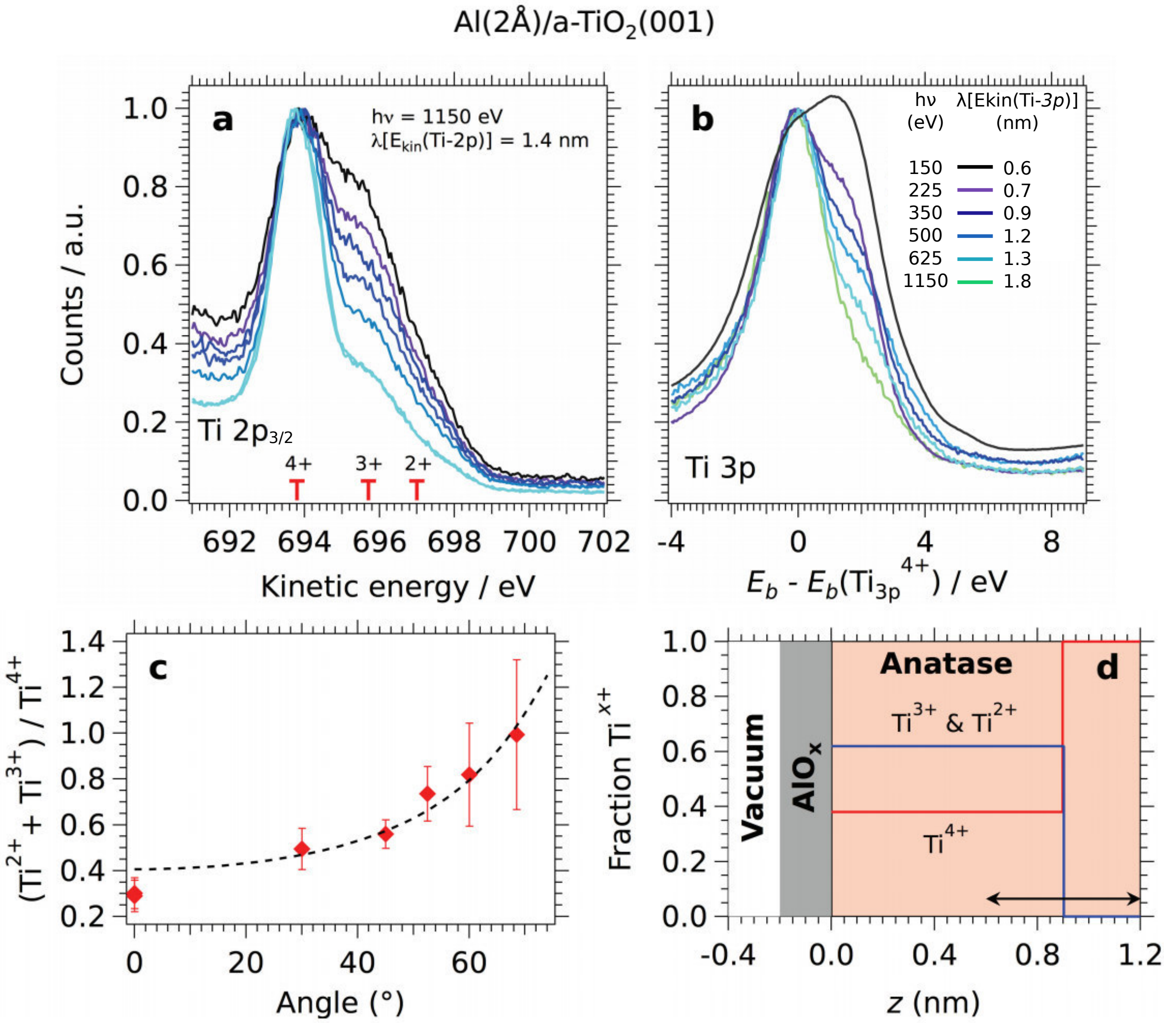

Figure 3.5: (a) XPS of the Ti-$2p_{3/2}$ core level of Al(2Å)/anatase(001) as a function of emission angle using $h\nu = 1150$ eV photons. At this photon energy, the universal inelastic mean free path of electrons emitted from the Ti-$2p_{3/2}$ peak corresponds to $\lambda[E_{kin}(\text{Ti-}2p)] = 1.4$ nm according to [114]. The red markers and corresponding error bars indicate the peak positions and uncertainties for the different Ti oxidation state (4+, 3+, and 2+). (b) XPS of the Ti-$3p$ core level of anatase (001) at normal emission as a function of photon energy. The inelastic mean free path of electrons emitted from the Ti-$3p$ peak at different photon energies is specified in the inset table. The XPS intensity in panels (a) and (b) is normalized to the Ti^{4+} peak. (c) Ratio of intensities, from panel (a), between the Ti^{2+} + Ti^{3+} shoulder and the Ti^{4+} peak as a function of the electron ejection angle. The dashed curve is the best fit to the data assuming a step-like distribution of vacancies over 9 ± 3 Å below the surface, as schematized in panel (d). (d) Model used for the distribution of the different Ti oxidation states due to oxygen vacancies beneath the AlO_x/anatase interface: blue line for Ti^{2+} + Ti^{3+}, red line for Ti^{4+}. The double arrow indicates the error bar in the determination of the vacancy depth distribution. Published in reference [19].

the Al(2Å)/oxide interface. This method is presented in more detail in the following chapter.
As already discussed in section 1.2, the spatial distribution of these electron donors at the surface results in the creation of a potential well confining the electrons and forming the 2DES. To determine the distribution of vacancies, we measured the Ti-2p and Ti-3p core levels of anatase (001) using X-ray photoemission at $h\nu = 1150$ eV as a function of the electron emission angle, and at normal emission as a function of the X-ray photon energy, and fitted the peaks using either Voigt or Lorentzian line shapes together with a Shirley background. As can be seen in figures 3.5(a, b) on page 56, the core levels are composed of several peaks (red markers) corresponding to Ti ions of different oxidation state (4+, 3+, and 2+) due to the presence of oxygen vacancies. We observe that the fraction of Ti^{4+} of stoichiometric, insulating TiO_2 increases for larger electron escape depths, as evidenced by the angle and photon energy dependencies in figures 3.5(a, b). By contrats, the Ti^{3+} and Ti^{2+} components, associated to free carriers and oxygen vacancies, become increasingly important for smaller escape depths and thus, closer to the interface.

To obtain the concentration profile $c(z, Ti^{x+})$ of the Ti^{x+} species along the confinement direction z perpendicular to the surface, we calculate the total area of the corresponding core level peak by:

$$a(Ti) \propto \int dz \sum_{x=2,3,4} c(z, Ti^{x+}) \exp\left(-\frac{d(z)}{\lambda(E_{kin})}\right),$$

where $d(z)$ is the distance traveled by a photo-emitted electron inside matter (*i.e.*, anatase + AlO_x layer), which depends on the emission angle, and λ the inelastic mean free path for electrons photo-emitted with kinetic energy E_{kin}.

Figure 3.5(c) shows the ratio $[a(Ti^{2+}) + a(Ti^{3+})]/a(Ti^{4+})$ as a function of the electron emission angle. The error bars indicate the variation of this ratio using different line shapes and backgrounds to fit the various Ti peaks. We then fit the observed changes in such peak area ratio using a Heaviside function (see section 1.2) for the concentration profile of oxygen vacancies, as shown in figure 3.5(d). The result of the fit, shown by the dashed curve in figure 3.5(c), yields a depth of 9 ± 3 Å for the vacancy-rich layer below the surface, and a fraction of $(62 \pm 15)\%$ of Ti ions with oxidation states 3+ or 2+. As discussed in section 1.2 such a vacancy profile at the surface of oxides can create confined quantum well states with a quantized potential energies as evident from equation (1.4) on page 18. Note that a fraction of $\mathrm{Ti}^{3+/2+}$ of 62% corresponds to at least 16% percent of oxygen vacancies. The existence of these quantum well states at the surface of anatase will be demonstrated in the next section.

3.4 Anatase: 2DES at the (001) and (110) surfaces

We now focus on the electronic structure of the 2DES at the Fermi level in anatase, obtained at the Synchrotron Radiation Center once a stable band-bending has been attained after weak exposure to UV irradiation on cleaved samples (typically ∼ 20 min) – see figure 3.4(c) on page 54.

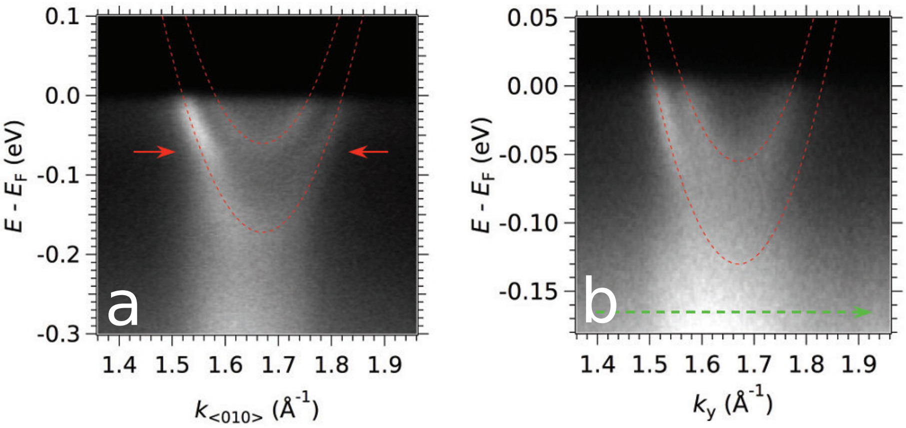

Figure 3.6: (a) Energy-momentum map intensity measured at the (001) surface of anatase at $h\nu = 47$ eV along the $\langle 010 \rangle$ direction showing the two d_{xy} subbands of the 2DES. Dashed red lines are parabolic fits to the dispersing light bands. Red arrows show a kink attributed to electron-phonon coupling [14].
(b) Same as (a) on the anatase (101) surface. The green dashed arrow indicates the direction of measurements along k_y as shown in figure 3.7 (e). Published in reference [15].

As can be seen in the energy-momentum intensity maps in figures 3.6(a,b) on page 58 there are two dispersing bands at the Fermi level E_F indicating a metallic state at the oxygen-deficient (001) and (101) surfaces of bulk-insulating anatase. As the conduction band minimum in anatase is made out of d_{xy} orbitals [61], it is likely that at least one of the observed bands is of d_{xy} character. In the following, based on the symmetry of the Fermi surfaces and on measured intensities for different light polarizations, I will show that both bands are of d_{xy} character. The existence of two bands of the same orbital character demonstrates directly that the observed band dispersions are not bulk-like but instead are quantum well states as discussed previously. This 2D character will be made evident by measuring the band structure along the confinement direction. In short, figures 3.6(a,b) show the $E-k$ dispersion of 2DESs at the surfaces of anatase. Note that, in this thesis, many measurements on Ti-based oxides were conducted at a photon energy of $h\nu = 47$ eV. This photon energy correspondence to a resonance excitation of the electrons in the occupied Ti $3p$ core level to the unoccupied Ti $3d$ states forming the conduction band: Ti $3p \rightarrow 3d$. Hence, there are two processes resulting in the emission of a photoelectron. One process is based on an energy transfer to the photoelectron due to the relaxation of the resonance excitation, the other on the direct excitation of the photoelectron by the incoming photons. The interference of these two processes can result in an increased photocurrent.

Anatase(001)

The energy-momentum intensity map in figure 3.6(a) was measured close to the bulk Γ_{102} point along the cut parallel to the $\langle 010 \rangle$ direction shown in the bulk Brillouin zone in figure 3.7(a) on page 59. The band bottom of the two dispersive bands are at -60 meV for the upper band, and -172 meV for the lower band. The Fermi momenta of $k_{F,1} = 0.09$ Å^{-1} and $k_{F,2} = 0.16$ Å^{-1} and

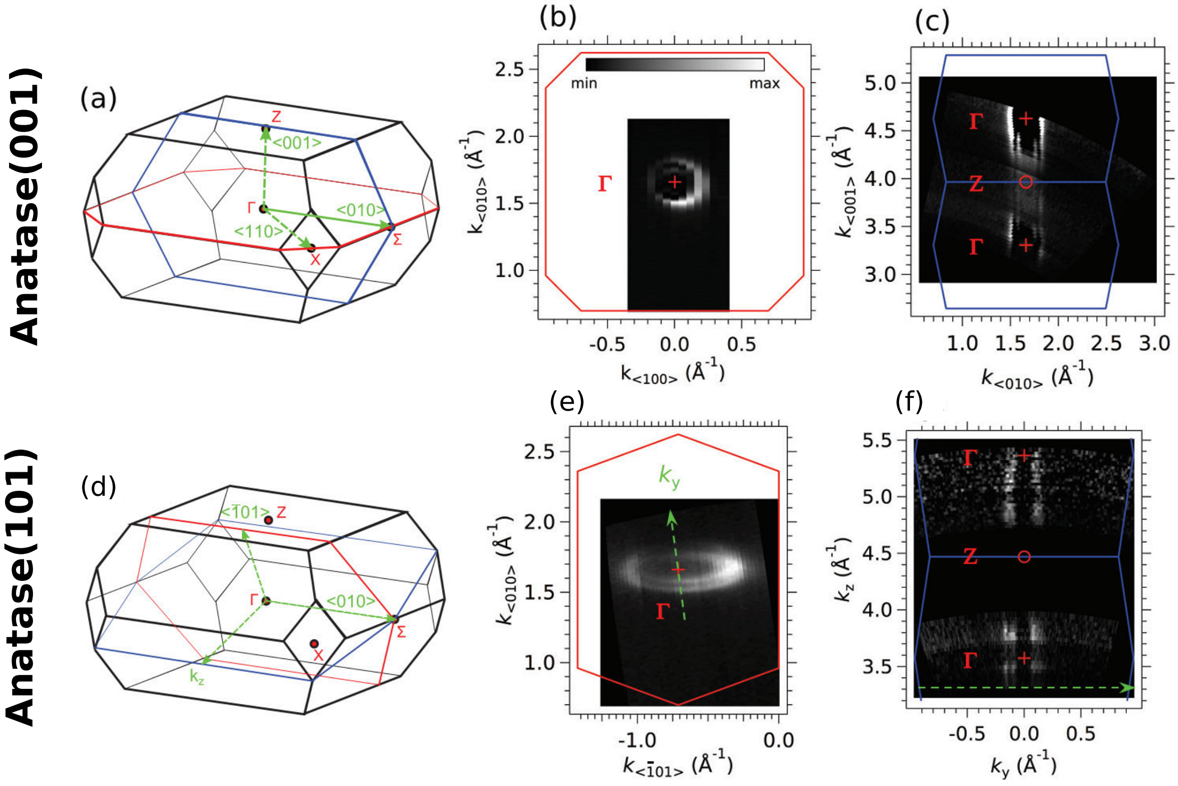

Figure 3.7: (a) Bulk Brillouin zone of anatase, showing the relevant high symmetry directions (green) and planes (red and blue) of the Fermi surfaces and band dispersion at the (001) surface. (b) Fermi surface map (second derivative of ARPES intensity, negative values) measured at $h\nu = 47$ eV on a cleaved, bulk insulating TiO_2 anatase (001) surface. The red lines indicate the edges of the bulk Brillouin zones in the (001) plane around Γ_{012}. The same relative color scale indicating minimum (min) to maximum (max) ARPES intensities is used in all color figures in the rest of this work. (c) Fermi surface map (second derivative of ARPES intensity, negative values) in the $k_{\langle 001\rangle} - k_{\langle 010\rangle}$, or (100) plane, acquired by varying the photon energy in 1 eV steps between $h\nu_1 = 38$ eV and $h\nu_2 = 85$ eV. To calculate the momentum perpendicular to the surface we set the inner potential to $V_0 = 13$ eV [14, 176]. The blue lines are the bulk Brillouin zones containing Γ_{102} and Γ_{103}.

(d-f) Same as (a-c) on the anatase (101) surface. Data in panel (e) was measured at $h\nu = 47$ eV. The green dashed arrow in (e) indicates the direction of measurements along k_y in (f) and figure 3.6(b) on page 58, which is slightly off $\langle 010\rangle$. The out-of-plane Fermi surface map (second derivative of ARPES intensity, negative values) in (f) was measured by varying the photon energy in 1 eV steps between $h\nu_1 = 33$ eV and $h\nu_2 = 51$ eV and between $h\nu_3 = 76$ eV and $h\nu_4 = 103$ eV. Published in reference [15].

the experimental band dispersions are given by the peak positions of the momentum distribution curves (MDCs) at and below E_F. A parabolic fit to the band dispersion yields an effective mass of approximately $0.5m_e$, which agrees well with theoretical [177, 178] and experimental [179] results on bulk Nb-doped anatase.

Note that a kink in the dispersion at a binding energy of about 70 meV is visible (red arrows). In the case of bulk states of anatase, such a kink has been attributed to electron-phonon coupling and studied in detail by Moser *et al.* [14]. The Fermi surface at the (001) plane, shown in figure 3.7(b), consists of two circles of d_{xy} orbital character, confirmed by light polarization dependent measurements presented later, similar to the case of $SrTiO_3$ [1, 2, 7].

The quasi-2D character of these two electronic states is strictly demonstrated by the Fermi surface map in the $\langle 010\rangle - \langle 001\rangle$ plane, perpendicular to the surface plane, shown in figure 3.7(c). This Fermi surface shows that the bands are essentially non dispersing along $k_{\langle 001\rangle}$ over a bulk Brillouin zone, thereby confirming the confined character of the electrons close to the surface.

To obtain the 2D carrier density $n_{2D} = A_F/2\pi^2$, the area A_F enclosed by each circular Fermi surface is calculated $A_F = \pi k_F^2$. This gives an electron concentration of $n_{2D}^{(001)} \approx 5.4\times10^{13}$ cm^{-2}, or about 0.08 electrons per a^2, where a is the short lattice constant of the tetragonal lattice and a^2 the cross section of the unit cell in the (001) plane.

Anatase(101)

Next, we present the ARPES measurements on the (101) surface of anatase. The bottom of the two bands shown in the energy-momentum intensity map in figure 3.6(b) are located at -60 meV and -130 meV, respectively. The Fermi momenta taken from the Fermi surface in Fig. 3.7(f) are 0.41 Å^{-1} & 0.33 Å^{-1} in the $\langle\bar{1}01\rangle$ direction and 0.15 Å^{-1} & 0.10 Å^{-1} in the $\langle 010\rangle$. The parabolic dispersion based on the experimental Fermi momenta and band bottom energies yields an effective mass of $m_{<010>}^{(101)} = 0.6m_e$ along the $\langle 010\rangle$ direction, very close to the one measured at the (001) surface along the same direction.

The bulk Brillouin zone is shown again for clarity in Fig. 3.7(d), together with relevant directions for the (101) surface and the planes of the measured Fermi surfaces.

Figure 3.7(e) shows the Fermi surface on the (101) plane. It consists of two ellipses of identical shape, corresponding again to d_{xy} orbitals.

The Fermi surface map in the $k_y - k_z$ plane, perpendicular to the cleaved surface, is shown in figure 3.7(f). The bands are essentially not dispersing along k_z, indicating their 2D character. Note that, in contrast to the (001) surface, the intensity of the 2DES states in the $k_z - k_y$ plane at the (101) surface drops quickly far from bulk Γ points, due to final-state effects in the photoemission cross-section (see discussion in section 5.2).

The measured Fermi momenta correspond to an electron concentration of $n_{2D}^{(101)} \approx 1.5\times10^{14}$ cm^{-2}, three times larger than the one at the (001) surface, which is probably related to the higher concentration of oxygen vacancies at the (101) surface [172].

Raw data of Fermi surface maps

Figure 3.8 on page 62 shows the raw Fermi surface maps and energy distribution curves (EDCs) of the data presented in figures 3.6 on page 58 and 3.7 on page 59 . Comparing the raw maps of Figs. 3.8(a, b, d, e) with the second-derivative maps of Figs. 3.7(b, c, e, f), it is evident that the second derivative in the Fermi surface maps only enhances the peak-to-background ratio, and does not create artifacts in the intensity distribution.

Additionally, the Fermi surface maps in figures 3.8(a, d), which span a portion of in-plane momentum space larger than in Fig. 3.7, show that the periodicity of the electronic structure at the cleaved (001) and (101) surfaces, respectively, corresponds to the one expected at unreconstructed surfaces.

Note that the Fermi surface map of Figure 3.8(b), and the corresponding dispersions at $h\nu = 47$ eV ($k_z = 3.45$ Å^{-1}) shown in Fig. 3.7, were not obtained at normal emission, but in the second Brillouin zone. Thus, the mere geometry of measurements imposes already extrinsic intensity asymmetries between the the left and right branches of the 2DES electron bands.

Orbital character and light polarization dependence

We discuss now the orbital character and the subband structure of the observed 2DESs. The Fermi surface sheets corresponding to the two light bands are identical in their shape and dependence in light polarization, suggesting an identical orbital character of d_{xy} as shown in the following paragraphs.

The polarization dependence of the t_{2g} orbitals (d_{xy},d_{xz},d_{yz}) forming the 2DES at the (001) surface of SrTiO$_3$ was discussed in previous works [1, 6] and can be directly applied to the (001) surface of anatase. To understand the photoemission selection rules, the geometry of the experimental setup is essential and shown in figure 3.9(a) on page 63. We used light polarized horizontally (LH, in the $x-z$ plane) and vertically (LV, along the y-direction). The slits of the analyzer are aligned vertically along the y-direction and the sample was rotated around the x axis. In this geometry, the measurement plane containing the electrons ejected from the surface and entering the detector through the vertical slits, coincides with the yz plane.

The measurements were conducted at a photon energy of $h\nu = 47$ eV both at normal emission and tilted by 26° around the x-axis. The corresponding positions in reciprocal space of bulk anatase, labeled A and B, are shown in figure 3.9(b).

To measure a non-zero intensity, the final state needs to be even with respect to the $y-z$ measurement plane. As LV polarization is even with respect to this plane, only states with an orbital character even to the $y-z$ plane, hence d_{yz} states, can be detected using LV. The LH polarization has even as well as odd components with respect to the $y-z$ plane, and states of all t_{2g} orbitals have non-zero matrix elements using this polarization.

The ARPES spectra in figures 3.9(c, d) show the measured intensities at the point B in reciprocal space for LH and LV polarizations, respectively. The almost zero intensity in LV polarization demonstrates that the orbital character is not d_{yz}. To exclude one more orbital character we turn to the measured intensities at normal emission (point A) in Fig. 3.9(e). To

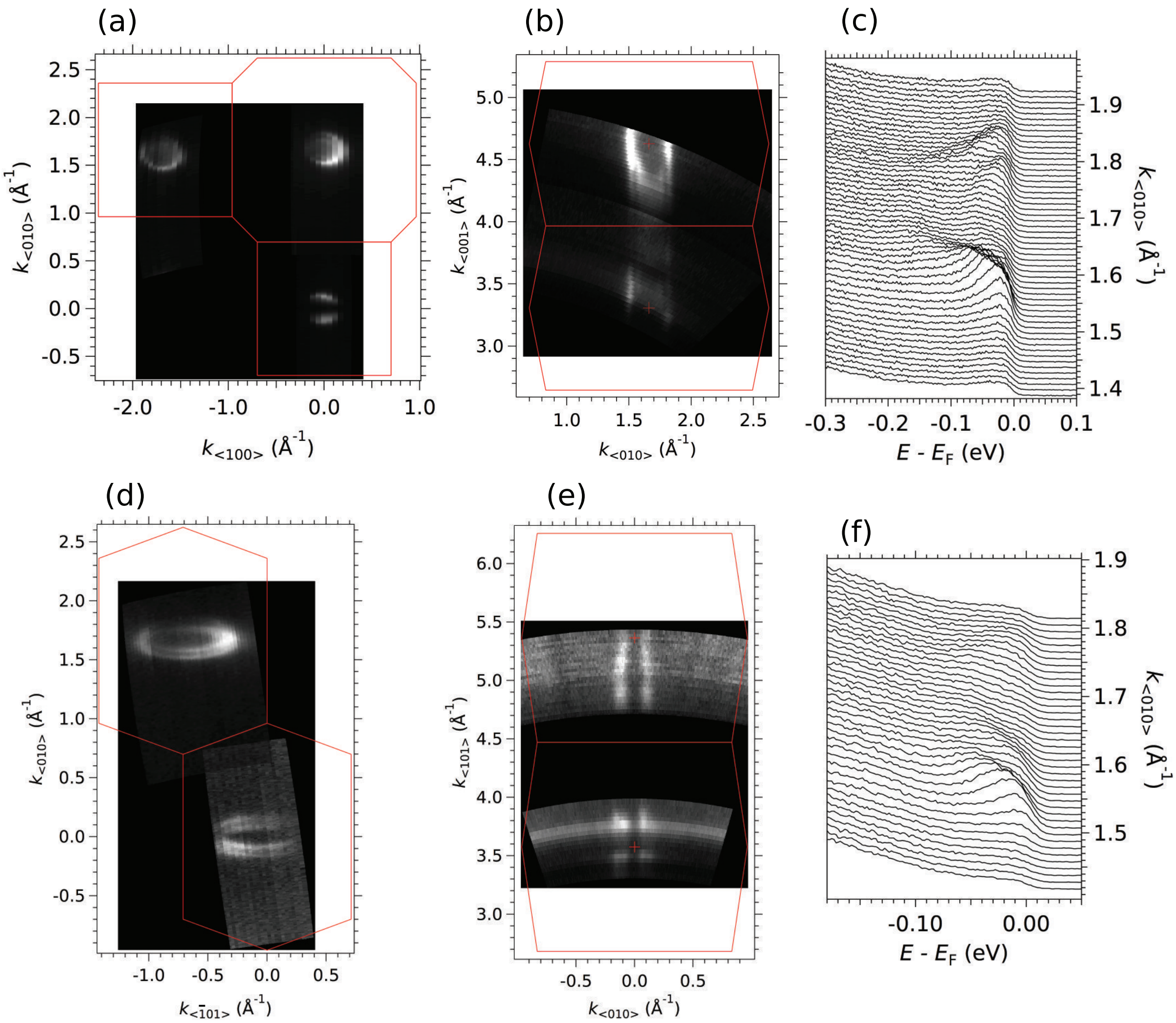

Figure 3.8: (a) Raw Fermi surface map measured at $h\nu = 47$ eV on a cleaved, bulk insulating TiO_2 anatase (001) surface. The red lines indicate the edges of the bulk Brillouin zones in the (001) plane of Γ_{102}. (b) Raw Fermi surface map in the $k_{\langle 001\rangle} - k_{\langle 010\rangle}$, or (100) plane. The red lines are the bulk Brillouin zones containing Γ_{102} and Γ_{103}. (c) Raw EDCs measured at $h\nu = 47$ eV ($k_z = 3.45$ Å^{-1}) along the $\langle 010\rangle$ direction on the (001) surface. They correspond to the energy-momentum map shown in figure 3.7(d).
(d) Raw Fermi surface map measured at $h\nu = 47$ eV on a cleaved, bulk insulating TiO_2 anatase (101) surface. The red lines indicate the edges of the unreconstructed Brillouin zones in the (101) plane of Γ_{002}. (e) Raw Fermi surface map in the $k_y - k_z$ plane measured on a cleaved, bulk insulating TiO_2 anatase (101) surface. The red lines are the bulk Brillouin zones containing Γ_{200} and Γ_{300}. (f) Raw EDCs measured at $h\nu = 47$ eV ($k_z = 3.45$ Å^{-1}) along the $\langle 010\rangle$ direction on the (101) surface. They correspond to the energy-momentum map shown in figure 3.7(h). Published in reference [15].

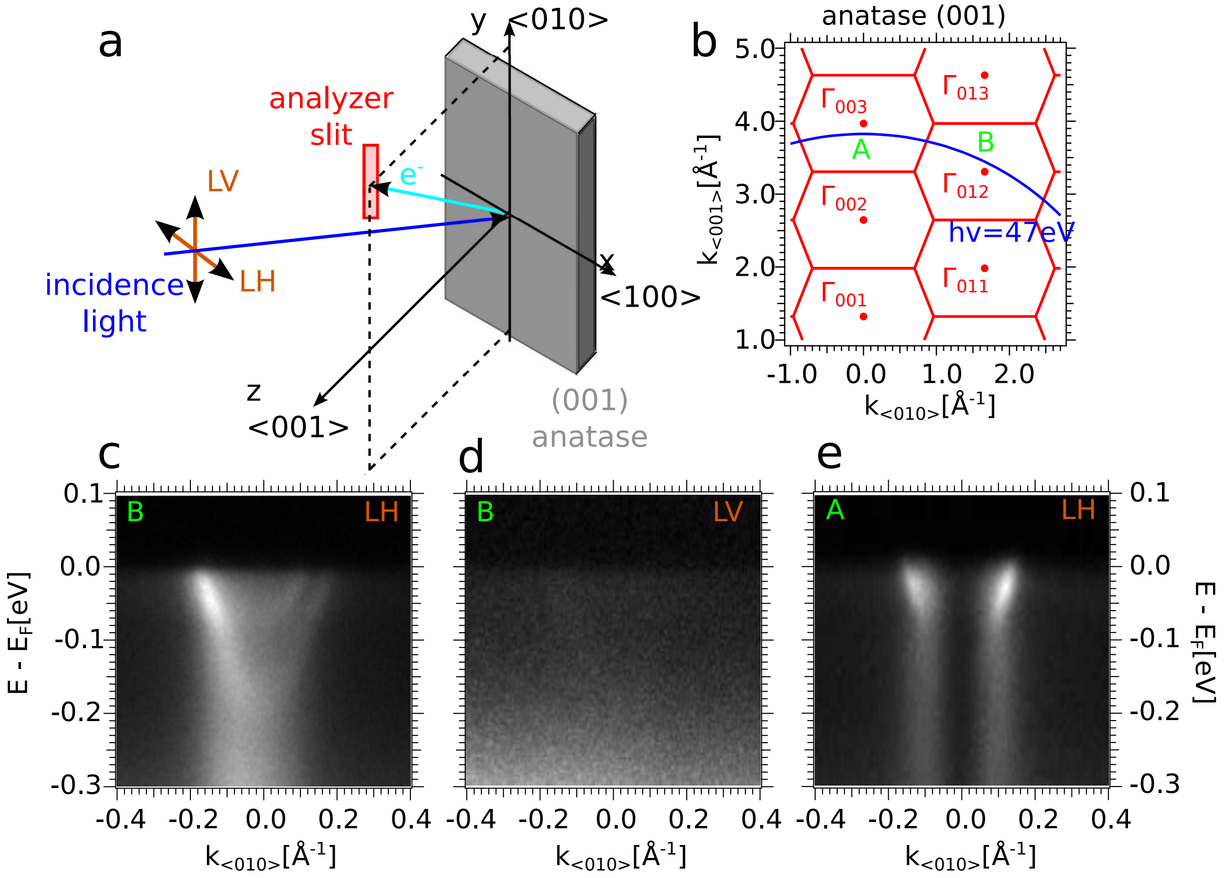

Figure 3.9: (a) Sketch of the experimental ARPES setup. (b) Schematic representation of the reciprocal space of bulk TiO_2 anatase over several Brillouin zones in the (100) plane. (c) Energy momentum map measured at $h\nu = 47$ eV with linear horizontal light polarization (LH) at the surface of a tilted sample corresponding to position B in reciprocal space in (b). (d) Same as (c) but with linear vertical light polarization (LV). (e) Same as (c) but at normal emission, position A in (b). Published in reference [15].

have a non-zero matrix element at the Γ point in normal emission, the final state has to be even with respect to both the $x-z$ and $y-z$ planes. Hence, as the LH polarization is even with respect to the $x-z$ plane, only states with an orbital character even to the $x-z$ plane (d_{xz}) can be detected. The measured intensity at and close to normal emission in figure 3.9(e), *i.e.* around $k=0$, is zero and thus, the bands are not of d_{xz} character.

Consequently, the orbital character of the bands is d_{xy}, in agreement with the circular Fermi surfaces in figure 2(b) of the main text and the non-degeneracy of the t_{2g} orbitals in the bulk of anatase. We verified the matrix elements at a different photon energy to affirm that the matrix elements are due to orbital character and not photon energy.

2D *vs* 3D: dimensionality of the observed electronic states

The presence of two non-degenerate bands of identical orbital character directly implies that the probed electronic structure is not simply the one expected for bulk anatase. For $SrTiO_3$, the existence of different subbands has been related to the confinement of the electronic states in a quantum well at the surface [1, 2].

As discussed in section 1.2 the splitting in energy of two bands of the same orbital character can be used to estimate of the spatial extension of the 2DES. For anatase, the effective mass along the confinement direction is $m_{eff}^{\langle 001\rangle}=4.65m_e$. [178], yielding 1.8 nm for the spatial extension of the 2DES at the anatase (001) surface. However, contrary to our results, Moser *et al.* observed only one dispersing subband of 3D character (*i.e.*, dispersing along the direction perpendicular to the surface) at low charge carrier densities. Moser *et al.* [14] characterized the polaronic conduction for different charge carrier densities (controlled by the oxygen partial pressure sample chamber) at the anatase $TiO_2(001)$ surface using ARPES. In the present work, we only show data after reaching the saturation value of the charge carrier density. Intermediate values of the charge carrier density can be observed but are not stable long enough to measure with a sufficient signal-to-noise ratio without controlling the oxygen partial pressure in the measurement chamber. Note that for a low concentration of oxygen vacancies and charge carriers, the potential well at the surface is rather shallow and the electrons are thus barely confined. But, even for charge carrier densities comparable to our results ($n_{3D,\text{Moser}}\approx 2\times10^{20}$ cm^{-3} to $n_{3D}\approx (n_{2D}^{(001)})^{(3/2)}\approx 4\times10^{20}$ cm^{-2}) Moser *et al.* observed only one dispersing band.

Such discrepancy in the number of bands and dimensionality occurred already in the case of the electronic structure at the surface of $SrTiO_3$: Chang *et al.* [46], using the same ARPES setup as Moser *et al.*, measured only one dispersing band of d_{xy} character and attributed it to the bulk, whereas two d_{xy} bands and 2D behavior were observed in other works [1, 2, 7]. Both studies observing only one d_{xy} band were conducted at the same synchrotron endstation at the Advanced Light Source. Thus, the discrepancy in the number of bands might be related to the specifics of the ARPES endstation. Possible reasons are a lower photon flux or different photoemission selection rules due to different measurement geometries.

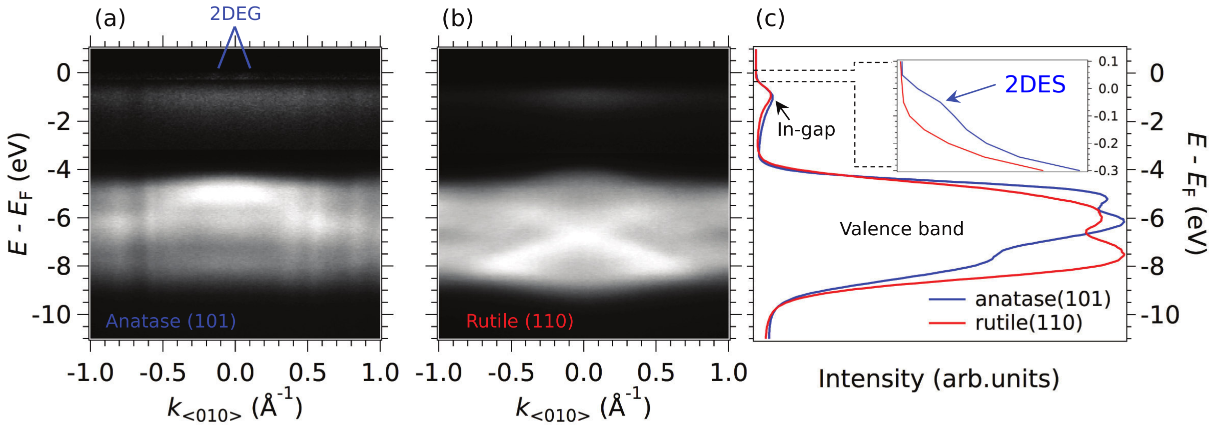

Figure 3.10: (a,b) Energy-momentum maps measured at $h\nu = 100$ eV along the $\langle 010 \rangle$ or the $\langle 001 \rangle$ direction at the anatase (101) and rutile (110) surface. The intensities in different energy intervals (valence band, in-gap, 2DES) were normalized to make all the features visible. (c) Angle-integrated, raw spectra of the two energy-momentum maps in (a,b). The inset shows a zoom of the angle-integrated spectra (log scale) for angles close to normal emission. The spectral weight at the Fermi level in the case of the anatase (101) surface corresponds to the 2DES. Published in reference [15].

Comparison to other 2DESs

Compared to the 2DESs at the surface of $SrTiO_3$ and $KTaO_3$, our ARPES data in TiO_2 anatase reveal the presence of only light (d_{xy}) and no heavy (d_{zx} or d_{yz}) subbands. In fact, the degeneracy of the three t_{2g} orbitals is lifted in bulk anatase [61] due its tetragonal crystal structure and the nonequivalent Ti-O bonding in the $x - y$ plane compared to the z direction (distorted oxygen octahedra surrounding the Ti cation as shown in figure 1.4 on page 13). Due to this degeneracy lift, the electron system confined at the surface of TiO_2 anatase is only composed of electrons of d_{xy}-orbital character.

Rutile vs anatase

The last sections demonstrated the existence of a 2DES consisting of d_{xy} subbands at the (001) and (101) surface of anatase. Although, oxygen vacancies at the surface of rutile can be created in an identical manner as in the case of anatase, namely by synchrotron radiation, we failed to detect a 2DES at the (110) surface of rutile.

The different behavior of excess electrons induced by oxygen vacancies in rutile and anatase was already mentioned before. In contrast to anatase, the excess electrons in rutile do not fill up the conduction band (forming the 2DES), but are localized at lattice Ti sites [103]. Accordingly, we did not detect any dispersing features at the Fermi level at the surface of rutile (110), neither for cleaved nor for *in situ* prepared surfaces under various measurement conditions (photon energy, emission angle, light polarization) at $T = 7$ K.

To illustrate the difference between the two systems, figure 3.10(a,b) on page 65 shows the valence band, the in-gap state corresponding to the localized electrons, and in the case of anatase the

2DES measured at normal emission at $h\nu = 100$ eV. The angle-integrated data in figure 3.10(c) demonstrates that the concentration of oxygen vacancies is similar in the two cases, as the in-gap states have similar intensities. The failure to observe dispersing features at the Fermi level of rutile shows that oxygen vacancies at the surface are not sufficient to create a 2DES, and that structural factors play a crucial role regarding the localization/delocalization of excess electrons.

Disorder due to a large concentration of oxygen vacancies

The 2DESs at the surfaces of anatase exist due to electron donors confined at the surface: the oxygen vacancies. In this and the following sections, I will focus on changes induced by concentrations of oxygen vacancies larger than the ones discussed in the previous sections. As will be shown, the oxygen vacancy can be the origin as well as the reason for the disappearance of the 2DES.

We conducted our measurements at two different synchrotrons: SRC (2^{nd} generation) and Soleil (3^{rd} generation). The normal measurement conditions (photon flux density at the surface of the sample, vacuum pressure, temperature) at SRC enable to reduce the surface, create the 2DES, and study a stable 2DES for days. In contrast, the much higher photon flux density on the sample (roughly a factor of 50) at Soleil creates so many oxygen vacancies that the induced disorder at the surface lead to the disappearance of the 2DES within about one hour at $T = 7$ K at the anatase (101) surface. As this effect was never observed for the 2DES at the surface of $SrTiO_3$ and $KTaO_3$, we conclude that the anatase surfaces are much more sensitive to the UV-irradiation.

The effects of the synchrotron UV light on the (001) surface are shown in figure 3.11 on page 67. An approximate upper limit for the effects is shown in Fig. 3.11(a), where we present the angle-integrated spectra measured at $h\nu = 100$ eV on a fractured (001) anatase sample for binding energies between -45 eV and 2 eV. The red curve corresponds to a weakly reduced surface, similar to the data in figure 3.4, and the blue curve to the electronic structure of the surface after exposing the sample to high intensity 0^{th} irradiation of the synchrotron. As can be seen from figure 3.11, there are the same (but enhanced) changes in the electronic structure induced by the severe exposure to UV light as discussed in figure 3.1. For example, the shoulder of the Ti-3p peak, corresponding to Ti^{3+} states, transforms to become the main Ti-3p peak at even lower binding energies, indicating that the majority of Ti atoms close to the surface have a low valency ($\leq 3+$) due to the creation of many oxygen vacancies. Based on the previous discussion of the oxygen vacancy concentration at the Al/anatase(001) interface (2DES still exists), the concentration after 0^{th} irradiation is larger than 16%. Figures 3.11(b, c) show the angle-resolved measurements corresponding to the spectra in figure 3.11(a), zooming over the valence-band region. The clear dispersion of the valence band in the weakly reduced surface, Fig. 3.11(b), is a direct consequence of the good surface crystallinity (Bloch theorem). After intense UV irradiation, Fig. 3.11(c), the surface crystallinity is destroyed, and the valence-band becomes non-dispersive and featureless.

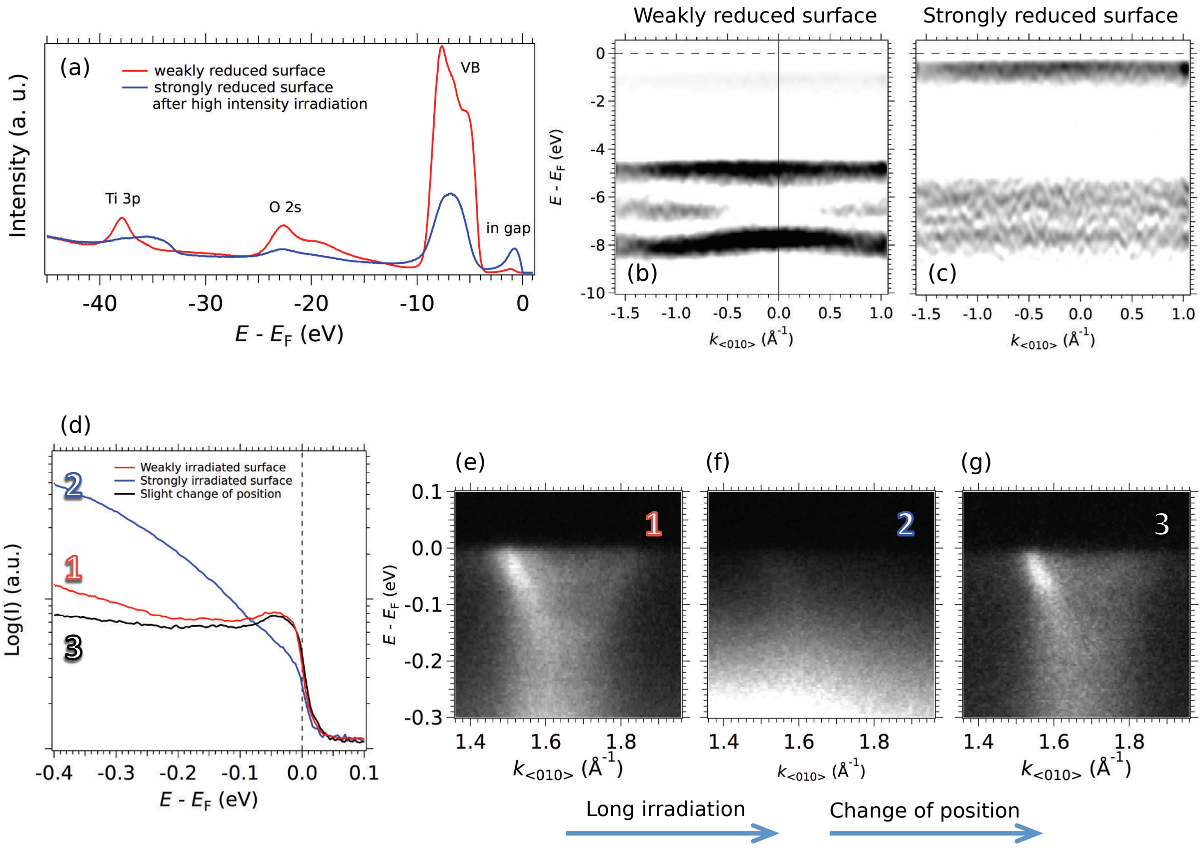

Figure 3.11: (a) Angle-integrated spectra of a cleaved $TiO_2(001)$ anatase sample measured at $h\nu = 100$ eV showing the density of states for binding energies between -45 eV and 2 eV. The red curve corresponds to a weakly reduced surface, the blue one to a surface exposed to the intense zero-order light irradiation of the synchrotron. (b, c) Corresponding angle-resolved energy-momentum maps (second energy derivatives, negative values only) zoomed over the valence-band region. While the valence band is dispersive in the crystalline, weakly irradiated surface, it becomes non-dispersive and featureless in the amorphous, strongly irradiated surface. (d) Angle-integrated spectra measured at $h\nu = 47$ eV (log scale for spectral intensity), showing the tail of the in-gap peak and the intensity at the Fermi level. The red curve (labeled 1) corresponds to a freshly cleaved sample irradiated for a first sweep, the blue curve (labeled 2) to a surface exposed to irradiation for several hours, and the black curve (labeled 3) to the electronic structure after changing the sample position. (e, f, g) Energy-momentum maps measured at $h\nu = 47$ eV along the $\langle 010 \rangle$ direction. The momentum-integrated curves of these maps corresponds to the data shown in (d) as indicated by the labels 1, 2 and 3. Published in reference [15].

Anatase(001): Disappearance of 2DES under synchrotron irradiation

Even without the zero-order irradiation, the reduction of the surface can lead to the disappearance of the 2DES. The angle-integrated spectra in figure 3.11(d) were measured at $h\nu = 47$ eV and show the tail of the in-gap peak and the intensity at the Fermi level for binding energies between -0.4 eV and 0.1 eV. After several hours of irradiation (blue curve), the intensity of the in gap state increases and the intensity at the Fermi level corresponding to the 2DES decreases. The state of the weakly irradiated surface (red curve) can be retrieved by slightly changing the position of the UV light spot on the sample surface (black curve). As the size of the beam spot is only $\approx 50 \times 50\ \mu\text{m}^2$, the strong reduction of the surface is local. This results suggests that UV light can be used to tailor locally the surface order/disorder in anatase, and thus write mesoscopic or nanoscopic patches of metallic 2DES intercalated with patches of disordered less conducting material.

The energy momentum maps corresponding to the angle-integrated spectra in figure 3.11(d) are shown in figures 3.11(e,f,g). The 2DES is clearly visible in figure 3.11(e), whereas there is almost no intensity at the Fermi level in figure 3.11(f) at the strongly reduced surface, and the 2DES is recovered in figure 3.11(g), after moving the UV spot to a neighboring region in the sample.

Anatase(101): Disappearance of 2DES under synchrotron irradiation

Another interesting fact is that the anatase (101) surface degrades more rapidly than the (001) surface. The data corresponding to this degradation are shown in figure 3.12 on page 69. The angle-integrated spectra (red curves) in Fig. 3.12(a) were measured at equal time intervals (of approximately 2.5 minutes) at a photon energy $h\nu = 47$ eV, and show the increase of the intensity of the in-gap peak and decrease in the intensity at the Fermi level for binding energies between -2.5 eV and 0.2 eV. Three of the curves highlighted in black, green and blue correspond to the start, a midpoint and the end of these measurements.
The intensity of the 2DES is evident in the momentum distribution curves at the Fermi level in figure 3.12(b). At the beginning (black curve) two peaks, corresponding to the dispersing bands shown in figure 2(h) of the main text, are visible. Their intensity decays rapidly after several minutes, is barely visible (green curve) and disappears completely (blue curve). Note that the Fermi momenta in the MDCs does not increase –compare black and green curve in Fig. 3.12(b), although more oxygen vacancies are created as evidenced by the increase in intensity of the in-gap state in Fig. 3.12(a). As the electron density in the conduction band is proportional to area of the Fermi surface (and hence, the Fermi momenta), the excess electrons due to oxygen vacancies seem to populate the in-gap state (localized electrons) and not any longer the conduction band (delocalized electrons). This observation is in agreement with the observed saturation of the band bending discussed previously.

A high concentration of oxygen vacancies induced by the synchrotron irradiation creates a high degree of disorder at the surface. If the degree of disorder at the surface is sufficiently high, no dispersing bands exist as there is no longer the periodicity of the lattice, and the 2DES

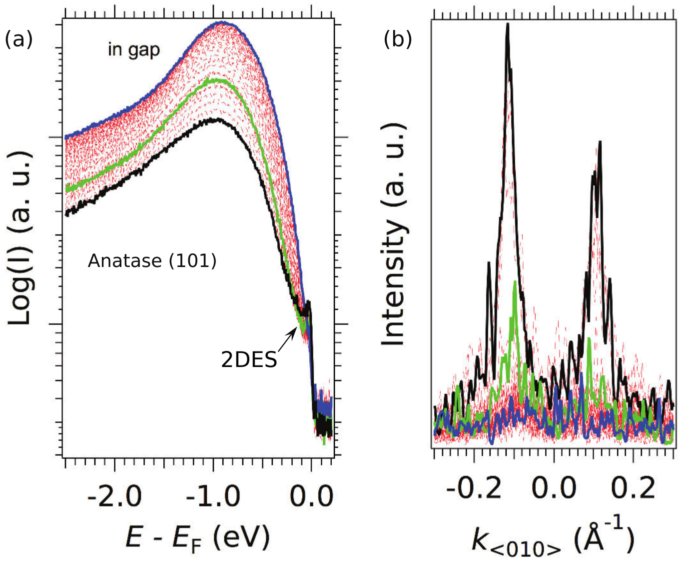

Figure 3.12: (a) Angle-integrated spectra (log scale for intensities) measured at equal time intervals at $h\nu = 47$ eV for binding energies between -2.5 eV and 0.2 eV. One observes the in-gap peak and the intensity of the 2DES at the Fermi level. Three of the curves are highlighted in black, green and blue corresponding to the start, a midpoint and the end of these measurements. (b) Corresponding momentum distribution curves at the Fermi level. Published in reference [15].

disappears, as effectively seen in Fig. 3.12(b).

Conclusion

In conclusion, we found that light irradiation locally dopes the anatase surfaces, while the behavior of the excess electrons, *i.e.* delocalized or localized, depends on the concentration of oxygen vacancies at the surface, eventually resulting in the local destruction of the 2DES after a high UV irradiation dose. This effect , never observed for 2DESs at other oxide surfaces, shows that UV light can be used to tailor locally the surface order/disorder in anatase. Moreover, in rutile all excess electrons are localized demonstrating that different lattice configurations in the *same material* (*i.e.* TiO_2) influence if a 2DES exists or not.

The 2DESs at the (001) and (101) surface of TiO_2 anatase consist of two d_{xy} subbands forming circular Fermi surface sheets at the (001) termination and ellipsoidal ones at the (101) termination. Such orientational tuning of the Fermi sea symmetries is wholly analogous to the one found at different surfaces of $SrTiO_3$ [10] as will be presented in chapter 5.

Chapter 4

2DESs at the interface of oxides and ultrathin metal layers

The last chapter demonstrated the existence of a 2DES at the surface of cleaved anatase crystals due to oxygen desorption induced by the synchrotron irradiation. One motivation of my thesis was to create 2DESs in a reproducible manner (in contrast, to the rather uncontrolled process of cleaving or fracturing) and without the need of a synchrotron providing a high enough photon flux and energy to create sufficient oxygen vacancies. At the same time, the method should be easy to implement in different UHV setups.

Note that, one can also study the 2DES at the $LaAlO_3/SrTiO_3$ interface by angle-resolved photoemission. [180] However, the critical thickness of the $LaAlO_3$ layer to create a 2DES in $LaAlO_3/SrTiO_3$ is 4 unit cells ($\approx$ 1.6 nm), *i.e.* a layer thickness of at at least 4 u.c., and thus, too thick to enable high-resolution ARPES measurements in the UV range (see universal curve in figure 2.4 on page 28). The existence of this critical thickness was related to the polar catastrophe scenario [26], a electrostatic mechanism for creating the 2DES not necessarily related to oxygen vacancies.

As will be shown in the next section, we explored the creation of 2DESs in oxides using ultra-thin (several Å) metal films.

4.1 Growth of ultrathin metal layers on oxide surfaces

We tried to achieve the electron doping of the surface of the oxide by ultra-thin metal films using two different approaches. Firstly, creation of oxygen vacancies due oxygen diffusion from the oxide to the metal as *e.g.* Al (see section 4.2). Secondly, doping by electron transfer using a metal of low work function, *e.g.* potassium or cesium (see section 4.4).

Additionally, we also used metal films to passivate the $in-situ$ cleaned surface from contamination in ambient conditions. This method enabled us to conduct ARPES measurement on prepared surfaces in synchrotron setups in which surface preparation tools are not available. We used gold thin films to passivate the surface and studied them with ARPES after removing the gold film using the top-post method discussed in section 2.4. Some of the data on $SrTiO_3(111)$

Material	$SrTiO_3$	Cs	K	Al	Au
Work function Φ [eV]	4.2	1.9	2.3	4.2	5.3
Heat of formation ΔH_f^O [kJ/mol O]	-	-350	-370	-560	+50

Table 4.1: Work functions Φ and heat of formation ΔH_f^O of the metals most stable oxide of the metals deposited on oxides in this thesis. For comparison, the work function of $SrTiO_3$ is given in the second column. Values taken from reference [123].

presented in section 5.2 was obtained on Au-capped sample.

Substantial work on metal/oxide interfaces has been conducted. Two reviews summarizing many results are the ones of Diebold and Fu & Wagner. Diebold [80]reviewed the growth of metal layers on the surfaces of TiO_2, Fu and Wagner [123] of both TiO_2 and $SrTiO_3$. The following paragraphs are mostly based on the review of Fu and Wagner.

In section 4.2, we will study the deposition of Al on the surface of various oxides. Due to a redox reaction between Al and the oxide, a 2DES is created. Whether the metal will be oxidized or not is given by the heat of formation ΔH_f^O of the corresponding metal oxide. Diebold concluded that the metal oxidation is favored if $\Delta H_f^O < -250$kJ/mol O for TiO_2. This criterion is applicable to $SrTiO_3$ as well. As evident from table 4.1, the heat of formation of Al is -560kJ/mol O and thus, easily fulfills the criterion.

More generally, metal/oxide interfaces can be approximated as a metal/ n-type semiconductor interface in the sense that the Fermi level of $SrTiO_3$ is close to the conduction band minimum. Metal/semiconductor interfaces have been extensively studied, two of the pioneers being Schottky [181] and Mott [182] who described the band bending at these interfaces. The types of band bending at the interface are given by the relation of work functions of the metal Φ_M and $SrTiO_3$ Φ_S and are shown in figure 4.1 on page 72. For both types, a space charge layer in the n-type semiconductor forms which results in a band bending at the interface. If $\Phi_M > \Phi_S$ the positively charged space layer creates a Schottky barrier. If $\Phi_M < \Phi_S$ the negatively charged space layer creates a Ohmic contact. Hence, to achieve electron doping (creation of a 2DES) at interface of metal and oxide, one should deposit metals of low work functions as *e.g.* alkali metals. That is why in section 4.4, I will discuss the interfaces of K and Cs with $SrTiO_3$. As can be seen, in table 4.1 on page 71 the work function of K is 1.9 eV lower, the one of Cs 2.3 eV, than in $SrTiO_3$ and thus, one would expect a downward band bending at the interface.

Finally, Au is not oxidized and should result in an upward band bending.

First, I will focus on the Al/oxide interface.

4.2 Redox reaction at the interface of oxides & Al

2DESs in TMOs have been original discovered at the $LaAlO_3/SrTiO_3$ interface by Ohtomo and Hwang [20]. As already discussed in section 1.2, there are different ways to create 2DESs in $SrTiO_3$, which can be classified into electrostatic doping and local chemical doping.

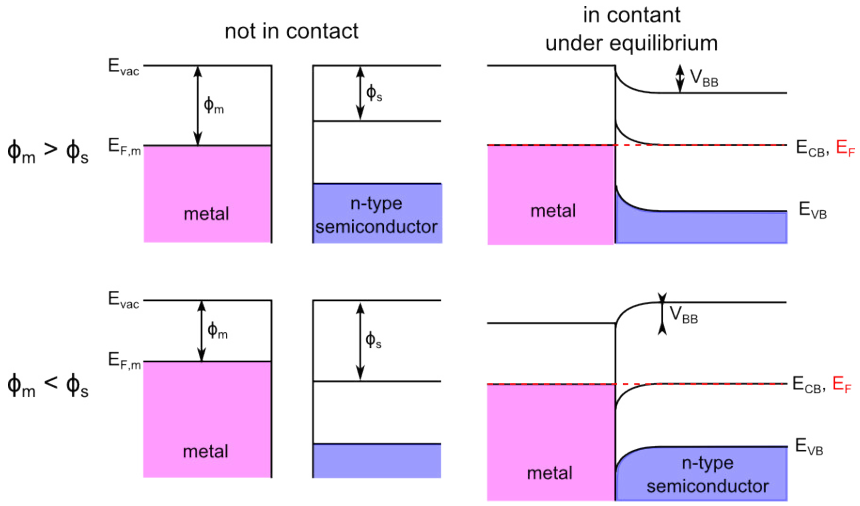

Figure 4.1: a) Band diagram of a metal and a n-type semiconductor. The metal is characterized by its work function Φ_m and its Fermi level $E_{F,m}$, the semiconductor by its work function Φ_s, the energy of the valence band maximum E_{VB} and conduction band minimum E_{CB} which is equal to its Fermi level $E_{F,s} = E_{CB}$. b) Band bending V_{BB} at the interface of the metal and the n-type semiconductor. Depending on the relation of the work functions, a Schottky barrier ($\Phi_m > \Phi_s$) or ohmic contact ($\Phi_m < \Phi_s$) is created.

Complicated oxide heterostructures and unstable oxygen-deficient surfaces

However, the fabrication of 2DESs in oxide heterostructures, like $LaAlO_3/SrTiO_3$, requires growing a layer of binary (*e.g.* Al_2O_3) or ternary (*e.g.* $LaAlO_3$) oxides with a "critical thickness" of at least 20 Å using evolved deposition techniques, such as pulsed laser deposition [20, 26, 29, 49, 73, 97, 183, 184]. Thus, the reproducibility of their properties depends crucially on the growth parameters, while their fabrication is complex, expensive, and unsuitable for mass production. Moreover, the existence of a critical thickness of 20 Å for the onset of conductivity severely limits the control of the 2DES's properties, hampering tunneling spectroscopy studies or applications that rely on charge or spin injection [185].

Similarly, the realization of 2DESs at the surface of $SrTiO_3$ or other oxides requires the use of intense UV or X-ray synchrotron radiation, to desorb oxygen from the surface [1–4, 8, 10, 11, 15]. Thus, these 2DESs can be only manipulated and studied in ultra-high vacuum (UHV), to preserve the vacancies from re-oxidation, and are obviously not suited for experiments or applications at ambient conditions.

A simple and versatile method to create 2DESs in TMOs

In this chapter a new, wholly general, extremely simple and cost-effective method to generate 2DESs in functional oxides will be presented. Thermal evaporation from a Knudsen cell is used to deposit, at room temperature in UHV, an atomically-thin layer of an *elementary* reducing agent, such as pure aluminum, on the oxide surface.

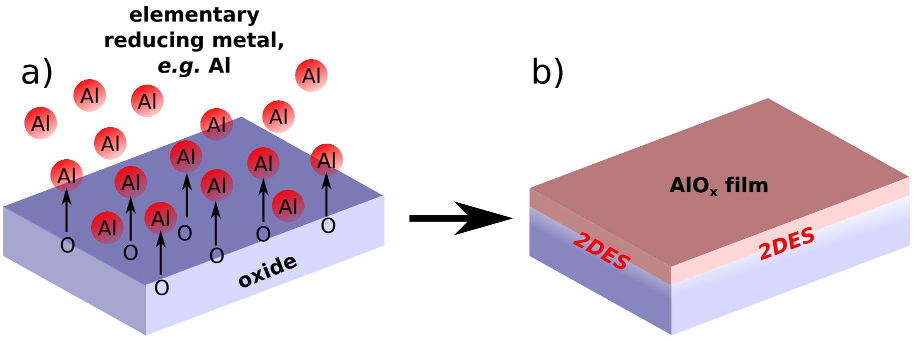

Figure 4.2: (a) Deposition of an elementary reducing agent to create 2DESs in oxides. Due to a redox reaction oxygen is pumped out of the oxide. (b) For Al film thicknesses of ≈ 2 Å , the film is completely oxidized. At the interface of the oxidized Al film and the oxide 2DESs can emerge.

Due to an efficient redox reaction, the Al film pumps oxygen from the substrate, oxidizes into insulating AlO$_x$, and forms a pristine, homogeneous 2DES in the first atomic planes of the underlying oxide. This principle is shown in figure 4.2. The principle of redox reactions induced by metals at the surface of oxides is well documented [123, 186]. However, the simple idea of using a pure, elementary reducing agent to create a 2DES at a metal-oxide interface was not explored so far. This overcomes the complexity of growing an oxide thin film, the requirement of a critical thickness of insulating capping layer to create the 2DES in UHV, and the necessity, in the case of surfaces, of strong synchrotron radiation to desorb oxygen.

The method to create 2DESs due to a redox reaction with Al works for numerous oxides. I will discuss the interface of Al and SrTiO$_3$(001) in detail in the next sections. However, this method can also be used to create 2DESs not only in SrTiO$_3$(001), but also in anatase(001), ZnO (see section 4.3), BaTiO$_3$ (6.2) and CaTiO$_3$ (6.3).

ARPES: 2DESs at the Al/Anatase(001) interface

The existence of a 2DES at the interface between the oxidized Al layer and anatase(001), is evidenced by our angle-resolved photoemission spectroscopy (ARPES) data presented in figure 4.3 on page 74. Note that all photoemission measurements presented in this chapter were conducted at a temperature of $T = 7$ K if not specified otherwise. As discussed previously (see section 3.4), the 2DES in anatase is composed of two d_{xy} subbands with an effective mass of about $0.5m_e$. The Fermi-surface areas and, hence, the electron densities of the 2DESs at the Al(2Å)/anatase(001) interface are about 2 times larger than at the cleaved surface of anatase (compare figures 4.3 and 3.7 on page 59), due to a higher concentration of oxygen vacancies.

Note that the measurements presented in figure 4.3 were conducted using a different geometry than the ones in figure 3.6 on page 58. Instead of measuring close to Γ_{012} using LH photons, data was recorded close to Γ_{102} using LV photons. Practically, this means that the sample was rotated instead of tilted. As the two configurations have different mirror planes (see section 2.2

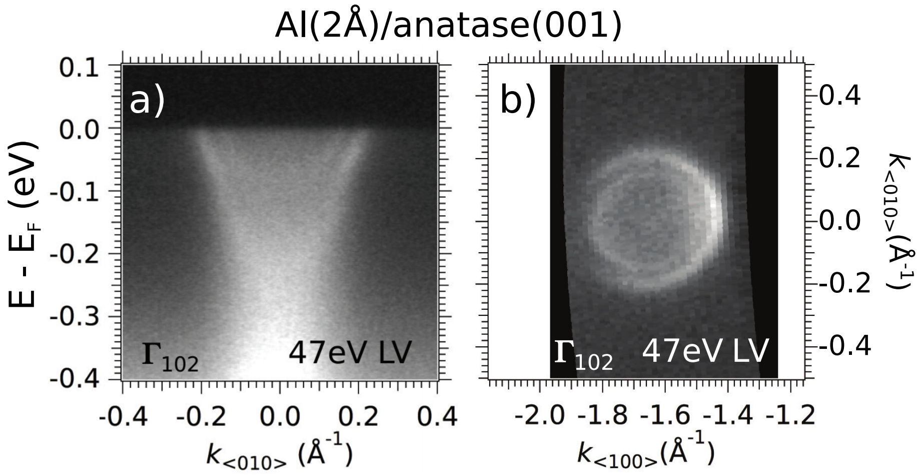

Figure 4.3: Energy-momentum intensity map (a) and Fermi surface map (b) measured at the Al(2Å)/anatase(001) interfaces prepared *in-situ* using a photon energy of $h\nu$=47 eV and linear vertical polarized (LV) photons. The observed band structure is similar to the 2DES measured at the cleaved surface of anatase as discussed in the previous chapter (see section 3.4). Published in reference [19].

and table 2.1 on page 31), the light polarizations sensitive to d_{xy} orbitals are different. Another difference between the two measurements is that the thin film growth of Al was conducted on prepared surfaces as discussed in section 2.4 and not on cleaved or fractured crystals.

For simplicity, and to recall that we are simply depositing pure Al (*not aluminum oxide*) on top of the oxide surfaces, all throughout this thesis we note the resulting oxidized Al capping layer simply as "Al", specifying in parenthesis the evaporated thickness.

ARPES: 2DESs at the Al/SrTiO$_3$(001) interface

The electronic structure of the 2DES in anatase(001) helps to understand the ARPES data of the 2DES at the interface between the oxidized Al layer and SrTiO$_3$(001) presented in figure 4.4 on page 75. Under identical measurement conditions (position in reciprocal space, photon energy and polarization) one can see in both materials the two d_{xy} subbands forming two circular Fermi surfaces as shown in figures 4.3 and 4.4(a,c). The effective masses along <010> are different in SrTiO$_3$ $0.7m_e$ and anatase $0.5m_e$ but comparable as the local bonding environment in the oxygen octrahedron surrounding the Ti ion are similar. However, as discussed previously, due to the different crystal lattices (compare figure 1.1(a) on page 8 and 1.4 on page 13), the crystal field is different. While, in cubic SrTiO$_3$ the t_{2g}-orbital manifold (d_{xy}, d_{xz}, d_{yz}) is degenerate, the degeneracy is lifted in tetragonal anatase.

Consequently, one can measure d_{xz}, d_{yz} orbitals in the 2DES at the Al/SrTiO$_3$ interface as shown in figures 4.4(b,d). As pointed out by Plumb *et al.*, the d_{xz}, d_{yz}-states are neither strictly 2D nor 3D [7] as they are only weakly confined in the "upper" part of the quantum well due to their small effective mass along the confinement direction. Hence, to measure the d_{xz}, d_{yz} bands, one needs to chose positions in reciprocal space which are close to the bulk Γ point. As shown in the

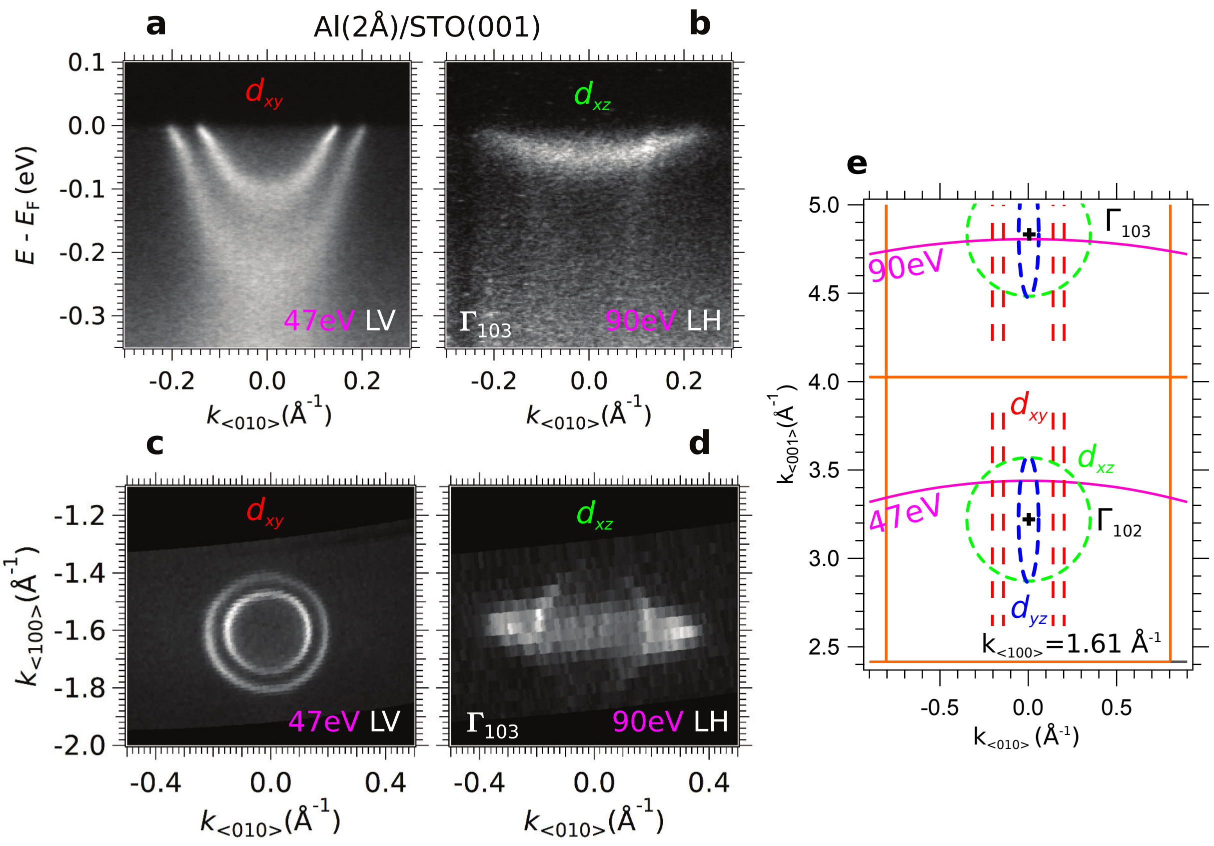

Figure 4.4: (a, b) ARPES energy-momentum intensity maps measured at the Al(2Å)/$SrTiO_3$(001) interface prepared *in-situ*, using respectively 47 eV (LV) and 90 eV (LH) photons. (a) Two d_{xy} subbands with effective mass of $m^*_{xy} \approx 0.7$ and band bottoms at $E_{xy,1} = 223$ meV and $E_{xy,2} = 110$ meV. Using the nomenclature in section 2.2, the mirror plane is the xz plane and thus, only bands of d_{xy} and d_{yz} character have non-zero matrix elements at $k_{<010>} = 0$ using LV photons (see table 2.1 on page 31). As shown in (e), $h\nu = 47$ eV corresponds to position in reciprocal space which are off the bulk Γ point. That is why only d_{xy} bands are visible. (b) d_{xz} subband with effective mass of $m^*_{xy} \approx 7$ and a band bottom at $E_{xz} = 50$ meV. Only d_{xz} orbitals can be detected at $k_{<010>} = 0$ using LH photons given that the photon energy $h\nu = 90$ eV corresponds or is close to a bulk Γ point.
(c, d) Corresponding Fermi surface maps. Data at $h\nu = 47$ eV were measured in the Brillouin zone of the Γ_{102} point, while data at $h\nu = 90$ eV were measured around Γ_{103}. The two d_{xy} subbands are forming two circular Fermi surfaces in (c) while the d_{xz} subband is forming an ellipsoidal Fermi surface in (d).
(e) Reciprocal space of $SrTiO_3$ in the <100>-<001> plane. The orange lines correspond to the bulk Brillouin zone and the black markers to the Γ points. The red, green and blue dashed lines represent the Fermi surface of the t_{2g} manifold in the 2DES at the surface of $SrTiO_3$(001) as measured by Plumb *el al.* [7] The pink line are the cuts in reciprocal space measured by ARPES at the given photon energies.
Unless specified otherwise, all spectra in this and remaining figures in this section were measured at $T = 8$ K. (a-d) Published in reference [19].

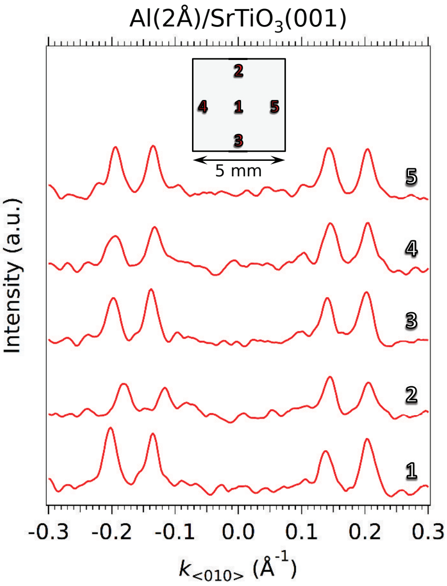

Figure 4.5: Momentum distribution curves integrated over $E_F \pm 5$ meV for the Al/SrTiO$_3$(001) interface prepared *in-situ*, measured at different positions (see inset) separated by at least 4 mm from each other - or over 100 times the size of the UV spot. Each spectrum was obtained within minutes on a part of the sample that had not been illuminated before. The similarity of the curves demonstrated the homogeneity of the 2DES at the Al/SrTiO$_3$(001). Published in reference [19].

reciprocal space map in figure 4.4(e), a photon energy of $h\nu = 90$ eV corresponds to Γ_{103} in the used geometry (rotated sample). Hence, one can measure the d_{xz} subband as shown in figures 4.4(b,d).

The energy-momentum and Fermi surface maps formed by the t_{2g} orbitals, shown in figure 4.4, agree with previous ARPES studies at the reduced (001) surface of SrTiO$_3$ [1, 2, 7], demonstrating that in both cases the same 2DESs are observed.

Homogeneous reduction of oxide surface

Instead of the local creation of oxygen vacancies using an intense UV beam over a time interval of tens of minutes, the evaporated Al certainly reduces the whole surface homogeneously and instantaneously. As a consequence, the data quality, evidenced by the line widths, is also much better than in previous studies. Thus, as shown in figure 4.4(a), a kink and change in intensity in the dispersion of the light bands at $E \approx -30$ meV, attributed to electron-phonon coupling [13], can be very clearly distinguished and will be discussed in section 8.2.

Additionally, in contrast to previous studies of the 2DES at the surface of SrTiO$_3$ at fractured [1, 2] or *in-situ* prepared surfaces [7, 10], the 2DES exists at the whole of surface of the crystal. The fracturing process results in locally ordered surfaces [122], while the *in-situ* preparation results in an ordered surface. The intense UV light irradiation at low temperature (spot size $\approx 100 \times 100$µm) create a local, high concentration of oxygen vacancies (roughly $\geq 5\%$) in the surface region of SrTiO$_3$ whose electrons (partly) dope the 2DES. This localization of the 2DES is overcome at the Al/SrTiO$_3$ interface as shown by the momentum distribution curves at E_F at five different sample positions in figure 4.5. The similarity of the curves demonstrates the homogeneity of the 2DES at the Al/SrTiO$_3$(001) over distances of several millimeters.

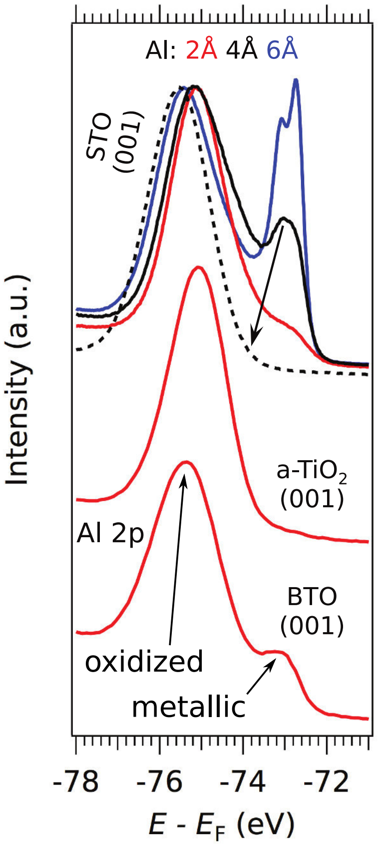

Figure 4.6: (a) Angle-integrated spectra of the Al-2p peak of the Al/SrTiO$_3$(001), Al/TiO$_2$ anatase and Al/BaTiO$_3$(001) interfaces measured at a photon energy of $h\nu = 100$ eV. The curves in different colors correspond to different thicknesses of Al (red 2Å, black 4Å, blue 6Å) and the dashed curve to the 4Å Al sample after an annealing at $T = 250$°C. The peak shape of the Al-2p peak indicates whether the Al layer is oxidized due to a redox reaction or metallic. The Al film of thickness of 2Å is almost completely oxidized, whereas the metallic contribution increases for thicknesses ≥4Å. The redox reaction occurs at all three oxide interfaces. Published in reference [19].

Thin film growth and redox reaction

To create a high concentration of oxygen vacancies localized in the surface region of TMOs due to a redox reaction, amorphous Al-films with thicknesses between $d = 2 - 10$ Å were grown on the prepared surface of the crystals (see section 2.4). Aluminum was evaporated from a Knudsen cell using an alumina crucible. The growth rate was of approximately 0.3 Å/min, corresponding to a temperature of about T=925°C of the crucible. The Al-flux was calibrated prior to the evaporation using a quartz microbalance. The cleanliness of the deposit was checked by evaporating a thin Al-film on a Cu substrate where no oxidation could be detected by Auger spectroscopy. The temperature of the crystals ranged between $T = 25 - 100$ °C during the Al deposition.

To understand the redox reaction at the Al/SrTiO$_3$ interface, the review by Fu and Wagner gives an extensive overview of the interactions between metals and oxide surfaces [123]. Insights in the redox reaction can be gained by probing the oxidation state of Al by measuring the Al-2p core levels, whose binding energies are very different for metallic and oxidized Al. As shown in figure 4.6(a) on page 77, the two contributions can be easily distinguished in the Al(6Å)/SrTiO$_3$ spectrum (blue curve), with the metallic component around 72.5 eV binding energy and the oxidized part around 75 eV binding energy. In contrast, the metallic Al component decreases for a thinner 4Å film (black curve), and the deposition of only 2Å of pure Al results in a nearly fully oxidized film of Al (red curves). In other words, *an ultra-thin layer of 2Å of pure Al is sufficient to pump the oxygen from the surface region of SrTiO$_3$.*

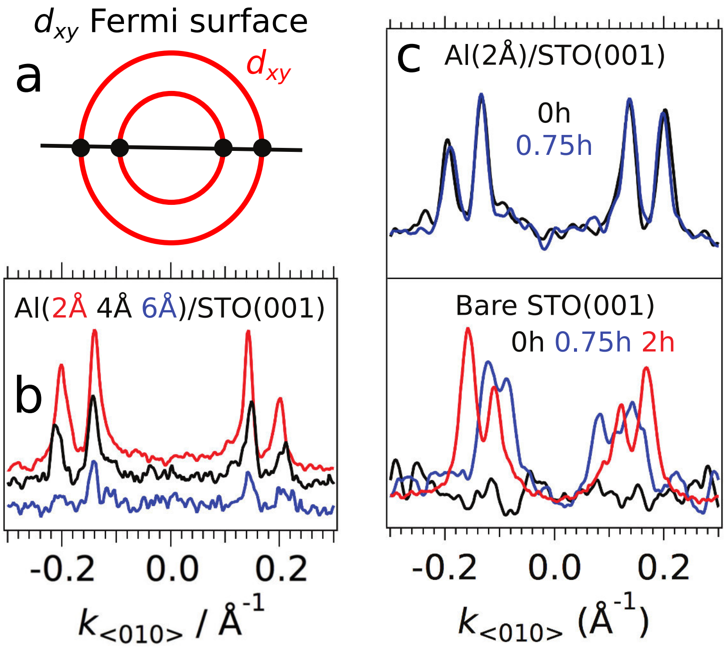

Figure 4.7: (a) Schematic of circular Fermi surfaces composed of the two $d_x y$ subbands measured at the Al/SrTiO$_3$(001) interface. The black line indicates the positions of the momentum distribution curves (MDCs) in (b-c). (b) Momentum distribution curves (MDCs) at E_F, measured at the Al/SrTiO$_3$(001) interface at $hv = 47$ eV for different Al thicknesses. Peaks in the MDCs correspond to the Fermi momenta, where the MDC cuts the Fermi surface. The curves in different colors correspond to different thicknesses of Al (red 2Å, black 4Å, blue 6Å). Fermi momenta are very similar for the different thicknesses indicating similar charge carrier densities. The decrease in intensity of the MDCs for increasing Al thickness is merely due to increasing damping of the photoemission signal. (c) MDCs integrated over $E_F \pm 5$ meV for increasing UV exposure times on the Al/SrTiO$_3$(001) interface and the bare SrTiO$_3$ surface measured under identical conditions. The similarity of the two MCDs at the interface is in strong contrast to the evolution under light irradiation of the MDCs at the bare surface. Published in reference [19].

This is also verified in all the other surfaces we studied, such as anatase-TiO$_2$(001), and BaTiO$_3$(001), as shown by the other red curves in figure 4.6(a). The remaining metallic Al in the thin film can be oxidized by a post-growth annealing at rather low temperatures of $T \approx 250°$ C, as the mobility of oxygen vacancies is increased –compare continuous and dashed black curves in figure 4.6(a). Note that the oxidation of the metallic Al results in an increased layer thickness: as the mass density of Al is 2.7 g/cm^3 and the one of amorphous Al$_2$O$_3$ is about 4 g/cm^3, the deposition of 2Å of Al yields an oxidized Al film of 2.5Å.

Thickness of Al film (0 to 6Å) and electronic structure of 2DES

To determine if the thickness of the Al-layer has an influence on the electron density of the 2DES, we turn to the momentum distribution curves (MDCs) at the Fermi level as shown in figure 4.7(b). The red MDC corresponds to a cut at E_F in the energy-momentum map of figure 4.4(a) on page 75, and hence shows four peaks at the Fermi momenta (k_F) of the two light bands. As can be seen in figure 4.7(b), the Fermi momenta are essentially the same, within 0.01 Å^{-1} for the 2Å (red MDC), 4Å (black) and 6Å (blue) thick Al films. As the 2D density of electrons is given by the area enclosed by the Fermi surfaces of the different 2DES subbands, which depend solely on the Fermi momenta, it is clear that this electron density already saturates at an Al film thickness of 2Å.

Previous studies on the bare surface of $SrTiO_3$ prepared *in-situ* showed that synchrotron UV-irradiation was necessary to create a 2DES [2, 7, 11, 15]. The irradiation process creates oxygen vacancies in the structure, releasing electrons that form the confined metallic states. Under the conditions of UV flux normally encountered in photoemission beamlines at 3^{rd} generation Synchrotrons such as SOLEIL, it usually takes about 30 min to obtain a 2DES with well-defined subbands. For instance, the lower panel of figure 4.7(c) shows the evolution with time of the MDC at E_F upon UV-irradiation on a bare $SrTiO_3(001)$ surface. The black MDC was measured at a freshly exposed spot ($t = 0$h) on the sample surface, the blue curve was recorded after 0.75 hours of beam exposure, and the red MDC after saturation of the light-induced effects, after approximately 2 hours. Thus, while the 2DES is absent at $t = 0$h, its carrier density increases up to saturation upon UV irradiation, as denoted by the increase of k_F for increasing exposure times.

Contrary to the bare surface, there is *no measurable influence* of the UV irradiation on the electronic structure of the Al/$SrTiO_3$ system, neither on the charge carrier density nor on the line-shapes or spectral weight of the 2DES, as demonstrated in the top panel of figure 4.7(c): the MDCs at E_F show a stable subband structure and a maximum electron density from the very beginning of the measurements. This indicates that the oxygen vacancy concentration and distribution, due the redox reaction at the interface between Al and $SrTiO_3$, is already saturated and stable upon irradiation.

2DES at room temperature and beyond

As demonstrated in figure 3.3 on page 53, the 2DES at the surface is not stable at room temperature as the oxygen vacancies created by intense synchrotron irradiation are filled up within approximately 2 h. However, at the Al(2Å)/$SrTiO_3$, the 2DES can be measured up to room temperature as shown in figure 4.8 on page 80. Hence, the oxygen vacancy distribution and concentration is stable at the interface. Figure 4.8(a) shows the energy-momentum maps at the Al/$SrTiO_3$ interface measured respectively at 21 K, 172 K, and 303 K, under the same conditions as the $E - k$ map in figure 4.4(a) on page 75. The dispersions of the two light bands of d_{xy}-character are still clearly visible at $T = 172$ K although the line widths are increased due to thermal broadening. At $T = 300$ K, the line widths are too large to identify the individual bands, although the left branch of the outer band is still visible close to the Fermi level E_F. Nevertheless, the spectral weight at the Fermi level demonstrates the existence and stability of the 2DES at room temperature. To compare the energy-momentum maps more directly, figure 4.8 shows the energy distribution curves at $k_{<010>} = 0$ and the momentum distribution curves at Fermi level E_F. As can be seen from the value of the Fermi momenta k_F of the peaks in the

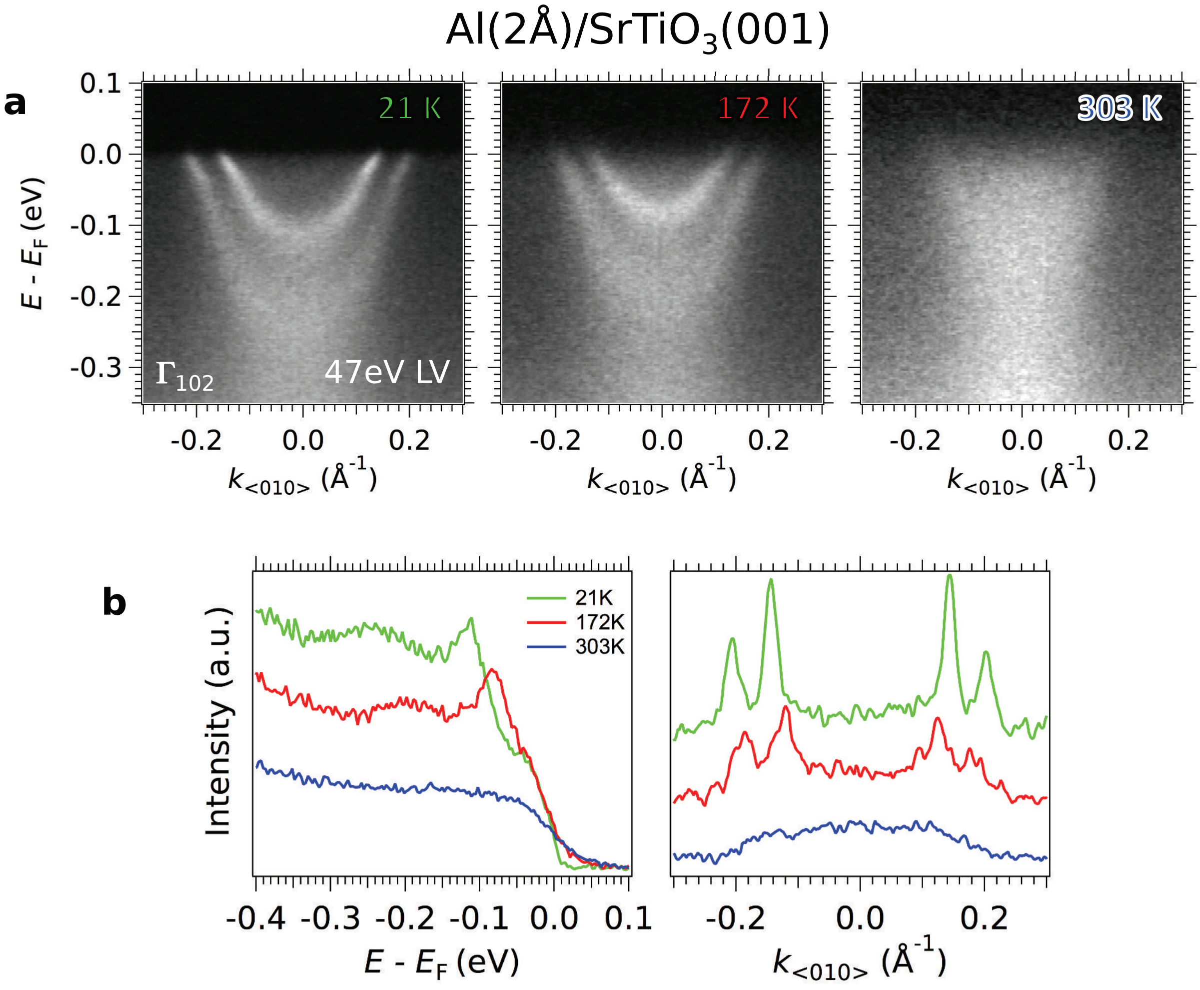

Figure 4.8: (a) Energy-momentum map measured at the Al(2 Å)/SrTiO$_3$(001) interface at different temperatures T =21 K, 172 K and 303 K. Data were collected close to the Γ_{102} point using LV photons at $h\nu = 47$ eV. (b) Energy and momentum distribution curves along $k_{<010>} = 0$ and the Fermi level of the $E - k$ maps in (a). Published in reference [19].

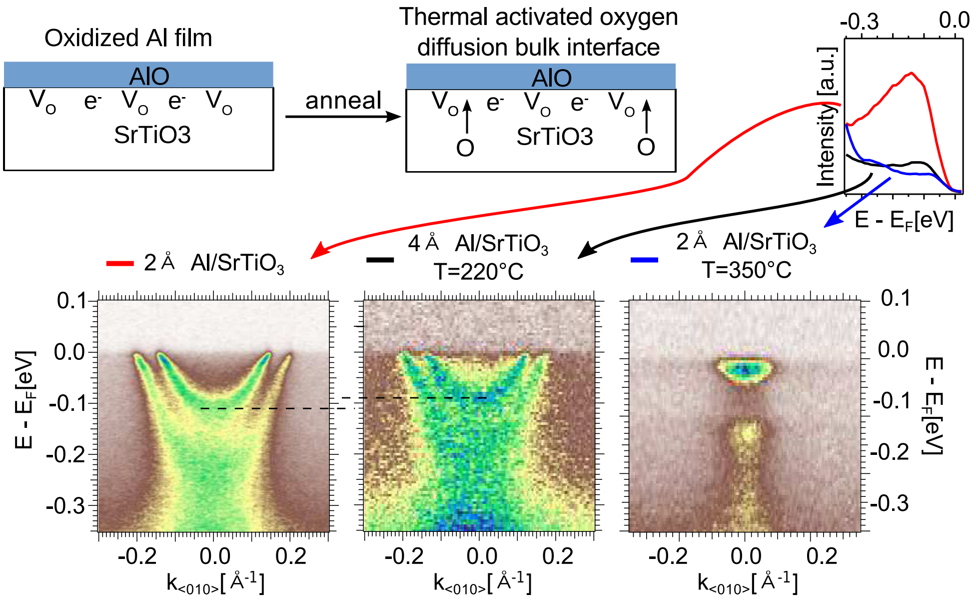

Figure 4.9: (a) Schematic of the oxygen diffusion from the bulk to the interface due to annealing the sample after the Al deposition. (b) In-gap state intensity corresponding to the oxygen vacancy concentration at the interface before annealing (red curve) and after annealing at $T = 220°C$ (black) or $T = 350°C$ (blue) for approximately 10 min. The oxygen vacancy concentration is strongly reduced after the annealing. (c) Energy momentum maps after the different annealing conditions. While the band dispersion is relatively unchanged after the $T = 220°C$ annealing, the charge carrier density is much lower after the $T = 350°C$ annealing. The ARPES measurements were conducted at $T = 7$ K.

MDCs as well as the binding energies of the peaks in the energy distribution curves (EDCs), the charge carrier density decreases slightly when temperature increases.

By increasing the temperature even further, the mobility of oxygen in the lattice of $SrTiO_3$ is increased and oxygen ions are transferred from the bulk to the interface as shown schematically in figure 4.9(a) on page 81. Thus, the concentration of oxygen vacancies at the interface can be controlled by annealing $SrTiO_3$ after the Al deposition. Depending on the annealing parameters the oxygen vacancies are refilled partially as can be seen at the intensity of the in gap state in figure 4.9(b). The higher the annealing temperature, the lower is the intensity of the in gap state corresponding to a lower concentration of oxygen vacancies. As the electron density of the 2DES depends on the concentration of oxygen vacancies, the electron density decreases as well. This is demonstrated in the energy momentum maps in figure 4.9(c-e). The Fermi momenta as well as the binding energy of the bottom of the dispersing bands are decreasing. Note that in a related system - the interface of amorphous $LaAlO_3$ and $SrTiO_3$ (001) - the sheet conductance drops to zero or respectively, the 2DES disappears at temperature $T = 300°C$ when annealed in ambient conditions. [187]

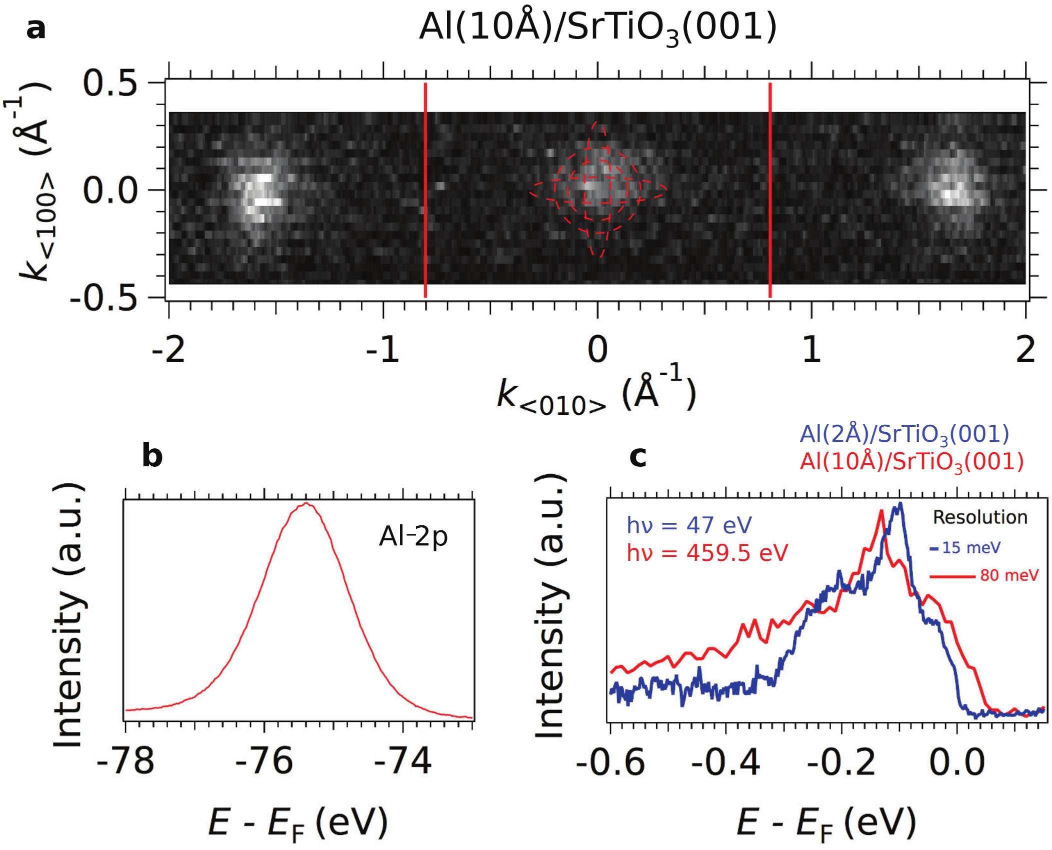

Figure 4.10: (a) Fermi surface map measured in three neighboring Brillouin zones at $h\nu$ = 459.5 eV on the Al(10Å)/SrTiO$_3$(001) interface prepared *in-situ* and subsequently exposed to air for t = 20 min. The red dashed circles and ellipses illustrate the Fermi surface shown in figures 4.4(c, d) on page 75. The thick red lines correspond to the borders of the bulk Brillouin zones. (b) Angle-integrated spectrum of the Al-2p peak of the Al(10Å)/SrTiO$_3$(001) interface measured at $h\nu$ = 458.4 eV. Due to the exposure to air, the Al film is completely oxidized –compare to figure 4.6 on page 77. (c) Energy distribution curves integrated around Γ measured at the Al(10Å)/SrTiO$_3$(001) and Al(2Å)/SrTiO$_3$(001) interfaces. To facilitate the comparison, a momentum-independent background, due to spectral weight from the in-gap state, was removed from the EDC of the Al(2Å)/SrTiO$_3$(001) data. Published in reference [19].

Stability of oxygen-deficient interface to air exposure

In principle, the thicker the oxidized Al film the better the passivation of the surface against re-oxidation in ambient air pressure. For amorphous Al_2O_3 films grown by atomic layer deposition on the surface of $SrTiO_3(001)$, a film thickness of ≥ 1.2 nm is sufficient to create a stable 2DES at the $Al_2O_3/SrTiO_3$ interface [97]. Note that this value is identical to the thickness of the natural oxidized layer at the surface of aluminum (1.24 nm) [188]. Hence, this thickness is sufficient to prevent oxygen diffusion through a homogenous Al_2O_3 capping layer.
In our case, the probing depth of the high-resolution ARPES measurements, such as the ones shown in figures 4.3 and 4.4, is limited by the mean free path of electrons which is ~ 5 Å at kinetic energies of $E_{kin} = 20 - 100$ eV. To increase the probing depth and probe the 2DES at buried interfaces, *e.g.* $LaAlO_3/SrTiO_3$, soft x-ray angle-resolved resonant photoelectron spectroscopy was applied previously [180]. Thus, to test the stability of the 2DES, we exposed an Al(10 Å)/$SrTiO_3$ sample to ambient conditions for about 30 minutes, and conducted soft x-ray resonant ARPES (hv=459.5 eV) at low temperatures. The photon energy of hv=459.5 eV corresponds to the resonance excitation of Ti $2p \rightarrow 3d$ and thus, the intensity of the 2DES is increased compared to photon energies off-resonance. Note that 1 nm of Al corresponds to about 1.25 nm of Al_2O_3 which is close to the "critical" passivation thickness mentioned above.

As can be seen from the Fermi surface in figure 4.10(a) on page 82, the 2DES at the Al(10 Å)/$SrTiO_3$ interface still exists after the exposure to air. For comparison, the red dashed circles and ellipses represent the Fermi surfaces measured at the ultra-thin Al(2 Å)/$SrTiO_3$ interface –see figures 4.4(c, d) on page 75. Note that the 10 Å Al layer was completely oxidized after exposure to air, as demonstrated by the peak shape of the Al-2p peak in figure 4.10(b). The data quality in these soft-X-ray ARPES measurements is lower compared to UV-measurements as the surface is not pristine anymore after exposure to air, the 2DES is buried below a thick oxidized Al film, the photoemission cross section of the valence states is much smaller at higher photon energies, and the total energy resolution at $hv = 459.5$ eV is about 80 meV, compared to 15 meV at $h\nu = 47$ eV. However, it is clear that the Fermi surface, and hence the charge-carrier density, are comparable between the Al(10Å)/$SrTiO_3$ sample exposed to air and the pristine Al(2Å)/$SrTiO_3$.

Figure 4.10(c) compares the momentum-integrated band structure around Γ for the two different interfaces, confirming that their electronic structures are comparable. Thus, these results demonstrate that the oxidized Al/$SrTiO_3$ interface effectively passivates the 2DES on $SrTiO_3$.

In order to adapt the method of creation of 2DES at the Al/oxide interface to transport measurements, and to be certain that the oxidized Al layer completely blocks oxygen diffusion, a capping layer thickness above the "critical" passivation value of ~ 1.2 nm is necessary. At the same time, the capping layer suitable for transport should be insulating without contributions of metallic Al. Several possibilities should be explored in future studies: optimization of growth parameters (*e.g.* applying an oxygen partial pressure [188] during deposition after the first 2 Å of Al and/or a slight increase of the temperature to oxidize Al thicknesses greater than 2 Å) or deposition of another type of insulating capping layer after the deposition of 2 Å of Al.

Conclusions

In conclusion, the method we present here for realizing 2DESs in oxides has the advantages of simplicity and versatility –for instance, it can be readily implemented in many UHV setups, allowing future investigations of 2DESs in complex oxides using non-synchrotron based spectroscopic techniques, like tunneling or Raman spectroscopies. This method is also pertinent for the study of transport phenomena in mesoscopic oxide devices. Indeed, $SrTiO_3$ has emerged as an exciting nano-electronics device platform [189], owing to the existence of superconductivity, spin-orbit interaction and magnetism which are controllable with a gate voltage. Our work opens up new possibilities to explore these questions by making a class range of transition-metal oxide 2DESs suitable for transport. Furthermore, the stability of the 2DES in ambient conditions can be achieved through a sufficiently thick layer of oxidized Al. This opens the possibility to integrate TMO 2DESs into functional devices without the need of evolved deposition techniques.

4.3 2DES at the Al(2Å)/ZnO interface: no Ti-based oxide and a d^{10} system

The previous section demonstrated that 2DESs can be created at the interface of Al and $SrTiO_3$ or TiO_2 anatase due to a redox reaction. In both systems, the 2DES can also be created by the desorption of oxygen due to the intense UV synchrotron irradiation. However, the mechanism of the oxygen desorption is material dependent. Tanaka *et al.* demonstrated that the photoexcitation of the core level of the transition metal (*e.g.* Ti or Zn) results in the desorption of oxygen in the case of TiO_2 rutile but not in ZnO. [120] Thus, the conductivity of the ZnO surfaces is usually related to the chemisorption of gases and not to oxygen-deficiency. The metallization of the surface by absorption of hydrogen, methanol and water was demonstrated using ARPES by Ozawa *et al.* [190, 191] and Piper *et al.* [192]. As in many other transition metal oxides, the oxygen vacancy is another possibility to dope ZnO with electrons, although there are theoretical studies demonstrating the deep donor character of the vacancy in bulk ZnO [193]. Note that the creation of a high concentration of oxygen vacancies can result in the formation of Zn interstitials. [194]

Here we show, using ARPES that the redox reaction at the Al/ZnO interface results in the creation of a 2DES due to the presence of oxygen vacancies. Contrary to the aforementioned ARPES studies on ZnO, we observe two subbands (and not just one) of the 4s conduction band due to a larger band bending/ electron doping.

Missing in-gap state

In contrast to the other oxygen-deficient surfaces of transition metal oxides, there is no in-gap state corresponding to localized electrons (see section 3.3). As shown in figure 4.11, the spectral weight in the band gap at the surface of almost stoichiometric ZnO (red curve) is comparable to

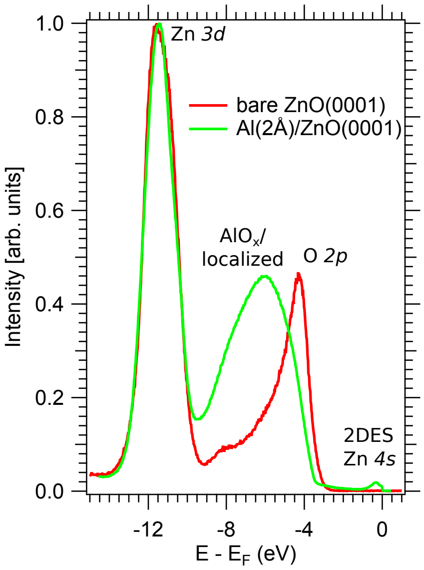

Figure 4.11: Angle-integrated photoemission spectra of the almost stoichiometric surface of ZnO(000$\bar{1}$) (red curve) and of the oxygen-deficient Al(2Å)/ZnO interface (green curve) measured at hν=88 eV. The intensity of the spectra is normalized to the Zn 3d states and the binding energy corresponding to the stoichiometric surface is set to the binding energy of the Zn 3d states of the metallic interface. Contrary to other oxygen-deficient interfaces, there is no peak in the band gap of ZnO. However, the binding energy and shape of the O2p peak are changed.

the one at the oxygen-deficient Al(2Å)/ZnO interface (green curve). However, there is a strong change in binding energy and peak shape of the O 2p valence band. One possible reason is that the O 2p valence band of the oxidized Al layer is at a binding energy of approximately 6 eV or that localized states close to the oxygen vacancy occur in this energy range (-9 to -4 eV).
The origin of the in-gap state in doped d^0 oxides is ascribed, from theoretical works, to localized electrons of e_g symmetry due to oxygen vacancies. [157] As ZnO is a doped d^{10} system, the d states are already filled and the electronic reconstruction due to two excess electrons per oxygen vacancy might be altered. Although DFT calculations predict states in the band-gap [193, 195], only small spectral weight can be experimentally measured (see figure 4.11). This demonstrates once more that the behavior of excess electrons at the oxygen-deficient surface/interface of oxides is not easy to predict (see discussion in section 3.3).

Characterization of the 2DES

We now characterize the 2DES measured at the interface of Al(2Å)/ZnO(000$\bar{1}$) using ARPES after preparing the surface similar to the procedure described in [144] and depositing Al (see section 4.2). The Fermi surface in the (000$\bar{1}$) plane is shown in figure 4.12(a) on page 86 and was measured at a photon energy of $h\nu$=88 eV using linear horizontal light polarization. In contrast to the materials discussed so far, the conduction band of ZnO consists of s orbitals and not the d orbitals manifold. Hence, the two circular Fermi surface sheets around $k_{\langle 1120\rangle} = k_{\langle 1010\rangle} = 0$ in figure 4.12 correspond to s orbitals. Similar to the other 2DESs, the existence of two bands of identical orbital character imply a subband structure due to confinement of the electrons in a quantum well. The in-plane periodicity of the electronic structure corresponds to the one of an unreconstructed surface as displayed in figure 4.12.
Figure 4.12(c) presents the energy-momentum maps close to the bulk Γ_{002} point measured at a photon energy of $h\nu$ = 25 eV along the cut parallel to the $\langle 1120\rangle$ direction. Two dispersive light bands are visible. Their band bottoms are located at a binding energy of approximately

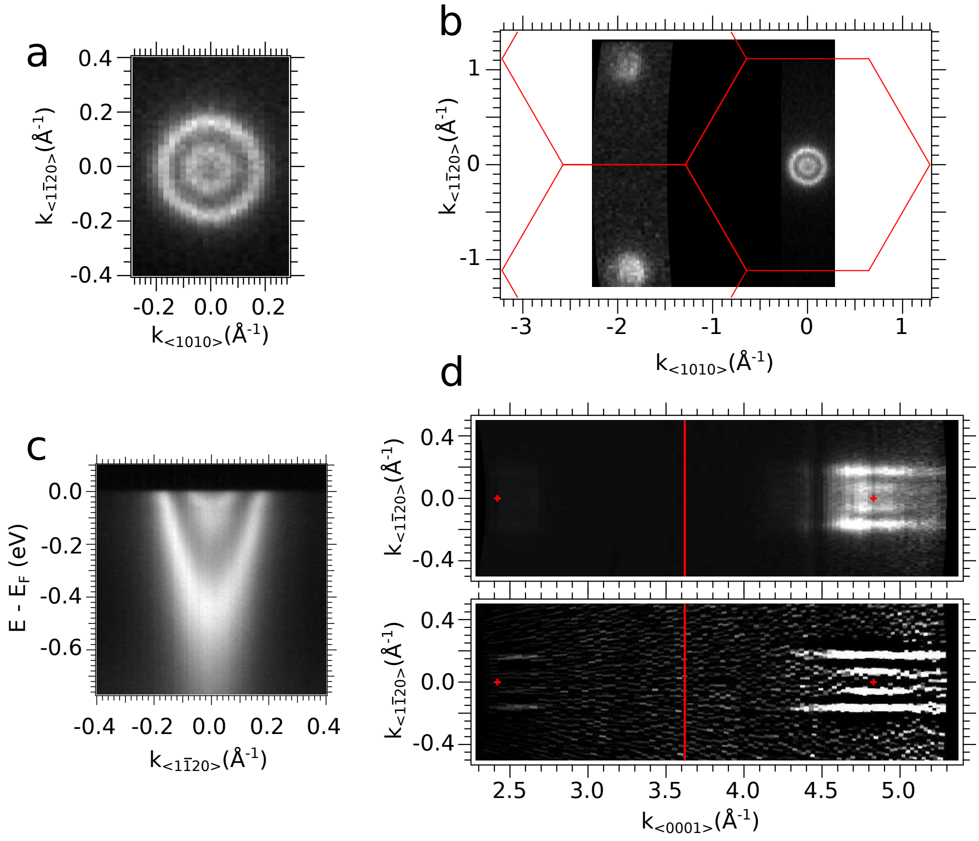

Figure 4.12: ARPES measurements of the 2DES at the Al(2A)/ZnO(000$\bar{1}$) interface. (a) Fermi surface measured at $h\nu = 88$ eV using linear horizontal polarization (LH) showing two circular Fermi surface sheets. (b) Same parameters as in (a) but over much larger momentum space. The red lines correspond to the border of the hexagonal Brillouin zone. (c) Energy momentum map measured at $h\nu = 25$ eV showing two parabolic dispersions. The smearing out and hump of the measured intensity at the bottom of the upper parabola indicates electron phonon coupling, as discussed in chapter 8. (d) Fermi surface maps and 2nd derivative in the $k_{\langle 0001\rangle} - k_{\langle 1\bar{1}20\rangle}$ plane measured by changing the photon energy between $h\nu = 20$ eV and $h\nu = 105$ eV in steps of 1 eV. An inner potential of $V_0 = 5$ eV was assumed to calculate the $k_{\langle 0001\rangle}$ values. The bands do not disperse along the $k_{\langle 0001\rangle}$ direction. There is no spectral weight at the Fermi level between $k_{\langle 0001\rangle} \approx 2.7Å^{-1}$ and $k_{\langle 0001\rangle} \approx 4.3Å^{-1}$. The red lines correspond to the border of the Brillouin zone and the red markers to bulk Γ points. All measurements were conducted at $T = 7$ K.

440 meV and 70 meV. The splitting of the subbands of 390 meV is larger by a factor three to four compared to the ones of the 2DESs at the (001) surface of the titanates which is of the order of 100 meV.

A parabolic fit of the outer band yields an effective mass of approximately $0.26m_e$ (see section 8.2 for a more rigorous analysis of the effective masses of the two subbands). The corresponding Fermi momenta are 0.17 Å^{-1} and 0.07 Å^{-1}.

The measurement of the photon energy dependence between $h\nu = 20$ eV and $h\nu = 105$ eV yields the Fermi surface perpendicular to the $(000\bar{1})$ surface which is shown in figure 4.12(d) as well as the Fermi surface based on 2nd derivatives. The bands shown in the Fermi surface map are non-dispersing in the $\langle 0001 \rangle$ direction. Although no intensity can be measured for momenta between $k_{\langle 0001 \rangle} \approx 2.7$ Å^{-1} and $k_{\langle 0001 \rangle} \approx 4.3$ Å^{-1}, the non-dispersing Fermi surface over half a Brillouin zone along (0001) is in contrast to the the rather isotropic Fermi surface in the bulk ($m^*_{0001}(\text{ZnO}) = 0.24$ and $m^*_{1120}(\text{ZnO}) = 0.28$ [196]). This demonstrates the 2D character to the electronic states (see also discussion in section 5.2). Note that the intensity around $k_{\langle 0001 \rangle} = 2.9$ is rather low because of a background resulting from second-order diffracted photons. The normalization procedure results in a lower intensity due to this increased background.

Additionally, it is somewhat ambiguous to determine $V_0 \approx 5$ eV based on our data. In principle, the symmetric Fermi surfaces around $k_{\langle 0001 \rangle,1} \approx 2.5$ Å^{-1} and $k_{\langle 0001 \rangle,2} \approx 4.8$ Å^{-1} should correspond to Γ points in reciprocal space as the conduction band minimum filled up by the 2DES is at Γ in ZnO. The inner potential $V_0 \approx 5$ eV was chosen so that these values correspond to a multiple of the absolute value of the reciprocal lattice vector along the $\langle 0001 \rangle$ direction: $\frac{4\pi}{c} = 2.4$ Å^{-1}. However, the corresponding photon energies $h\nu_1 \approx 22$ eV and $h\nu_2 \approx 88$ eV are close to resonance excitations (Zn $3p \rightarrow$ Zn $4s$ and O $2p \rightarrow$ Zn $4s$) which might influence the intensity distribution in the Fermi surface. The photon energies corresponding to Γ found by Piper *et al.* are $h\nu_{1,lit} \approx 32$ eV and $h\nu_{2,lit} \approx 88$ eV. Thus, while there is agreement in $h\nu_2$, there is a 10 eV discrepancy in $h\nu_1$.

The measured Fermi momenta correspond to an electron concentration of $n_{2D}^{(000\bar{1})} = A_F/2\pi^2 \approx 5.4 \times 10^{13}$ cm^{-2}, or about 0.14 electrons per hexagonal unit cell in the (0001) plane.

The ARPES results on the ZnO surface demonstrate once more that the creation of 2DESs can be generalized to many different oxides (not only Ti-based oxides like the ones presented in the previous chapters and also to d^{10} systems). This rises naturally the question if interfaces other than the $\text{LaAlO}_3/\text{SrTiO}_3$ interface show a similar range of unusual properties or if SrTiO_3 related interfaces are unique in their properties. However, as the t_{2g} manifold composes the 2DES in SrTiO_3 and other titanates, the properties of the 2DES in ZnO consisting of s orbitals might be simpler.

4.4 Another doping method: low electron doping with K or Cs

As discussed in section 4.1, in addition to the redox reaction presented in the previous sections, electron doping can in principle also be achieved by depositing alkali metals. This increase in electron density was already observed by ARPES on certain oxide surfaces due to the deposi-

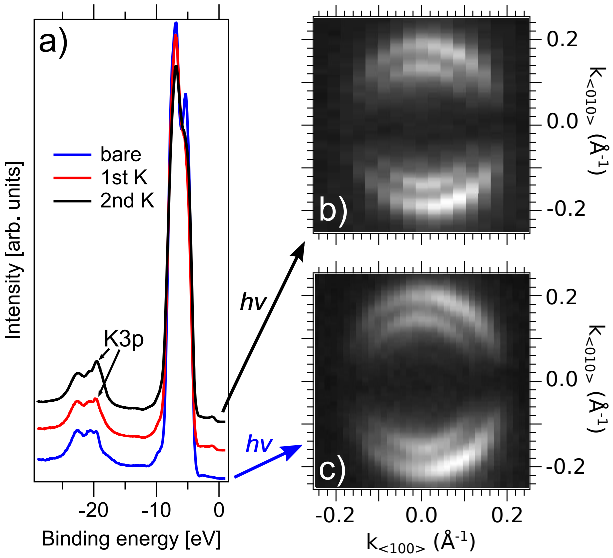

Figure 4.13: (a) Angle-integrated photoemission spectra measured at $h\nu$=100 eV before and after the deposition of K. An increase of the intensity of the K 3p and in-gap state is visible. (b,c) Fermi surface measured at $h\nu$=47 eV before and after the deposition of K. The size of the Fermi surface is equal in both cases.

tion of potassium. [197, 198]. We deposited alkali metals with low work functions: 2.3 eV for potassium (K) and 1.9 eV for cesium (Cs).

Deposition of K

We deposited K at room temperature on the *in situ* prepared surface of $SrTiO_3$. Electron transfer was observed due to K deposition at the TiO_2-rutile(110) surface for coverages smaller than one monolayer as evidenced by the in-gap state using photoemission spectroscopy. [199, 200] The intensity of the in gap state can be reduced by exposing the K/TiO_2 interface to oxygen [199] indicating that a redox reaction between alkali metal and oxide surface occurs. Different growth modes of potassium were observed on oxide surfaces. [201–203] Hayden and Nicholsan observed the growth of weakly bound metallic K mutilayers at a growth temperature of T=140 K on TiO_2(110) rutile. [201] In contrast, Lad and Dake observed the growth of stable oxidized K multilayers for growth of room temperature, also on the rutile surface. The growth of potassium on the $SrTiO_3$ surface occurs in 2D island growth mode. [203]

We measured photoemission spectra after the growth of varying amounts of K on the (001) and (111) surfaces of $SrTiO_3$. K was deposited from an alkali metal dispenser and the deposition rate controlled by adjusting the current through the dispenser. After the deposition of K on the (001), the intensity of the in gap state increases as shown in figure 4.13 on page 88 indicating electron transfer. However, the dominating effect for electron doping is the intense synchrotron irradiation - similar to the bare surface. Hence, the saturated electron density after irradiation is identical to ones observed at the bare surface as shown by the Fermi surfaces in figure 4.13. This is different in the case of Cs deposition as discussed below. One possible explanation is that 2D island growth [203] results in patches of a bare $SrTiO_3$ surface. Alternatively, too little potassium was deposited to cover the whole surface. Note that we deposited a larger amount of K on the (111) surface, but the saturation value after irradiation is still identical than the one at the bare surface.

Deposition of Cs

We deposited Cs at room temperature using an alkali metal dispenser. Auger spectroscopy was used to quantify the amount of Cs deposited on the surface. As can be seen in the Auger spectrum in figure 4.14(a) on page 90 the height of the Cs peak is identical for various different deposition parameters (duration of deposition and current to heat the Cs source) demonstrating a saturation of the amount of Cs at the surface. An annealing at T=400°C partly removes the Cs deposit. This observations are in agreement with the results of Grant and Campell [204] on the Cs/TiO_2(110) rutile interface. They found that the deposition of Cs at room temperature leads to the desorption of Cs for coverages higher than one monolayer and that annealing does not remove all of the Cs deposit.

To probe changes in the electronic structure induced by the deposition of one monolayer of Cs, we conducted photoemission experiments at low temperature $T = 8$ K. Figure 4.14(b) shows the angle-integrated photoemission spectrum in valence band and gap region of $SrTiO_3$ measured immediately after the first light exposure of the probed surface. A rather small in gap state is present which indicates charge transfer from the Cs layer to the surface region of $SrTiO_3$. A charge transfer was also observed at the Cs/TiO_2 interface at which most of the transferred electrons are localized near the topmost atomic layers, with Ti^{4+} being reduced to Ti^{3+}.

In $SrTiO_3$, the amount of transferred electrons is rather small as can be inferred from the energy momentum map close to the Fermi level as shown figure 4.14(c) and measured immediately after the first exposure of the sample to the synchrotron beam. From the Fermi momenta, we can estimate that the electron density is only 5% of the one observed after irradiating the bare surface $n_{Cs} < n_{hv}$. As described in section 3.1, the synchrotron irradiation creates oxygen vacancies at the surface. The same effect occurs also at the Cs/$SrTiO_3$ interface. After irradiating the interface for one to two hours, the electron density is much higher as displayed in figure 4.14. Interestingly, the electron density of the irradiated Cs interface is lower than the one of the irradiated bare surface $n_{Cs,hv} < n_{hv}$. Thus, the monolayer of Cs seems to change the desorption mechanism at the $SrTiO_3$ interface. The electron density can be further increased by depositing Al on top of the Cs/$SrTiO_3$ system as shown in figure 4.14(e). The Al acts as oxygen sink and pumps out more oxygen than the synchrotron beam. The higher concentration of oxygen vacancies is also evidenced by the increased intensity of the in gap state in the angle-integrated photoemission spectrum in figure 4.14(b).

To sum up, the charge transfer from Cs to the $SrTiO_3$ interface is rather small. It is unclear if the charge transfer is due to the direct transfer from metal to oxide or due to a redox reaction between oxide and metal.

Note that Akikubo *et al.* studied the Cs/$SrTiO_3$ interface by photoemission as well and observed different electronic states. [205] Firstly, they did not observe a saturation value for the Cs coverage. Secondly, they assigned the spectral weight at the Fermi level to an e_g state based on symmetry arguments deduced by the dependence of the states to the light polarization and based on a theoretical study [206]. Possible explanations for the difference are different sample preparations and bulk dopings as well as the fact that the photon dose in their study is much

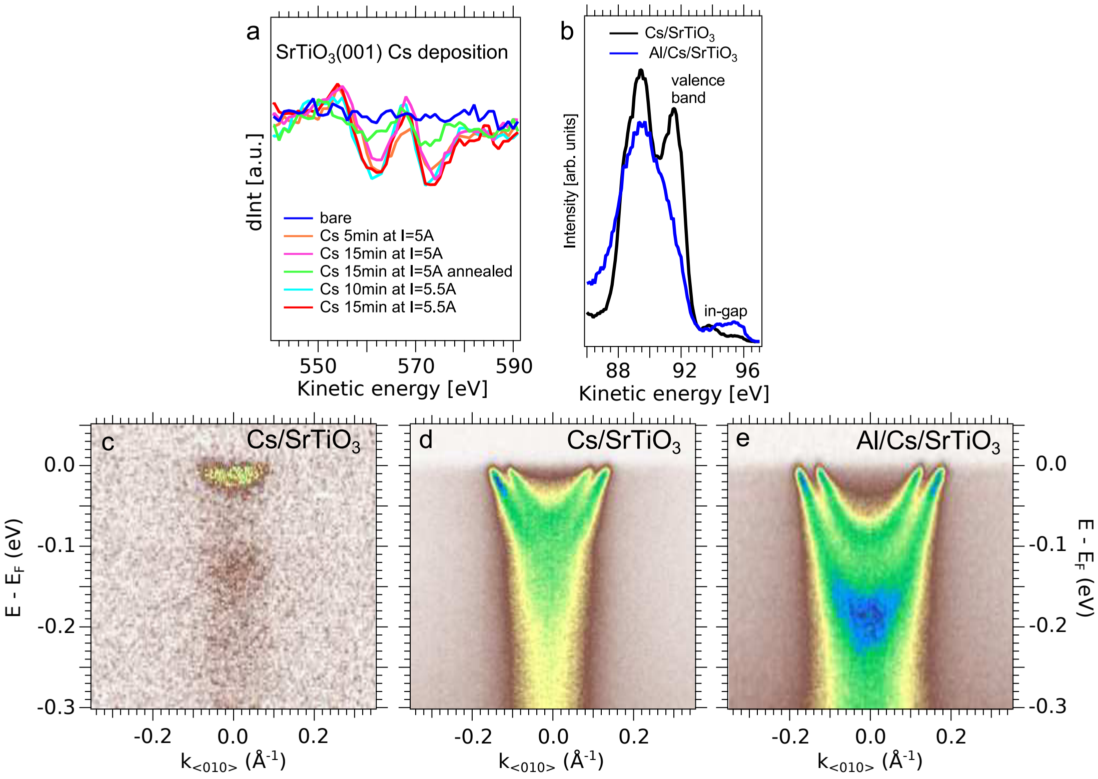

Figure 4.14: (a) Cs-Auger spectra of SrTiO$_3$ before and after deposition of Cs with various different parameters (duration of deposition and current to the Cs source). The energy of the incidents electrons was 2 kV. Independent of the deposition parameters the Cs peak height is identical indicating that maximal one monolayer of Cs can be deposited. (b) Angle-integrated photoemission spectra of valence band and band gap region of the Cs/SrTiO$_3$ as well as the Al/Cs/SrTiO$_3$ interface. The different intensities of the in-gap state indicate different concentration of oxygen vacancies in SrTiO$_3$ close to the interface. (c) - (e) Energy-momentum map close to the Fermi level measured at $h\nu = 47$ eV (Γ_{102}) at the SrTiO$_3$ based interfaces. (c) The lowest electron density is at the Cs/SrTiO$_3$ interface right after the fist exposure of the sample to the synchrotron irradiation. (d) After one to two hours of irradiation, the electron density reaches a saturation value. (e) The deposition of Al acting as oxygen sink further increases the electron density.

smaller and thus, the light does not create or creates only a small amount of oxygen vacancies.

Conclusions

More measurements are necessary to understand the growth mode of the alkali metal and the metal/$SrTiO_3$ interface. Nevertheless, it is clear that the naive idea of an efficient doping of oxide surfaces due to the deposition of an alkali metal and based on work function differences fails. Ideally, the deposition should be conducted at low temperatures while the sample is on the ARPES manipulator as for low temperature homogeneous coverages larger than one monolayer are much more likely. However, the first experiments presented here indicate that the charge transfer form the alkali metal to the oxide is much smaller compared to the doping due oxygen vacancies (either created by the synchrotron irradiation or by a redox reaction with Al).

Chapter 5

Orientational tuning of the 2DESs at the low index surfaces of $SrTiO_3$

The surging interest in the physical properties of the 2DES at the interface of $LaAlO_3/SrTiO_3(001)$ was discussed briefly in section 1.1. Recently, 2DESs at the (111) and (110) interfaces of $LaAlO_3/SrTiO_3$ were also reported [207]. The latter showed a highly anisotropic conductivity [208] and an anisotropic superconducting state spatially more extended than the one at the (001) interface [209]. Interestingly, theoretical works have also predicted that exotic, possibly topological, electronic states might occur at interfaces composed of (111) bilayers of cubic TMOs [210–213], as two (111) planes of transition-metal ions form a honeycomb lattice, similar to the one found in graphene.

In this chapter, we show that new types of 2DESs can be directly tailored at the bare (110) and (111) surfaces of $SrTiO_3$. Imaging their electronic structure *via* angle-resolved photoemission spectroscopy (ARPES), we find that their Fermi surfaces, subband masses, and orbital ordering are different from the ones of the 2DES at the $SrTiO_3$ (001) surface [1, 2] and the ones predicted for the bulk, being thus uniquely sensitive to the confining crystallographic direction. This occurs because the crystallographic symmetries of the surface plane, and the electron effective masses along the confinement direction, influence the symmetry of the electronic structure and the ordering of the t_{2g} orbitals. Furthermore, the observed carrier concentrations and 2DES thicknesses for different surfaces allow us to showcase the impact of oxygen vacancies and of the polar discontinuity on distinctive features of the confined conducting sheet.

Before discussing the ARPES results, I will discuss the tight-binding calculations which we used to model the electronic structure.

5.1 Tight-binding model

We use a simple tight-binding model [214] to rationalize the conduction band of a cubic perovskite which is formed by Ti-3d orbitals hybridized with O-2p orbitals. Such a tight-binding model has been applied quite successfully to model the electronic structure of *e.g.* $SrTiO_3$ [9, 10, 215, 216].

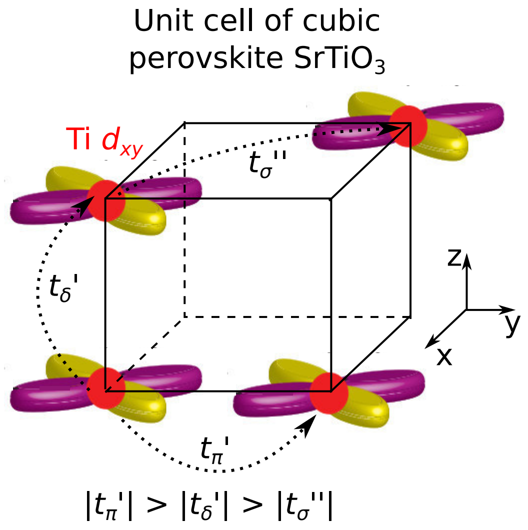

Figure 5.1: Illustration of electron hopping between d_{xy} orbitals in the cubic unit cell of SrTiO$_3$. The hopping between nearest neighbors of Ti cations is characterized by the hopping amplitudes $t_{\pi'}$ and $t_{\delta'}$ - next nearest neighbor hopping by $t_{\sigma''}$. The Greek letter in the index of the hopping amplitudes correspond to the type of chemical bonding (σ, π, δ). Adapted from reference [217].

Bulk

The interaction between the oxygen anions forming an octahedron as well as the Sr cation generates a large crystal field which splits the d states in a lower t_{2g} triplet and an higher e_g doublet. Hence, only the t_{2g} orbitals are considered in our tight-binding model.

In the bulk, the Hamiltonian H_{bulk} of the system in the basis $\{d_I\}$, where $I = (X, Y, Z)$ corresponds to the orbital character (yz, zx, xy) of the t_{2g} orbitals, is given by:

$$H_{bulk} = \begin{pmatrix} d_X^\dagger \\ d_Y^\dagger \\ d_Z^\dagger \end{pmatrix}^T \begin{pmatrix} \epsilon_X & & \\ & \epsilon_Y & \\ & & \epsilon_Z \end{pmatrix} \begin{pmatrix} d_X \\ d_Y \\ d_Z \end{pmatrix}$$

$$\begin{aligned}
\epsilon_X =& -2t_{\pi'}(\cos(a\ k_y) + \cos(a\ k_z)) - 2t_{\delta'}\cos(a\ k_x) \\
& -2t_{\sigma''}(\cos(a\ k_y + a\ k_z) + \cos(a\ k_y - a\ k_z)) \\
\epsilon_Y =& -2t_{\pi'}(\cos(a\ k_x) + \cos(a\ k_z)) - 2t_{\delta'}\cos(a\ k_y) \\
& -2t_{\sigma''}(\cos(a\ k_x + a\ k_z) + \cos(a\ k_x - a\ k_z)) \\
\epsilon_Z =& -2t_{\pi'}(\cos(a\ k_x) + \cos(a\ k_y)) - 2t_{\delta'}\cos(a\ k_z) \\
& -2t_{\sigma''}(\cos(a\ k_x + a\ k_y) + \cos(a\ k_x - a\ k_y))
\end{aligned}$$

Here, ϵ_I describes the inter-layer hopping between identical orbitals. Hoppings between orbitals of different character are negligible small in cubic SrTiO$_3$ and not considered. The hopping between nearest neighbors of Ti cations is characterized by the hopping amplitudes $t_{\pi'}$ and $t_{\delta'}$ - next nearest neighbor hopping by $t_{\sigma''}$ as illustrated in figure 5.1. The Greek letter in index of the hopping amplitudes correspond to the type of chemical bonding (σ, π, δ). As evident from figure 5.1, there is large overlap of the d_{xy} orbitals along the x and y direction but only a small overlap along the z direction. Thus, the d_{xy}-like band will be light in the $x-y$ plane and heavy along the z axis. This is expressed by the hopping amplitudes in the above equation where the cosine terms represent the periodicity of the band structure in reciprocal space.

Figure 5.2(a) on page 97 shows the bulk Fermi surface corresponding to an electron density of $n_{3D} = 1 \times 10^{21}\ e^-/\mathrm{cm}^3$ calculated using the above equations where the electron hopping amplitudes between the three t_{2g} orbitals of neighboring Ti^{4+} are $t_{\pi'} = -0.236$ eV, $t_{\delta'} = -0.035$ eV and $t_{\sigma''} = 0$ eV [215]. Note that we neglect spin-orbit coupling and tetragonal distortions at low temperatures.

Surface slab

As we study the electronic states confined at the surface, we are not so much interested in the electronic structure of the bulk but rather in the one of a few atomic layers at the surface. To model the atomic layers, one has to consider that the geometry and symmetry of the atoms in surface layer depend on the surface orientation. Figures 5.2(b,c) show that the symmetries are 4-fold for the (001) plane, 2-fold for the (110) surface, and 3-fold for the (111) surface. The tight-binding model to calculate the band structure of a few atomic layers is based on the calculations of Ref. [210] for the (111) surface and adapted to the (001) and (110) surfaces.

The Hamiltonian H of the electronic structure at the surface in the basis $\{d_{I,n}\}$, where $I = (X, Y, Z)$ corresponds again to the orbital character (yz, zx, xy) of the t_{2g} orbitals and $n = 1, 2, ..., N$ indicates the number of the layer of Ti cations, is given by:

$$H = \begin{pmatrix} d^\dagger_{X,1} \\ d^\dagger_{Y,1} \\ d^\dagger_{Z,1} \\ \vdots \\ d^\dagger_{X,N} \\ d^\dagger_{Y,N} \\ d^\dagger_{Z,N} \end{pmatrix}^T \begin{pmatrix} \epsilon_{X,0} & & & \cdots & \epsilon_{X,N-1} & & \\ & \epsilon_{Y,0} & & \cdots & & \epsilon_{Y,N-1} & \\ & & \epsilon_{Z,0} & \ddots & & & \epsilon_{Z,N-1} \\ \vdots & \vdots & \ddots & \ddots & \ddots & \vdots & \vdots \\ \epsilon^*_{X,N-1} & & & \ddots & \epsilon_{X,0} + V_N & & \\ & \epsilon^*_{Y,N-1} & & \cdots & & \epsilon_{Y,0} + V_N & \\ & & \epsilon^*_{Z,N-1} & \cdots & & & \epsilon_{Z,0} + V_N \end{pmatrix} \begin{pmatrix} d_{X,1} \\ d_{Y,1} \\ d_{Z,1} \\ \vdots \\ d_{X,N} \\ d_{Y,N} \\ d_{Z,N} \end{pmatrix}$$

Here, $\epsilon_{I,m}$ describes the hopping between the m^{th} nearest planes, *e.g.* $\epsilon_{I,0}$ describes the intra-layer hopping of electrons and $\epsilon_{I,1}$ the inter-layer hopping between neighboring planes. Note that the only difference between the layers is the potential difference V_N in the quantum well at the surface. To give an example, the Hamiltonian of a two-layer system would be:

$$H = \begin{pmatrix} d^\dagger_{X,1} \\ d^\dagger_{Y,1} \\ d^\dagger_{Z,1} \\ d^\dagger_{X,2} \\ d^\dagger_{Y,2} \\ d^\dagger_{Z,2} \end{pmatrix}^T \begin{pmatrix} \epsilon_{X,0} & & & \epsilon_{X,1} & & \\ & \epsilon_{Y,0} & & & \epsilon_{Y,1} & \\ & & \epsilon_{Z,0} & & & \epsilon_{Z,1} \\ \epsilon^*_{X,1} & & & \epsilon_{X,0} + V_2 & & \\ & \epsilon^*_{Y,1} & & & \epsilon_{Y,0} + V_2 & \\ & & \epsilon^*_{Z,1} & & & \epsilon_{Z,0} + V_2 \end{pmatrix} \begin{pmatrix} d_{X,1} \\ d_{Y,1} \\ d_{Z,1} \\ d_{X,2} \\ d_{Y,2} \\ d_{Z,2} \end{pmatrix}$$

The corresponding terms of the SrTiO$_3$ (001) surface are

$$\begin{aligned} \epsilon_{X,0} &= -2t_{\pi'} \cos(a\ k_y) - 2t_{\delta'} \cos(a\ k_x) \\ \epsilon_{Y,0} &= -2t_{\pi'} \cos(a\ k_x) - 2t_{\delta'} \cos(a\ k_y) \\ \epsilon_{Z,0} &= -2t_{\pi'} (\cos(a\ k_x) + \cos(a\ k_y)) - 2t_{\sigma''} (\cos(a\ k_x + a\ k_y) + \cos(a\ k_x - a\ k_y)) \\ \epsilon_{X,1} &= -t_{\pi'} - 2t_{\sigma''} \cos(a\ k_y) \\ \epsilon_{Y,1} &= -t_{\pi'} - 2t_{\sigma''} \cos(a\ k_x) \\ \epsilon_{Z,1} &= -t_{\delta'} \end{aligned}$$

where k_x corresponds to $k_{\langle 100 \rangle}$, k_y to $k_{\langle 010 \rangle}$ and a is the cubic lattice constant. Note that in contrast to the bulk, the periodicity of the surface slab is broken along the direction perpendicular to the surface. Thus, there are no cosine terms along k_z.

The hopping terms of the SrTiO$_3$ (110) surface are

$$\begin{aligned} \epsilon_{X,0} &= -2t_{\pi'} \cos(a\ k_y) \\ \epsilon_{Y,0} &= \tilde{\epsilon}_X \\ \epsilon_{Z,0} &= -2t_{\delta'} \cos(a\ k_y) - 2t_{\sigma''} \cos(\sqrt{2}a\ k_x) \\ \epsilon_{X,1} &= -t_{\pi'} e^{\frac{i}{\sqrt{2}}a\ k_x} - t_{\delta'} e^{-\frac{i}{\sqrt{2}}a\ k_x} - 2t_{\sigma''} e^{\frac{i}{\sqrt{2}}a\ k_x} \cos(a\ k_y) \\ \epsilon_{Y,1} &= -t_{\delta'} e^{\frac{i}{\sqrt{2}}a\ k_x} - t_{\pi'} e^{-\frac{i}{\sqrt{2}}a\ k_x} - 2t_{\sigma''} e^{-\frac{i}{\sqrt{2}}a\ k_x} \cos(a\ k_y) \\ \epsilon_{Z,1} &= -2t_{\pi'} \cos(-\frac{1}{\sqrt{2}}a\ k_x) \\ \epsilon_{Z,2} &= -2t_{\sigma''} \end{aligned}$$

where k_x is equal to $k_{\langle 1\bar{1}0\rangle}$ and k_y to $k_{\langle 001\rangle}$.
The geometry of the SrTiO$_3$ (111) surface yields

$$\begin{aligned}
\epsilon_{X,0} &= -2t_{\sigma''}\cos(-\frac{\sqrt{3}}{2}\tilde{a}\ k_x + \frac{3}{2}\tilde{a}\ k_y)\\
\epsilon_{Y,0} &= -2t_{\sigma''}\cos(\frac{\sqrt{3}}{2}\tilde{a}\ k_x + \frac{3}{2}\tilde{a}\ k_y)\\
\epsilon_{Z,0} &= -2t_{\sigma''}\cos(\sqrt{3}\tilde{a}\ k_x)\\
\epsilon_{X,1} &= -t_{\pi'}e^{-i\tilde{a}\ k_y}\left[1 + e^{i\frac{\tilde{a}}{2}(-\sqrt{3}k_x+3k_y)}\right] - t_{\delta'}e^{i\frac{\tilde{a}}{2}(\sqrt{3}k_x+k_y)}\\
\epsilon_{Y,1} &= -t_{\pi'}e^{-i\tilde{a}\ k_y}\left[1 + e^{i\frac{\tilde{a}}{2}(\sqrt{3}k_x+3k_y)}\right] - t_{\delta'}e^{i\frac{\tilde{a}}{2}(-\sqrt{3}k_x+k_y)}\\
\epsilon_{Z,1} &= -2t_{\pi'}e^{i\frac{\tilde{a}}{2}\ k_y}\cos(\frac{\sqrt{3}}{2}\tilde{a}\ k_x) - t_{\delta'}e^{-i\tilde{a}\ k_y}\\
\epsilon_{X,2} &= -t_{\sigma''}e^{-i\frac{\tilde{a}}{2}(\sqrt{3}\ k_x-k_y})\\
\epsilon_{Y,2} &= -t_{\sigma''}e^{i\frac{\tilde{a}}{2}(\sqrt{3}\ k_x-k_y})\\
\epsilon_{Z,2} &= -t_{\sigma''}e^{i\tilde{a}\ k_y}.
\end{aligned}$$

In the above expressions, k_x corresponds to $k_{\langle 1\bar{1}0\rangle}$, k_y to $k_{\langle \bar{1}\bar{1}2\rangle}$, and $\tilde{a}$ to the cubic lattice constant a projected in the (111) plane $\tilde{a} = \sqrt{2/3}a$.

To discuss the role of the confinement on the electronic structure it is quite intuitive to compare the Fermi surfaces obtained from the different orientations at the surface with the corresponding cross sections of the bulk Fermi surface along the same orientations as shown in figure 5.2(d,e). To do this, we assumed that the hopping parameters are the same than in the bulk ($t_{\pi'} = -0.236$ eV and $t_{\delta'} = -0.035$ eV) which wrongly implies that there is no lattice relaxation in the surface region. To better fit the experimental results, we defined $t_{\sigma''} = -0.03$ eV. We also assume that the oxygen vacancy distribution is similar for the three different surface orientations and has a depth profile of approximately 2 nm and thereby ignore any surface orientation dependent effects on the oxygen desorption. Finally, we assume that there is a constant potential difference between neighboring planes because a homogenous oxygen vacancy contribution results in a triangular potential well whose depth is fixed to 200 meV as discussed in section 1.2.

5.2 Characterization of 2DESs by ARPES

SrTiO$_3$(110)

We now present our experimental results. Figure 5.3(a) shows the Fermi surface measured at the fractured (110) surface of an undoped insulating SrTiO$_3$ sample. The metallic states we observe present the 2-fold symmetry of the unreconstructed (110) surface Brillouin zone (BZ), represented by red rectangles. This implies that *(i)* the macroscopic properties of this 2DES should be highly anisotropic, echoing the observed anisotropic transport characteristics reported in 2DESs at (110) LaAlO$_3$/SrTiO$_3$ interfaces [208], and *(ii)* any surface roughness or reconstructions, expected in this highly polar surface, do not affect the 2DES, which might reside

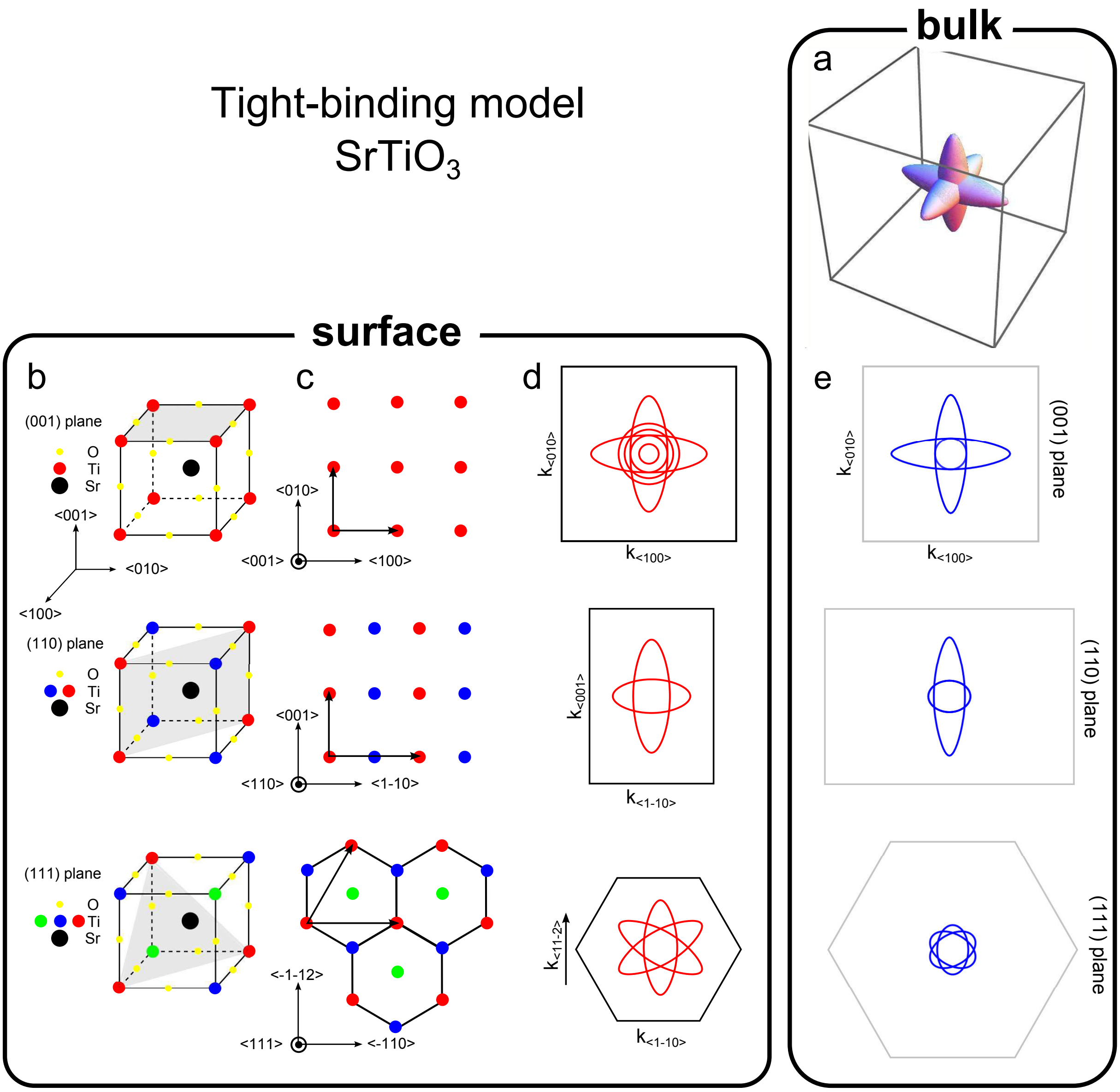

Figure 5.2: (a) Bulk Fermi surface, calculated using a tight-binding model with 10^{21} cm^{-3} for the bulk carrier density. Such carrier density is at least *three orders of magnitude* higher than the bulk carrier density of the samples prepared for this study. (b) Unit cell of the cubic perovskite lattice of SrTiO$_3$. The grey planes are the (001), (110) and (111) planes, respectively. The yellow dots represent the O^{2-} anions, the black dot in the center the Sr^{2+} cation, and the red/green/blue dots the Ti^{4+} cations in different (110) or (111) planes. Both orientations are highly polar, as the crystal is built of alternating layers of (SrTiO)$^{4+}$ and (O$_2$)$^{4-}$ or respectively, Ti^{4+} and (SrO$_3$)$^{4-}$. (c) Ti^{4+} cations of the crystal lattice in the (001), (110) and (111) planes. The black arrows indicate the lattice vectors of the Ti^{4+} cations in a (001), (110) or (111) plane. As indicated by the black lines a (111)-bilayer of Ti^{4+} cations forms a honeycomb lattice. (d) Calculated Fermi surface using a tight-binding model for electrons confined to a 2 nm region at the surface of SrTiO$_3$. The black lines correspond to the surface Brillouin zone. (e) Cross sections through the Γ point of the bulk Fermi surface in (a) along the (001), (110) and (111) planes, respectively. The gray lines show the cross section of the bulk 3D Brillouin zone.

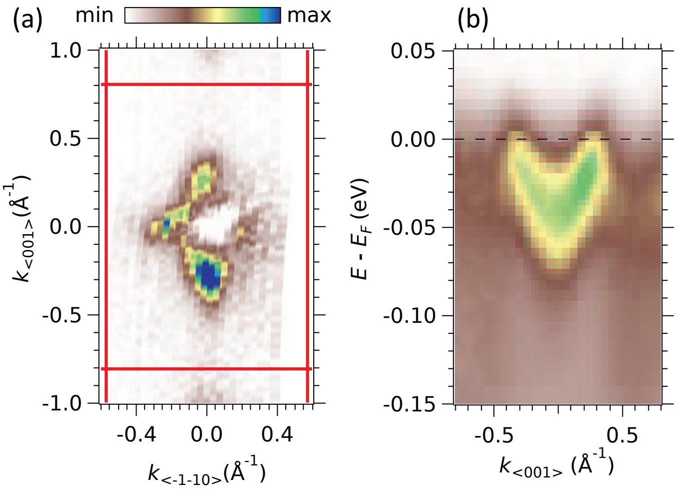

Figure 5.3: (a) ARPES Fermi surface map (second derivative) at $h\nu = 91$ eV in the (110) plane of a fractured insulating SrTiO$_3$ sample. The map is a superposition of intensities measured in the bulk Γ_{130} and Γ_{131} Brillouin zones. The red lines indicate the edges of the unreconstructed (110) Brillouin zones. (b) Energy-momentum intensity map at a Γ point along the $k_{\langle 001\rangle}$ direction. All measurements were conducted at a temperature of $T = 20$ K. Published in reference [10].

in the sub-surface layers –in agreement with our previous conclusions on fractured (111) surfaces of KTaO$_3$ [8]. Alternatively, the ARPES intensity of band structure folding due to a different periodicity of the surface layer in surface reconstructions might be to weak to be detected.

Figure 5.3(b) shows the dispersion along the $k_{\langle 001\rangle}$ direction, giving rise to the longest of the two ellipsoidal Fermi surfaces in figure 5.3(a). The band bottom and Fermi momenta are about -40 meV and 0.3 Å^{-1}, respectively. The band forming the shortest ellipsoid is eclipsed by photoemission selection rules along this direction.

From the data above, we model the Fermi surface of the 2DES at the SrTiO$_3$ (110) surface as two orthogonal ellipses, one along along $\langle 001\rangle$ with semi-axes of 0.3 Å^{-1} and 0.1 Å^{-1}, the other along $\langle 1\bar{1}0\rangle$ with semi-axes 0.25 Å^{-1} and 0.13 Å^{-1}. From the area A_F enclosed by the Fermi surfaces, we obtain a carrier density $n_{2D}^{(110)} = A_F/2\pi^2 \approx 1 \times 10^{14}$ cm^{-2}. The electronic states associated to such a high charge carrier density *must be confined to the region near the surface* –otherwise the bulk would be highly conductive, in contradiction with the insulating nature of the samples studied. Similarly, from the band bottom and Fermi momenta, using a parabolic approximation, we obtain the effective band masses along $\langle 001\rangle$ and $\langle \bar{1}\bar{1}0\rangle$ (and equivalent directions), listed in the third row of table 5.1 on page 101. Note that our observations (including the effective masses) are similar to the study of the 2DES at the SrTiO$_3$(110) surface in a Nb-doped sample prepared *in situ* by Wang *et al.* [9]. In our study, the band bottom of the heavy band, *c.f.* figure 5.3(b), and the carrier density of the 2DES are slightly lower, probably due to the different surface preparation techniques.

$SrTiO_3$(111)

Henceforth, we focus on experimental results at the (111) surface of $SrTiO_3$, which as we will see presents the triangular symmetry of the unreconstructed surface, and could thus be an interesting platform for the quest of new electronic states and macroscopic properties at oxide surfaces.

Figure 5.4(a) on page 100 shows the Fermi surface measured at the $SrTiO_3$ (111) surface prepared *in-situ* as described previously. It consists of three ellipses forming a six-pointed star, thus strongly differing from the Fermi surface at the $SrTiO_3$ (110) surface, shown in figure 5.3(a) on page 98, or the one at the $SrTiO_3$ (001) surface, discussed in previous works [1, 2, 7]. Additional experiments show that for surfaces prepared *in-situ* with either (1×1) or (3×3) reconstructions, the band structure and periodicity of the confined states are identical, and correspond to the one expected from an unreconstructed surface. This might indicate that the 2DES at the $SrTiO_3$(111) surface is located in the sub-surface layers, and is at best weakly affected by the surface reconstructions at the polar (111) surface.
The 2D-like character of the electronic states is strictly demonstrated from the Fermi surface map in the $\langle 111 \rangle - \langle \bar{1}\bar{1}2 \rangle$ plane, shown in figure 5.4(b) which will be discussed later on in more detail. Interestingly, note that the red rectangles in figures 5.3(a) and 5.4(b) represent the Brillouin zone in the (110) (or equivalent) plane. Yet, as seen from those figures, the shapes of the corresponding Fermi surfaces are completely different. This directly shows the orientational tuning of the Fermi surface due to different confinement directions. Figure 5.4(c) shows the energy-momentum map at the Γ point along the $\langle \bar{1}\bar{1}2 \rangle$ direction, corresponding to the major axis of the ellipsoids forming the 6-pointed-star Fermi surface. The dispersions of one light band and one heavy band are clearly visible. These constitute the ground state of the 2DES. Additional subbands are not observed, implying that the band bending at the surface is too low to populate the upper quantum-well states one would expect for a confined electron system (see section 1.2). Within our resolution, the heavy and light bands are degenerate at Γ, with their band bottom located at about -57 meV. We fit simultaneously these dispersions and the whole Fermi surface of figure 5.4(a) using the tight-binding model described previously. The fit, shown by the continuous blue lines, yields Fermi momenta of about 0.07 Å^{-1} and 0.36 Å^{-1} for, respectively, the light and heavy bands along $\langle \bar{1}\bar{1}2 \rangle$. This gives an electron concentration $n_{2D}^{(111)} \approx 1.0 \times 10^{14}$ cm^{-2}, and effective masses listed in the third row of table 5.1.

Orientational tuning of effective masses

We now draw some comparisons between the effective masses and of the 2DESs at the $SrTiO_3$ (001), (110) and (111) surfaces. Table 5.1 shows that, while the masses along the “natural” electron-hopping directions in the bulk ([001] and equivalent) are comparable between the 2DESs at the $SrTiO_3$ (001) and (110) surfaces, the masses along $[1\bar{1}0]$ at the (110) surface, and all the masses of the 2DES at the (111) surface, are very different from the ones expected from the tight-binding parameters describing the bulk or the 2DES at the (001) surface. In this respect, note that if the confinement direction is [110] or [111], then the electrons moving in the 2DES plane along

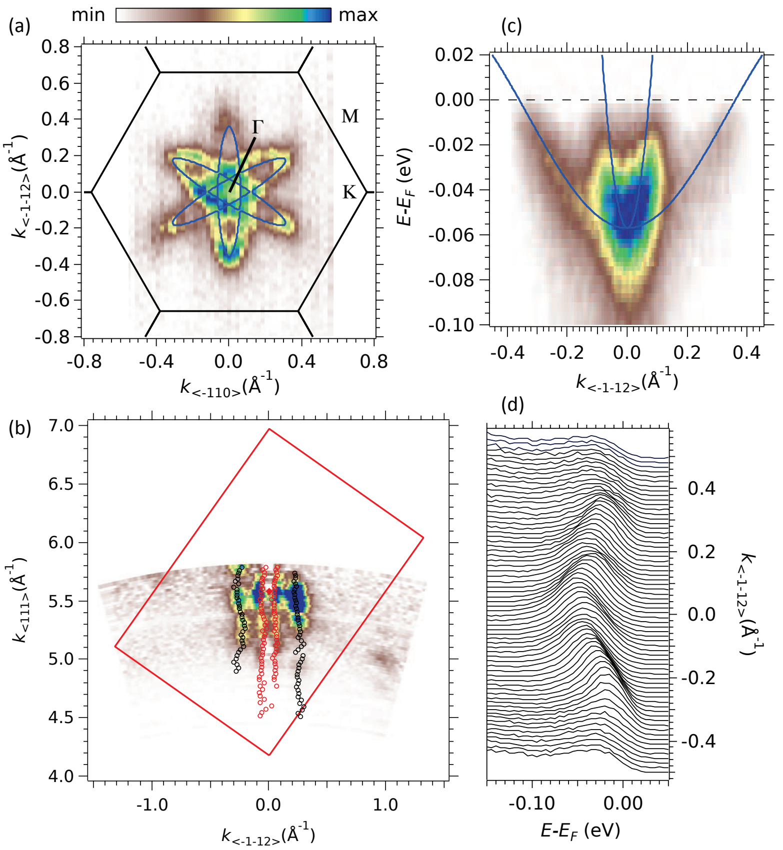

Figure 5.4: (a) Fermi surface map measured at $h\nu = 110$ eV on a SrTiO$_3$ (111) surface prepared *in-situ*. The black lines indicate the edges of the unreconstructed (111) Brillouin zones around Γ_{222}. (b) Fermi surface map (second derivative of ARPES intensity, negative values) in the $k_{\langle 111\rangle} - k_{\langle \bar{1}\bar{1}2\rangle}$, or $(1\bar{1}0)$ plane, acquired by measuring at normal emission while varying the photon energy in 1 eV steps between $h\nu_1 = 67$ eV and $h\nu_2 = 120$ eV. The experimental Fermi momenta, represented by the black and red circles, were obtained by fitting the momentum distribution curves (MDCs) integrated over $E_F \pm 5$ meV. The red rectangle is the bulk Brillouin zone in the $(1\bar{1}0)$ plane. (c) Energy-momentum map across the Γ point along the $\langle\bar{1}\bar{1}2\rangle$ direction. The dispersions of a heavy band and light bands are visible. (d) Raw energy distribution curves of the dispersions shown in panel (c). In panels (a) and (c), the blue lines are simultaneous TB fits to the Fermi surface and dispersions. All measurements were conducted at temperatures ranging between $T = 7 - 20$ K. Published in reference [10].

Table 5.1: Effective light (L) and heavy (H) masses predicted by a TB model in the bulk of $SrTiO_3$ (first row) and experimental in-plane masses of the 2DESs at the STO(001), STO(110), and STO(111) surfaces (other rows) along the different high-symmetry directions of the crystal lattice (columns). In the bulk, all the effective masses along [111] are identical. Published in reference [10].

	m_{100}/m_e		m_{110}/m_e		$m_{11\bar{2}}/m_e$		m_{111}/m_e
	L	H	L	H	L	H	
Theory bulk^a	1.06	7.16	1.06	1.85	1.24	2.46	1.48
STO(001)	0.7^b	10.0^b	0.7^c	1.3^c	0.8^c	1.8^c	1.0^c
STO(110)	1.0	8.5	1.6	6.0	–	–	–
STO(111)	–	–	0.27	1.08	0.33	8.67	–

^{a} From Ref. [215], ^{b} From Ref. [1], ^{c} From TB model using experimental masses along [100]

a direction *other than* [001] will experience the confining potential gradient and the modified crystal field outside the surface, as they will hop in staircase patterns between first neighbors along [001] (or equivalent) directions –see figures 5.2(a-d) and Ref. [8, 208]. The understanding of these mass differences should be the subject of further theoretical works and was already observed in quantum well states. [218, 219]

2D ≡ non-dispersing bands along the confinement direction

As already mentioned previously, the Fermi surface map along the direction perpendicular to the confinement direction in figure 5.4(b) demonstrates the 2D character of the states. Here, one sees that the bands do not disperse along $k_{\langle 111\rangle}$ over more than half of the bulk Brillouin zone, thereby confirming the confined (*i.e.*, localized) character of the electrons along the [111] direction in real space.

We now discuss the modulation of the intensity in the Fermi surface map which is a typical feature of quantum well states [220, 221]. Although the states do not disperse, confirming their confined nature, the intensity of the states drops rather quickly moving away from Γ_{222}. This observation is similar to the intensity modulation as a function of the photon energy reported previously at the (001) surface of $SrTiO_3$ [1] and $KTaO_3$ [3], as well as in quantum well states of metals [220, 221]. This modulation is due to photoemission dipole selection rules: the optical excitation of the electrons occurs from initial states in the near surface region that do not disperse along the confinement direction (the confined electrons) to dispersing bulk final states. Moreover, if the wave function of the confined states is not exactly localized in a 2D layer, but exists over several unit cells, the dispersion along the confinement direction will be affected. This can be

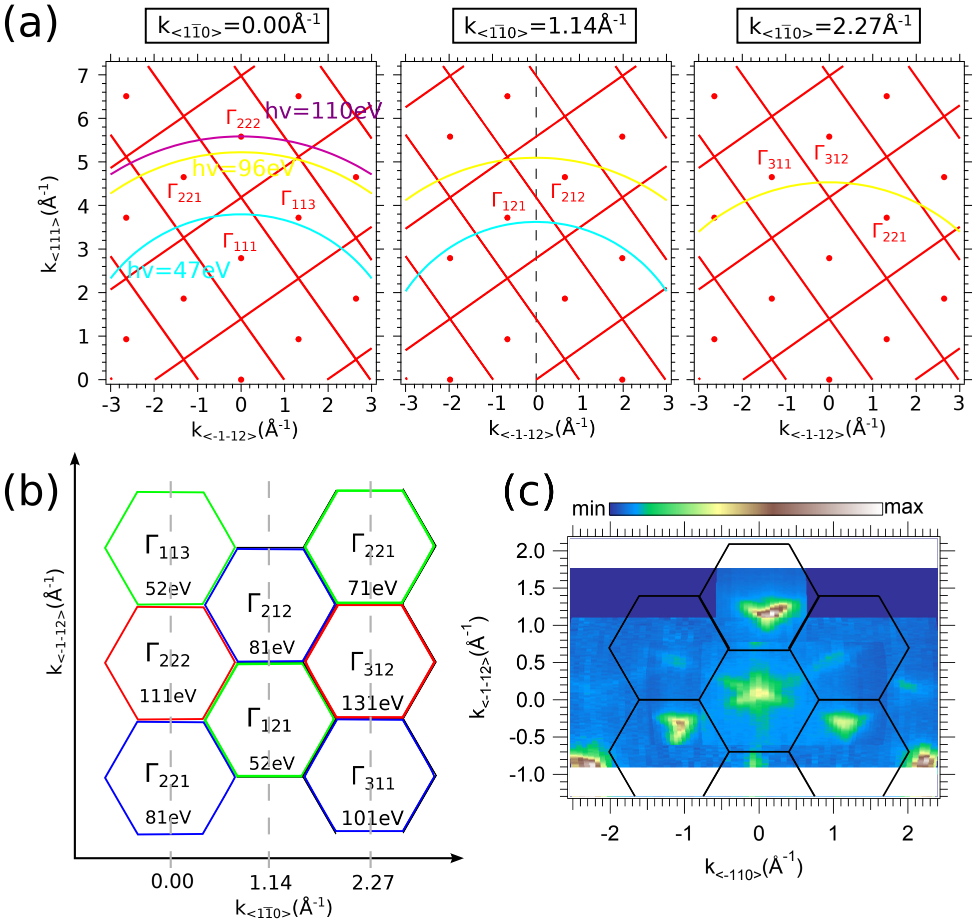

Figure 5.5: (a) Bulk reciprocal lattice of SrTiO$_3$ in the $k_{\langle 111\rangle} - k_{\langle \bar{1}\bar{1}2\rangle}$ plane for different $k_{\langle 1\bar{1}0\rangle}$ values as indicated in (b). Practically, different $k_{\langle 1\bar{1}0\rangle}$ values are chosen by rotating the sample. The pink, yellow and cyan lines correspond to the cuts in reciprocal space measured by ARPES at the specified photon energies. If the cut is close to a Γ point, the states corresponding to the 2DES have non-zero ARPES intensities. (b) Reciprocal 2D space in the (111) plane. Inside each Brillouin zone the projections of the different bulk Γ points corresponding to available final states during the photoemission process at the specified photon energy are indicated. The color (red, blue, green) of the hexagons indicates which Γ points are located in the same (111) plane in reciprocal space. The figures in (a,b) help understanding the Fermi-surface intensities shown in panel (c). (c) Superposition of Fermi surface maps measured for *in situ* prepared SrTiO$_3$ (111) sample ((3 × 3) reconstructed surface) at photon energies of $h\nu = 47$ eV and $h\nu = 96$ eV.

intuitively understood from Heisenberg uncertainty principle: only a strict 2D confinement in real space yields a complete indetermination of the electron momentum along the confinement direction, hence an exactly cylindrical Fermi surface. Some delocalization along the confinement direction, as in quantum-well states, implies a small dispersion of the Fermi surface along that direction.

Bearing these effects (selection rules in quantum wells, finite delocalization) in mind, one can comprehend the data in figure 5.5(c) on page 102, which show a superposition of Fermi surface maps measured at different photon energies, for a (111) surface prepared *in-situ*. The black hexagons are the Brillouin zones assuming an unreconstructed surface. Thus, due to selection rules, the intensity of the photoemission peak from the confined states is highest close to positions corresponding to Γ points of the bulk, where final states at the same $k_{\langle 111 \rangle}$ momentum are available for the optical transition. But this intensity will decrease rapidly by moving along $k_{\langle 111 \rangle}$, away from the bulk Γ points [220]. Experimentally, this is done by changing the photon energy. This results in the necessity to measure in-plane Fermi surface maps at different photon energies, and then superpose them to retrieve the complete periodicity of the electronic states, as illustrated in figures 5.5(a,b). Figure (b) shows the positions of the experimentally observed Γ points projected in the (111) plane. The photon energy inside each Brillouin zone corresponds to the $k_\perp$ value of the Γ points assuming a work function of $W = 4.25$ eV and an inner potential of $V_0 = 12$ eV.

Spatial extension of 2DESs

We discuss next the spatial extension of the 2DESs at the $SrTiO_3$ (110) and (111) surfaces. Note that, in our data at these surfaces, only the lowest-energy subbands are observed. To estimate the maximal extension d_{max} of the corresponding confined states, we suppose that the second subbands are slightly above the Fermi level. We then use a triangular potential well model as introduced in section 1.2, and take as effective masses along the [110] and [111] confinement directions, respectively, $m_{110} \approx 1.6 m_e$ (the lightest of the masses gives the largest 2DES thickness) and $m_{111} = 1.0 m_e$ (given by extrapolating the experimental masses at the (001) surface to the bulk [111] direction) – see table 5.1 on page 101. We obtain $d^{110}_{max} \approx 1.7$ nm, which amounts to 6 2D-layers or 3 bulk unit cells along [110], and $d^{111}_{max} \approx 1.9$ nm, corresponding to ~ 9 layers of Ti (111), or again about 3 bulk unit cells along [111].

Orientational tuning of orbital order

Finally, we note that the orbital ordering of the electronic states at the (110) and (111) surfaces of $SrTiO_3$ is different from the one at the (100) surface. In the first two cases, the bands are degenerate within our experimental resolution, whereas at the (001) surface the smallest observed splitting between bands of different orbital character is of 50 meV [1]. As the eigenenergy of each band is inversely proportional to its effective mass along the confinement direction (see equation (1.4) on page 18), different surface orientations result in different orbital ordering. But along the [111] direction the effective masses of the three t_{2g} bands are identical, and so their degeneracy at the Γ point is not lifted by the confinement. Similarly, the effective masses of bands of different orbital character along [110] are quite similar (see table 5.1). Hence, the degeneracy lift is rather small, and cannot be observed in our data. This demonstrates the influence of the confinement direction on the orbital ordering.

Conclusions

Several scenarios have been proposed to explain the origin of the 2DES at the $LaAlO_3/SrTiO_3$ (001) interface. According to one of these, the formation of a conducting sheet prevents the occurrence of a polar catastrophe in the material. Yet, the discovery of a confined 2DES at the (001) surface of $SrTiO_3$, with characteristics similar to those of the above heterostructure, suggests that the driving mechanism may not be unique, as in the bare $SrTiO_3$ all the layers are electrically neutral. Instead, in the latter case, surface oxygen vacancies cause and to confine the 2DES [1, 2, 9]. Additionally, for the (110) and (111) $SrTiO_3$ surfaces, of nominal polar charge $4e$, one would expect a much larger carrier concentration in the 2DES, and a very strong electric field confining the electrons in a narrow sheet at the surface. However, we observe that the carrier concentrations and thicknesses of the 2DESs are quite comparable for all three orientations (this work and Ref. [1]): $n_{2D} \sim 10^{14}$ cm^{-2}, $d_{max} \sim 2$ nm. In fact, in the polar $SrTiO_3$ surfaces studied here, the polar catastrophe does not seem to be compensated by the electrons of the 2DES but by surface reconstructions, while the 2DES might lie in the subsurface layers. Note that the creation of the 2DES and of the surface reconstruction do not occur at the same time. During preparation of polar surfaces (either fracturing or annealing in O_2) surface reconstructions compensate the overall dipole moment in stoichiometric $SrTiO_3$. Next, oxygen vacancies are created at the already reconstructed surface using either synchrotron irradiation or a reactive metal deposited on the surface. Note that oxygen vacancies can influence the surface reconstruction. As discussed in section 2.4 and in [124], the occurrence of surface reconstructions due to UHV annealing can be related to the creation of oxygen vacancies. In our case, the creation of vacancies occurs at relative low temperatures ($T \approx 20$ K for synchrotron irradiation and $T \approx 300$ K for metal deposition). As the diffusion of ions in $SrTiO_3$ is limited at these temperatures, surface reconstructions observed at a given oxygen deficiency during UHV annealing might not be equivalent to the case of creation of oxygen vacancies at low temperatures.

To sum up, although the 2D electronic structure (effective masses, orbital ordering and Fermi surfaces) depends on the surface orientation, the thickness and carrier concentration of the 2DES is controlled by oxygen vacancies.

Chapter 6

2DESs in ATiO$_3$ titanates: lattice distortions and electronic structure

Another approach to tune the properties of the 2DES at the surface of ATiO$_3$ perovskites is to change the lattice geometry by changing the A-site cation. As already discussed in section 1.1, the tolerance factor gives first insights in the distortions of the unit cell of the lattice depending on the size of the ions constituting the perovskite. In this chapter, I will discuss how different A-site cations influence the electronic structure of the 2DES in CaTiO$_3$ and BaTiO$_3$.

The 2DES at the (001) surface of SrTiO$_3$ is a reference system to understand the changes induced in the 2DES at the surface of CaTiO$_3$ and BaTiO$_3$. In cubic SrTiO$_3$, the oxygen octahedra surrounding the Ti cations are neither deformed nor rotated. However, in orthorhombic CaTiO$_3$, the octahedra are rotated. This breaking in symmetry results in the mixing of different d-orbitals which is not observed in SrTiO$_3$ (see ARPES measurements in section 6.3). In BaTiO$_3$, the off-center movement of the Ti cation results in ferroelectricity. Normally, ferroelectricity and metallicity are two exclusive phenomena as mobile carriers screen the long-range Coulomb interaction of electric dipoles. However, by locally doping the surface region and thus, creating a 2DES, the two phenomena coexist, although spatially separated, in the *same material* (see ARPES measurements in section 6.2).

On a macroscopic scale, the lattice distortions of the unit cell determine the dielectric properties of solids. I will briefly discuss the properties of quantum paraelectrics and ferroelectrics in the following section. While ferroelectricity is a well-known phenomena occurring in many different materials, quantum paraelectricity occurs only in a few materials (SrTiO$_3$, KTaO$_3$, CaTiO$_3$, TiO$_2$ rutile). However, 2DESs at the surface of three out of four quantum paraelectrics were discovered. Although there is no direct correlation between the existence of quantum paraelectricity and 2DESs, an understanding of this dielectric phase is necessary to better understand emerging properties in these materials.

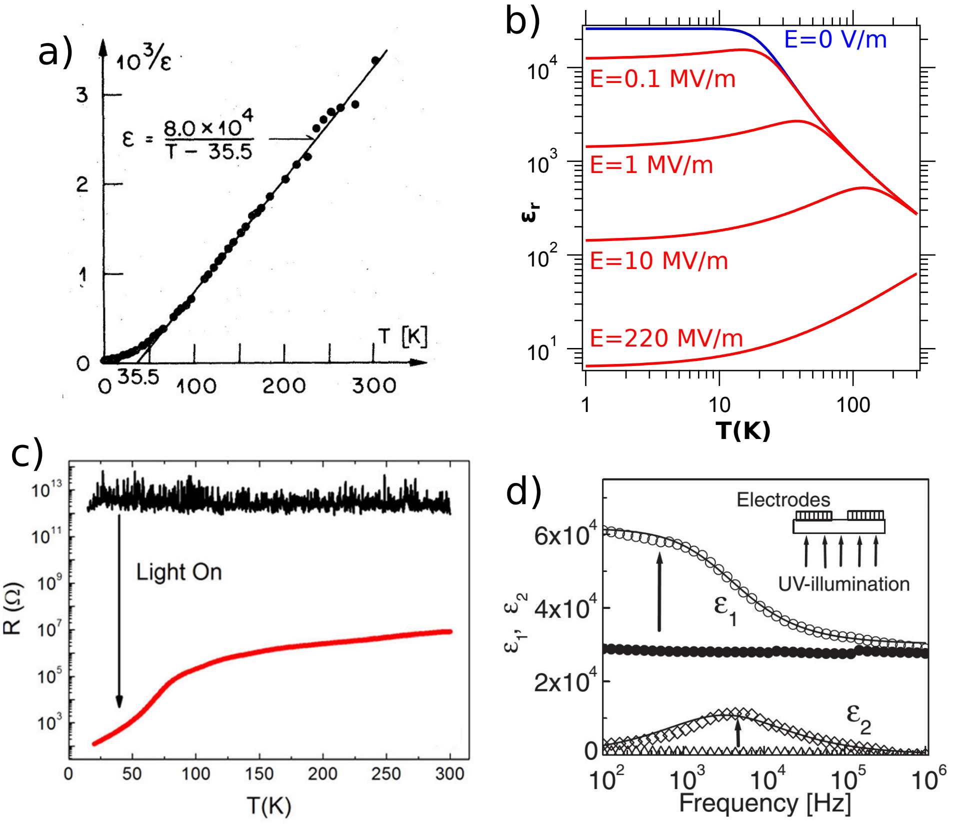

Figure 6.1: (a) Inverse dielectric constant of SrTiO$_3$ as a function of temperature. The divergence from the linear dependence at low temperatures occurs due to the quantum paraeletric phase (from [76]). (b) Same as in (a) but for different electric fields applied to the sample. The curves are based on the empirical formula of Yamamoto *et al.* [222]. Note that $E = 220$ MV/m corresponds to the electric field confining the electrons in the 2DEG at the (001) surface of SrTiO$_3$. (c) Resistance of SrTiO$_3$ as a function of temperature. UV irradiation can change the resistance up to eleven orders of magnitude (from [223]). (d) Photoinduced change of the dielectric constant fo SrTiO$_3$ as as function of temperature (from [224]).

6.1 Polar orders in ATiO$_3$: Quantum paraelectricity and ferroelectricity

The linear macroscopic response of the polarization $\vec{P}$ in a solid to an external perturbation by an electric field $\vec{E}$ is described by the electric susceptibility χ

$$\vec{P}(\vec{q},\omega) = \epsilon_0 \chi(\vec{q},\omega) \vec{E}(\vec{q},\omega)$$

which is related to the dielectric function by $\epsilon(\vec{q},\omega) = \chi(\vec{q},\omega) + 1$.

Barrett formula in quantum paraelectrics

The dielectric function of quantum paraelectrics (QPEs) are rather high ($\epsilon_r > 100$, see table in [225]) compared to semiconductors ($\epsilon_r \approx 10$). Hence, in QPEs the lattice is rather easily polarized. Instead of a transition to a ferroelectric phase like many other perovskites (*e.g.* BaTiO$_3$), the paralectric phase is quantum-mechanically stabilized.

The temperature dependence of the electric susceptibility of QPEs is given by the Barrett formula [226]:

$$\chi(\vec{0},0) \propto ((T_1/2)\coth(T_1/2T) - T_C)^{-1} \tag{6.1}$$

For temperatures $T > T_1$ the Barrett formula can be approximated to:

$$\chi(\vec{0},0) \propto \frac{1}{T - T_C} \tag{6.2}$$

which is the Curie-Weiss law describing the electric susceptibility of a ferroelectric in the paraelectric regime. Below the Curie temperature T_C, a phase transition from the paraelectric to the ferroelectric phase occurs. This phase transition is based on a change in the lattice structure.

As shown in figure 6.1(a) on page 106, the Curie-Weiss law does not fit the experimental data of the dielectric function but deviates according to the Barrett formula. As the Barrett formula in equation 6.1 deviates from the Curie-Weiss law in equation 6.2 for temperatures $T < T_1$, T_1 can be identified as the critical temperature at which a quantum paraelectric starts to behave differently to a classical paraelectric material.

In SrTiO$_3$, the characteristic temperatures are $T_1 = 80$ K and $T_C = 35.5$ K [76]; the inverse of the dielectric constant remains constant at temperatures smaller than 4 K [76] or, as recent experiments show has a minimum at about 2K [77]. In SrTiO$_3$ the relative permittivity ranges from about 300 at room-temperature to several ten of thousands at temperatures close to zero. Note that the Barrett formula fits the temperature dependence of dielectric function of SrTiO$_3$ only approximately. [76] The reason is that the formula describing the paraelectric phase was derived based on the consideration of a single soft phonon mode (it is the freezing of this mode which can lead to ferroelectric phase transitions). In SrTiO$_3$ other phonon modes need to be considered to describe the dielectric function $\epsilon_r(T)$. [227]

The given values of the relative permittivity shown in figure 6.1(a) were obtained on stoichiometric, insulating samples using weak electric fields (E < 10 kV/m). However, in the 2DES at the surface of SrTiO$_3$(001), the electron density is high $n_{2D} = 1.2 \times 10^{14}$ cm^{-2} and the confining field is about 220 MV/m (see previous sections). The itinerant electrons alter the screening of local charges and hence, the dielectric response. Similar, large electric fields can alter the dielectric response as shown in figure 6.1(b). The shown curves are based on the phenomenological describtion by Yamamoto *et al.*: [222]

$$\epsilon_r(E,T)^{-2} = \epsilon_r(0,T)^{-2} + \left(\frac{E}{b(T)}\right)^2 \tag{6.3}$$

where $\epsilon_r(0,T)$ is the relative premittivity at zero-field given by the Barrett formula and $b(T) = 1.37 \times 10^9\text{V/m} + 4.29 \times 10^7\text{V/(Km)}\ T$.

Other quantum paraelectrics are: KTaO$_3$ [228], CaTiO$_3$ [225] and TiO$_2$ rutile [229].

Effect of large relative permittivity ϵ_r

The high relative permittivity affects various properties, one of them being the electronic transport [230]. As the focus of this thesis is on the insulating d^0 transition metal oxides, it is necessary to dope the material in order to achieve electrical conductivity. In semiconductor physics, the electrons of shallow donors are modeled as the ones bonded to an hydrogen atom. Thus, the donor binding energy E_D and Bohr radius a_B are given by

$$E_D = -13.6\mathrm{eV}\frac{m_e^*}{m_e}\frac{1}{\epsilon_r^2}, \quad a_B = 0.53\mathrm{\mathring{A}}\frac{m_e^*}{m_e}\epsilon_r.$$

Due to the high relative permittivity the donor binding energy E_D is rather low and below the thermal energy even at low temperatures. Thus, the temperature dependence of the charge carrier density is rather small and the transport is rather metallic than semiconducting.

The rather large Bohr radius a_B results in a rather low critical charge density n_c to induce a metal to insulator transition. The wave functions of the donor atoms are spatially far extended and hence, overlap at rather low critical carrier densities n_c as expressed by the Mott criterion $n_c^{1/3} \propto 1/a_B$ [231]. Experimentally, the critical carrier density n_c for SrTiO$_3$ is about $n_c = 8.5 \times 10^{15}\mathrm{cm}^{-3}$ [230].

The metal to insulator transition can be induced optically [223, 232]. As shown in figure 6.1(b), the resistance of SrTiO$_3$ can be changed by six orders of magnitude at room temperature due to UV light. Depending on the defects in SrTiO$_3$, the photoconductivity can be persistent even at room temperature [233]. Kozuka *et al.* found that the photo-induced charge carrier density and the effective electronic thickness can be controlled by the light intensity and the wavelength [234].

Note that the dielectric function also influences the potential well (see equations (1.2) and (1.3) on page 17) confining electrons at the surface or interfaces of quantum paralectrics. [235]

Transition to ferroelectric state due to pertubations

The quantum paralectric state is not very stable and can change its phase (locally or globally) to a ferroelectric one under various external pertubations, *e.g.* stress [236–238], substitution of the A site cation in the perovskite lattice [239, 240], isotope substitution of O anions [241] or high electric fields [242].

Even perturbations intrinsic to the crystal can introduce polar moments. Salje *et al.* demonstrated that ferroelastic twin walls in SrTiO$_3$ are polar at low temperatures [243] and ferrielectric in CaTiO$_3$ [244–246].

Other possible perturbations which are of special interest for this thesis are UV light and dipole moments induced by the relaxation of the atoms near the surface or by the electric fields at the surface confining the electrons in the solid. The reason being that the focus of our experiments are surface-sensitive ARPES measurements at synchrotron facilities using photons in the UV/ soft x-ray range.

The influence of UV light is observed experimentally using photon energies larger than the band gap of QPEs. A light-induced increase of the dielectric constant was observed in SrTiO$_3$ and KTaO$_3$ [224, 247, 248] - one example is shown in figure 6.1(c). In all three publications photo-induced polar domains or metallic clusters are given as possible explanations of the observed effects. Further evidence for polar distortions in QPEs induced by UV light, are given by absorption and emission spectroscopy measurements. [249, 250]

Conclusion

As already discussed in section 3.1, the dominating effect of the UV synchrotron radiation in our experiments is to create oxygen vacancies. Nevertheless, the previous paragraphs emphasize that UV irradiation in SrTiO$_3$ and related materials can have different influences in the electronic and lattice structure. A decisive factor for the response of QPEs to UV light is, if the crystal is stoichiometric or electron doped. In stoichiometric oxides, the charge transfer induced by UV light might be screened by a response of the lattice (*e.g.* polar distortions) whereas in electron doped oxides, the screening might be dominated by the itinerant electrons. Moreover, the quantum paraelectric state can change to the ferroelectric phase under various perturbations. This demonstrates again that different ground states are quite close in energy in transition metal oxides.

Ferroelectric BaTiO$_3$

Many ABO$_3$ perovskites are ferroelectric, a typical example being BaTiO$_3$. In BaTiO$_3$, the crystal undergoes a phase transition from the centrosymmetric cubic to the non-centrosymmetric tetragonal structure at a Curie temperature of $T_{C,BTO} = 120°\text{C}$. The shifting of the cations and anions in opposite directions results in a local dipole moment and a macroscopic polarization in the tetragonal phase. A material is classified as a ferroelectric if this polarization can be switched by the application of an electric field.

To minimize stray electric fields due to the polarization, the formation of domains of opposite polarizations is energetically favorable. Later on, I will discuss measurements on thin films of BaTiO$_3$. In contrast to the bulk crystals, the 30 nm-thick BaTiO$_3$ films deposited on Nb:SrTiO$_3$ show a single domain state, with the ferroelectric polarization aligned along the [001] axis, due to the in-plane compressive strain induced by the epitaxial growth [251–253]. This is illustrated in figure 6.2(a) on page 110 by the atomic force microscopy (AFM, top) and piezoreponse force microscopy (PFM, bottom) images of a BaTiO$_3$/Nb:SrTiO$_3$ thin film. The AFM image shows atomic steps characteristic of a smoothly-terminated surface. However, we could not detect any ferroelectric domain in the film, neither on the 100 nm (substrate terrace width) scale, as shown by the PFM image taken on the same region as the AFM topography, nor on the 10 μm scale. Nevertheless, we were able to reverse the ferroelectric polarization upon applying a DC voltage to the PFM cantilever, as illustrated in figure 6.2(b), thus proving that the BaTiO$_3$ thin film is indeed ferroelectric with a single domain configuration. For the PFM measurements, a probing signal of 2 V$_{\text{pp}}$ at a frequency of 25 kHz was applied to a Co/Cr coated cantilever with ∼ 5 N/m

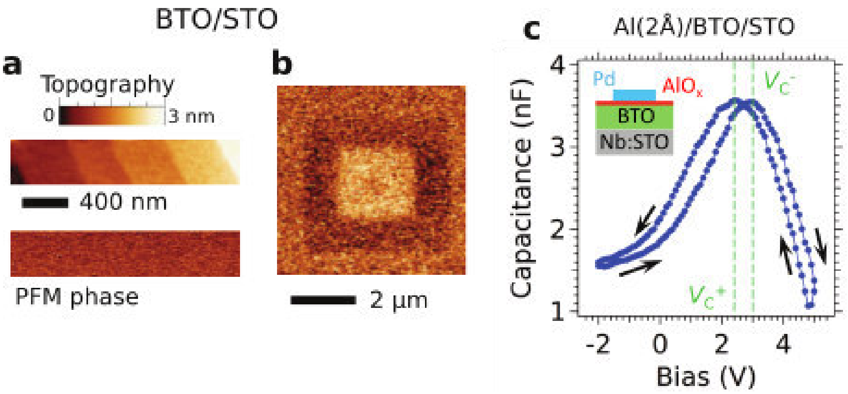

Figure 6.2: (a) AFM topography and corresponding PFM phase signal measured on a 30 nm-thick $BaTiO_3$/Nb:$SrTiO_3$ film. No ferroelectric domains could be detected in the as-grown film, while such domains can be written, as shown in (b), with +6 V on the AFM tip in the outer square (4×4 μm^2) and −6 V in the inner square (2×2 μm^2). The PFM signal was recorded with an AC probing signal at 25 kHz frequency using 0.5 V_{pp} amplitude in (a) and 2 V_{pp} in (b). (c) Capacitance-voltage curve on the Al(2Å)/$BaTiO_3$ interface measured previously by ARPES, showing the butterfly shape characteristic of a ferroelectric hysteresis. A Pd circular pad and the Nb:STO substrate were used as top and bottom electrodes, respectively. Note that, due to the voltage drop through the thin alumina layer, the voltages (V_c^+ and V_c^-) required to reverse the polarization (P) are rather high. Thus, it was not possible to perform a polarization reversal in PFM mode. Published in reference [19].

force constant. A lower probing signal of 0.5 V_{pp} was also used with no change on the observed phase images such as the ones shown in figure 6.2(a).

In $BaTiO_3$, we created the 2DES by depositing an ultra-thin film of aluminum as discussed in section 4.1. Finally, figure 6.2(c) shows a measurement of the capacitance-voltage curve on the *same* Al(2Å)/$BaTiO_3$ interface that was measured by ARPES. The hysteretic response, with a coercive field difference corresponding to about $V_c^- - V_c^+ \approx 0.5$ V, demonstrates that the BTO film is still ferroelectric after deposition of the Al layer and ARPES measurements, thus keeping its functional behavior. In order to assess the ferroelectric character of the $BaTiO_3$ film measured by ARPES, 300 μm-diameter Pd electrodes (200 nm thickness) were deposited through a shadow mask on top of the Al oxide (AlO_x) layer.

The C-V measurements were performed using a LCR meter with a 30 mV_{pp} AC amplitude at 10 kHz, while a source-meter allowed for the DC biasing with 0.1 V steps of 500 ms duration. The C-V curve, figure 6.2(c), shows the characteristic butterfly shape of a ferroelectric material. Note that due to the ultra-thin AlO_x layer, the required voltages to reverse the polarization (V_c) are rather high and shifted towards the positive voltage side, indicating an internal upward electric field in the BTO layer. For these reasons it was not possible to achieve a polarization reversal in PFM configuration on this sample.

After characterizing the dielectric properties of the $BaTiO_3$ thin film, the electronic structure of $BaTiO_3$ will be the focus of the next section. The ARPES results show the existence of an 2DES at the interface of an ultrathin (2Å) Al layer and a $BaTiO_3$ thin film.

6.2 $BaTiO_3$: ferroelectricity and confined metallicity in the same material

$BaTiO_3$ is a prototype ferroelectric perovskite as discussed in the previous section. In principle, the interaction of the electric dipoles resulting in their long range order and a macroscopic polarization is screened if mobile charge carrier are present. Hence, a ferroelectric material should be insulating. But up to certain threshold mobile charge carriers/ metallicity and ferroelectricity coexist. Rault *et al.* used UHV and oxygen annealing to control the oxygen vacancy concentration/ electron density and imaged the domain structure at the surface depending on the doping level. [141]

Here, we use the redox reaction induced by the deposition of Al (see section 4.2) to locally create a high concentration of oxygen vacancies close to the Al/$BaTiO_3$(001) interface. This spatially separates two regions of the $BaTiO_3$ crystal: one which is far above the charge carrier threshold for the existence of ferroelectricity and one far below. Thus, spatially separated insulating ferroelectricity and highly doped metallicity confined to the interface coexist in the same material. The question how and if the metallic state at the interface influence the polar order in the bulk of $BaTiO_3$ (and *vice-versa*) is still open. While it was possible to create and measure by ARPES the confined metallic states at the interface of Al and a mono-domain $BaTiO_3$(001) thin film, charging was observed at the interface of Al and multi-domain bulk crystals of $BaTiO_3$(001). Although more experiments have to be conducted to confirm this observation, the domain configuration might influence the formation of the confined metallic states.

Characterization of 2DES in $BaTiO_3$ by ARPES

Similar to the other perovskite titanates $SrTiO_3$ and $CaTiO_3$ (see sections 4.2 and 6.3), the electronic structure of $BaTiO_3$ is composed of circular Fermi surface (d_{xy}) and elliptical Fermi surface sheets (d_{xz}, d_{yz}). The ARPES spectra in figures 6.3 on page 112 and 6.4 on page 114 show broad bands and also a broad Fermi level (a factor 2-3 larger than expected based on temperature and experimental resolution), possibly due to inferior surface quality compared to the other studies and/or due to stray electric fields because of the polarization of the $BaTiO_3$ thin film.

Figure 6.3 displays the Fermi surfaces measured at $h\nu = 80$ eV using LV photons in figure 6.3(a) and LH photons in (b). They indicate the presence of two ellipses with a major axis larger than the Brillouin zone and a minor axis of roughly 0.1 Å^{-1}. The light polarization dependence of the d_{xz} and d_{yz} orbitals can be explained based on table 2.1 on page 31. The open red circles show the Fermi momenta obtained from Lorentzian fits of the momentum distribution curves (MDCs) at E_F. Figure 6.3(c) shows one of such MDCs, corresponding to a cut at the left edge of the Brillouin zone in (a) (light blue arrows). This MDC clearly shows a double-peak structure, corresponding to the two Fermi sheets of the ellipsoidal Fermi surface, which is thus open at the Brillouin-zone edge. The ellipsoidal Fermi surface can be approximated as a rectangular stripe with an average distance between opposite Fermi momenta of $k_s \approx 0.15 \pm 0.02$ Å^{-1} along the

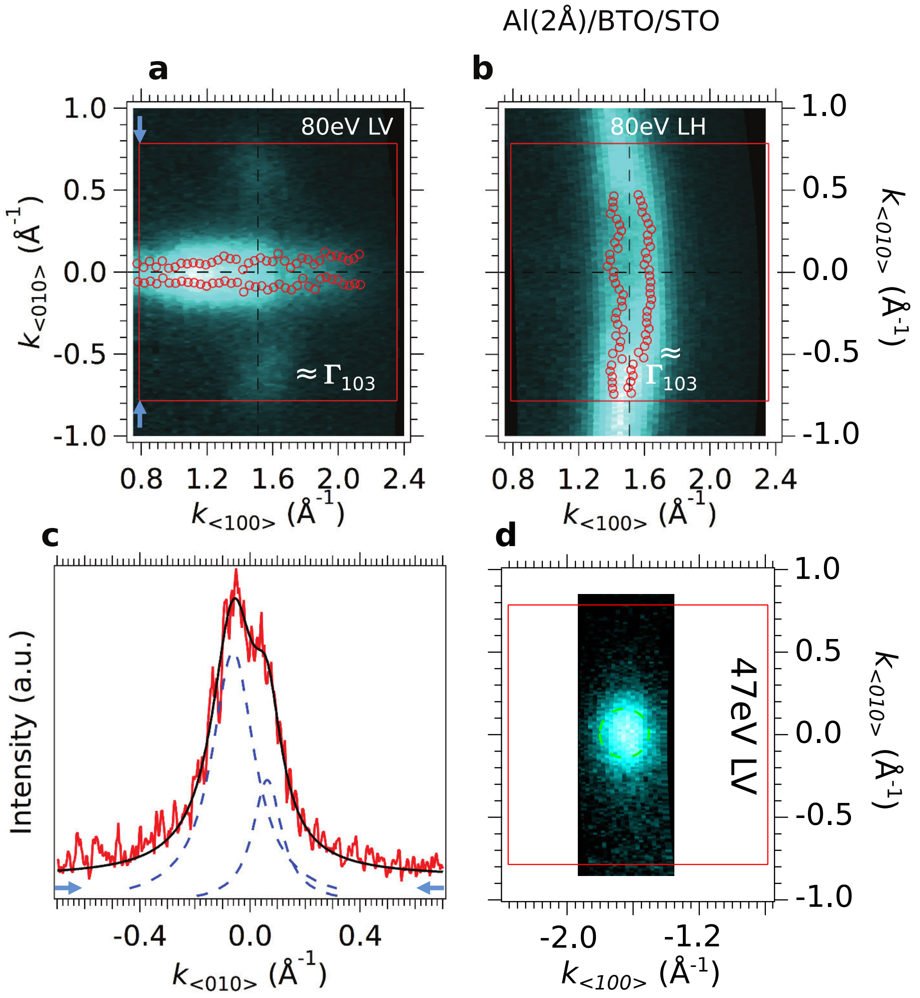

Figure 6.3: 2DES in BaTiO$_3$. (a, b) Fermi surface maps (spectral weight integrated over $E_F \pm 5$ meV) at the the Al(2Å)/BaTiO$_3$ interface using 80 eV LV and LH photons, respectively. Data were collected close to the Γ_{103} point. The open red circles show the Fermi momenta obtained from Lorentzian fits to the MDCs at E_F. The red squares show the Brillouin-zone edges. The two ellipsoidal Fermi surfaces correspond to d_{xz} and d_{yz} orbitals. Using the nomenclature in section 2.2, the mirror plane is the xz plane and thus, only bands of d_{xy} and d_{yz} character have non-zero matrix elements at $k_{<010>} = 0$ using LV photons (a) or respectively d_{xz} in (b) (see table 2.1 on page 31) (c) MDC integrated over $E_F \pm 10$ meV along the left edge of the Γ_{103} Brillouin zone, corresponding to a cut along the light blue arrows in panel (a). The blue dashed curves are Lorentzian peaks, and the black curve is the resulting total fit. (d) Fermi surface measured at $h\nu = 47$ eV using LV polarization (spectral weight integrated over $E_F \pm 5$ meV) showing a disk corresponding to the d_{xy} orbital. All the measurements were conducted at $T = 8$ K. Published in reference [19].

short side of the stripe.

The Fermi surface measured at the Ti $3p \rightarrow 3d$ resonance at $h\nu = 47$ eV is displayed in figure 6.3(f) and shows a circular symmetry typical for the d_{xy} orbital in the (001) plane. The intensity of the Fermi surface is rather blurred and thus, only a rough estimate of the Fermi momenta $k_F = 0.15 \pm 0.03$ is possible.

Based on the given Fermi momenta, the electron density of the 2DES in BaTiO$_3$ is $n_{2D} = A_F/2\pi^2 = 2.8 \times 10^{14}$ cm^{-2}.

The t_{2g} manifold is also evident in the ARPES $E - k$ intensity maps shown in figure 6.4. The d_{xy} band is displayed in figure 6.4(a) - no dispersing features are visible probably due to the large band width. The dispersion of the d_{xz} band is evident in figures 6.4(b,c), the one of the d_{yz} band in figures 6.4(d,e). The large band width make it difficult to discern whether the d_{xz} and d_{yz} band is crossing the Fermi level E_f or whether only spectral weight of the broad bands overlaps with E_f. However, the fits of the energy distribution curves (ECDs) are shown by the yellow markers representing the peak positions in figures 6.4(b,e) and indicate that the bands are not crossing E_f. The red curves in figure 6.4(b,f) are a cosine fit of the peak positions in the EDCs. The fit yields band masses of approximately 8-12m_e and a band bottom of approximately 120 meV. Note that effective mass might be different for the bands in figures 6.4(b,f) as the cuts in reciprocal space ($k_{<001>}$ values) are not identical.

Photon energy dependence

Figures 6.5(a,b) show the out-of-plane Fermi-surface map of the 2DES at the surface of BaTiO$_3$, obtained from the photon-energy dependence of the electronic structure measured over more than an entire bulk Brillouin zone. The inner cylinder, yellow dashed lines in figure 6.5(b), is associated to the light d_{xy}-like band forming the Fermi circle in the plane. As its Fermi surface does not disperse along the confinement direction, it corresponds to a 2D-like state.

The data also show a large ellipse dispersing along $k_{<001>}$, best seen in the lower part of the Γ_{003} Brillouin zone by the purple dashed lines in figure 6.5(b). This Fermi sheet is associated to the d_{xz} band forming the ellipsoidal Fermi in the plane. Note that the dispersion does not correspond to pure 3D/ bulk state. As already mentioned, this 2D-3D dichotomy was also observed in the 2DES at the surface of SrTiO$_3$ [7] and can be qualitatively understood as arising from confinement itself.

The parameters (electron density, effective mass, binding energy of band bottom) characterizing the electronic structure of the 2DES in BaTiO$_3$ will be compared to the ones in SrTiO$_3$ and CaTiO$_3$ in section 6.4.

Conclusion

The 2DES at the interface of BaTiO$_3$ discussed in this section is in essence an intrinsic metal/ ferroelectric interface. Polarization switching of the bulk material, for instance by strain, could allow a direct gating of the 2DES, while the capping alumina layer protects it against re-oxidation

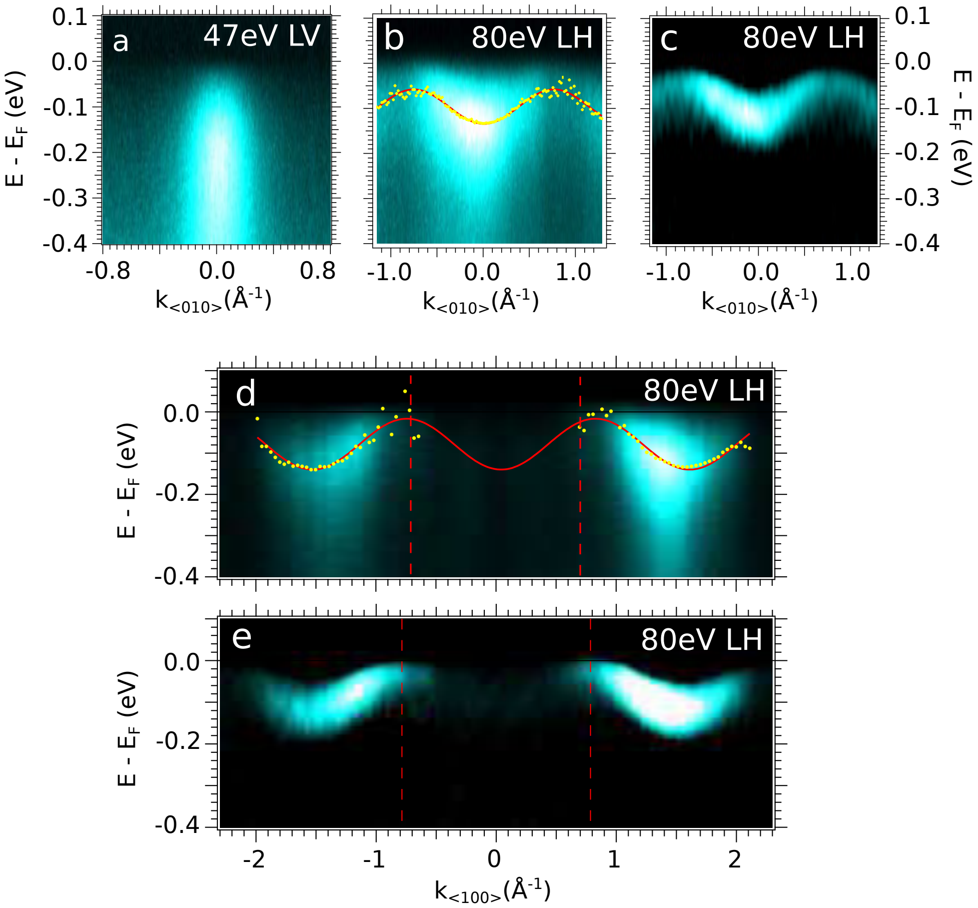

Figure 6.4: 2DES in BaTiO$_3$. (a) Energy momentum intensity map measured at the Al(2Å)/BaTiO$_3$(001) interface and at $k_{<100>} = 1.53$ Å^{-1} using a photon energy of $h\nu = 47$ eV and LV polarization showing the d_{xy} subband. (b) $E - k$ map ($k_{<100>} = 1.53$ Å^{-1}, $h\nu = 80$ eV, LV) showing the d_{xz} subband which does not cross E_F. The yellow markers are the peak positions of the fitted EDCs and the red line a cosine fit of the peak positions. (c) 2^{nd} derivative of (b). (d) $E - k$ maps ($k_{<010>} = 0$ Å^{-1}, $h\nu = 80$ eV, LH) along the <100> direction spanning over three Brillouin zones and showing the d_{yz} band. The red dashed lines indicate the Brillouin zone border. (e) 2^{nd} derivative of (d). All the measurements were conducted at $T = 8$ K. (a-c) Published in reference [19].

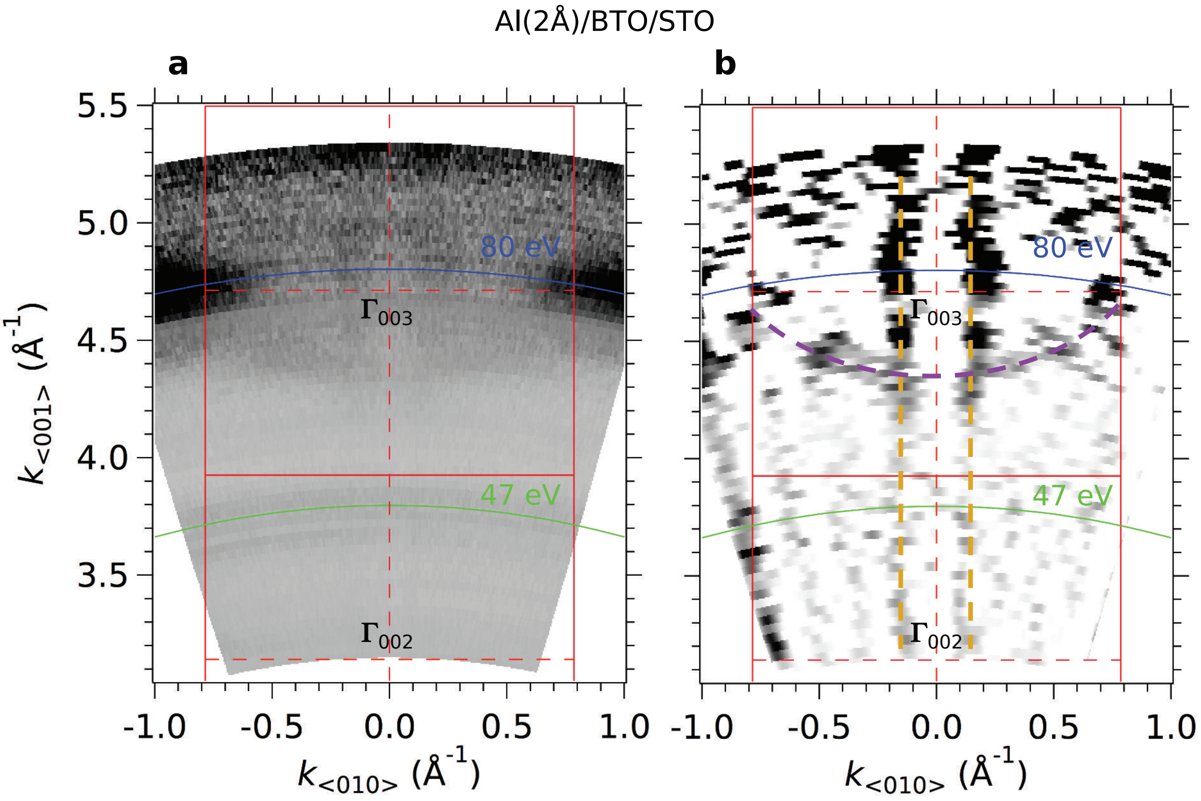

Figure 6.5: 2DES in BaTiO$_3$. (a) Raw Fermi surface map at the the Al(2Å)/BaTiO$_3$ interface in the $k_{\langle 001\rangle} - k_{\langle 010\rangle}$ plane, acquired by varying the photon energy in 1 eV steps between $h\nu_1 = 30$ eV and $h\nu_2 = 100$ eV using LH photons. To calculate the momentum perpendicular to the surface, we use a free-electron final-state approximation, and set the inner potential to $V_0 = 12$ eV. The spectral weight was integrated over $[E_F - 30, E_F + 5]$ meV. The red square shows the edges of the Γ_{003} bulk Brillouin zone. The blue and green arcs show the spherical cuts in 3D reciprocal space obtained with $h\nu = 80$ eV and $h\nu = 47$ eV. Note that the data shown in figures 6.3 and 6.4 were obtained in different Brillouin zones, namely the ones of Γ_{103} and Γ_{102}. (b) Second derivative (negative values only) of the Fermi surface map in (a). The yellow and purple dashed curves are guides to the eye showing, respectively, the non-dispersive Fermi surface of the light d_{xy}-like states, and the dispersive Fermi surface of the heavy $d_{xz/yz}$-like states. The measurement was conducted at a temperature of $T = 8$ K. Published in reference [19].

at ambient conditions, and can be even used to draw metallic nanocircuits of intrinsic ferroelectric tunnel junctions. Thus, this system provides a realistic platform for the realization of non-volatile memories using ferroelectric resistive switching. [254, 255].

6.3 $CaTiO_3$: orbital mixing due to oxygen octahedra rotations

The perovskite family owes its name to the mineral $CaTiO_3$ which was discovered in 1839 and named after a Russian mineralogist. Similar to other perovskites ($SrTiO_3$ and $KTaO_3$) hosting a 2DES at their surface, $CaTiO_3$ is a quantum paraelectric [225] as discussed briefly in section 6.1.

As discussed previously, in the titanate family ($CaTiO_3$, $SrTiO_3$ and $BaTiO_3$), the size of the A site cation determines the lattice distortions and hence, the polar orders. In $CaTiO_3$ the oxygen octahedra surrounding the Ti^{4+} ions are slightly tilted. The value of tilt angle is directly coupled to the electronic properties, *e.g.* in mangenites or nickelates and recently the control of the properties of interfaces of oxide heterostructure related to octahedra tilts has attracted much attention. [59].

The magnetism at the interfaces between $LaAlO_3$ and the three discussed titanates was studied by Gnaguli and Kelly. [256] They predicted that a large tilting of octahedra results in a more robust interface magnetism in $LaAlO_3/CaTiO_3$ compared to the $SrTiO_3$ and $BaTiO_3$ interfaces, demonstrating the influence of octahedra rotations on the properties of the 2DES.

Characterization of 2DES in $CaTiO_3$ by ARPES

We now characterize the electronic structure measured by ARPES. Again, a 2DES is observed due the creation of oxygen vacancies induced either by synchrotron irradiation of the surface of cleaved $CaTiO_3$ single crystals or by a redox reaction with an Al film.

The Fermi surfaces in the (001) plane and the corresponding 2^{nd} derivatives are shown in figures 6.6(a-f) on page 117 and were measured at photon energies of $h\nu$=57 eV and $h\nu$=67 eV using different light polarizations (linear vertical and horizontal). These photon energies correspond to bulk Γ points in reciprocal space: Γ_{002} ($h\nu$=57 eV) and Γ_{102} ($h\nu$=67 eV) based on a notation using the quasi-cubic unit cell.

Based on the characterization of the t_{2g} orbitals in the 2DES in $SrTiO_3$, one can assign the orbital character to the different Fermi surface sheets in the 2DES in $CaTiO_3$. Two Fermi surface sheets are circular as seen in figures 6.6(b,c,e,f) and correspond to d_{xy} orbitals. Note that the shape of the smaller Fermi surface sheet is not unambiguous in figure 6.6(b,c,e,f). However, the d_{xy} orbital character is assigned to it based on the non-dispersing character of this Fermi sheet along the confinement direction as best seen in figure 6.7(c) on page 119. The third Fermi sheet consists of a four-pointed star corresponding to orbital mix of d_{xz} and d_{yz} bands as shown in figure 6.6(a,d).

In the 2DES at the (001) surface $SrTiO_3$, the d_{xz} and d_{yz} bands have a pure orbital character [1] and form two ellipses whereas in $KTaO_3$ the orbital character is mixed due to spin-orbit

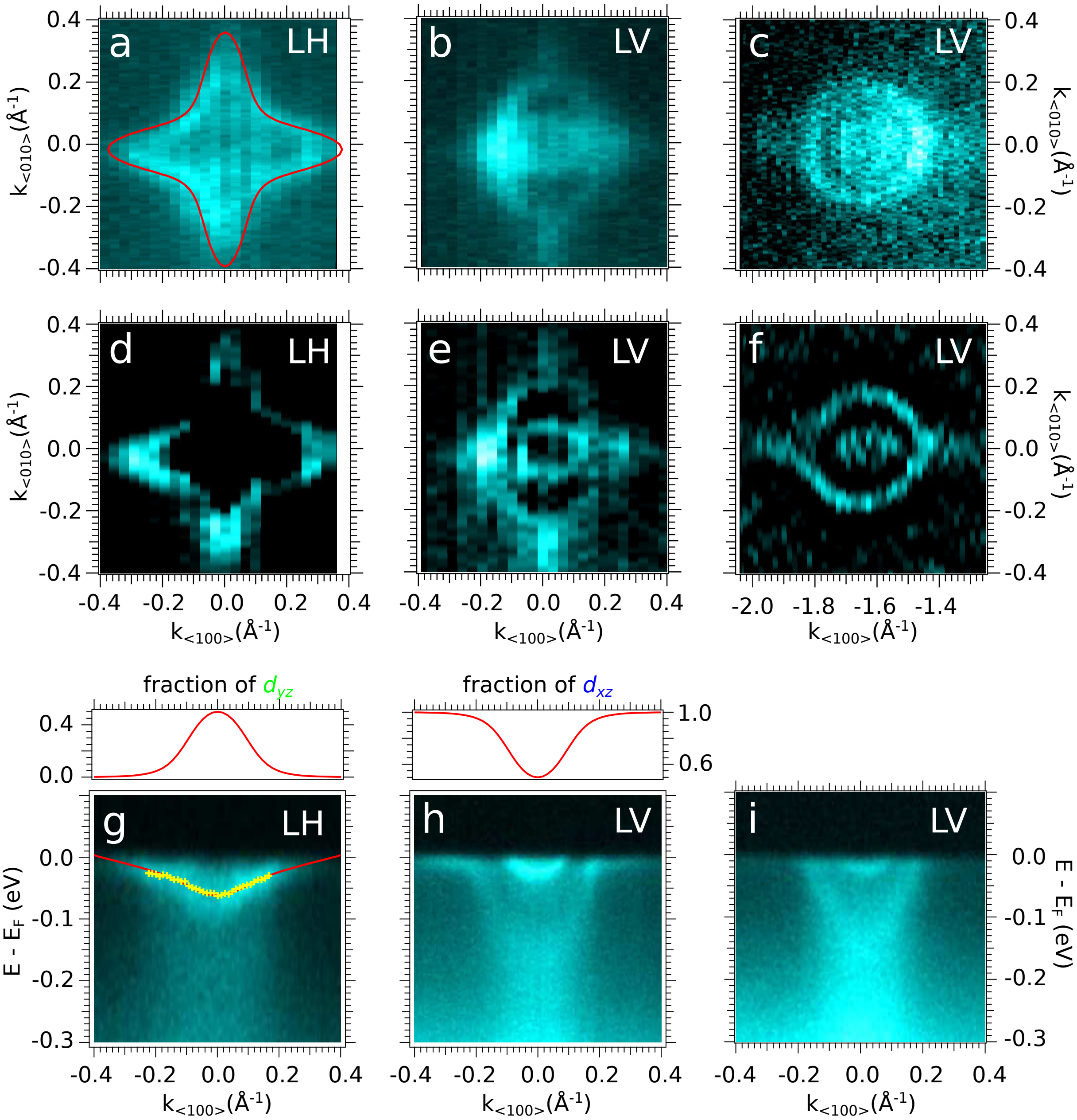

Figure 6.6: 2DES in CaTiO$_3$. (a,b) Fermi measured at $h\nu = 57$ eV using linear horizontal (LH) (a) and linear vertical polarization (LV) (b). (a) The red curve is based on a single layer tight-binding model (TB). (c) FS at $h\nu = 67$ eV using LV polarization. (d-f) Same as (a-c) but based on 2nd derivatives of energy momentum maps of along the energy axis d/dE^2. (g,h) E-k maps measured at $h\nu = 57$ eV using LH and LV polarization. The red graphs on top of the E-k maps show the orbital character (d_{yz} in (g) and d_{xz} in (h)) of the heavy band depending on momentum. (g) Yellow markers are the peak positions of the EDC fits and the red curve is based on a TB model. (i) E-k map at $h\nu = 67$ eV using LV polarization. All measurements were conducted at temperatures ranging between $T = 7 - 20$ K.

coupling [3]. In $CaTiO_3$, the breaking of symmetries due to the oxygen octahedra tilt results in an electron hopping between orbitals of different character. The red star drawn on panel (a) of figure 6.6 is based on a single layer tight-binding model. Compared to the model presented in section 5.1, an additional hopping term $t_{xz,yz}$ characterizing the hopping between the d_{xz} and d_{yz} orbitals results in the star shaped Fermi surface (tight-binding parameters: $N = 1$, $t_{xz,yz}$=9 meV and $t_{\delta'}$=15 meV).

Figures 6.6(g-i) present the energy-momentum maps using different polarizations close to the bulk Γ_{002} (g,h) and Γ_{102} (i) points along the cut parallel to the $\langle 010 \rangle$ direction. Two dispersive light bands are visible in figure 6.6(h,i) and the outer part of one heavy band close to the Fermi level can be observed in figure 6.6(h) whereas the center part of the heavy band, 62 meV below E_F, can be seen in figure 6.6(g). The polarization dependence of the heavy band demonstrates its mixed orbital character. The fraction of d_{xz} and d_{dz} orbital character in the heavy band based on the TB model is shown by the red graphs on top of figure 6.6(g,h). The green markers in figure 6.6(g) are the peak positions of the EDC fits and the red curve is based on the tight binding model discussed above. Their band bottoms are located at a binding energy of 158 meV (d_{xy}), 62 meV (d_{xz}, d_{dz}) and 27 meV (d_{xy}).

A parabolic fit yields an effective mass of approximately $1.1 m_e$ for the d_{xy} bands and $2.65 m_e$ for the mixed d_{xz}, d_{dz} band close to the Γ point. The corresponding Fermi momenta are 0.20 Å^{-1}, 0.38 Å^{-1} and 0.07 Å^{-1}.

This gives an electron concentration of $n_{2D}^{(001)} \approx 1.2 \times 10^{14}$ cm^{-2}, or about 0.17 electrons per a^2, where a is the pseudo-cubic lattice constant of the orthorhombic lattice and a^2 the cross section of the unit cell in the (001) plane.

The quasi-2D character of the d_{xy} electronic states is demonstrated by the cylindrical shape of the confined states as evidenced in the Fermi surface map in the $\langle 010 \rangle - \langle 001 \rangle$ plane, shown in figure 6.7(b,c). On the other hand, the bands of d_{xz} and d_{yz} character are dispersing along the [001] direction as shown in figure 6.7(a). The non-2D character of the d_{xz} and d_{yz} bands corresponding to these orbital character was already observed in the 2DES at the surface of $SrTiO_3$ [7] and $BaTiO_3$ (see previous section), and ascribed to the finite confinement length of the electrons in the quantum-well.

6.4 Comparison of 2DESs in $ATiO_3$ perovskites

The study of perovskite oxides as a function of tolerance factor or respectively, the A-site cation is a common approach to change their properties. In the previous section, the existence of a 2DES at the surfaces or interfaces of $BaTiO_3$ and $CaTiO_3$ was demonstrated. These results show again that confined metallic states can be created at the surface/ interface of various insulating perovskites and are not unique to $SrTiO_3$. The ARPES results on the 2DES are summarized in the schematic drawings of the band dispersion in figure 6.8 on page 121 and in table 6.1 on page 120. The differences in the electron structure will be discussed in the next paragraphs.

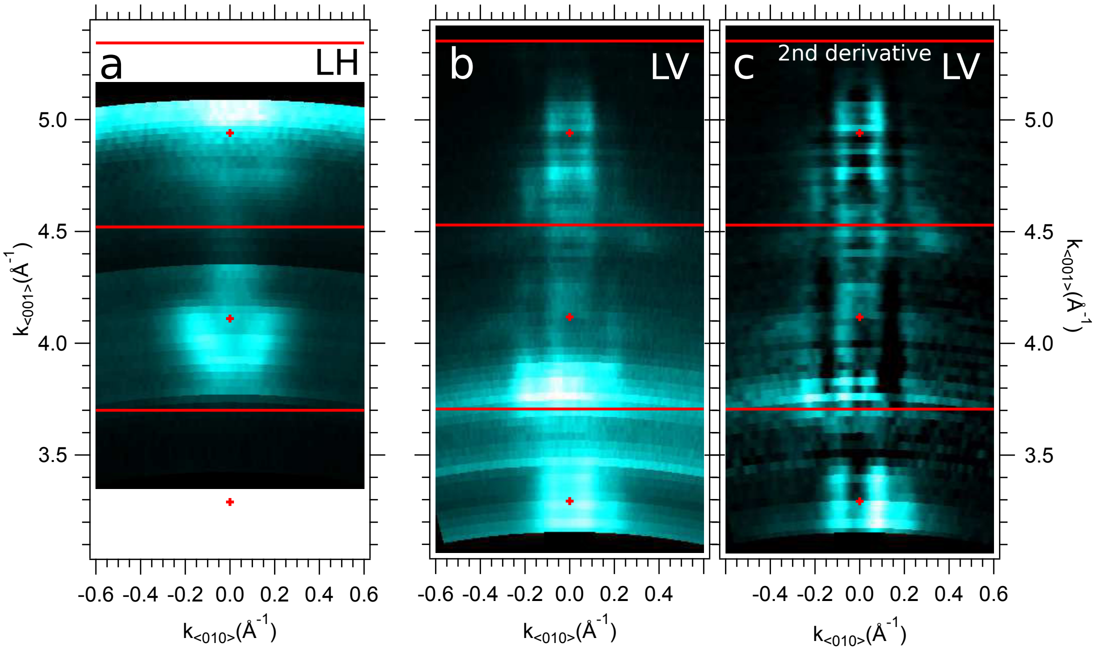

Figure 6.7: 2DES in CaTiO$_3$. (a) Fermi surface map in the $k_{\langle 001\rangle} - k_{\langle 010\rangle}$ plane measured by changing the photon energy between $h\nu = 37$ eV and $h\nu = 90$ eV using LH polarization. (b) FS map with photon energies ranging between $h\nu = 30$ eV and $h\nu = 100$ eV using LV polarization. (c) Same as (b) but based on 2^{nd} derivatives of the energy momentum maps. The red lines show the Brillouin zone border of the orthorhombic lattice and the red markers correspond to Γ points of the reciprocal lattice. All measurements were conducted at temperatures ranging between $T = 7 - 20$ K.

Table 6.1: Summary of parameters of t_{2g} bands forming the 2DES at the surface of CaTiO$_3$, SrTiO$_3$ and BaTiO$_3$. The size of the A-site cation and the lattice symmetry are given in the first two rows. The effective masses m^* (in units of the free electron mass) of the d_{xy} and d_{xz},d_{yz} bands are given in the next two rows. In the next four rows, the binding energies of the band bottoms of the bands $E_{t_{2g}}$ are given as well as the energy difference between the two d_{xy} subbands $\Delta E_{d_{xy}}$. Finally, the electron density n_{2D} of the 2DES is given in the last row.

	CaTiO$_3$	SrTiO$_3$	BaTiO$_3$
size A-site [Å]	1.12	1.26	1.42
phase at RT	orthorhombic	cubic	tetragonal
$m^*_{d_{xy}}$	1.1	0.7	$\approx 0.3^a$
$m^*_{d_{xz},d_{yz}}$	2.7	6 - 8	8 - 12
$E_{d_{xy},1}$ [meV]	158	223	120 - 180
$E_{d_{xy},2}$ [meV]	27	110	-
$\Delta E_{d_{xy}}$ [meV]	131	113	-
$E_{d_{xz,yz}}$ [meV]	62	50	115
orbital order	$d_{xy} - d_{xz,yz} - d_{xy}$	$d_{xy} - d_{xy} - d_{xz}, d_{yz}$	$d_{xy} - d_{xz}, d_{yz}$
n_{2D} [10^{14}cm^{-2}]	1.2	1.4	2.8 ± 0.4

[a] The light effective mass in BaTiO$_3$ is estimated based on $E_{d_{xz,yz}}$ and the Fermi momenta along the minor axis of the ellipsoidal Fermi surface.

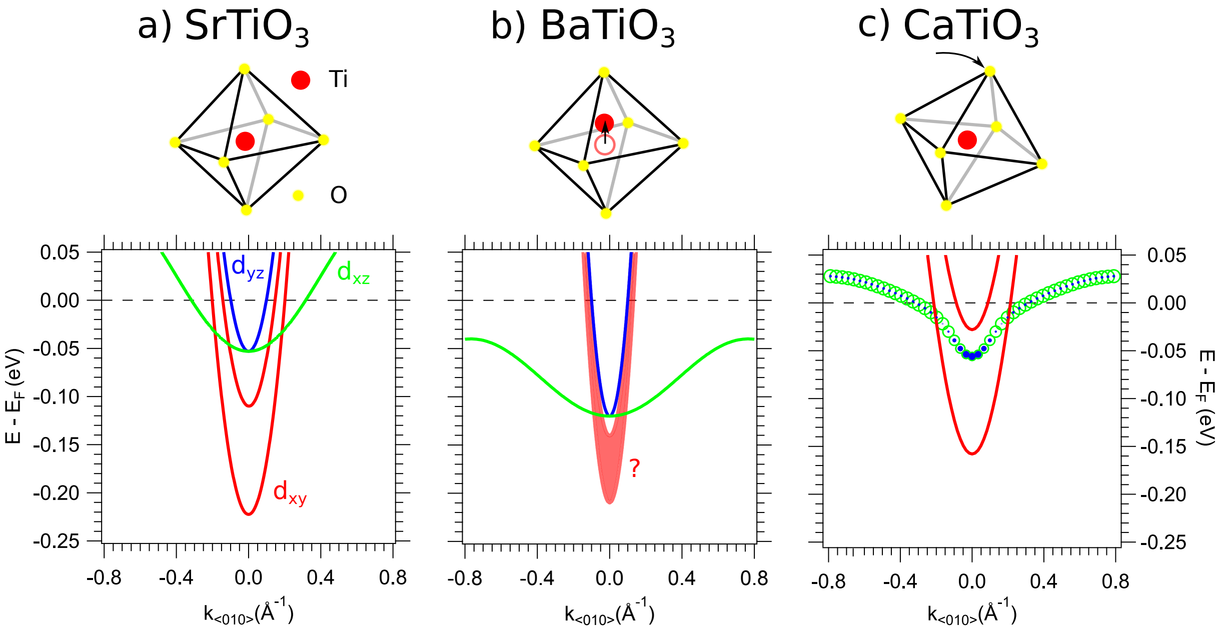

Figure 6.8: Oxygen octahedron in ATiO$_3$ (A=Sr,Ba,Ca) perovskites and schematic of band dispersion observed in the 2DESs in SrTiO$_3$ (a), BaTiO$_3$ (b) and CaTiO$_3$ (c). The broad red band and the question mark in (b) indicate that the band structure of the d_{xy} band was not determined precisely in BaTiO$_3$. The colors of the bands corresponds to different orbital characters. The size of filled and empty markers in (c) represent the fraction of the d_{xz} (green) and the d_{yz} (blue) in the band dispersion.

Effective masses m^*

The effective mass of the d_{xy} orbital is larger by a factor of 1.6 in CaTiO$_3$ compared to SrTiO$_3$. This change can be understood in the simple picture that the rotation of the oxygen octahedra decreases the orbital overlap of the d_{xy} orbitals an thus, decreases the Ti d bandwidth. [257] This reduced bandwidth or respectively, increased density of states was related to a more robust ferromagnetism at the LaAlO$_3$/CaTiO$_3$ interface compared to the LaAlO$_3$/SrTiO$_3$ interface although the driving force for the magnetic order are the d_{xz}, d_{yz} not the d_{xy} orbitals. [256] Due to the orbital mixing of the d_{xz}, d_{yz} bands, $m^*_{d_{xz,yz}}$ is a factor of about 3 smaller close to Γ but larger off-Γ as seen by comparing figures 6.8(a,c). This demonstrates that the octahedra rotations influence the effective masses up to a factor of 3. These insights are also of relevance for SrTiO$_3$-based interfaces, as rotations of octahedra can occur at the interface. [257–259]

In BaTiO$_3$, it was not possible to directly determine the effective mass $m^*_{d_{xy}}$ due to the broad band dispersions. In bulk BaTiO$_3$, the lattice constant is about 0.1 Å larger than in SrTiO$_3$. This increased atomic distance should result in an increased m^* or respectively, decreased band width. However, the in-plane lattice constant at the surface of the strained BaTiO$_3$(001) film lies in between the bulk value and the one of the substrate (SrTiO$_3$) depending on the thin film thickness. The effective mass of the heavy bands d_{xy}, d_{yz} is slightly increased $m^*_{d_{xy},d_{yz}}(\mathrm{BaTiO_3}) \approx 1.4 m^*_{d_{xy},d_{yz}}(\mathrm{SrTiO_3})$ compared to SrTiO$_3$.

Orbital order

As discussed in previous chapters (*e.g.* chapter 5), the orbital order is mainly determined by the effective mass along the confinement direction m_z^*. The orbital mixing in CaTiO$_3$ influences $m^*_{d_{xz,yz}}$ in the surface plane as discussed in the previous section. This hybridization will also influence m_z^* of this band and thus, the orbital order. Consequently, as seen in figure 6.8 and summarized in table 6.1, the hybridized band in CaTiO$_3$ is in between two d_{xy} subbands (in contrast to the $d_{xy} - d_{xy} - d_{xz}, d_{yz}$ order in SrTiO$_3$).
Contrary to the orbital order in SrTiO$_3$ and CaTiO$_3$, no 2^{nd} d_{xy} subband can be observed in BaTiO$_3$. Another difference is that the heavy band is at higher binding energies (see figure 6.8) compared to the other two perovskites. As the d_{xy} subband is difficult to characterize in our ARPES measurements, a more detailed discussion of the orbital order in BaTiO$_3$ is omitted.
The orbital order in the 2DES at the LaAlO$_3$/SrTiO$_3$ interface is essential to understand its properties. [209] Many of the unusual phenomena at this interface are related to the Lifshitz transition occurring at electron densities at which the heavy bands d_{xz}, d_{yz} start to be populated. [260, 261] New insights in these properties (*e.g.* magnetism) could be gained by studying this transition in similar interfaces based on CaTiO$_3$ and BaTiO$_3$ (*e.g.* AlO$_x$/ATiO$_3$ interfaces based on Al evaporation as discussed in section 4.2).

Electron densities n_{2D}

Whereas the electron densities are rather similar in CaTiO$_3$ and SrTiO$_3$ (factor of 1.2), n_{2D} in BaTiO$_3$ is at least twice as large compared to the other oxides. The ferroelectric polarization in mono-domain BaTiO$_3$ thin films is in upward direction, *i.e.* towards the surface. [253] The resulting electric field will influence the confining electric field of the 2DES and thus, the electron density can be altered. Hence, in principle, n_{2D} can be controlled by the polarization in the thin film. One possibility to change the amplitude or direction of the polarization of the thin film is by choosing different substrates [253] or by applying strain gradients [262].

This chapter demonstrated that 2DESs can be created at the surface or interfaces of various ATiO$_3$ perovskites. The electronic structures obtained by ARPES on 2DESs of three oxides (A=Sr,Ba,Ca) were compared and differences identified. The next chapter will focus again on the 2DES in SrTiO$_3$. But, whereas this chapter was motivated by the dielectric properties of solids, the following chapter is dedicated to magnetism and other spin-related phenomena.

Chapter 7

Search for spin polarization in a doped d^0 oxide: $\mathrm{SrTiO_3}$

In this manuscript, the characterization of electrons in solids using ARPES was so far discussed in terms of binding energy and momentum of the electron. This is sufficient if the Hamiltonian of the electron in the solid is invariant to inversion and time reversal:

- If the crystal lattice has an inversion symmetry the eigenstates of the energies of the electron are degenerate for momenta of opposing sign $E(\vec{k},\uparrow) = E(-\vec{k},\uparrow)$.
- If the Hamiltonian is invariant to time reversal, the bands of opposing spin and momenta are degenerate $E(\vec{k},\uparrow) = E(-\vec{k},\downarrow)$.
- These two equation yield thus, that the bands are degenerate in spin: $E(\vec{k},\uparrow) = E(\vec{k},\downarrow)$.

However, if either inversion or time reversal symmetry are broken (*e.g.* at the surface of a crystal $\equiv$ surface Rashba effect or due to a magnetic field $\equiv$ Zeeman effect), bands of opposing spins are split in energy. Prominent examples are Rashba systems [263] and topological insulators [264] which have potential applications in the field of spintronics [265].

The discussion based on the invariance of the Hamiltonian demonstrates under what criteria bands of opposing spin are split in energy. However, it is insufficient to deduce quantitative information. In this chapter I will focus on spin-related effects in doped d^0 or d^{10} transition metal oxides, starting with a short review of d^0 magnetism.

7.1 Diluted magnetic oxides and d^0 magnetism

Introduction to diluted magnetic oxides

ZnO and $\mathrm{TiO_2}$ have been model systems to study ferromagnetism in diluted magnetic oxides. In these systems, magnetic dopants (*e.g.* Mn) are diluted into the bulk material, resulting in localized magnetic moments. However, to understand the collective magnetic response, the consideration of only these (isolated) localized magnetic moments (*i.e.* Langevin paramagnetism) is not sufficient. The concentration, type and spatial distribution of magnetic extrinsic dopants, intrinsic defects and itinerant charge carriers all influence the magnetic properties. Although there is a huge number of studies and reviews [266–271] the understanding and control of the magnetism in these systems is still far from complete and reproducibility is often problematic. One major complication is the variation of the preparation method of the studied crystals: thin films grown using different techniques, growth parameters and substrates (see review by Pan *et al.* [268]) as well as nanostructures (see *e.g.* [272–274] for observation of ferromagnetism in 2D, 1D, 0D nanostructures) all show magnetic order under specific conditions. Additionally, magnetism is related to grain boundaries [275, 276], interfaces[68] and surfaces[277]; one possible explanation is the accumulation of point defects which are energetically favorable at interfaces [158, 278, 279]. A review of different theoretical models proposed to explain the magnetic order in diluted magnetic oxides is given by Dietl. [280]

d^0 or d^{10} magnetism in $SrTiO_3$, TiO_2 and ZnO

As we study single crystals of transition metal oxides which are not diluted with other transition metals (except impurities introduced in the growth process of the single crystal), I will focus on the so called d^0-magnetism due to intrinsic defects. As one of the major topics of this thesis is the creation of oxygen vacancies close to the surface of band insulating TMOs and the role of oxygen vacancies is discussed in many papers related to diluted magnetic oxides, I will discuss briefly the literature on oxygen deficient single crystals and thin-films of $SrTiO_3$, TiO_2 and ZnO. Note that many studies also exist on the role of oxygen vacancies in diluted transition metal oxides (see reviews cited above). Those studies will not be discussed.

The first observation of d^0 magnetism was made in HfO_2 thin films and attributed to intrinsic defects of the thin film. [281, 282] These results were contested later by Abraham *et al.* who did not find any magnetism in HfO_2 thin films and argued that a contamination by handling samples with stainless steel tweezers can lead to the magnetic signal.[283] Note that most of the experimental studies cited in this introduction were conducted using a superconducting quantum interference device (SQUID) magnetometer to measure the magnetization curves as a function of applied magnetic field. While these measurements are sensitive to very small magnetic moments, the macroscopic characterization of systems potentially exhibiting d^0 magnetism has major drawbacks. For example, it is difficult to differentiate between the magnetic contributions of impurities (*e.g.* Fe, Co, Ni) and intrinsic magnetic moments. Additionally, as already mentioned, surfaces, interfaces and grain boundaries might be at the origin of the magnetism. Hence, a direct characterization of magnetic moments at these interfaces on the nanoscale would give new insights. Spectromicroscopic, surface sensitive photoemission experiments as discussed in section 7.2 can overcome some of these drawbacks.

TiO_2 thin films

Ferromagnetism has been observed in thin films of oxygen deficient TiO_2 on $LaAlO_3$. [284–286] In all three studies the magnetic properties depend on the oxygen partial pressure during film growth and/ or on post-growth annealing in oxygen-rich atmosphere. The magnetization increases with decreasing thickness of the deposited films which indicates that oxygen-vacancies at the $TiO_2/LaAlO_3$ interface are the main contributor to the magnetic properties. [284, 285] The magnetic ordering is estimated to be stable up to a temperature of $T = 880$ K. [285] Again, extreme care has to be taken handling the samples: Golmar *et al.* measured a ferromagnetic signal due to Ag paint attached to the $LaAlO_3$ substrate used for thin film growth. [287]

$SrTiO_3$ single crystals

Liu *et al.* studied the room-temperature ferromagnetism in Nb-doped $SrTiO_3$ single crystals. [40] They did a systematic study of the magnetism depending on the concentration of oxygen vacancies as well as Nb dopants. The ferromagnetism can be controlled by annealing the samples either in air or in UHV indicating the essential role of oxygen vacancies in the magnetism. The magnetization can be significantly reduced by low-temperature ($T = 250$°C) annealing in air for 30 min. As oxygen diffusion under this conditions is spatially very limited, the origin of the magnetism seems to be related to the near-surface region. The magnetization scales with the concentration of Nb dopants for samples with a similar concentration of oxygen vacancies indicating that free electrons donated by Nb atoms enhance the magnetism.

Potzger *et al.* also identified oxygen vacancies induced by vacuum annealing or ion irradiation as the source of a (weak) ferromagnetism in $SrTiO_3$. [288] The creation of oxygen-deficient second phases by annealing at too high temperature or too intense ion irradiation result in the disappearance of the ferromagnetism. Contrary to the study of Liu *et al.*, they did not observe a correlation between electric conductivity (free electrons) and the intensity of the ferromagnetic signal.

Crandles *et al.* did not find any ferromagnetism in strongly reduced $SrTiO_{3-\delta}$ samples with polished surfaces questioning the role of oxygen vacancies regarding ferromagnetism. [289] However, they measured a ferromagnetic signal for samples with unpolished surfaces, probably because of iron contaminants introduced by the tools used to cut the grown single-crystal.

Khalid *et al.* studied the magnetic response of as-supplied single crystals of various nominally diamagnetic oxides (*e.g.* $SrTiO_3$).[290] They observe that all oxides have a similar ferromagnetic contribution which is probably not correlated to magnetic impurities. They suggest that the ferromagnetic mass is likely concentrated in the near-surface area.

Recently, J.M.D. Coey, M. Venkatesan and P. Stamenov studied two-side polished $SrTiO_3$ crystals as well as their ground powders. [291] Both, single crystals and powders were annealed in vacuum to create oxygen vacancies. The magnetic moments of the stoichiometric and oxygen-deficient samples were compared using SQUID magnetometry. As these researchers have abundant experience in the field of d^0 magnetism (discovery in thin films of HfO_2 [281] as well as several reviews [68, 292]), I will discuss this study in more detail.

To identify d^0 magnetism an understanding of the intrinsic bulk magnetism as well as the extrinsic magnetism due to unavoidable magnetic impurities is necessary. In insulating stoichiometric $SrTiO_3$, there are no unpaired spins as all electronic shells are fully occupied. Thus, the intrinsic magnetic response is a mixture of Larmor diamagnetism and Van Vleck paramagnetism resulting in a magnetic susceptibility of about $\chi_{mag} = -6.5 \times 10^{-6}$ (or a magnetization of about 5 Am^{-1} at a magnetic field corresponding to 1 T).

During the growth process and surface polishing of $SrTiO_3$, magnetic impurities (*e.g.* Fe, Co, Ni) are introduced in the system yielding unpaired localized spins. Usually, the concentration of these paramagnetic impurities is smaller than 1 ppm, but is highly dependent on the supplier of the $SrTiO_3$ crystals with differences as large as one order of magnitude. The resulting Langevin-paramagnetism corresponds to a saturation magnetization $M_S^{ex,para} = c\,\mu_{eff} \approx 0.9\ Am^{-1}$ where c is the concentration of magnetic impurities (assumed to be every millionth unit cell) and $\mu_{eff} = 5.9\mu_B$ the effective magnetic moment for Fe^{3+} ions. For samples with an impurity concentration larger than 1 ppm, the magnetic moment due to this paramagnetism can be comparable to the intrinsic bulk magnetism at low temperatures $T = 4$ K. Additionally, the polishing process can result in ferromagnetic inclusions at the surface of $SrTiO_3$ yielding a typical magnetic saturation of about $M_S^{ex,ferro} = 0.75\ Am^{-1}$ averaged over the volume of the sample (value is sample dependent). The magnetic contributions discussed so far are independent of the shape of the sample (single crystal or powder) or the oxygen stoichiometry (UHV annealed or not).

However, Coey et al also identified an intrinsic high temperature surface magnetism which can be increased by grinding the samples to powder (increase of surface area) or/and by annealing in vacuum (creation of oxygen vacancies). To reduce the increased magnetism, annealing in oxygen or immersion of $SrTiO_3$ in solvents can be used which indicates surface defects, probably oxygen vacancies, as origin of the magnetism. This anhysterectic "ferromagnetism" with an estimated Curie temperature larger than 1000 K can exhibit a saturation magnetization averaged over the volume of the sample larger than $M_S^{in,surface} = 6\ Am^{-1}$ in UHV annealed powders of $SrTiO_3$ (equivalent to approximately 1 μ_B per surface unit cell). Thus, this intrinsic saturation magnetization exceeds the extrinsic effects $M_S^{in,surface} > M_S^{ex,para} \approx M_S^{ex,ferro}$. Possible explanations for such a surface magnetism will be discussed in the next section.

Similar to the studies on $SrTiO_3$ and TiO_2, there are several studies relating oxygen vacancies to magnetism in ZnO thin films [275, 293–296].

Interfaces and surfaces

Many of the studies presented above stress the importance of surface or interfaces as the magnetic moments seem to be localized close to them. Another indication for the essential role of the surface is the observation of magnetism in nanoparticles of TMOs [297] which have a large surface to bulk ratio.

Various photoemission studies on oxygen-deficient $SrTiO_3$ and TiO_2 anatase demonstrated that the excess electrons due to oxygen vacancies is of dual character: localized electrons at the site of a Ti ion and itinerant electrons. Although the dual character of the excess electrons, doped $SrTiO_3$ and TiO_2 are usually not seen as a correlated materials. But to understand magnetism, electron correlation effects might be essential, as suggested by recent DFT+DMFT calculations. [298, 299] In fact, there are numerous recent studies based on density functional calculations dealing with the magnetism in bulk [300, 301] as well as surfaces and interfaces of

$SrTiO_3$ [163, 302, 303]. Note that in the case of the interface of $LaAlO_3/SrTiO_3$, various mechanisms not-related to oxygen vacancies have been proposed for the emergence of magnetism [256, 304–306]

Although the theoretical *ab-initio* studies mentioned above predict a magnetic ground state, conventional models fail to explain the observed magnetism especially if the Curie temperature of the surface magnetism is of the order of $T_C = 900 - 1000$ K as predicted by Coey *el al.* [291] and measured by Taniuchi *et al.* [307] (these photoemission results are briefly discussed in the next section). One difficulty is the lack of knowledge on the precise distribution of the oxygen vacancies: are clusters or a random distribution energetically favorable ?

The dual character of excess electrons yields three basic possibilities to model magnetism: 1. magnetism due to localized electrons/ magnetic moments; 2. magnetism due to itinerant electrons; 3. magnetic exchange between localized magnetic moments mediated by itinerant electrons.

The concentration of oxygen vacancies in the surface region seems to be too low to explain the ferromagnetism due to Heisenberg exchange between localized moments. Even in the case of strongly reduced $SrTiO_{2.5}$, the exchange interaction would need to be unprecedentedly large to generate the high T_C [291]. Similar an indirect exchange interaction in which the coupling of the magnetic moments is mediated by the itinerant electrons has not yet resulted in a T_C close to 1000 K. In the diluted magnetic semiconductor Mn_xGe_{1-x}, Curie temperatures up to 285 K were observed due to the indirect RKKY interaction. [308, 309] Finally, a Stoner-type magnetism is unlikely as the density of states at the Fermi level is rather low in $SrTiO_3$ single crystals which were reduced by UHV annealing as conducted in the two studies reporting high T_Cs. Coey *el al.* proposed that Stoner magnetism might occur due to a partially filled impurity band at the Fermi level related to oxygen vacancies. [291] However, the photoemission results presented in section 3 demonstrate that the major part of the density of the states of the vacancy-induced in-gap states is far below (≈1 eV) the Fermi level.

This brief review highlights once again that oxygen vacancies play a crucial role in the determination of the properties of doped insulating transition metal oxides. However, the understanding of the origin of the magnetism is far from complete: what are the minimal requirements to induce magnetism in d^0 oxides? Are oxygen vacancies sufficient? Are interfaces, surfaces or grain boundaries essential? [276]

One technique to obtain information on the spin structure of electrons in solids is spin-resolved ARPES which will be presented next.

7.2 Spin-ARPES on $SrTiO_3$

This section gives a brief introduction to the technique of spin resolved-ARPES, and is mainly based on the reviews by H. Dil [310] and T. Okuda & A. Kimura [311].

To experimentally characterize the complex spin texture of ferromagnets, Rashba systems and topological insulators on a microscopic level, spin-resolved ARPES (SARPES) made major progress over the last two decades.

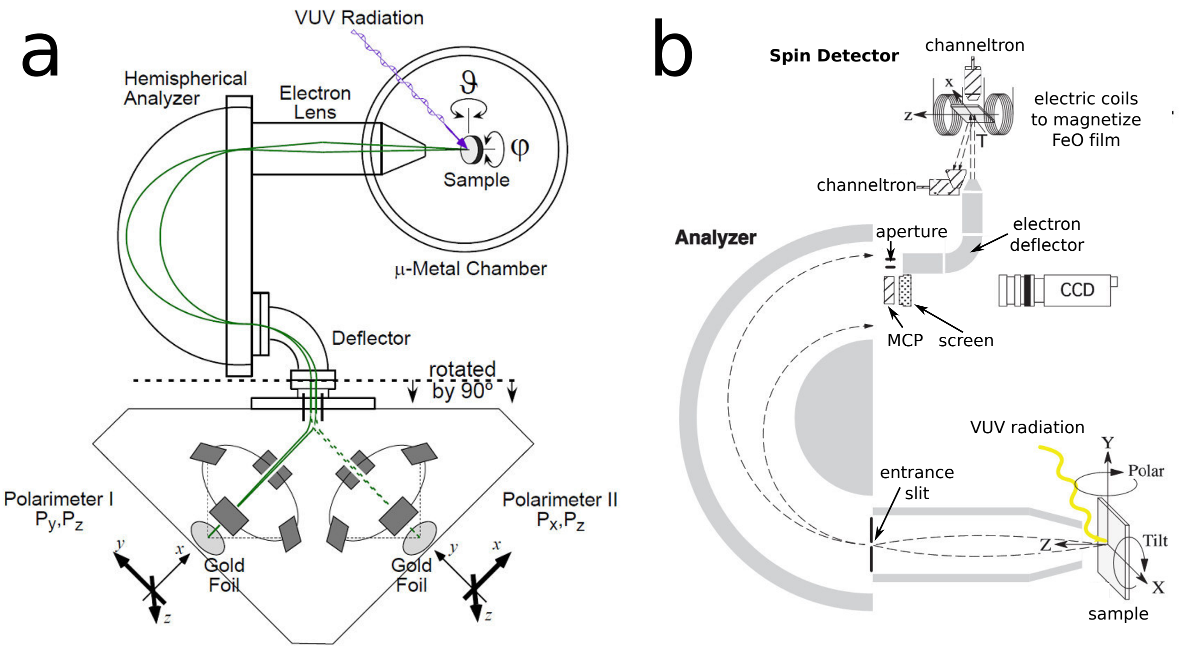

Figure 7.1: Experimental setups to conduct spin-resolved ARPES measurements (a) at the COPHEE machine at the Swiss light source [310] and (b) at the ESPRESSO machine at HiSOR synchrotron [314]. As in conventional ARPES, the selection of kinetic energy and angle of the photoelectron is obtained by using an electrostatic lens with a retarding potential and a hemispherical analyzer as discussed in section 2.1 (see figure 2.1). At the exit of the analyzer, the electrons are deflected to the spin detectors which are Mott detectors in (a) and VLEED detectors in (b). Both setups allow to measure all three components (x,y,z) of the spin polarization using two differently oriented spin detectors. Note that the second spin detector is not shown in the schematic in (b). Taken from [310, 314]

Nevertheless, SARPES is far from being a “plug & play” technique. In conventional ARPES, the photocurrent (see equation (2.9) on page 28) can be factorized into the spectral function times the matrix elements. The latter are governed amongst others by light polarization and photon energy. Hence, matrix elements can modulate the measured intensity but not alter the spectral function which is the entity the experimentalist wants to measure. In SARPES, final state effects depending on light polarization and photon energy can alter the spin polarization during the optical excitation of the photoelectron from its initial to its final state in the solid [312, 313] and thus, understanding of matrix elements is essential to interpret the measured data. However, there are not many theory groups working on the calculations of (S)ARPES matrix elements compared to the number of experimental studies.

Spin detection

In the framework of this thesis, the spin of the photoelectrons was detected using two different spin detectors. The setup of the SARPES analyzer at the Swiss Light Source and at HiSOR Synchrotron are shown in figure 7.1 on page 128. Spin detection of electrons is quite challenging and detection efficiencies are rather low (ranging from 1×10^{-4} to 2×10^{-2}) [311] and thus, far below of an ideal Stern and Gerlach-type spin separation of spin polarized, charge neutral particles. Note that using magnetic fields, as in the Stern-Gerlach apparatus, is not possible in SARPES, as the Lorentz force would alter the electron trajectory and "scramble" the momenta of the electrons. Instead, the mechanism of spin separation in SARPES is based on spin-dependent electron scattering using *e.g.* Mott or very low energy electron diffraction (VLEED) spin detectors.

The Mott detector in the COPHEE machine is based on the spin dependent scattering of electrons of high kinetic energy (≤25 kV) from heavy nuclei (*e.g.* gold atoms). Two opposing channeltrons (see figure 7.1) detect the partially spin polarized electrons after the scattering process. The spin selection in the VLEED detector in the ESPRESSO machine is based on the scattering of the photoelectrons at a Fe(001)-p(1 × 1)-O film grown on a MgO(001) substrate. The scattering mechanism is very sensitive to the condition of the surface (contamination, reconstruction, ...). Hence, regular and reproducible preparation of the film are necessary and consequently, the spin detection chamber is connected to a UHV chamber dedicated to the preparation of the film. Before hitting the FeO film, the kinetic energy of the electrons is regulated to $E_k \approx 6$ eV yielding the highest efficiency. After scattering, the intensity of the electrons is detected using a channeltron. The spin asymmetry of the electron beam is measured by switching the magnetization of the of FeO film. Here, the asymmetry A describes the spin asymmetry of the photoelectrons after the spin selective scattering process:

$$A = \frac{I_a - I_b}{I_a + I_b} \tag{7.1}$$

where I_a and I_b are the intensities measured at the channeltron using opposing magnetizations of the FeO film (VLEED) or the intensities of two opposing channeltrons (Mott). Due to the inefficient spin detection, the spin polarization P of the photoelectrons can be much larger than the asymmetry of the scattered electrons:

$$A = SP \quad \text{with} \quad P = \frac{I_\uparrow - I_\downarrow}{I_\uparrow + I_\downarrow} \tag{7.2}$$

where S is the energy dependent Sherman function and $I_\uparrow$ & $I_\downarrow$ are the spin populations of opposing spin. Using the previous equation, the spin up and spin down populations can be obtained:

$$I_\uparrow = \frac{1 + A/S}{2} I \quad \text{and} \quad I_\downarrow = \frac{1 - A/S}{2} I \quad \text{with} \quad I = I_\uparrow + I_\downarrow \tag{7.3}$$

To measure the spin polarization vector $P = (P_x, P_y, P_z)$, all three components need to be measured. Using one Mott detector one can measure simultaneously two components using two perpendicular pairs of opposing channeltrons. Using a VLEED detector, two pairs of electric coils can magnetize the FeO film in perpendicular directions yielding again two components. To obtain the third component, a second spin detector of different spatial orientation is necessary.

To normalize the measured intensity between the two detectors, both detectors measure one common component.

Insights from photoemission at the surface of oxygen deficient $SrTiO_3$

The observed band structure of the 2DES at the surface of $SrTiO_3(001)$ can be modeled by assuming an electron confinement in a triangular potential well as discussed in section 1.2. Hence, neither magnetism nor any other spin-related effects (*e.g.* spin-orbit coupling) are necessary to explain the essentials of the observed band dispersions of the 2DES.

One reason is that atomic spin-orbit coupling is rather small in $SrTiO_3$ as titanium is a relatively light element. The spin splitting due to atomic spin-orbit coupling in the 2DES is predicted to be up to 18 meV at the crossing point of the d_{xy} with the d_{xz}, d_{yz} bands [216] which has not yet been observed experimentally in ARPES. In contrast, the tantalum atom is heavier by a factor of about 3.8 and thus, spin-orbit coupling is much larger. Consequently, the band structure of the 2DES at the surface of $KTaO_3$ measured by ARPES can only be understood taking into account spin-orbit coupling. [3, 8]

As the 2DES is confined by an electric field at the surface, there is also a Rashba-type spin splitting. In the reference system of the electron moving in the surface plane, this confining field corresponds to a magnetic field which results in a momentum dependent splitting of the bands structure into two spin polarized bands. Assuming that the confining electric field of $F \approx 100$ MVm^{-1} determines the splitting, the predicted splitting should be small: about 6 $\times 10^{-3}$ Å^{-1} at the Fermi level due to confining electric field. [12] Note that the Rashba formalism will not be discussed in this thesis.

To sum up the last two paragraphs, the electronic structure measured by spin-integrated ARPES and a simple Rashba model do not indicate the presence of a large splitting in the band structure of the 2DES at the surface of $SrTiO_3(001)$. However, both the discussion on d^0 magnetism and the observed magnetism at the interfaces of $LaAlO_3/SrTiO_3$ [22, 24, 25, 41, 163, 315] and $Al_2O_3/SrTiO_3$ [316] cast doubt on this conclusion. Additionally, as shown in figure 7.2 on page 131, Caviglia *et al.* showed that the size of the Rashba splitting (maximal 10 meV in their study) can be controlled by a gate voltage or respectively the electron density in the 2DES at the $LaAlO_3/SrTiO_3$ interface. [317] The influence of the electron density (proportional to the square of the Fermi momenta $\propto k_F^2$) is emphasized by the finding of a cubic (instead of linear) Rashba effect, *i.e.* the Rashba splitting is proportional to the third power of the momentum $\propto k^3$. [318, 319] As shown in figure 7.2(c), the phase diagram in the study of Wang *et al.* [17] indicates that electron densities in the 2DES at the surface of $SrTiO_3$ can be larger (up to factor of 10) compared to the $LaAlO_3/SrTiO_3$ interface. Hence, large Rashba splittings (>> 10 meV) can be possible based on the comparison of figures 7.2(b,c).

Recent spin-resolved photoemission experiments

The spin resolved ARPES (SARPES) measurements on the 2DES at the $SrTiO_3(001)$ surface conducted by our group in cooperation with one of the photoemission groups at the SLS re-

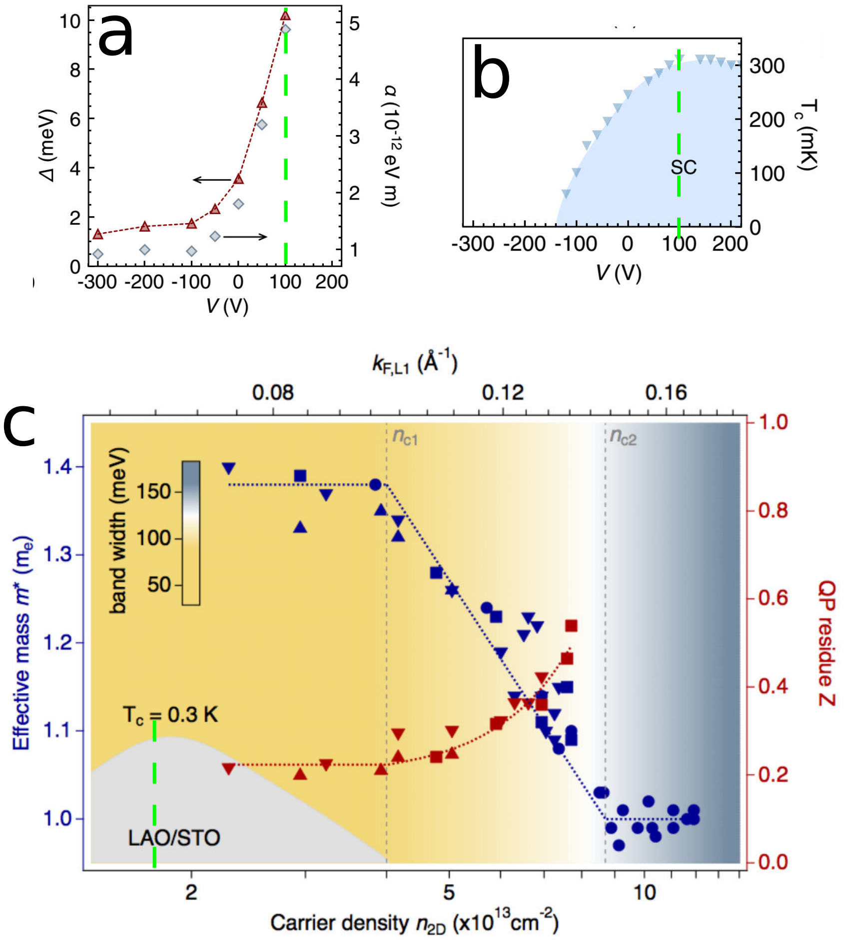

Figure 7.2: (a,b) Transport measurements of the 2DES at the $LaAlO_3/SrTiO_3(001)$ interface conducted by Caviglia *et al.* [317] (a) Tunability of the Rashba splitting in energy Δ ranging from about 2 meV to 10 meV and the Rashba constant α as a function of gate voltage V. The gate voltage V determines the electron density n_{2D} in the 2DES but it is difficult to simultaneously measure both. To correlate the gate voltage with the electron density n_{2D} of the 2DES at the $LaAlO_3/SrTiO_3(001)$ interface and at the $SrTiO_3(001)$ surface, we use figures (b) and (c). (b) Critical temperature T_C as a function of gate voltage V showing the superconducting dome of the same $LaAlO_3/SrTiO_3(001)$ sample as in (a). [317] (c) Phase diagram proposed by Wang *et al.* showing the effective mass m^* of the d_{xy} band as a function of electron density of the 2DES at the surface of $SrTiO_3$ measured by ARPES. [17] The superconducting dome as function of electron density was deduced from transport studies at the $LaAlO_3/SrTiO_3$ interface. The maximum critical temperature T_C at the $LaAlO_3/SrTiO_3(001)$ interface is at an electron density of $n_{2D} \approx 2 \times 10^{13}$ cm^{-2} which is one order of magnitude lower than the densities observed at the $SrTiO_3$ surface. By comparing figures (a),(b) and (c) (see green dashed line to compare electron densities) one can reason that the Rashba splitting at an electron density of $n_{2D} \approx 2 \times 10^{14}$ cm^{-2} should be much larger than 10 meV.

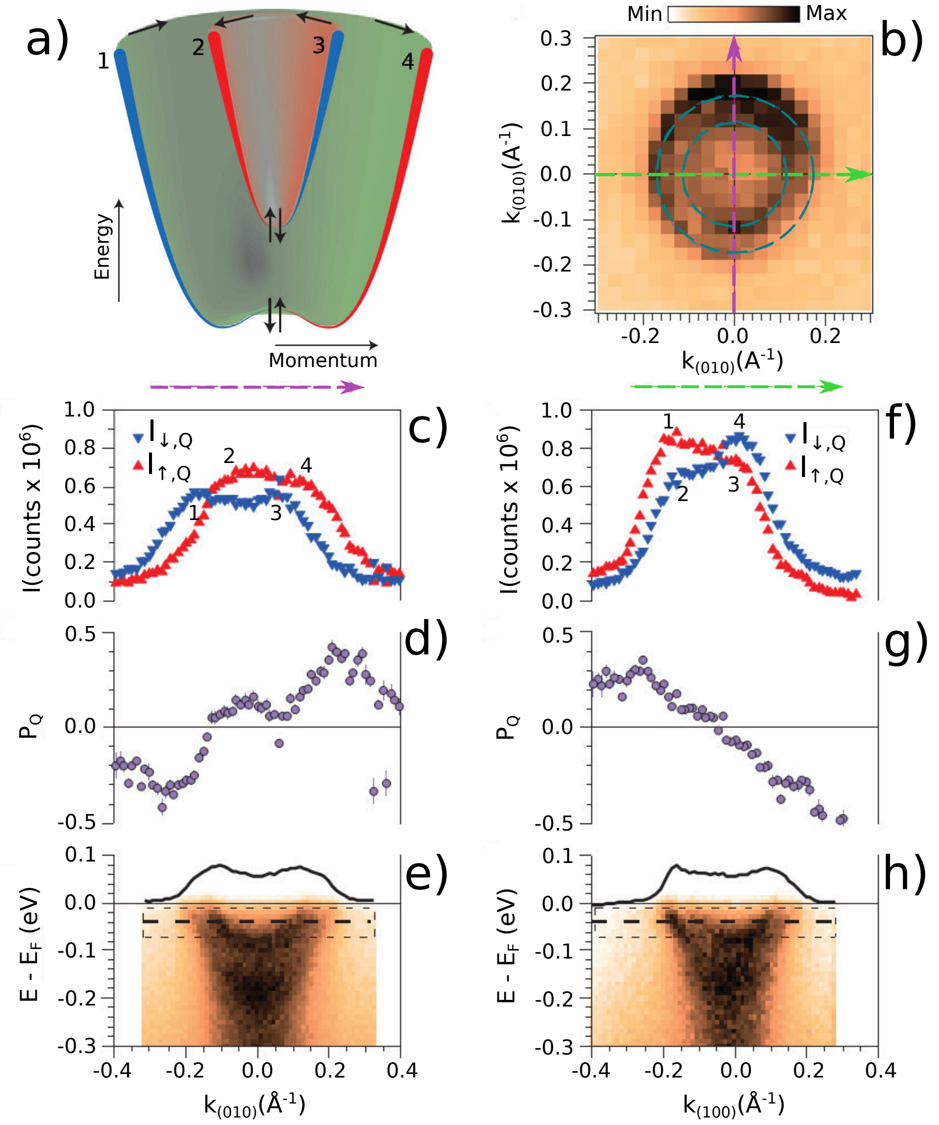

Figure 7.3: (a) Schematic representation of the spin-split d_{xy} subbands at the surface of SrTiO$_3$. A number is assigned to each of the subband branches. The two subbands are separated by an energy gap of about 100 meV for all momenta from $k = 0$ to k_F. Each subband is spin-polarized, with spins winding in opposite directions for opposite momenta at a given binding energy. This is depicted by the arrows and the red and blue hues in different subband branches. For each band, the measured in-plane spin polarization decreases as one approaches the bottom of the band, and is schematically represented by the width of the parabola. (b) ARPES Fermi surface map of the 2DES at the surface of SrTiO$_3$(001). The dashed blue circles are guides to the eye for the two Fermi surfaces generated by the light parabolic subbands. (c) Spin-MDC: spin-resolved populations of spin-up $I_\uparrow$ and spin-down $I_\downarrow$ electrons around the Fermi level E_F with respect to the local quantization axis Q and as a function of electron momentum along (010). At the Fermi level E_F, the direction of the local quantization axis Q is approximately the direction tangential to the circular Fermi surfaces. The numbers 1-4 correspond to the different branches in (a). (d) Resulting angle-resolved spin polarization P around E_F along Q.(e) Energy-momentum intensity map along (010), violet dashed arrow in (b), showing the two light d_{xy} subbands. The dashed rectangle and bold line in this and other figures indicate the Gaussian energy broadening and energy setting for the SARPES measurements. The black curve on top of the color plot is the ARPES momentum distribution curve (MDC) integrated over the dashed rectangle. (f-h) same as (c-e) along the orthogonal momentum direction (100), green dashed arrow in (b). All data in this figure were measured at T= 20 K. Taken from reference [12].

vealed a complex spin texture and implied a giant spin splitting, which was interpreted as to be present due to both magnetism and a Rashba-type like interaction. [12] The spin splitting at the Fermi level observed in this study is shown in figure 7.3 on page 132. Note that later on, we will compare these results to the ones obtained with a different SARPES setup. To clearly differentiate between the different results, I will refer to the already published findings obtained at the SLS using the term "results by Santander *et al.*".

The observation of the giant Rashba-like splitting of the two d_{xy} subbands of approximately 0.1 Å^{-1} at the Fermi level is in strong contrast with the small expected value of 6 $\times 10^{-3}$ Å^{-1} (factor of 17) and was justified by an enhancement due to surface corrugations. Such an enhancement of the Rashba splitting was previously observed, both experimentally and theoretically, at metal surfaces [320–322]. Note that the splitting of the heavy bands (d_{xz}, d_{yz}) was not discussed in this study. However, so far other SARPES experiments [323] (and results shown in section 7.2) struggled to reproduce the results of this complex spin-texture. Similarly, theoretical papers motivated by the SARPES results presented different conclusions. [302, 324, 325].

New insights on the magnetism were gained by Taniuchi *et al.* who imaged ferromagnetic domains of typical sizes of approximately 40 nm at the oxygen-deficient surface of $SrTiO_3$(001) using laser-based photoemission electron microscopy (laser-PEEM) as summarized in figure 7.4 on page 134. [307] In this study the Curie temperature was estimated to be 900 K and thus, far above room temperature. The orientation of the magnetic polarizations in the different domains seems to be rather random although the direction of the magnetic polarization cannot be determined exactly using this experimental technique. This study was based on the collaboration between the group of S. Shin - notably T. Taniuchi - at the Institute of Solid State Physics at the University of Tokyo and our group. As already discussed in previous chapters, light (probe in photoemission experiments) can alter the properties of $SrTiO_3$, including its magnetic properties. [78, 326]

Compared to the SQUID studies discussed in section 7.1, laser-PEEM has the major advantages of surface sensitivity and imaging of magnetic domains with a spatial resolution on the nanoscale. However, with this technique the magnetic moments cannot be quantified (even though the measured asymmetry is proportional to the magnetic moment no absolute values can be assigned as the factor characterizing the photoexcitation process is unknown) and the concentrations of oxygen vacancies and itinerant electrons at the surface are unknown. Note that spot size of the UV probe in SARPES measurements is of the order of at least tens of µm and hence, one always averages over many magnetic nanodomains. Consequently, the contribution of ferromagnetic nanodomains with random orientation of the magnetic moment to the spin polarization cannot be measured using SARPES.

Contradicting results: SARPES at HiSOR synchrotron

The results presented below were obtained using the ESPRESSO machine at the HiSOR synchrotron on Al(2Å)/$SrTiO_3$(001) interfaces, as the UV light brilliance at HiSOR is not large enough to induce a sufficient concentration of oxygen vacancies to create the 2DES (see section

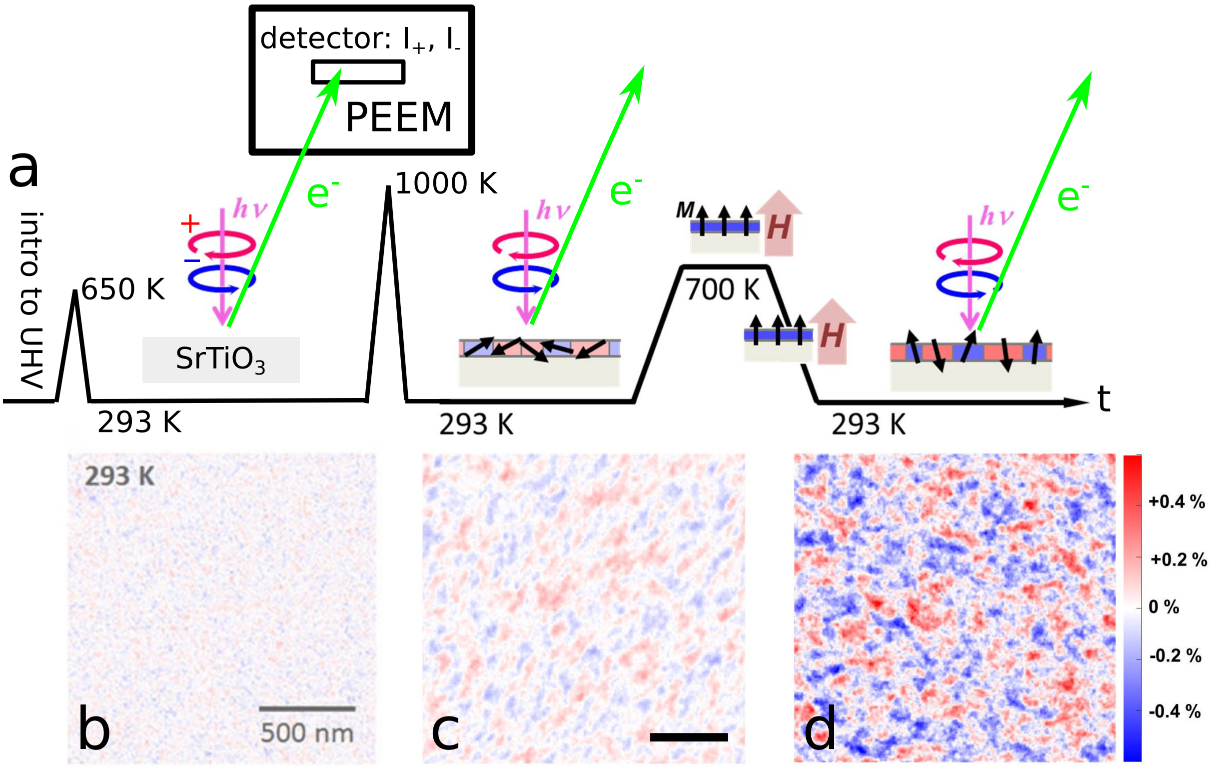

Figure 7.4: (a) Procedures (annealing, PEEM measurement and application of a magnetic field H) applied to a TiO_2-terminated $SrTiO_3(001)$ sample after introducing it into the UHV system. The detection of magnetic domains is based on the circular dichroism of the photoemitted conduction band electrons excited by a laser with photons of $h\nu = 4.7$ eV. The circular dichroism CD is defined as the asymmetry of the intensity of the photoelectrons emitted using circular polarized light - clockwise I_+ and counter-clockwise I_-: $CD = (I_+ - I_-)/(I_+ + I_-)$. The CD signal can be proportional to the magnetic moments in the solid. In contrast to the other photoemission techniques used in this thesis, the use of a laser-PEEM yields spatially-resolved spectroscopic data with a resolution of 2.6 nm. (b) After annealing the $SrTiO_3$ sample at $T = 650$ K, no magnetic domains can be seen in PEEM-CD image. The color map corresponds to the CD value defined by the scale bar at the right side of (d) (*e.g.* white means CD=0). (c) However, an annealing at higher temperatures $T = 1000$ K cleans the surface of organic contamination and creates oxygen vacancies which result in the appearance of magnetic domains. To correlate the observed CD to magnetism a magnetic field at temperatures close to the Curie temperature is applied. Consequently, an increased CD signal can seen in the PEEM-CD image in (d). All PEEM measurements were conducted at room temperature. Taken and adapted from reference [307].

3.2). The SARPES results obtained by Santander *et al.*, discussed in the previous section, were obtained at the COPHEE machine at the Swiss Light Source SLS on bare surface of $SrTiO_3(001)$, using the synchrotron UV light to generate the 2DES (see figure 7.3 on page 132 in previous section). As shown in figure 7.3(d,g), the measured spin polarization along the local axes Q (approximately tangential component of the circular Fermi surface) is about $P_{Q,SLS} = 0.4$ at the Fermi level E_F. It is this tangential component which is characteristic for a Rashba-type like splitting. As already discussed previously multi-domain magnetism is difficult to detect using SARPES as the average magnetic moment over several magnetic domains can be zero. Hence, during our experiments at the HiSOR synchrotron we focused on the tangential component of the spin polarization.

The measurements presented in this section were conducted using experimental parameters similar to the study at the COPHEE machine. The experimental geometry is shown in figure 7.5(a) on page 136. As illustrated in this figure, the measured X component of the spin (laboratory frame) includes X' and Z' components in the reference frame of the sample due to the rotation of the sample. Thus, the spin-MDC intensities I_a and I_b of opposite spin directions along X in figure 7.5 correspond to approximately 75% of the component X' in the sample's frame. Note that the Y and Y' components of the electron spin coincide in the two reference frames. Figure 7.5(b) shows a schematic of the Fermi surface and figure 7.5(c) the energy-momentum map measured at $h\nu = 47$ eV using ARPES. Although the bands in the $E - k$ map are broader compared to the data shown in figure 4.4 on page 75, the characteristic electronic structure of the 2DES at the $Al/SrTiO_3$ interface composed of two d_{xy} bands can be clearly observed. Figures 7.5(b,c) also display, respectively, the directions in reciprocal space and binding energy of the spin-resolved measurements, with the experimental resolution represented by the width of the measurement lines. Figures 7.5(d-g) shows the spin-MDC intensities I_a and I_b and the spin asymmetry A along the tangential component close to the Fermi level E_F (figures 7.5(d,e)) and 30 meV below E_F (figures 7.5(f,g)) measured at the $Al(2\text{Å})/SrTiO_3(001)$ interface at a photon energy of $h\nu = 47$ eV. The tangential component of the spin was measured either along Y, for electron momentum parallel to (100) (figures 7.5(d,f)) or along X, for electron momentum parallel to (010) (figures 7.5(e,g)).

Due to different Sherman factors at different machines, the spin-MDCs I_a, I_b and spin asymmetries A shown in figure 7.5(d-f) cannot be directly compared to the spin-up and spin-down intensities $I_{\uparrow,SLS}$, $I_{\downarrow,SLS}$ and the spin polarization $P_{Q,SLS}$ in figure 7.3(c,d,f,g). However, I prefer to show the almost raw data (only subtraction of background) to eliminate any errors due to further data treatment (*e.g.* value of Sherman function S). The polarization of $P_{Q,SLS} = 0.4$ measured at the Fermi level E_F at SLS should correspond to a spin asymmetry of $A = 0.12$ at HiSOR assuming a Sherman function of $S = 0.3$ [314] and using equation (7.2) on page 129. However, the measured asymmetry A as shown in figure 7.5 is $A < 0.02$ for momenta corresponding to the peaks due to the two bands. There is not only quantitative disagreement but also qualitative. While there is a clear change in sign in the polarization $P_{Q,SLS}$ for momenta smaller or larger than Γ in figure 7.3(d,g), this change in sign can only be observed in figure 7.5(d) but not in figures 7.5(e-f).

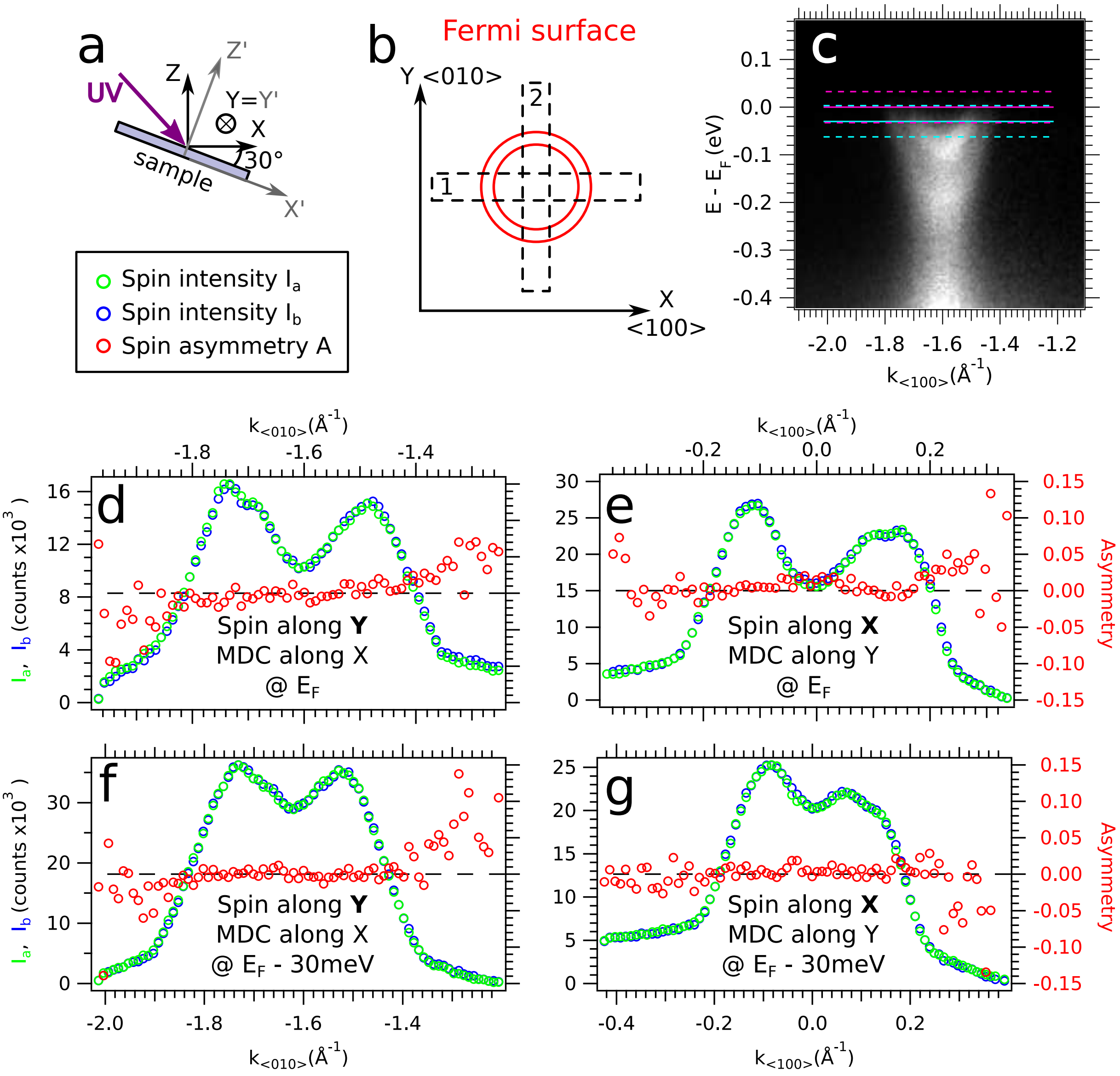

Figure 7.5: Spin momentum distribution curves (SMDCs) measured at the Al/SrTiO$_3$(001) interface at a photon energy of $h\nu = 47$ eV. (a) Definition of coordinate system and schematic of sample. As the spin detector measures the components of the spin in the X,Y,Z coordinate frame, the rotation of the sample by 30° can result in a mixture in the measurement of the spin components in the sample's coordinate frame: X'=cos(30°) X + sin(30°) Z, Y'=Y, Z'= sin(30°) X + cos(30°) Z. (b) Schematic of Fermi surface (red circles). The dashed black rectangle corresponds to the positions of the SMDCs in reciprocal space and its width to the angular resolution of the measurement. (c) E-k intensity map along the k_x direction obtained by ARPES at the ESPRESSO machine and showing the dispersions of the 2DES d_{xy} subbands discussed in section 4.2. The pink and turquoise lines correspond to the two cuts of the SMDC shown in (d-g) and the corresponding dashed lines refer to the energy resolution. (d-g) SMDC I_a, I_b and spin asymmetry A with momenta along the specified directions and the spin corresponding mainly to the tangential components of the Fermi surface. Note that all SMDCs show a four-peak structure, expected from the two subbands crossing E_F, and attesting of the high-quality of the data. All measurements were conducted at $T = 20$ K.

The absence of a giant spin splitting on the measurements at HiSOR is confirmed by measurements of the spin-EDCs on the same sample as displayed in figure 7.6. The figure is of the same structure as figure 7.5 and shows again a maximal asymmetry of $A = 0.02$.

Differences in observed spin splitting

To sum up, there is a clear discrepancy between the giant spin splitting in the 2DES at the surface of $SrTiO_3$ measured at SLS and the much smaller polarization measured at the Al(2Å)/$SrTiO_3$ interface, quantitatively (factor of ≈ 6) as well as qualitatively. This is unexpected as both measurements were conducted under very similar conditions (photon energy and polarization, temperature, experimental resolution). Note that a recent study by Walker *et al.* [323], working at BESSY synchrotron, also reported the absence of a giant spin splitting of the 2DES at the surface of $SrTiO_3$(001), although in their case all the experimental conditions were different from our original work at SLS: fractured surfaces (implying admixture of different surface terminations), photon energy of 80 eV (yielding a poor energy resolution, 2-3 times larger than in our case, and concomitantly a poorer momentum resolution), measurements at normal emission (implying the superposition of light and heavy bands, with potentially very complex superposition of spin structures), and measurements of only spin-EDCs which however fail to show the double-peak structure expected for the two d_{xy} subbands.

As pointed out before, one difference between the two measurements we conducted at SLS and at HiSOR, is that the 2DES is either created by UV-irradiation at the bare surface of $SrTiO_3$ (SLS) as discussed in section 3.2 or by a redox reaction at the Al/$SrTiO_3$ interface (HiSOR) as discussed in section 4.2. However, the electronic band structure (band mass, electron density of 2DES) are very similar in both cases and thus, there is no obvious reason why the spin texture of the two systems should be so different.

Another difference is that the measurements were conducted at different synchrotrons using different spin detectors. However, if and why one of the measurements is showing an experimental artifact is unclear. Note that when our group's first spin-ARPES experiments on $SrTiO_3$ were performed at SLS, and until recently, the COPHEE machine was the only synchrotron based SARPES experiment able to measure all three spin components. The development of similar setups in other synchrotrons (*e.g.* ESPRESSO at HiSOR) now facilitates comparisons and the validity of experimental results can be verified or negated.

As already discussed in section 7.2, there are experimental and theoretical studies at the $LaAlO_3$/$SrTiO_3$ interface as well as at the oxygen-deficient surface of $SrTiO_3$ which confirm the presence of magnetism whereas the (size of the) Rashba splitting is more controversial. Hence, more work is necessary to obtain further insights.

To validate one of the contradicting SARPES results, I will neither discuss in more detail the aforementioned studies nor the difference between the two SARPES setups. However, in section 7.3, I will briefly discuss the SARPES with respect to all the other ARPES results obtained in the framework of this thesis. As the presence of exactly two subbands of the same orbital character is a quite general feature in the 2DESs of many different oxides discussed in this thesis,

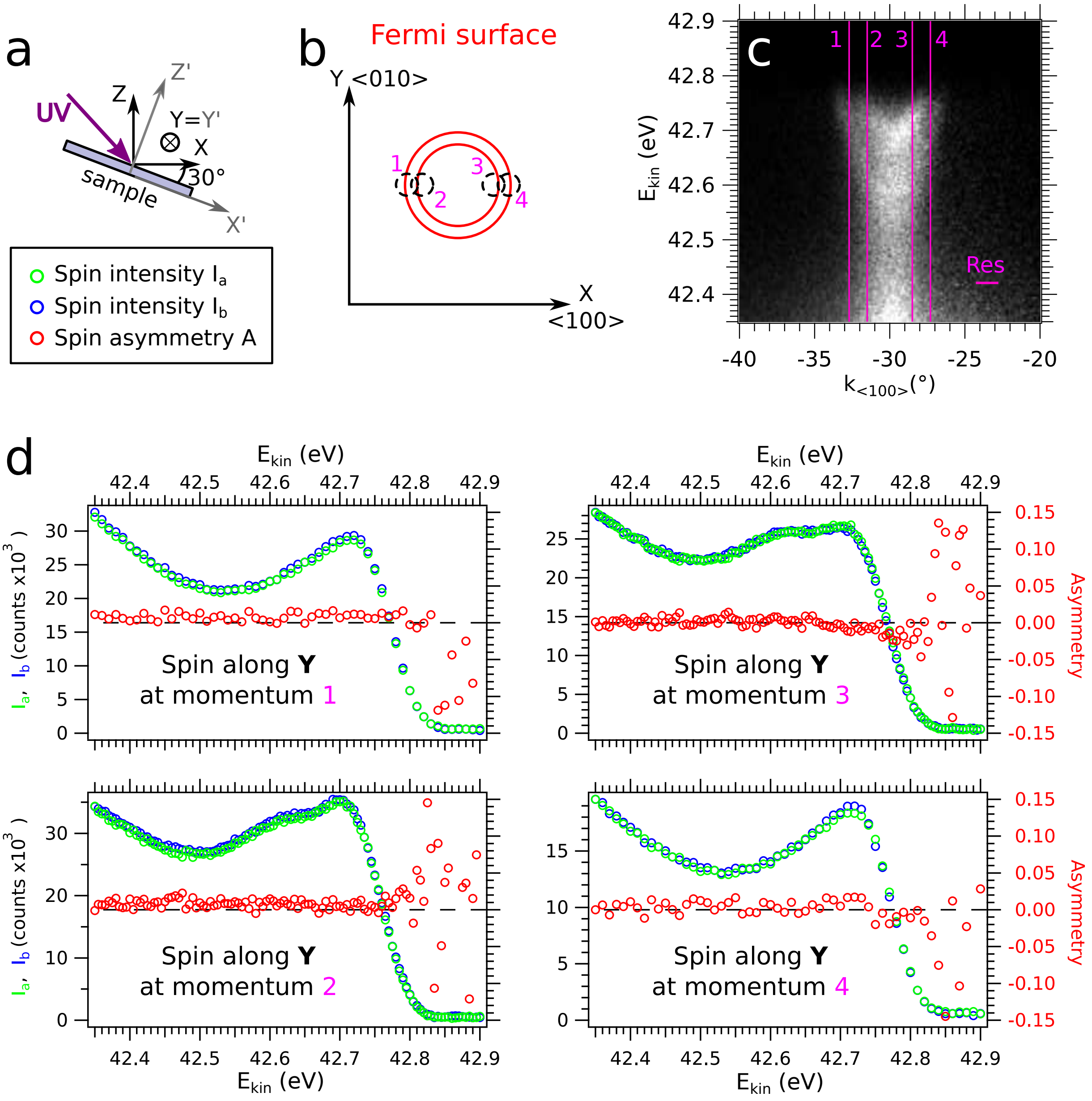

Figure 7.6: Spin energy distribution curves (SEDCs) measured at the Al/SrTiO$_3$(0001) interface at a photon energy of $h\nu = 47$ eV. As the spin detector measures the components of the spin in the X,Y,Z coordinate frame, the rotation of the sample by 30° can result in a mixture in the measurement of the spin components in the sample's coordinate frame: X'=cos(30°) X + sin(30°) Z, Y'=Y, Z'= sin(30°) X + cos(30°) Z. (b) Schematic of Fermi surface (red circles). The dashed black circles correspond to the positions of the SEDCs in reciprocal space and its diameter to the angular resolution of the measurement. (c) E-k intensity map along the k_x direction obtained by ARPES at the ESPRESSO machine and showing the dispersions of the 2DES discussed in section 4.2. The pink vertical lines correspond to the cuts of the SEDCs shown in (d) and the horizontal line shows the width of the angle resolution. (d) SEDC I_a, I_b and spin asymmetry A measured at the momenta defined in (b,c) with the spin along the Y direction corresponding to the tangential component of the Fermi surface. Note that the SEDCs cutting through the two subbands clearly show a two-peak structure, while those cutting only through the outer subband show a single peak -attesting the high-quality of the data. All measurements were conducted at $T = 20$ K.

Table 7.1: Binding energies of the bottom of the d_{xy} subbands in the 2DES at the (001) surfaces SrTiO$_3$ and CaTiO$_3$, the (001) and (101) surface of anatase and of the 4s subbands in the 2DES of ZnO(0001) as well as electron density deduced from the measured Fermi surface.

	CaTiO$_3$	Al/SrTiO$_3$	TiO$_2$(001)		TiO$_2$(110)	Al/ZnO
$E_{xy,1}$ [meV]	158	223	230[a]	170	130	445[b]
$E_{xy,2}$ [meV]	27	110	100[a]	60	60	70[b]
ΔE_{xy} [meV]	131	113	130[a]	110	70	375[b]
n [10^{14} cm^{-2}]	1.2	1.4	1.1[a]	0.5	1.5	0.5

[a] At the Al/Anatase(001) interface. [19]
[b] In ZnO, the 4s states are forming the 2DES and not the 3d d_{xy} states.

a spin splitting in other systems than SrTiO$_3$ is possible.

7.3 SARPES results in perspective with other ARPES results

For the Ti-based oxides, the energy splitting ΔE_{xy} between the two d_{xy} subbands is of the same order of magnitude for similar electron densities n_{2D} as shown in table 7.1. Thus, one can make the assumption that the nature of the splitting is of the same origin (*i.e.* either confinement in a quantum well or magnetism & Rashba). Furthermore, it is instructive to discuss the difference in the energy splitting of the two subbands in the 2DESs at different surface orientations of anatase (almost a factor of 2). In fact, the splitting is larger at the anatase (001) surface although the charge carrier density is lower compared to anatase(101) (see table 7.1). If one makes the very simple assumption that magnetism is proportional either to the electron density n_{2D} of the 2DES (itinerant magnetism) or the oxygen vacancy concentration (localized magnetic moments) which is not necessarily $\propto n_{2D}$ as discussed in section 3.3, the splitting should be larger at the anatase(101) surface.

Another instructive comparison is the energy splitting of the subbands in the 2DES of ZnO(0001) with the one of Anatase(001) at similar charge carrier densities. As evident from table 7.1, the splitting at the ZnO surface is larger by a factor of 3.4. This difference can be explained using the quantum well model discussed in section 1.2. As evident from equation (1.4) on page 18, ΔE_{xy} is proportional to $(m_z^*)^{-\frac{1}{3}}$ where m_z^* is the effective electron mass perpendicular to the surface. As the 2DES in ZnO is composed of isotropic 4s orbitals the effective mass of the electrons is almost isotropic ($m_z^*(\text{ZnO}) = 0.24$ and $m_{||}^*(\text{ZnO}) = 0.28$ [196]). Contrary, the d_{xy} orbital is highly anisotropic and thus, the effective mass as well ($m_z^*(\text{Anatase}) = 4.65$ and $m_{||}^*(\text{Anatase}) = 0.5$ [178]). Hence, m_z^* differs by a factor of approximately 19 corresponding to a factor of 2.7 for $(m_z^*)^{-\frac{1}{3}}$. This factor is comparable with the factor 3.4 found experimentally when comparing the energy splittings at the anatase and ZnO surfaces. Note that details on the shape of the potential well model, *i.e.* electric field and spatial extension, were ignored in this simple consideration.

On the other hand, the experimental observation of exactly two subbands (and not three or more) in the 2DESs at the (001) surfaces of TMOs could correspond to a spin-up and spin-down state induced by Zeeman splitting -if intrinsic magnetism is present. This observation contradicts the tight-binding model discussed in section 5.1: in figure 5.2(d) on page 97, the tight-binding Fermi surface of the 2DES at the $SrTiO_3$(001) surfaces shows four circles corresponding to four subbands of d_{xy} character. In contrast to our measurements, King *et al.* observed a low-intensity third d_{xy} subband at the (001) surface of fractured $SrTiO_3$ [13], which we never observed in our data on well-prepared TiO2-terminated surfaces. The origin of discrepancy in the measurements is unclear. Note that quality of the studied surfaces is similar in both studies if one takes the imaginary part of the self energy as reference (compare figure 3(b) in [13], where $\Sigma_2(E = E_F) \approx 30$ meV, and figure 8.3 on page 149, where $\Sigma_2(E = E_F) \approx 26$ meV).

Conclusions

In conclusion, the ARPES results on the 2DESs can be explained using models based on the electron confinement in a quantum well. The numerous reports on magnetism and Rashba splitting at the surface and related interfaces emphasize that considering only electron confinement is not enough to explain the observed band structure. However, whether the spin-related splitting in the energy is only of the magnitude of several meV and hence, results in a line broadening of the bands observed by ARPES, or if the splitting is of several tens of meV and and thus the dominating effect, is at this stage unclear. Based on the results (2DES at the surfaces of numerous oxides and the SARPES results at HiSOR) obtained during my thesis, the splitting of the subbands seems to originate from electron confinement and not the lifting of the spin-degeneracy. Note however that the SARPES data on the SrTiO3(001) surface obtained at COPHEE and ESPRESSO were both reproduced by our team several times. The origin of the discrepancy remains at this point unclear, and further studies, for instance comparing SARPES data obtained on the same machine on both UV-irradiated and Al-capped surfaces, should be undertaken in the future.

Chapter 8

Electron phonon coupling

So far the discussion of the ARPES data in this manuscript has been based on the band structure of 2DESs at the surface or interface of transition metal oxides. To rationalize the data, I discussed electron confinement in a quantum well (section 1.2), a tight-binding model (5.1) and spin-related effects (7). But as mentioned in section 2.2, ARPES or more specifically the measured spectral function in equation (2.13) on page 31 can give information beyond the band structure.

This became evident during the discussions of the ARPES data of $SrTiO_3(001)$ (section 4.2), Anatase(001) (3.4) and ZnO$(000\bar{1})$ (4.3) in which features in the $E-k$ intensity maps were attributed to electron-phonon (e-ph) coupling. In this chapter, I will focus on such features by analyzing the spectral function and deduce the e-ph coupling parameter λ for these three materials.

More generally, e-ph interactions give rise to many different phenomena in solid-state physics, *e.g.* the temperature dependence of the electrical resistivity in metals or conventional superconductivity. Another example is the relaxation/ thermalization of optically excited electrons also occurring during photoemission experiments.

8.1 e-ph coupling parameter λ, Einstein phonon and spectral function analysis

The interaction between electrons and phonons in solids is material dependent. To quantify the interaction strength, one can use the probability amplitude g of a scattering event of an electron from its initial state (i) with momentum $\vec{k}$ to a final state (f) by a phonon with momentum $\vec{q}$ and mode index ν:[327]

$$g^{i,f}(\vec{k},\vec{q},\nu) \propto (2M\omega_{\vec{q},\nu})^{-\frac{1}{2}} \left\langle \Psi_{\vec{k},i} \left| H_{int} \right| \Psi_{\vec{k}+\vec{q},i} \right\rangle . \tag{8.1}$$

Here, M is the atomic mass (in an elementary metal) and $\omega_{\vec{q},\nu}$ the frequency of the phonon mode $(\vec{q},\nu)$. The probability amplitude in the above equation can be approximately compared to Fermi's Golden Rule (equation 2.8 on page 27) giving the probability of an optical excitation of an electron. In the case of photons, the perturbation Hamiltonian is given by the oscillating vector field of electromagnetic radiation whereas for phonons the perturbation originates from the oscillating atoms (or ions in oxides).

Usually, the movements of the nuclei of the atoms and the electrons in a solid are decoupled based on their different masses in the adiabatic approximation. But, due to the Coulomb force between the charged particles (*i.e.* electron and nucleus), e-ph coupling can emerge. The e-ph interaction is assumed to be linear with the nuclear displacement. [328] To have a basic idea of the effect of this interaction, it is worth to consider a 1D harmonic oscillator of frequency ω (*e.g.* single ion in a lattice of mass M) linearly coupled to a single electron. The potential energy $V(x)$ of the system is thus given by

$$V(x) = \frac{1}{2}M\omega^2x^2 - \alpha x = \frac{1}{2}M\omega^2(x - x_0)^2 - \frac{\alpha^2}{2M\omega^2} \tag{8.2}$$

where α corresponds to the coupling strength. Based on the above equation, the system is still a harmonic oscillator but its energy is renormalized by $\alpha^2/(2M\omega^2)$ and its equilibrium position is displaced to $x_0 = \alpha/(M\omega^2)$. Both quantities are thus proportional to the coupling strength α^n. For $\alpha > 0$, this interaction results in a lowering of the energy of the system. In solids, an itinerant electron can distort the lattice atoms similarly - dragging along the distortion on its path and forming a polaron (see next section). Note that not only the harmonic oscillator is affected but also the electron, namely its effective mass m^*. The increase of m^* at the Fermi level E_F is described by the e-ph coupling parameter λ (see below for definition of λ): $m^* = m_0(1+\lambda)$ where m_0 is the effective mass of the bare band unaffected by e-ph interactions.

More specifically, the total probability for an electron in a given initial state (with energy E_i and momentum k) to be scattered by a phonon of frequency ω is given by the Eliashberg function $\alpha^2F(\omega)$: [327]

$$\alpha^2F(E_i, \vec{k}, \omega) = \sum_{\vec{q},\nu,f} \delta(E_i - E_f \mp \omega_{\vec{q},\nu})|g^{i,f}(\vec{k}, \vec{q}, \nu)|^2\delta(\omega - \omega_{\vec{q},\nu}). \tag{8.3}$$

The delta functions correspond to energy conservation, the $\mp$ to the emission or absorption of a phonon. Hence, to get the total probability, one sums over the probabilities of single scattering events in equation (8.1) where the sum runs over all phonon momenta $\vec{q}$ and modes ν as well as all electron final states f with energy E_f. Note that equation (8.3) corresponds to the phonon density of states $D(\omega) \propto \sum_{\vec{q},\nu} \delta(\omega - \omega_{\vec{q},\nu})$ weighted by the scattering probability $|g^{i,f}(\vec{k}, \vec{q}, \nu)|^2$ to all possible finals states (f).

While the phonon density of states $D(\omega)$ is not accessible by angle-resolved photoemission spectroscopy, information about the initial electron state $(E_i, \vec{k})$ can be gained from the ARPES spectral function (see next section). Hence, ARPES can characterize the Eliashberg function "averaged" over all phonon energies, namely the e-ph coupling parameter λ: [327]

$$\lambda(E_i, \vec{k}) = 2\int_0^{\omega_{max}} d\omega \quad \frac{\alpha^2F(E_i, \vec{k}, \omega)}{\omega} \tag{8.4}$$

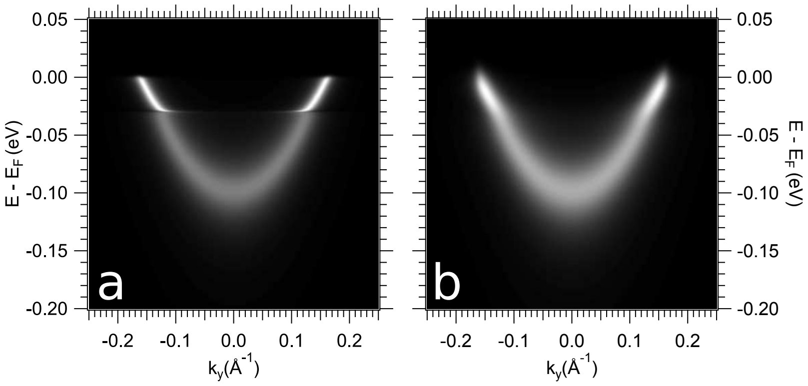

Figure 8.1: (a) Simulated ARPES $E-k$ intensity map to demonstrate the "kink" feature in the spectral function due to the coupling of electrons with Einstein phonons. The bottom of the parabolic bare band is at $E_0 = 100$ meV and its effective mass is $m^* = 1$. Close to the energy of the Einstein phonon $\omega_E = 30$ meV, the energy of the bare band is renormalized due to the e-ph interaction. As an additional scattering channel exists for electrons with $|E - E_F| > \omega_E$ the line width increases (in this example by a factor of 2) and hence, the intensity decreases. (b) Convoluted spectra of (a) using a Gaussian function of 10 meV width corresponding to a typical experimental resolution.

where ω_{max} is the phonon energy cutoff (maximum energy of phonons in the solid). Note that the above equation is based on the assumption of a quasielastic scattering mechanism $\delta(E_i - E_f \mp \omega_{\vec{q},\nu}) \approx \delta(E_i - E_f)$. The four given equations are a brief introduction to the formalism of e-ph coupling, details can be found in published reviews [327, 329–331].

Einstein phonon

The phonon dispersion in a lattice with a motif comprising more than one atom is composed of acoustic and optical phonons. In acoustic phonons the atoms of the motif oscillate in phase whereas for optical phonons they oscillate in phase opposition. The dispersion of acoustic phonons $\omega(\vec{q})$ is characterized by a linear dispersion close to Γ: $\omega(\vec{q}) \propto |\,\vec{q}\,|$ (Debye approximation) - the one of optical phonons is rather constant - *i.e.* independent of $\vec{q}$ - at phonon energy ω_E (Einstein approximation). Hence, the phonon density of states $D(\omega)$ of an Einstein phonon is: $D(\omega) \propto \delta(\omega - \omega_E)$. Thus, if the absolute value of the binding energy of the electrons in the solid is larger than the energy of the optical phonon an additional scattering mechanism is introduced. This e-ph scattering renormalizes the binding energy of the electron's spectral function close to the energy of the optical phonon and influences the lifetime of the electrons/ bandwidth of the dispersion. This results in the characteristic "kink" feature in the ARPES dispersions as shown in the simulated $E-k$ intensity map in figure 8.1 on page 143. For the simulation, the self energy of the Einstein phonon (discussed in the next paragraph) and a parabolic dispersion define the spectral function $A(\vec{k}, E)$ in equation (8.10) on page 145. Next, the photocurrent was simulated assuming a constant matrix element in equation (2.9) on 28: $I(E, h\nu) \propto A(\vec{k}, E) f(E, T)$.

Self energy of an Einstein phonon

The above discussed additional scattering channel affects the lifetime of the electron which is described by the imaginary part Σ_2 of the self-energy. In the quasielastic approximation, the relation between Σ_2 and the Eliashberg function $\alpha^2 F(E_i, \vec{k}, \omega)$ is given by: [327]

$$\Gamma_{e-ph}(E_i, \vec{k}, T) = 2\Sigma_2(E_i, \vec{k}, T) \tag{8.5}$$

$$= 2\pi \int_0^{\omega_{max}} d\omega\ \alpha^2 F(E_i, \vec{k}, \omega)[\underbrace{n(\omega, T) + 1 - f(E_i - \omega, T)}_{\text{ph emission}} + \underbrace{n(\omega, T) + f(E_i + \omega, T)}_{\text{ph absorption}}] \tag{8.6}$$

where $f(E, T)$ and $n(\omega, T)$ are the Fermi-Dirac and Bose distribution functions. As discussed previously, the Eliashberg function (8.3) on page 142 corresponds to the density of states $D(\omega)$ weighted by the e-ph interaction. For an Einstein phonon $D(\omega) \propto \delta(\omega - \omega_E)$ and thus, based on the above equation Σ_2 is given by a Heaviside function $\Theta(E)$:

$$\Sigma_2(E) = \frac{1}{2}\Gamma_0 + \frac{1}{2}\underbrace{\pi\lambda\omega_E}_{\Gamma_{e^- - ph}}\Theta(E - \omega_E) \tag{8.7}$$

where λ is the e-ph coupling parameter introduced previously. Hence, the strength of the e-ph coupling λ can be quantified by analyzing the energy dependence of the imaginary part of the self-energy Σ_2 (see table 3 in [331]). Note that, the e-ph parameter $\lambda(E_i, \vec{k})$ in equation (8.4) is a constant λ in the Einstein model ($\vec{k}$ independent and Heaviside function in E). The coupling constant can also be accessed under certain conditions by studying the temperature dependence of the imaginary part Σ_2 or the gradient of the real part of the self-energy Σ_1 close to the Fermi level E_F:[327]

$$\lambda = \begin{cases} \Gamma_{e-ph}/(\pi\omega_E) \\ \Gamma_{e-ph}(T)/(2\pi k_B T) \quad \text{if} \quad k_B T > \omega_{max} \\ \frac{\partial\Sigma_1}{\partial E}|_{E=E_F, T=0K} \approx \frac{v_{F,0}}{v_F} - 1 = \frac{m^*}{m_0} - 1 \end{cases} \tag{8.8}$$

where $v_{F,0}$ is the band velocity at the Fermi level of the bare band (no e-ph interaction) and v_F the one of the dispersion of the spectral function. Note that the last equation in (8.8) is not specific to e-ph interactions but more generally valid for many-body phenomena. The value $Z = \frac{m^*}{m_0}$ is the so-called quasiparticle residue which is characteristic for the mass renormalization in Fermi liquids.

The real Σ_1 and imaginary Σ_2 part of the spectral function are Kramers-Kronig related. Hence, the knowledge of the imaginary part allows the calculation of the real part of the spectral function (and vice versa). Thus, using equation 8.7, one can calculate analytically the real part of the self-energy for electron coupling to an Einstein phonon [332]:

$$\Sigma_1(E) = \frac{1}{2}\lambda\omega_E \log\left(\frac{E - \omega_E}{E + \omega_E}\right). \tag{8.9}$$

For illustration, Σ_1 and Σ_2 in the case of an Einstein phonon are plotted in figure 8.2.

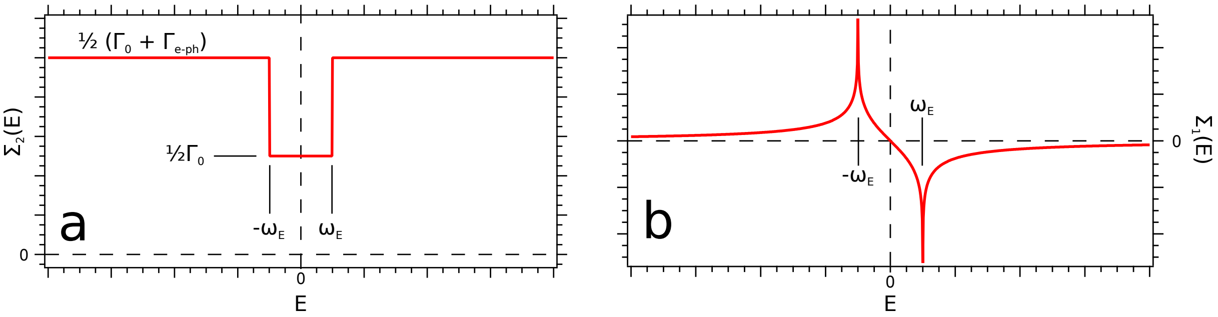

Figure 8.2: Imaginary (a) and real part (b) of the spectral function of an electron coupled to an Einstein phonon of energy ω_E

Spectral function analysis

To extract the values of the self energy from the experimentally observed ARPES data, an analysis of the spectral function is necessary. For the sake of readability of this section, I will write down again the spectral function given in equation (2.13) on page 31:

$$A(\vec{k}, E) = \frac{1}{\pi} \frac{\Sigma_2(\vec{k}, E)}{(E - E^0(\vec{k}) - \Sigma_1(\vec{k}, E))^2 + (\Sigma_2(\vec{k}, E))^2}. \tag{8.10}$$

The self-energies can be extracted from the momentum (MDCs) and energy distribution curves (EDCs). First, we focus on the MDCs, *i.e.* the discussion of the spectral function at a fixed energy $E = \widetilde{E}$ and assume that the spectral function is independent of k (*e.g.* electron-Einstein phonon coupling). A 1^{st}-degree Taylor expansion of $E^0(\vec{k})$ around $\vec{k} = \vec{k}_m$: $E^0(\vec{k}) = E^0(\vec{k_m}) + \frac{\partial E^0(k)}{\partial k}|_{k=k_m}(k - k_m) + \dots$ gives for the spectral function in equation (8.10) [333]:

$$A_{\widetilde{E}}(k) = \underbrace{\frac{1}{\pi \Sigma_{2,\widetilde{E}}}}_{\text{Amplitude}} \cdot \underbrace{\frac{(\Delta k_m)^2}{(k - k_m)^2 + (\Delta k_m)^2}}_{\text{line shape in } k} \tag{8.11}$$

with self-energy $\Sigma_{1,\widetilde{E}} = \widetilde{E} - E^0(k_m)$ and $\Sigma_{2,\widetilde{E}} = \frac{\partial E^0(k)}{\partial k}|_{k=k_m}\Delta k_m$. Using the 1^{st}-degree Taylor expansion, the spectral function $A_{\widetilde{E}}(k)$ is a Lorentz distribution with k_m being the position of the peak and Δk_m the half-width at half maximum. Both values are directly accessible in the ARPES data.

Next we turn to the discussion of the spectral function of the EDCs, *i.e.* at a fixed momentum $k = \widetilde{k}$ assuming that the $\Sigma_1(\widetilde{k}, E) \approx 0$. This approximation is for example valid in the case of coupling to an Einstein phonon without any other contributions to the self-energy (*e.g.* electron-electron interactions). As can be seen in figure 8.2(b) for energies substantially larger than the phonon energy $|E| > |\omega_E|$ the real part of the self energy is approximately zero $\Sigma_1(\widetilde{k}, |E| > |\omega_E|) \approx 0$ and the imaginary part constant $\Sigma_2(\widetilde{k}, |E| > |\omega_E|) = \frac{1}{2}\Gamma_0 + \frac{1}{2}\Gamma_{e-ph} \equiv \Delta E_m$. Hence, the spectral function is:

$$A_{\widetilde{k}}(E) = \underbrace{\frac{1}{\pi \Delta E_m}}_{\text{Amplitude}} \cdot \underbrace{\frac{(\Delta E_m)^2}{(E_m - E^0(\widetilde{k}))^2 + (\Delta E_m)^2}}_{\text{line shape in } E} \tag{8.12}$$

Again, the spectral function yields a Lorentz distribution with peak position E_m and half-width at half maximum ΔE_m.

I will use the spectral function analysis described in this section to deduce the self-energies and the e-ph coupling parameter in the ARPES data on the 2DESs in $SrTiO_3$, TiO_2 anatase and ZnO.

8.2 e-ph coupling in doped $SrTiO_3$, TiO_2 anatase and ZnO

Polarons

In insulating oxides (*e.g.* $SrTiO_3$ and TiO_2) e-ph coupling or polaron formation from excess electrons in the conduction band due to *e.g.* oxygen vacancies has been studied. Generally, one can distinguish different types of polarons: localized electronic states coupled to lattice distortions are classified as small polarons and delocalized states as large polarons. The distinction between small and large corresponds to the spatial extension of the polaronic wave function and the corresponding lattice distortions. The range of the lattice distortion is of the order of the lattice constant for a small polaron and several lattice constants for a large polaron.

Some authors attribute the localized electronic states at Ti sites due to oxygen vacancies in $SrTiO_3$ and TiO_2 (the in-gap state measured by photoemssion as *e.g.* shown and discussed in sections 3.2 and 3.3) to small polarons [103, 121, 173] and the delocalized states to large polarons [103, 173]. In contrast, other authors to do not relate the electronic states due to oxygen vacancies to polarons although stating the importance of lattice deformations in the formation of a 2DES at the oxygen-deficient surface of $SrTiO_3$ and in the binding energy of the localized states. [157, 299].

Hao *et al.* calculated that the character of the polaron (small/ localized or large/ delocalized) depends on the charge carrier density: low densities result in the formation of large polarons and large ones in the formation of small polarons. [173]

The electron density not only determines the type of the polaron but also two different e-ph coupling regimes as demonstrated by recent ARPES measurements on $TiO_2(001)$ [14] and $SrTiO_3(001)$ [17]. At low electron densities, a quasi particle peak at the Fermi level plus a spectral weight spread at lower binding energies (the so called "hump") can be observed; characteristic for a large polaron (see also references [18, 46, 48, 334]). At high electron densities, the band dispersion corresponding to the quasi particle peak shows a "kink" at the binding energy corresponding to the energy of an optical phonon (see also references [13, 47]). The crossover from one regime to the other occurs as the polaronic wave functions significantly overlap and thus, the polaron gas transforms to a Fermi liquid with e-ph coupling. [14] In the two regimes

the screening mechanism of the oscillating ions is different: for very low electron densities the screening occurs due to the dielectric polarization of the almost insulating crystal (polaron formation) whereas at higher electron densities the screening occurs due to the mobile electrons (Fermi liquid). [329]
In most of the cases, we studied the 2DES in the high electron density regime (one exception is the dispersion measured at the Cs/$SrTiO_3$ interface in figure 4.14 on page 90). Thus, in the following sections I will characterize a Fermi liquid (2DES) coupled to phonons and not polarons. To obtain the characteristics of the e-ph coupling from ARPES data, the analysis of the spectral function is necessary and will be discussed in the next section.

Self-energy analysis in $SrTiO_3$, Anatase and ZnO

The band structure of the 2DES at the surface of $SrTiO_3$(001), Anatase(001) and ZnO(000$\bar{1}$) was discussed in previous sections. In this section we focus on the characterization of the self energy in the presence of e-ph coupling. The analysis of the spectral function is limited to the fitting of the MDCs close to the Fermi level. While this is not a complete analysis, it is sufficient to characterize the prominent "kink" feature related to e-ph coupling. We will use a simplified analysis using the above Einsten phonon model, which as we will see, describes extremely well the data. The self energies shown in figures 8.3 - 8.5 on pages 149 - 151 were obtained using the following procedure:

1. Fit of MDCs (using Lorentzian peaks) and EDCs (using Voigt peaks) of the measured ARPES $E-k$ intensity dispersion
2. Self-consistent fit of the self energy (Kramers-Kronig related) using a parabolic bare band whose parameters are constrained by the fit results of step 1.

The fitting of the MDCs and EDCs in step 1 is somewhat ambiguous. In the case of $SrTiO_3$(001) and Anatase(001), the background close to the Fermi-level is relatively large due to spectral weight induced by the tail of the in-gap state. The choice of background line shape influences the results of MDC and EDC fits and hence, the self energy. In the case of ZnO(000$\bar{1}$), the bandwidth is relatively large (approximately a factor of five compared to $SrTiO_3$ - see later discussion) probably due to defects at the surface resulting in a reduced lifetime of the electrons. This large bandwidth complicates the band fitting. Fits using several different backgrounds and fitting parameters were conducted and the "best" fit chosen for the results shown in the next section. Note that especially for the MDC fitting close to Fermi level this choice is not critical for the results of the self energy analysis.

Description of figures

The results of the analysis are summarized in figures 8.3 - 8.5 on pages 149 - 151. In each figure, panel (a) shows the $E-k$ intensity map measured at temperatures of $T = 7-20$ K - in the case of $SrTiO_3$ and Anatase after the normalization of the background. For the background normalization, each MDC was divided by a linear fit of the MDC's background. Panel (b) displays the simulated data based on the self energies in panels (d,e) and convoluted with a Gaussian whose width is given by the experimental energy resolution. Panel (c) shows the peak positions of the MDC (green line) and EDC fits (blue dots) as well as the used bare band dispersion (dashed red line).

Finally, panels (d,e) show the self energies of different branches of the bands or different data sets. The red markers correspond to the self energies obtained from fits to the data, while the black curves are the Kramers-Kronig transformations. The values of the self energies (red markers) were obtained using the peak positions and peak widths of the MDC fits (see equation (8.11) on page 145). In panel (e), the blue markers are the inverse of the peak amplitude of the MDC fits, which according to equation (8.11) are proportional to $\Sigma_{2,\widetilde{E}}$ in the case of a k-independent self-energy. It is difficult to obtain quantitative information on the spectral function based on intensities as the measured photocurrent depends not only on the spectral function but also on many other factors (see section 2.2). Nevertheless, in the case of $SrTiO_3$ and Anatase, the peak amplitude can be used to obtain the qualitative behavior of $\Sigma_{2,\widetilde{E}}$.

In the case of anatase, figure 8.4(f) on page 150 shows the EDCs in the range marked by the dashed blue lines in figure 8.4(a). One can clearly identify three peaks in some of the EDCs although only two bands disperse in figure 8.4(a). This is a direct consequence of the “kink” feature due to e-ph coupling, resulting in a “peak-dip-hump” that creates a “replica” of the band peak.

Summary of results

In all three materials ZnO, $SrTiO_3$ and anatase, one can see the “kink” feature characteristic of e-ph coupling in figures 8.3 - 8.5(a). In all three cases, the experimental self energies are self-consistent, *i.e.* the Kramers-Kronig transform of the $\Sigma_{1,\widetilde{E}}$ fits $\Sigma_{2,\widetilde{E}}$ rather well and vice versa. As already mentioned, the “kink” feature was already analyzed in $SrTiO_3$ [13] and anatase [14] but so far not in ZnO.

Discussion of imaginary part of self-energy: $\Sigma_2(E_F)$ & $\Delta\Sigma_2$

The value of imaginary part of the self energy at the Fermi level $\Sigma_2(E_F)$ and its change $\Delta\Sigma_2$ at energies larger than the phonon energy ω_E are summarized in the first two columns of table 8.1 on page 152. The imaginary part of self energy at the Fermi level is proportional to the inverse of the time interval between two scattering events of the electron with defects $\Sigma_2(E_F) = 0.5\Gamma_0$ in equation (2.14) on page 31. Defects can range from point defects as oxygen vacancies to 1D or 2D defects and low-energy acoustic phonons but can also describe more generally the surface quality (*e.g.* surface roughness). The change in $\Sigma_2(E)$ between E_F and energies larger than the typical phonon energies quantifies the e-ph coupling strength in the simple model of an Einstein phonon. From figures 8.3 - 8.5(d,e), on sees that, although the experimental self-energy is not exactly that of an Einstein phonon (for instance, $\Sigma_2(E)$ is not a unit step function of energy), there are marked qualitative resemblances with such simple model: a steep increase in $\Sigma_2(E)$ followed by a plateau at the same energy where $\Sigma_1(E)$ shows a peak.

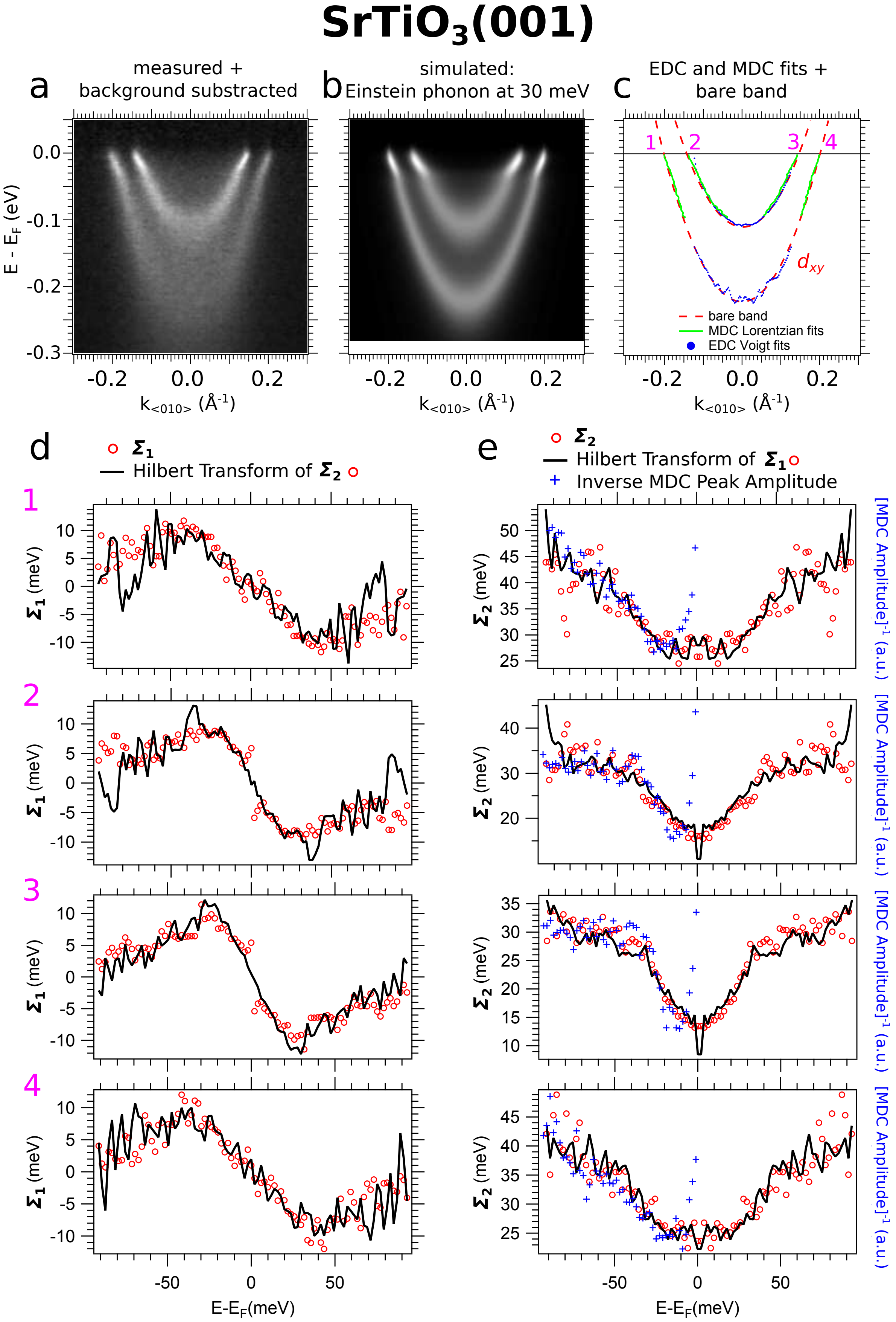

Figure 8.3: Self-energy analysis of of 2DES in SrTiO$_3$. See description in main text on page 147.

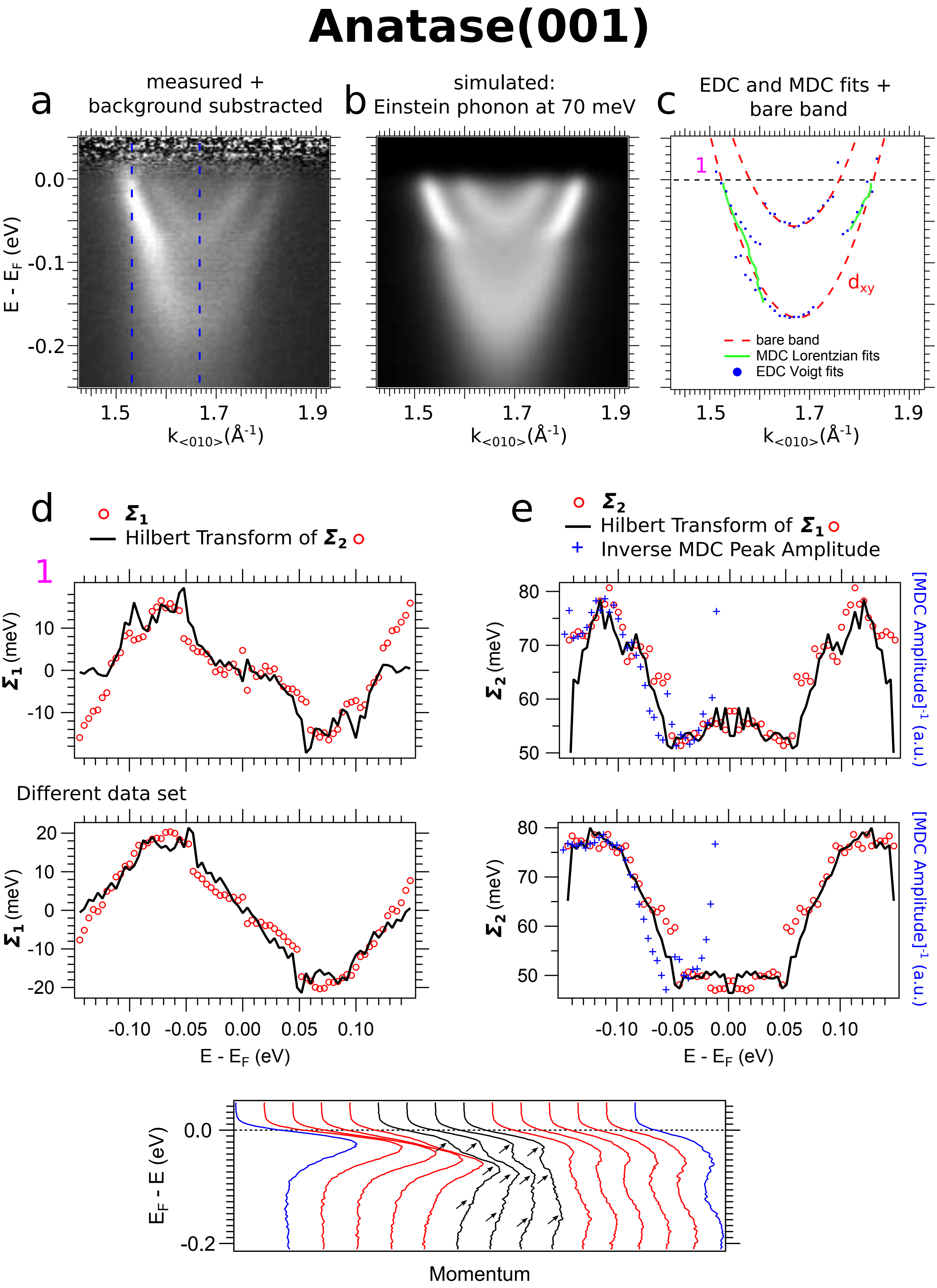

Figure 8.4: Self-energy analysis of 2DES in anatase. See description in main text on page 147.

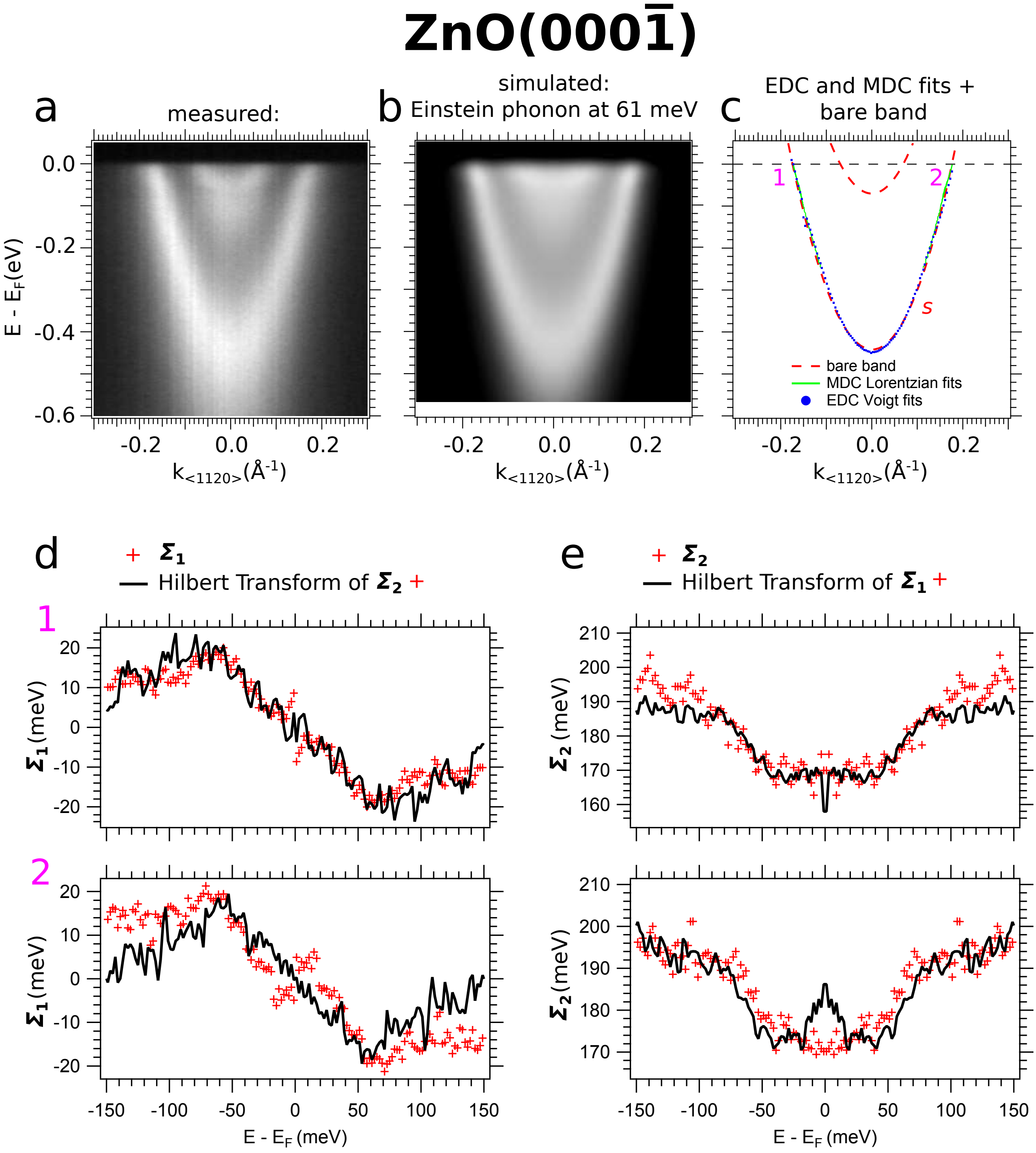

Figure 8.5: Self-energy analysis of 2DES in ZnO. See description in main text on page 147.

Table 8.1: Values deduced from the self-energy analysis in figures 8.3 - 8.5 on pages 149 - 151 of the $E - k$ intensity maps at the Γ point in the 2DESs at the surfaces/ interfaces of $SrTiO_3$, Anatase and ZnO. The given errors are based on the uncertainty in the determination of the values from figures 8.3 - 8.5(d,e) and the discrepancy between the right and left branch of a band in the self energy analysis.
1^{st} & 2^{nd} column: Name of oxide and the quantum number of the subband in the quantum well of the 2DES.
3^{rd} & 4^{th} column: Imaginary part of the self energy at the Fermi level $\Sigma_2(E_F)$ (*i.e.*, inelastic scattering rate plus experimental resolution) and its change $\Delta\Sigma_2$ at energies larger than the phonon energy ω_E. In an Einstein model, $\Delta\Sigma_2$ corresponds to the height of the Heaviside step function.
5^{th} & 6^{th} column: Energy of phonon ω_E and coupling constant λ obtained using equation (8.8) on 144.
7^{th} & 8^{th} column: Bare band parameters (band bottom E_0 & effective mass m^*) using a parabolic-band dispersion.

		Self Energy Σ (meV)		e-ph coupling		bare band $E^0(\vec{k})$	
	n	$\Sigma_2(E_F) \pm 2$	$\Delta\Sigma_2 \pm 3$	$\omega_E \pm 4$ meV	λ	E_0 (meV)	m_0
$SrTiO_3$	1	26	9.5	37	0.16 ± 0.05	223	0.70
	2	15	14	32	0.28 ± 0.07	110	0.73
Anatase	1	51	26	68	0.24 ± 0.03	170	0.55
	2					56	≈ 0.55
ZnO	1	170	19	61	0.20 ± 0.03	442	0.26
	2	^{a}	^{a}	^{a}	^{a}	$\approx 72^a$	$\approx 0.26^b$

[a] The fitting and self-energy analysis of the upper band are difficult due to the “peak-dip-hump” structure and the large band width.
[b] Values based on the assumption that the effective masses of the lower and upper band are identical.

The surface preparation of $SrTiO_3$ discussed in section 2.4 is well studied and hence, atomically-flat and crystalline surfaces can be obtained. In contrast, the shown anatase data was obtained on a cleaved crystal. These different surface preparations result in a different surface quality and hence, the line widths in anatase are larger by a factor of 2 to 4 compared to $SrTiO_3$. Although the ZnO surface was prepared by sputtering and annealing as described in section 2.4, the line widths in ZnO are much larger (factor of 6 to 11 compared to $SrTiO_3$). Again, differences in surface quality can be a possible explanation. However, another factor could be the different electronic structure due to the oxygen vacancies at the surface/ interface of ZnO and the other two systems. As discussed in sections 4.3 and 3.2, the excess electrons in the titanates partly form localized states in the band gap whereas in ZnO the in-gap states do not exist. This difference could alter the screening of the electric fields related to the defects.

Another factor affecting the screening of oxygen vacancies is the static dielectric constant which is the highest in $SrTiO_3$ ($\epsilon \approx 300$) compared to anatase ($\epsilon \approx 31$) and ZnO ($\epsilon \approx 8$) at room temperature. Due to this high dielectric constant, charged defects can be effectively screened by the lattice. Note that these dielectric constants correspond to the response of the systems in their stoichiometric, insulating phase. The creation of a metallic 2DES will alter the dielectric response of the system as screening is dominated by itinerant electrons - but a quantitative study of the dielectric constant of the 2DESs in these oxides is still missing.

In the case of $SrTiO_3$, the different subbands show different values of $\Sigma_2(E_F)$ as deduced from the self-energy analysis. Usually, $\Sigma_2(E_F)$ or Γ_0 is assumed to be independent of momentum k, and hence, should be the same for all subbands at E_F. Hence, the discrepancy might originate from errors in the fitting procedure. Alternatively, note that the electrons in different subbands of the quantum well have different spatial extensions. As the defect distribution of oxygen vacancies is not homogenous and the localized or itinerant character of the excess electrons is different in the surface and subsurface layer [157], the discrepancy in $\Sigma_2(E_F)$ could also originate from spatial inhomogeneities.

Similarly, the change $\Delta\Sigma_2$ (4^{th} column in table 8.1) due to the e-ph interaction and the energy of the phonon ω_E should be k independent ((hence, band-independent) in the case of an Einstein phonon. Again, errors in the fitting procedure might be responsible for the disagreement. Additionally, as pointed out earlier, the model of one non-dispersing Einstein phonon is too simple, as obviously the experimental $\Sigma_2(E)$ is not a Heaviside function. Nevertheless, we see that the simple picture of the Einstein phonon provides consistent values of the phonon energies and coupling constants for all the bands.

The change $\Delta\Sigma_2$ is largest in anatase (68 ± 4 meV) by a factor of approximately two compared to $SrTiO_3$ and 10% compared to ZnO. This means that either the phonon density of states and/ or the e-ph scattering amplitude of this phonon mode in anatase are larger compared to the other two oxides.

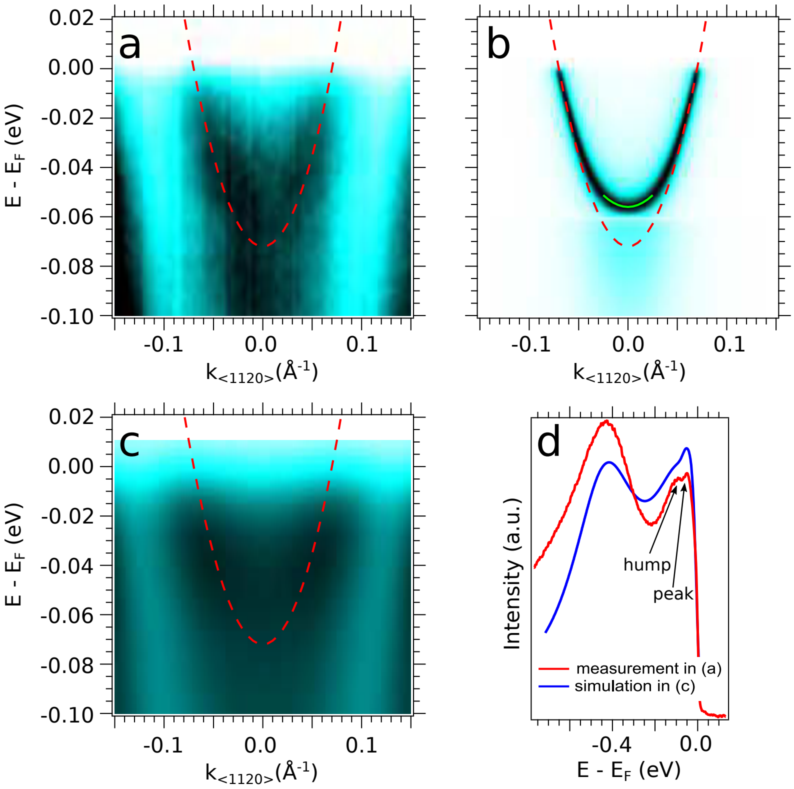

Figure 8.6: (a) $E-k$ intensity map zooming on the upper subband of the 2DES at the surface of Zn(000$\bar{1}$) measured at $h\nu = 25$ eV. The red dashed line is the bare band dispersion of the lower subband, simply shifted up in energy (quantum-well state model) to account for the Fermi momenta of the upper subband. (b) Simulated $E-k$ map of the upper subband using an Einstein model based on the bare mass and the self energy of the outer band. To enhance visibility, the band width was set to a small value of $\Sigma_2(E_F) = 10$ meV. The green line is a parabolic fit of the renormalized band bottom. The increase of the effective mass is approximately a factor of two between the bare and the renormalized band. (c) Same as in (b) but with the experimental band width $\Sigma_2(E_F) = 170$ meV and convoluted with a Gaussian of $FWHM = 20$ meV. (d) Momentum-integrated spectrum of (a) and (c) over a range of $k_{<1120>} = [-0.05\ \text{Å}^{-1}, 0.05\ \text{Å}^{-1}]$. One can identify the "peak-dip-hump" feature of the peak of the upper subband due to the coupling with a phonon mode.

Discussion of phonon energy ω_E and bare band parameters E_0 & m^*

The energy of the Einstein phonon with respect to the bottom of the upper (u) and the lower (l) subband of the 2DES is different in the three materials at the given electron densities in figures 8.3 - 8.5:

- SrTiO$_3$: $\omega_E << E_{0,u} << E_{0,l}$ $\Rightarrow$ two bands show "kink" feature
- Anatase: $E_{0,u} < \omega_E << E_{0,l}$ $\Rightarrow$ one band shows "kink" feature
- ZnO: $\omega_E \approx E_{0,u} << E_{0,l}$ $\Rightarrow$ one band shows "kink" feature, the other a smeared out band bottom resulting in a "peak-dip-hump" structure in the spectral function near Γ.

In ZnO, the large line width and similar values for $\omega_E \approx E_{0,u}$ make it difficult to fit the peak positions of the upper band of the 2DES. To deduce the bare band dispersion of the upper band, I assume that the effective mass of the upper band is identical to the one of the lower subband which is a reasonable assumption for subbands of a quantum well state. Together with the Fermi momenta of $k_F = 0.07$ Å^{-1} (see section 4.3), this yields a band bottom of $E_0 = 72$ meV.

As evident from figure 8.6(a) on page 154, the effective mass as well as the bottom of the bare band (red dashed line) do not correspond to the experimental dispersion. In the case of $\omega_E \approx E_{0,u}$, the energy renormalization of the bare band due the interaction between electrons and phonons does not result in a "kink" feature. Instead, the band bottom is shifted to lower binding energies and some of its spectral weight is smeared out for energies larger than ω_E forming a "peak-dip-hump" shape. This is evident from the simulated $E-k$ map in figure 8.6(b) based on the parameters in table 8.1 except setting $\Sigma_2(E_F)$=10 meV to enhance the visibility of the energy renormalization. To compare this model to the experimental data, figure 8.6(c) shows the simulated $E-k$ map using $\Sigma_2(E_F)$=170 meV, the value deduced from the outer band plus a convolution with a Gaussian representing the instrumental energy resolution. The "peak-dip-hump" feature is visible in the momentum-integrated curves in figure 8.6(d). Based on the simulation in figure 8.6(b), the shift in energy of the band bottom is about 16 meV. The resulting effective mass is roughly 0.5 close to Γ [$\Gamma - 0.25$ Å^{-1}; $\Gamma + 0.25$ Å^{-1}] as shown by the green line in 8.6(b) and hence, almost a factor of two larger than the bare band mass. This is a nice textbook example of how e-ph interaction can renormalize the whole electron dispersion when the phonon energy is close to the band bottom.

In principle, the e-ph interaction should be similar in the case of the coupling between the Einstein phonon and the heavy band in $SrTiO_3$. The experimentally observed band bottom of the d_{xz} heavy band in figure 4.4(b) on page 75 is about $E_{xz} \approx 50$ meV and thus, relatively close to the phonon energy $\omega_E \approx 35$ meV. However, the renormalization of spectral weight or any indication of the e-ph interaction are not evident from figure 4.4(b) on page 75.

As evident from table 8.1, ω_E is different for the two subbands in $SrTiO_3$. The phonon mode is probably of t_{2u} symmetry whose energy is $\omega_\Gamma^{lit} \approx 32$ meV at Γ ([335] and references therein) and disperses approximately 5 meV from Γ to the Brillouin zone border in <100> direction ([336] and references therein). This demonstrates once more that the Einstein approximation is too simple to correctly reproduce the data.

In anatase, the energy of ω_Γ in table 8.1 is close to a A_{1g} ($\omega_\Gamma^{lit} \approx 64$ meV) and B_{2u} ($E_{ph}^{lit} \approx 67$ meV) phonon mode ([337, 338] and references therein).

Finally, in ZnO, the value of E_{ph} based on the self-energy analysis lies in a gap between a e_2 ($\omega_\Gamma^{lit} \approx 55$ meV) and a b_1 ($\omega_\Gamma^{lit} \approx 71$ meV) mode ([335, 339] and references therein).

Discussion of coupling constant λ

The coupling constants shown in the 6th column in table 8.1 on page 152 are quite comparable for all three materials and ranging between 0.16 and 0.28 (weak coupling regime). Naively, one could assume that the coupling strength depends on the value of the dielectric constant: the higher its value, the higher the polarization/ deformation of the lattice induced by an electric field/ itinerant electron. As discussed previously, even at room temperature there is large difference (up to a factor of ≈ 40) in the dielectric constant between the three oxides in their stoichiometric, insulating phase. However, the dielectric constant in the metallic phase (2DES) of the three oxides can be largely different from the one in its insulating form. As already discussed previously, the e-ph interaction at high electron densities ($n_{2D} > 1 \times 10^{14}\text{cm}^{-2}$ in $SrTiO_3$ [17]) corresponds to an optical phonon coupled to a Fermi liquid (no polarons). In this regime, the dielectric constant ϵ does not relate to the coupling constant λ, probably because the metallic screening dominates the dielectric response of the material.

Hence, although the dielectric constant of $SrTiO_3$ is much larger (up to two orders of magnitude) than in semiconductors or metals, the coupling constant λ is comparable to the one of some metals (see table 4 in [340], *e.g.* Cu(110): $\lambda_{Cu} = 0.23$) and much smaller than in other oxides as *e.g.* the doped Mott insulator $La_{0.01}Sr_{0.09}CuO_4$ with $\lambda_{LSCO} = 2.7$ [47]. The value of $\lambda^u_{STO} = 0.28$ in the upper subband of $SrTiO_3$ is similar to the one found by Meevasana *et al.* for the heavy band $\lambda^{xz}_{STO} = 0.3$ at the surface of $La_{0.01}Sr_{0.99}TiO_{3-\delta}$ [47]. Note that King *et al.* used the slope of the real part of the self-energy at E_F (see equation (8.8) on page 144) to determine a coupling constant of $\lambda^l_{STO} = 0.7$ for the lower subband. [13] Based on the plots of Σ_1 in $SrTiO_3$ in figures 8.3(d) on page 149 this method yields, in our case, $\lambda^l_{STO} \approx 0.27$ for the lower subband and $\lambda^u_{STO} \approx 0.43$ for the upper subband. The origin of the discrepancy with the value obtained by King *et al.* is unclear. Note that the advantage of determining λ using the slope of the real part of the self-energy is that the value is independent of the used model, *e.g.* Einstein or Debye phonon. However, such "slope method" suffers from a serious difficulty: it relies on the accurate determination of the band dispersion and line width close to E_F, precisely where the Fermi-Dirac cutoff and the experimental resolution can bias the precise determination of these two quantities. [341]

Conclusions

The results on the e-ph coupling presented here are only a preliminary analysis. The analysis should include a larger binding energy range, an analysis of the energy-distribution curves and models different from the simple Einstein model should be considered. For example, in the case of $SrTiO_3$, multiple phonon modes in an energy range of $\approx 20 - 100$ meV should be considered. [13, 342] Additionally, the self-energy analysis of the $E-k$ maps measured at different temperatures gives another possibility to determine the e-ph coupling constant λ.

Nevertheless, the simple model of a single Einstein phonon reproduces the central features of the measured spectral function. This model reproduces the "kink" feature in the band dispersions as well as the renormalization of the band bottom in the case of $\omega_e \approx E_0$. The quantitative analysis reveals that in the 2DES of all three oxides the coupling constants are of a similar values and lie in a narrow range of 0.18 to 0.28 although the oxides have different lattice structures/ phonon dispersions, different dielectric constants and their conduction is composed either of s or of d orbitals.

Chapter 9

Outlook

The origin of this thesis was the discovery of a two-dimensional electron system (2DES) at the oxygen-deficient surface of fractured $SrTiO_3$ by ARPES. [1, 2]. This unexpected finding together with the interest in 2DESs at $SrTiO_3$-based interfaces (*e.g.* $LaAlO_3/SrTiO_3$) make this field one of the most active areas of research in modern condensed matter physics.

Generalization of the creation of 2DESs in oxides

A major achievement of this thesis is the generalization of the aforementioned surprising revelation to many other oxygen-deficient surfaces (including different surface orientations) and interfaces of transition metal oxides (TiO_2 anatase, $CaTiO_3$, $BaTiO_3$, ZnO) within only five years after the initial results - and during the 3 years of duration of my PhD work.

As shown in chapter 3, such generalization is limited by the behavior of excess electrons introduced by oxygen vacancies. In electron-doped d^0 transition metal oxides, both localized and itinerant electrons can exist due to oxygen vacancies. Which of the two cases is energetically favorable can depend on subtle differences as demonstrated by studying two polymorphs of the same material (TiO_2 anatase and rutile as discussed in section 3.4 and references [14, 103]).

Another, more practical, limitation to the generalization is the availability of single crystals of transition metal oxides and the preparation of crystalline and clean surfaces. As shown in section 6.2, the growth of thin films of transition metal oxides (*e.g.* $BaTiO_3$) can circumvent this problem. Ideally, growth of thin films and the characterization of their surfaces/ interfaces are conducted without breaking vacuum.

Based on this generalization of the creation of the 2DESs, the question naturally arises which other oxide-based 2DESs could be interesting either from the perspective of fundamental or applied science. Regarding research towards applications, I will discuss the functionalization of 2DESs below.

If one makes once more the comparison with two dimensional electron gases (2DEGs) in semiconductors, transition metal oxides show a variety of properties usually not observed in semiconductors: *e.g.* ferroelectricity, ferromagnetism, superconductivity and strong electron correlations. One could for example imagine to create oxygen vacancies at the surface of a Mott insulator which could result in the creation of a strongly correlated two-dimensional electron system. However, as the on-site Coulomb repulsion U is large in Mott insulators, the excess electrons due to oxygen vacancies might be localized and not itinerant.

Additionally, instead of focusing on the variety of properties of transition metal oxides, one can turn to insulating oxides not including a transition metal but already used in some form in the electronics industry - similar to the 2DES in ZnO unveiled in this thesis. The feasibility of the creation of 2DESs at the surface of non-transition metal oxides was for instance demonstrated for In_2O_3 [343]. Sn-doped In_2O_3 (ITO) is one of the most widely used transparent conducting oxides. Due to the scarcity of indium, low-cost alternatives like ZnO, SnO_2 and CdO are studied. [344]. Note that 2DESs exist at surfaces or interfaces of both ZnO (see section 4.3 and references [93, 190, 192]) and CdO [345].

In this thesis, 2DESs at the surface of d^0 oxides and the d^{10} system ZnO were studied. In one case, the 2DES is composed of d orbitals (more specifically the t_{2g} orbitals) and in the other of s orbitals. One approach to alter the properties of the 2DES is by changing the orbital character (defined by the azimuthal quantum number of the atomic orbitals) of the valence electrons. While 2DESs composed of s, p (*e.g.* 2DESs in classical semiconductors like Si) and d orbitals have already been studied, 2DESs composed of f electrons have not been reported so-far. The large atomic mass of rare earth atoms results in a large spin-orbit coupling and the localized character of f electrons favor electron correlation effects. However, similar to Mott insulators discussed above, f electrons are rather localized and the possibility to create a confined and itinerant electron gas at the surface of a rare earth oxide is still an open question.

Better understanding of microscopic electronic structure

In the framework of this thesis, the understanding of the microscopic electronic structure of oxide 2DESs measured by ARPES advanced based on two different approaches. Firstly, through a more detailed analysis of the 2DES at the surface of $SrTiO_3(001)$ compared to the initial studies [1, 2] and the study of changes in the electronic structure at related surfaces.

To enable a more detailed analysis of the 2DES at the $SrTiO_3(001)$ surface, the measured ARPES data should show the intrinsic line width of the bands. Hence, extrinsic effects like a surface of poor crystallinity should be minimized. To achieve this goal, a first step was to control the surface preparation to obtain crystalline and atomically flat surfaces in a reproducible manner. Thus, instead of fracturing the crystals [1, 2], preparation techniques based on chemical etching and annealing were applied (see section 2.4 and reference [7]). This approach resulted in a narrower line-width, allowing a detailed analysis of phenomena like the renormalization of the self-energy due to electron-phonon interaction (see chapter 8 and references [17, 18]).

The understanding of the electronic structure of the 2DES at the surface of $SrTiO_3(001)$ [13] was given an additional turn by the surprising discovery of a complex spin texture in this 2DES measured by SARPES and indicating that the splitting of the d_{xy} subbands originates from the lifting of the spin degeneracy. However, more recent SARPES measurements conducted at other synchrotrons could not reproduce the findings (see section 7.2 and [323]). These conflicting results were discussed in chapter 7 with the conclusion that the large splitting of approximately 100 meV may not originate form the lifting of the spin degeneracy.

The study of 2DESs at the (110) and (111) surface revealed that the electronic band structure of the 2DES can be tuned by confining the electrons at different surface orientations of the same material, namely $SrTiO_3$ (see section 5). The geometry of the surface lattice depends on the surface orientation and alters the orbital ordering, the symmetry of the Fermi surface as well as the effective mass along a specific crystallographic direction of the 2DES. Identical results were obtained in other studies conducted almost simultaneously. [9, 11]

Compared to cubic $SrTiO_3$, the building block of perovskite oxide lattices - the oxygen octahedron with the transition metal at its center - is slightly tilted in $CaTiO_3$. This symmetry breaking results in the mixing of different d-orbitals which is not observed in $SrTiO_3$ (see section 6.3) demonstrating again why and how the electronic structure can be altered.

Simple and versatile creation of 2DESs: studies beyond photoemission and ultra high vacuum

The major achievement of this thesis is the demonstration of a simple and versatile technique for the creation of 2DESs, namely the evaporation of Al on oxide surfaces. In this thesis the study of such interfacial 2DESs was limited to photoemission studies in ultra high vacuum. However, this technique opens up the possibility to study 2DES at the AlO_x/oxide interface in ambient conditions by *e.g.* transport techniques.

As we demonstrate in section 4.2, there is no critical thickness to create the 2DES. The only requirement is a homogenously distributed reducing agent. But to stabilize the 2DES there is a critical thickness of AlO_x to block the re-oxidation of the interface by oxygen diffusion through the AlO_x capping layer. According to the literature this thickness is of about 1.2 nm at the interface of amorphous Al_2O_3 with $SrTiO_3$ [97]. This value is confirmed by the natural thickness of the oxidized layer at the surface of a piece of aluminum: 1.24 nm [188]. Hence, one can assume that by depositing this thickness of Al the 2DES can be stabilized. This is the ideal, simplest scenario.

In fact, our first transport results indicate the feasibility of this approach as shown in figure 9.1 on page 160. The interface is insulating for Al thicknesses smaller than 10 Å. Between 10 Å and 15 Å the resistance fluctuates and is not necessarily ohmic. At 15 Å , the square resistance $R_\square$ is 44 kOhm which is of the same order of magnitude as the values reported in the literature for other SrTiO3-based interfaces. [97, 183] Note that 15 Å of Al can be fully oxidized given that the growth mode is not a perfect layer-by-layer growth: 2 Å (oxygen from redox reaction with $SrTiO_3$) + 12 Å (oxygen from air)≈ 14 Å. For thicker Al films the resistance continues to drop, probably due to the contribution of metallic Al. Hence, the approach based solely on Al deposition at room temperature seems to be feasible.

These first results motivate several future studies. The first question is whether the properties of

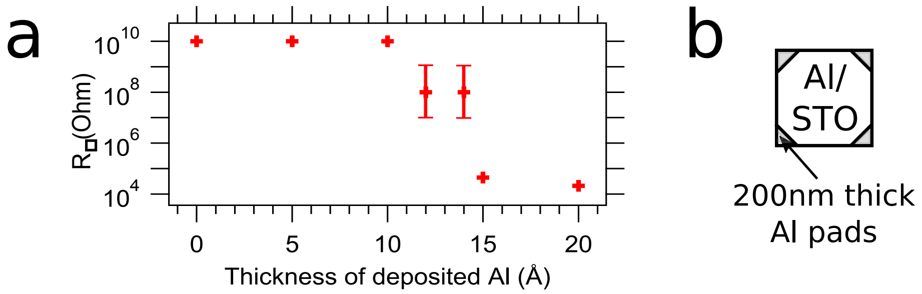

Figure 9.1: (a) Square resistance $R_\square$ on a logarithmic scale measured at the Al/$SrTiO_3$ interface as a function of thickness of the Al layer and using the Van-der-Pauw method. (b) Schematics of the configuration of the 200 nm-thick Al electrodes at the corners of the sample. The surface of the $SrTiO_3$ samples was TiO_2-terminated as described in section 2.4. To ensure a stoichiometric and insulating bulk but a clean surface, the samples were cleaned in ozone using an UV-lamp just before introducing them in the UHV chamber and annealed at low temperature $T \approx 250°C$ in UHV before depositing the Al film. Thus, in contrast to the high temperature annealing $T \approx 600°C$ used for the ARPES studies, there might be more organic contamination on the surface/ at the interface with the AlO_x layer.

the 2DES at the $AlO_x/SrTiO_3$ interface are similar to the ones of the $LaAlO_3/SrTiO_3$ interface. As already mentioned, one major advantage of the $AlO_x/SrTiO_3$ interface is the simplicity of the thin film growth as crystalline $LaAlO_3$ films are obtained by the relatively complicated and expensive pulsed laser deposition technique.

Functionalization of 2DESs at oxide interfaces

Additionally, the findings in this thesis open up the possibility to study 2DESs at the interface of AlO_x with various oxides other than $SrTiO_3$. The discovery of the 2DES at the $AlO_x/BaTiO_3$ discussed in section 6.2 could be an example for the functionalization of the 2DES. We studied $BaTiO_3$ thin films in which the ferroelectric polarization is uniform in the whole film (*i.e.* monodomain). One could assume that the conductivity of the 2DES at the $AlO_x/BaTiO_3$ interface depends on the polarization direction of the thin film. This ferroelectric, non-volatile control of the conductivity was already demonstrated in more complicated multi-oxide heterostructures such as $Pb(Zr_{0.2}Ti_{0.8})O_3/LaAlO_3/SrTiO_3$. [254, 255] The field-induced switching between a high and low resistance state corresponds to the binary language of today's electronics and hence, applications in electronics can be envisioned.

In principle, this approach is not limited to ferroelectrics but can be adapted to any material showing a hysteresis (*e.g.* ferromagnetic and ferroelastic materials). Hence, one could imagine a non-volatile control of the conductivity of the 2DES by a magnetic or stress field if one manages to create a 2DES at the interface of AlO_x and an insulating ferromagnetic or ferroelastic material. This idea of functionalizing the 2DES is illustrated in figure 9.2 on page 161.

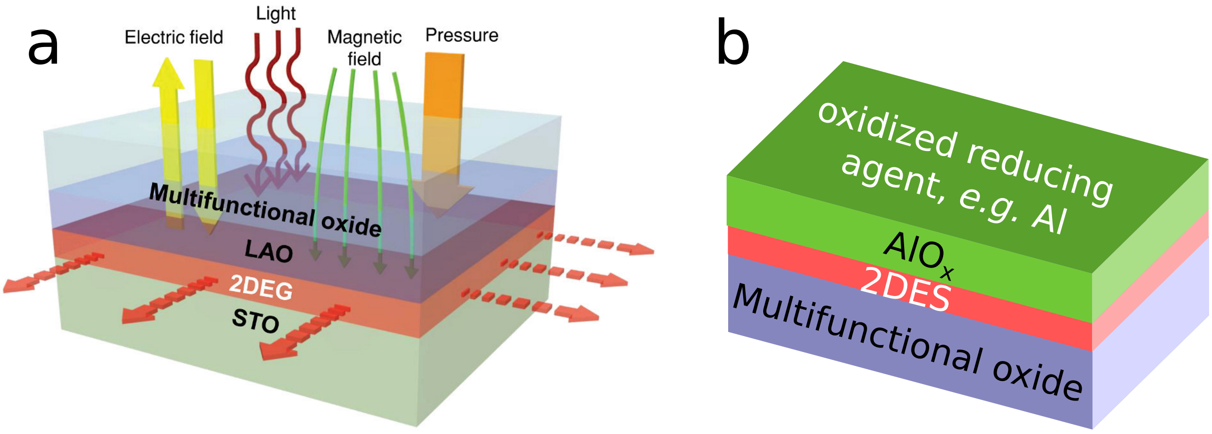

Figure 9.2: (a) Schematic illustration of the functionalization of the 2DES at the LaAlO$_3$/SrTiO$_3$ interface using epitaxial heterostructuring proposed by Kim *et al.*. [254] (b) Instead of altering the properties of the 2DES at the LaAlO$_3$/SrTiO$_3$ interface using a multifunctional oxide on top of LaAlO$_3$, we propose to create and control a 2DES in the multifunctional oxide *itself* using an elementary reducing agent (*e.g.* Al).

Publications in the framework of this thesis

- T. C. Rödel, F. Fortuna, S. Sengupta, E. Frantzeskakis, P. Le Fèvre, F. Bertran, B. Mercey, S. Matzen, G. Agnus, T. Maroutian, P. Lecoeur, and A. F. Santander-Syro. Universal Fabrication of 2D Electron Systems in Functional Oxides. *Adv. Mater.*, 28:1976, 2016
- T. C. Rödel, F. Fortuna, F. Bertran, M. Gabay, M. J. Rozenberg, A. F. Santander-Syro, and P. Le Fèvre. Engineering two-dimensional electron gases at the (001) and (101) surfaces of TiO_2 anatase using light. *Phys. Rev. B*, 92:041106(R), 2015
- T. C. Rödel, C. Bareille, F. Fortuna, C. Baumier, F. Bertran, P. Le Fèvre, M. Gabay, O Hijano Cubelos, M. J. Rozenberg, T. Maroutian, P. Lecoeur, and A. F. Santander-Syro. Orientational tuning of the Fermi sea of confined electrons at the $SrTiO_3$ (110) and (111) surfaces. *Phys. Rev. Appl.*, 1(5):051002, 2014
- A. F. Santander-Syro, F. Fortuna, C. Bareille, T. C. Rödel, G. Landolt, N. C. Plumb, J. H. Dil, and M. Radovic. Giant spin splitting of the two-dimensional electron gas at the surface of $SrTiO_3$. *Nat. Mater.*, 13(12):1085, 2014
- C. Bareille, F. Fortuna, T. C. Rödel, F. Bertran, M. Gabay, O. Hijano Cubelos, A. Taleb-Ibrahimi, P. Le Fèvre, M. Bibes, A. Barthélémy, T. Maroutian, P. Lecoeur, M. J. Rozenberg, and A. F. Santander-Syro. Two-dimensional electron gas with six-fold symmetry at the (111) surface of $KTaO_3$. *Sci. Rep.*, 4:3586, 2014

Works in which I participated during my thesis

- T. Taniuchi, Y. Motoyui, K. Morozumi, T.C. Rödel, F. Fortuna, A.F. Santander-Syro, and S. Shin. Imaging of room-temperature ferromagnetic nano-domains at the surface of a non-magnetic oxide. *Nat. Commun.*, 7:11781, 2016
- S. Backes, T. C. Rödel, F. Fortuna, E. Frantzeskakis, P. Le Fèvre, F. Bertran, M. Kobayashi, R. Yukawa, T. Mitsuhashi, M. Kitamura, K. Horiba, H. Kumigashira, R. Saint-Martin, A. Fouchet, B. Berini, Y. Dumont, A. J. Kim, F. Lechermann, H. O. Jeschke, M. J. Rozenberg, R. Valentí, and A. F. Santander-Syro. Hubbard band or oxygen vacancy states in the correlated electron metal $SrVO_3$? *arXiv Prepr.*, page 1602.06909v1, 2016

Bibliography

[1] A. F. Santander-Syro, O. Copie, T. Kondo, F. Fortuna, S. Pailhès, R. Weht, X. G. Qiu, F. Bertran, A. Nicolaou, A. Taleb-Ibrahimi, P. Le Fèvre, G. Herranz, M. Bibes, N. Reyren, Y. Apertet, P. Lecoeur, A. Barthélémy, and M. J. Rozenberg. Two-dimensional electron gas with universal subbands at the surface of $SrTiO_3$. *Nature*, 469(7329):189–93, 2011.

[2] W. Meevasana, P. D. C. King, R. H. He, S.-K. Mo, M. Hashimoto, A. Tamai, P. Songsiririthigul, F. Baumberger, and Z.-X. Shen. Creation and control of a two-dimensional electron liquid at the bare $SrTiO_3$ surface. *Nat. Mater.*, 10:114–8, 2011.

[3] A. F. Santander-Syro, C. Bareille, F. Fortuna, O. Copie, M. Gabay, F. Bertran, A. Taleb-Ibrahimi, P. Le Fèvre, G. Herranz, N. Reyren, M. Bibes, A. Barthélémy, P. Lecoeur, J. Guevara, and M. J. Rozenberg. Orbital symmetry reconstruction and strong mass renormalization in the two-dimensional electron gas at the surface of $KTaO_3$. *Phys. Rev. B*, 86:121107(R), 2012.

[4] P. D. C. King, R. H. He, T. Eknapakul, P. Buaphet, S.-K. Mo, Y. Kaneko, S. Harashima, Y. Hikita, M. S. Bahramy, C. Bell, Z. Hussain, Y. Tokura, Z.-X. Shen, H. Y. Hwang, F. Baumberger, and W. Meevasana. Subband Structure of a Two-Dimensional Electron Gas Formed at the Polar Surface of the Strong Spin-Orbit Perovskite $KTaO_3$. *Phys. Rev. Lett.*, 108(March):117602, 2012.

[5] M. D'Angelo, R. Yukawa, K. Ozawa, S. Yamamoto, T. Hirahara, S. Hasegawa, M. Silly, F. Sirotti, and I. Matsuda. Hydrogen-Induced Surface Metallization of $SrTiO_3(001)$. *Phys. Rev. Lett.*, 108:116802, 2012.

[6] R. Yukawa, S. Yamamoto, K. Ozawa, M. D'Angelo, M. Ogawa, M. G. Silly, F. Sirotti, and I. Matsuda. Electronic structure of the hydrogen-adsorbed $SrTiO_3(001)$ surface studied by polarization-dependent photoemission spectroscopy. *Phys. Rev. B*, 87:115314, 2013.

[7] N. C. Plumb, M. Salluzzo, E. Razzoli, M. Månsson, M. Falub, J. Krempasky, C. E. Matt, J. Chang, M. Schulte, J. Braun, H. Ebert, J. Minár, B. Delley, K.-J. Zhou, T. Schmitt, M. Shi, J. Mesot, L. Patthey, and M. Radović. Mixed Dimensionality of Confined Conducting Electrons in the Surface Region of $SrTiO_3$. *Phys. Rev. Lett.*, 113(8):086801, 2014.

[8] C. Bareille, F. Fortuna, T. C. Rödel, F. Bertran, M. Gabay, O. Hijano Cubelos, A. Taleb-Ibrahimi, P. Le Fèvre, M. Bibes, A. Barthélémy, T. Maroutian, P. Lecoeur, M. J. Rozen-

berg, and A. F. Santander-Syro. Two-dimensional electron gas with six-fold symmetry at the (111) surface of $KTaO_3$. *Sci. Rep.*, 4:3586, 2014.

[9] Z. Wang, Z. Zhong, X. Hao, S. Gerhold, B. Stoger, M. Schmid, J. Sanchez-Barriga, A. Varykhalov, C. Franchini, K. Held, and U. Diebold. Anisotropic two-dimensional electron gas at $SrTiO_3$(110). *Proc. Natl. Acad. Sci.*, 111(11):3933, 2014.

[10] T. C. Rödel, C. Bareille, F. Fortuna, C. Baumier, F. Bertran, P. Le Fèvre, M. Gabay, O Hijano Cubelos, M. J. Rozenberg, T. Maroutian, P. Lecoeur, and A. F. Santander-Syro. Orientational tuning of the Fermi sea of confined electrons at the $SrTiO_3$ (110) and (111) surfaces. *Phys. Rev. Appl.*, 1(5):051002, 2014.

[11] S. McKeown Walker, A. de la Torre, F. Y. Bruno, A. Tamai, T. K. Kim, M. Hoesch, M. Shi, M. S. Bahramy, P. D. C. King, and F. Baumberger. Control of a Two-Dimensional Electron Gas on $SrTiO(111)_3$ by Atomic Oxygen. *Phys. Rev. Lett.*, 113(17):177601, 2014.

[12] A. F. Santander-Syro, F. Fortuna, C. Bareille, T. C. Rödel, G. Landolt, N. C. Plumb, J. H. Dil, and M. Radovic. Giant spin splitting of the two-dimensional electron gas at the surface of $SrTiO_3$. *Nat. Mater.*, 13(12):1085, 2014.

[13] P. D. C. King, S. McKeown Walker, A. Tamai, A. de la Torre, T. Eknapakul, P. Buaphet, S.-K. Mo, W. Meevasana, M. S. Bahramy, and F. Baumberger. Quasiparticle dynamics and spin-orbital texture of the $SrTiO_3$ two-dimensional electron gas. *Nat. Commun.*, 5:3414, 2014.

[14] S. Moser, L. Moreschini, J. Jaćimović, O. S. Barišić, H. Berger, A. Magrez, Y. J. Chang, K. S. Kim, A. Bostwick, E. Rotenberg, L. Forró, and M. Grioni. Tunable Polaronic Conduction in Anatase TiO_2. *Phys. Rev. Lett.*, 110(19):196403, 2013.

[15] T. C. Rödel, F. Fortuna, F. Bertran, M. Gabay, M. J. Rozenberg, A. F. Santander-Syro, and P. Le Fèvre. Engineering two-dimensional electron gases at the (001) and (101) surfaces of TiO_2 anatase using light. *Phys. Rev. B*, 92:041106(R), 2015.

[16] S. M. Walker, F. Y. Bruno, Z. Wang, A. de la Torre, S. Riccó, A. Tamai, T. K. Kim, M. Hoesch, M. Shi, M. S. Bahramy, P. D. C. King, and F. Baumberger. Carrier-Density Control of the $SrTiO_3$(001) Surface 2D Electron Gas studied by ARPES. *Adv. Mater.*, 27(26):3894–3899, 2015.

[17] Z. Wang, S. McKeown Walker, A. Tamai, Z. Ristic, F. Y. Bruno, A. de la Torre, S. Riccò, N.C. Plumb, M. Shi, P. Hlawenka, J. Sanchez-Barriga, A. Varykhalov, T. K. Kim, M. Hoesch, P. D. C. King, W. Meevasana, U. Diebold, J. Mesot, M. Radović, and F. Baumberger. Tailoring the nature and strength of electron–phonon interactions in the $SrTiO_3$ (001) 2D electron liquid. *Nat. Mater.*, 15:835–839, 2016.

[18] C. Chen, J. Avila, E. Frantzeskakis, A. Levy, and M. C. Asensio. Observation of a two-dimensional liquid of Fröhlich polarons at the bare SrTiO3 surface. *Nat. Commun.*, 6:8585, 2015.

[19] T. C. Rödel, F. Fortuna, S. Sengupta, E. Frantzeskakis, P. Le Fèvre, F. Bertran, B. Mercey, S. Matzen, G. Agnus, T. Maroutian, P. Lecoeur, and A. F. Santander-Syro. Universal Fabrication of 2D Electron Systems in Functional Oxides. *Adv. Mater.*, 28:1976, 2016.

[20] A. Ohtomo and H. Y. Hwang. A high-mobility electron gas at the $LaAlO_3/SrTiO_3$ heterointerface. *Nature*, 427(6973):423–6, 2004.

[21] A. D. Caviglia, S. Gariglio, N. Reyren, D. Jaccard, T. Schneider, M. Gabay, S. Thiel, G. Hammerl, J. Mannhart, and J.-M. Triscone. Electric field control of the $LaAlO_3/SrTiO_3$ interface ground state. *Nature*, 456(7222):624–7, 2008.

[22] A. Brinkman, M. Huijben, M. van Zalk, J. Huijben, U. Zeitler, J. C. Maan, W. G. van der Wiel, G. Rijnders, D. H. A. Blank, and H. Hilgenkamp. Magnetic effects at the interface between non-magnetic oxides. *Nat. Mater.*, 6(7):493–6, 2007.

[23] D. A. Dikin, M. Mehta, C. W. Bark, C. M. Folkman, C. B. Eom, and V. Chandrasekhar. Coexistence of Superconductivity and Ferromagnetism in Two Dimensions. *Phys. Rev. Lett.*, 107(5):056802, 2011.

[24] Lu Li, C. Richter, J. Mannhart, and R. C. Ashoori. Coexistence of magnetic order and two-dimensional superconductivity at $LaAlO_3/SrTiO_3$ interfaces. *Nat. Phys.*, 7(10):762–766, 2011.

[25] J. A. Bert, B. Kalisky, C. Bell, M. Kim, Y. Hikita, H. Y. Hwang, and K. A. Moler. Direct imaging of the coexistence of ferromagnetism and superconductivity at the $LaAlO_3/SrTiO_3$ interface. *Nat. Phys.*, 7(10):767–771, 2011.

[26] N. Nakagawa, H. Y. Hwang, and D. A. Muller. Why some interfaces cannot be sharp. *Nat. Mater.*, 5(3):204–209, 2006.

[27] G. Herranz, M. Basletić, M. Bibes, C. Carrétéro, E. Tafra, E. Jacquet, K. Bouzehouane, C. Deranlot, A. Hamzić, J.-M. Broto, A. Barthélémy, and A. Fert. High Mobility in $LaAlO_3/SrTiO_3$ Heterostructures: Origin, Dimensionality, and Perspectives. *Phys. Rev. Lett.*, 98(21):216803, 2007.

[28] A. Kalabukhov, Yu. A. Boikov, I. T. Serenkov, V. I. Sakharov, J. Börjesson, N. Ljustina, E. Olsson, D. Winkler, and T. Claeson. Improved cationic stoichiometry and insulating behavior at the interface of $LaAlO_3/SrTiO_3$ formed at high oxygen pressure during pulsed-laser deposition. *EPL (Europhysics Lett.*, 93:37001, 2011.

[29] H. Y. Hwang, Y. Iwasa, M. Kawasaki, B. Keimer, N. Nagaosa, and Y. Tokura. Emergent phenomena at oxide interfaces. *Nat. Mater.*, 11(2):103–113, 2012.

[30] H. L. Stormer, D. C. Tsui, and A. C. Gossard. The fractional quantum Hall effect. *Rev. Mod. Phys*, 71(2):S298–305, 1999.

[31] S. Sze and K. K. Ng. *Physics of Semiconductor Devices.* Wiley-Interscience, 3rd edition, 2006.

[32] Y. Tokura. Orbital Physics in Transition-Metal Oxides. *Science*, 288(5465):462–468, 2000.

[33] E. Dagotto. Complexity in strongly correlated electronic systems. *Science*, 309(5732):257–62, 2005.

[34] E. Dagotto and Y. Tokura. Strongly Correlated Electronic Materials: Present and Future. *MRS Bull.*, 33(11):1037–1045, 2008.

[35] M. V. Ganduglia-Pirovano, A. Hofmann, and J. Sauer. Oxygen vacancies in transition metal and rare earth oxides: Current state of understanding and remaining challenges. *Surf. Sci. Rep.*, 62(6):219–270, 2007.

[36] Y. Wang, K. Zhao, X. Shi, G. Li, G. Xie, X. Lai, J. Ni, and L. Zhang. Mechanical writing of n-type conductive layers on the $SrTiO_3$ surface in nanoscale. *Sci. Rep.*, 5:10841, 2015.

[37] R. Waser, R. Dittmann, G. Staikov, and K. Szot. Redox-Based Resistive Switching Memories - Nanoionic Mechanisms, Prospects, and Challenges. *Adv. Mater.*, 21:2632–2663, 2009.

[38] K. Szot, M. Rogala, W. Speier, Z. Klusek, A. Besmehn, and R. Waser. TiO_2–a prototypical memristive material. *Nanotechnology*, 22(25):254001, 2011.

[39] W. Heckel, M. Wehlau, S. B. Maisel, T. Frauenheim, J. M. Knaup, and S. Müller. How the aggregation of oxygen vacanies in rutile based $TiO_{2-\delta}$ phases causes memristive behavior. *Phys. Rev. B*, 92:214104, 2015.

[40] Z. Q. Liu, W. M. Lü, S. L. Lim, X. P. Qiu, N. N. Bao, M. Motapothula, J. B. Yi, M. Yang, S. Dhar, and T. Venkatesan. Reversible room-temperature ferromagnetism in Nb-doped $SrTiO_3$ single crystals. *Phys. Rev. B*, 87(22):220405, 2013.

[41] M. Salluzzo, S. Gariglio, D. Stornaiuolo, V. Sessi, S. Rusponi, C. Piamonteze, G. M. De Luca, M. Minola, D. Marré, A. Gadaleta, H. Brune, F. Nolting, N. B. Brookes, and G. Ghiringhelli. Origin of Interface Magnetism in $BiMnO_3/SrTiO_3$ and $LaAlO_3/SrTiO_3$ Heterostructures. *Phys. Rev. Lett.*, 111(8):087204, 2013.

[42] G. Pacchioni. Oxygen Vacancy: The Invisible Agent on Oxide Surfaces. *ChemPhysChem*, 4(10):1041–1047, 2003.

[43] M. A. Henderson. A surface science perspective on TiO_2 photocatalysis. *Surf. Sci. Rep.*, 66:185–297, jun 2011.

[44] H. Jeen, W. S. Choi, M. D. Biegalski, C. M. Folkman, I-C. Tung, D. D. Fong, J. W. Freeland, D. Shin, H. Ohta, M. F. Chisholm, and H. N. Lee. Reversible redox reactions in an epitaxially stabilized $SrCoO_x$ oxygen sponge. *Nat. Mater.*, 12:1057–63, 2013.

[45] H. Tan, Z. Zhao, W. Zhu, E. N. Coker, B. Li, M. Zheng, W. Yu, H. Fan, and Z. Sun. Oxygen Vacancy Enhanced Photocatalytic Activity of Pervoskite $SrTiO_3$. *ACS Appl. Mater. & Interfaces*, 6(21):19184, 2014.

[46] Y. J. Chang, A. Bostwick, Y. S. Kim, K. Horn, and E. Rotenberg. Structure and correlation effects in semiconducting $SrTiO_3$. *Phys. Rev. B*, 81(23):235109, 2010.

[47] W. Meevasana, X. J. Zhou, B. Moritz, C.-C. Chen, R. H. He, S.-I. Fujimori, D. H. Lu, S.-K. Mo, R. G. Moore, F. Baumberger, T. P. Devereaux, D. van der Marel, N. Nagaosa, J. Zaanen, and Z.-X. Shen. Strong energy-momentum dispersion of phonon-dressed carriers in the lightly doped band insulator $SrTiO_3$. *New J. Phys.*, 12(2):023004, 2010.

[48] C. Cancellieri, A.S. Mishchenko, U. Aschauer, A. Filippetti, C. Faber, O. S. Barišić, V. A. Rogalev, T. Schmitt, N. Nagaosa, and VN Strocov. Polaronic metal state at the $LaAlO_3/SrTiO_3$ interface. *Nat. Commun.*, 7:10386, 2015.

[49] H. Takagi and H. Y. Hwang. An emergent change of phase for electronics. *Science*, 327(5973):1601–2, 2010.

[50] G. Kotliar and D. Vollhardt. Strongly Correlated Materials: Insights From Dynamical Mean-Field Theory. *Phys. Today*, 57(3):53, 2004.

[51] C. Noguera. Polar oxide surfaces. *J. Phys. Condens. Matter*, 12:R367, 2000.

[52] V. M. Goldschmidt. Die Gesetze der Krystallochemie. *Naturwissenschaften*, 14(21):477–485, 1926.

[53] P. Zubko, S. Gariglio, M. Gabay, P. Ghosez, and J.-M. Triscone. Interface physics in comlex oxide heterostructures. *Annu. Rev. Condens. Matter Phys.*, 2(1):141–165, 2011.

[54] R. D. Shannon. Revised effective ionic radii and systematic studies of interatomic distances in halides and chalcogenides. *Acta Crystallogr.*, A32:751, 1976.

[55] M. L. Medarde. Structural, magnetic and electronic properties of $RiNiO_3$ perovskites (R= rare earth). *J. Phys. Condens. Matter*, 9:1679–1707, 1997.

[56] T. Kimura, S. Ishihara, H. Shintani, T. Arima, K. Takahashi, K. Ishizaka, and Y. Tokura. Distorted perovskite with e_g^1 configuration as a frustrated spin system. *Phys. Rev. B*, 68(6):060403, 2003.

[57] J. Hemberger, A. Krimmel, T. Kurz, H.-A. Krug von Nidda, V. Ivanov, A. Mukhin, A. Balbashov, and A. Loidl. Structural, magnetic, and electrical properties of single-crystalline $La_{1-x}Sr_xMnO_3$ ($0.4 \leq x \leq 0.85$). *Phys. Rev. B*, 66(9):094410, 2002.

[58] K. H. Ahn, T. Lookman, and A. R. Bishop. Strain-induced metal-insulator phase coexistence in perovskite manganites. *Nature*, 804:401–404, 2004.

[59] J. M. Rondinelli, S. J. May, and J. W. Freeland. Control of octahedral connectivity in perovskite oxide heterostructures: An emerging route to multifunctional materials discovery. *MRS Bull.*, 37:261–270, 2012.

[60] M. Imada, A. Fujimori, and Y. Tokura. Metal-insulator transitions. *Rev. Mod. Phys.*, 70(4):1039–1263, 1998.

[61] R. Asahi, Y. Taga, W. Mannstadt, and A. J. Freeman. Electronic and optical properties of anatase TiO_2. *Phys. Rev. B*, 61(11):7459–7465, 2000.

[62] Y. Tokura. Critical features of colossal magnetoresistive manganites. *Reports Prog. Phys.*, 69(3):797–851, 2006.

[63] G. Catalan and J. F. Scott. Physics and Applications of Bismuth Ferrite. *Adv. Mater.*, 21(24):2463–2485, 2009.

[64] H. M. Christen and G. Eres. Recent advances in pulsed-laser deposition of complex oxides. *J. Phys. Condens. Mat.*, 20(26):264005, 2008.

[65] M. Huijben, A. Brinkman, G. Koster, G. Rijnders, H. Hilgenkamp, and D. H. A. Blank. Structure-Property Relation of $SrTiO_3/LaAlO_3$ Interfaces. *Adv. Mater.*, 21(17):1665–1677, 2009.

[66] F. M. Granozio, G. Koster, and G. Rijnders. Functional oxide interfaces. *MRS Bull.*, 38(12):1017–1023, 2013.

[67] H. Hilgenkamp. Novel transport phenomena at complex oxide interfaces. *MRS Bull.*, 38(12):1026–1031, 2013.

[68] J.M.D. Coey and W.E. Pickett. Magnetism at the edge: New phenomena at oxide interfaces. *MRS Bull.*, 38(12):1040–1047, 2013.

[69] M. Dawber and E. Bousquet. New developments in artificially layered ferroelectric oxide superlattices. *MRS Bull.*, 38(12):1048–1055, 2013.

[70] S. Stemmer and A. J. Millis. Quantum confinement in oxide quantum wells. *MRS Bull.*, 38(12):1032–1039, 2013.

[71] J. Mannhart, D. H. A. Blank, H. Y. Hwang, A. J. Millis, and J.-M. Triscone. Two-dimensional electron gases at oxide interfaces. *MRS Bull.*, 33:1027–1034, 2008.

[72] C. Cen, S. Thiel, J. Mannhart, and J. Levy. Oxide nanoelectronics on demand. *Science*, 323:1026–1030, 2009.

[73] J. Mannhart and D. G. Schlom. Oxide interfaces–an opportunity for electronics. *Science*, 327(5973):1607–11, 2010.

[74] J. F. Schooley, W. R. Hosler, and M. L. Cohen. Superconductivity in Semiconducting $SrTiO_3$. *Phys. Rev. Lett.*, 12(17):474–475, 1964.

[75] X. Lin, G. Bridoux, A. Gourgout, G. Seyfarth, S. Krämer, M. Nardone, B. Fauqué, and K. Behnia. Critical Doping for the Onset of a Two-Band Superconducting Ground State in $SrTiO_3$. *Phys. Rev. Lett.*, 112(20):207002, 2014.

[76] K. A. Müller and H. Burkard. $SrTiO_3$: An intrinsic qunatum paraelectric below 4K. *Phys. Rev. B*, 19(7):3593–602, 1979.

[77] S. E. Rowley, L. J. Spalek, R. P. Smith, M. P. M. Dean, M. Itoh, J. F. Scott, G. G. Lonzarich, and S. S. Saxena. Ferroelectric quantum criticality. *Nat. Phys.*, 10:367–372, 2014.

[78] W. D. Rice, P. Ambwani, M. Bombeck, J. D. Thompson, G. Haugstad, C. Leighton, and S. A. Crooker. Persistent optically induced magnetism in oxygen-deficient strontium titanate. *Nat. Mater.*, 13:481–487, 2014.

[79] J. H. Haeni, P. Irvin, W. Chang, R. Uecker, P. Reiche, Y. L. Li, S. Choudhury, W. Tian, M. E. Hawley, B. Craigo, A. K. Tagantsev, X. Q. Pan, S. K. Streiffer, L. Q. Chen, S. W. Kirchoefer, J. Levy, and D. G. Schlom. Room-temperature ferroelectricity in strained $SrTiO_3$. *Nature*, 430:583–586, 2004.

[80] U. Diebold. The surface science of titanium dioxide. *Surf. Sci. Rep.*, 48:53–229, 2003.

[81] Z. Zhang and J. T. Yates. Band bending in semiconductors: chemical and physical consequences at surfaces and interfaces. *Chem. Rev.*, 112(10):5520–51, 2012.

[82] A. Fujishima, X. Zhang, and D. Tryk. TiO_2 photocatalysis and related surface phenomena. *Surf. Sci. Rep.*, 63(12):515–582, 2008.

[83] A. Hagfeldt, G. Boschloo, L. Sun, L. Kloo, and H. Pettersson. Dye-sensitized solar cells. *Chem. Rev.*, 110(11):6595–663, 2010.

[84] M. Grätzel. Recent advances in sensitized mesoscopic solar cells. *Acc. Chem. Res.*, 42(11):1788–1798, 2009.

[85] Y. Furubayashi, T. Hitosugi, Y. Yamamoto, K. Inaba, G. Kinoda, Y. Hirose, T. Shimada, and T. Hasegawa. A transparent metal: Nb-doped anatase TiO_2. *Appl. Phys. Lett.*, 86(25):252101, 2005.

[86] D. B. Strukov, G. S. Snider, D. R. Stewart, and R. S. Williams. The missing memristor found. *Nature*, 453(7191):80–3, 2008.

[87] Y. Matsumoto, M. Murakami, T. Shono, T. Hasegawa, T. Fukumura, M. Kawasaki, P. Ahmet, T. Chikyow, S. Koshihara, and H. Koinuma. Room-Temperature Ferromagnetism in Transparent Transition Metal-Doped Titanium Dioxide. *Science*, 291(5505):854–856, 2001.

[88] T. Fukumura, Y. Yamada, H. Toyosaki, T. Hasegawa, H. Koinuma, and M. Kawasaki. Exploration of oxide-based diluted magnetic semiconductors toward transparent spintronics. *Appl. Surf. Sci.*, 223(1-3):62–67, 2004.

[89] A. Janotti and C. G. Van de Walle. Fundamentals of zinc oxide as a semiconductor. *Reports Prog. Phys.*, 72(12):126501, 2009.

[90] Ü. Özgür, D. Hofstetter, and H. Morkoç. ZnO devices and applications: a review of current status and future prospects. *Proc. IEEE*, 98(7):1255–1268, 2010.

[91] C. F. Klingshirn, B. K. Meyer, A. Waag, A. Hoffmann, and J. Geurts. *Zinc Oxide: From Fundamental Properties Towards Novel Applications.* Springer, 2010.

[92] J. Jagadish and S. J. Pearton. *Zinc Oxide Bulk, Thin Films and Nanostructures: Processing, Properties, and Applications.* Elsevier Science, 2011.

[93] A. Tsukazaki, A. Ohtomo, T. Kita, Y. Ohno, H. Ohno, and M. Kawasaki. Quantum Hall effect in polar oxide heterostructures. *Science*, 315(5817):1388–91, 2007.

[94] A. Tsukazaki, S. Akasaka, K. Nakahara, Y. Ohno, H. Ohno, D. Maryenko, A. Ohtomo, and M. Kawasaki. Observation of the fractional quantum Hall effect in an oxide. *Nat. Mater.*, 9(11):889–893, 2010.

[95] Y. Kozuka, M. Kim, C. Bell, B. G. Kim, Y. Hikita, and H. Y. Hwang. Two-dimensional normal-state quantum oscillations in a superconducting heterostructure. *Nature*, 462(7272):487–90, 2009.

[96] B. Jalan, S. Stemmer, S. Mack, and S. J. Allen. Two-dimensional electron gas in δ-doped $SrTiO_3$. *Phys. Rev. B*, 82(8):081103, 2010.

[97] M.M. Lee, J. Teuscher, T. Miyasaka, T. N. Murakami, and H. J. Snaith. Efficient hybrid solar cells based on meso-superstructured organometal halide perovskites. *Science*, 338:643, 2012.

[98] K. Ueno, S. Nakamura, H. Shimotani, A. Ohtomo, N. Kimura, T. Nojima, H. Aoki, Y. Iwasa, and M. Kawasaki. Electric-field-induced superconductivity in an insulator. *Nat. Mater.*, 7:855–858, 2008.

[99] K. Ueno, S. Nakamura, H. Shimotani, H. T. Yuan, N. Kimura, T. Nojima, H. Aoki, Y. Iwasa, and M. Kawasaki. Discovery of superconductivity in $KTaO_3$ by electrostatic carrier doping. *Nat. Nanotechnol.*, 6(7):408–12, 2011.

[100] T. Ando, A. B. Fowler, and F. Stern. Electronic properties of two-dimensional systems. *Rev. Mod. Phys.*, 54(2):437–621, 1982.

[101] P. D. C. King, T. D. Veal, and C. F. McConville. Nonparabolic coupled Poisson-Schrödinger solutions for quantized electron accumulation layers: Band bending, charge profile, and subbands at InN surfaces. *Phys. Rev. B - Condens. Matter Mater. Phys.*, 77(12):1–7, 2008.

[102] M. Stengel. First-Principles Modeling of Electrostatically Doped Perovskite Systems. *Phys. Rev. Lett.*, 106(13):136803, 2011.

[103] M. Setvin, C. Franchini, X. Hao, M. Schmid, M. Kaltak, G. Kresse, U. Diebold, A. Janotti, and C. G. Van de Walle. A direct view at polarons in TiO_2 rutile and anatase. *Phys. Rev. Lett.*, 113:086402, 2014.

[104] D. Kan, T. Terashima, R. Kanda, A. Masuno, K. Tanaka, S. Chu, H. Kan, A. Ishizumi, Y. Kanemitsu, Y. Shimakawa, and M. Takano. Blue-light emission at room temperature from Ar^+-irradiated $SrTiO_3$. *Nat. Mater.*, 4:816–819, 2005.

[105] A. Rubano, D. Paparo, F. Miletto Granozio, U. Scotti di Uccio, and L. Marrucci. Blue luminescence of $SrTiO_3$ under intense optical excitation. *J. Appl. Phys.*, 106(10):103515, 2009.

[106] Y. Yamada, H. Yasuda, T. Tayagaki, and Y. Kanemitsu. Temperature Dependence of Photoluminescence Spectra of Nondoped and Electron-Doped $SrTiO_3$: Crossover from Auger Recombination to Single-Carrier Trapping. *Phys. Rev. Lett.*, 102(24):247401, 2009.

[107] R. A. Van Der Berg, P. W. M. Blom, J. F. M. Cillessen, and R. M. Wolf. Field dependent permittivity in metal-semiconducting $SrTiO_3$ Schottky diodes. *Appl. Phys. Lett.*, 66:697, 1995.

[108] S. Suzuki, T. Yamamoto, H. Suzuki, K. Kawaguchi, K. Takahashi, and Y. Yoshisato. Fabrication and characterization of $Ba_{1-x}K_xBiO_3$/Nb-doped $SrTiO_3$ all-oxide-type Schottky junctions. *J. Appl. Phys.*, 81(10):6830–6836, 1997.

[109] A. Damascelli. Probing the Electronic Structure of Complex Systems by ARPES. *Phys. Scr.*, T109:61, 2004.

[110] F. Reinert and S. Hüfner. Photoemission spectroscopy - from early days to recent applications. *New J. Phys.*, 7:97, 2005.

[111] T. C. Rödel. Surface preparation and characterization of the 2DEGs at the surfaces of $SrTiO_3$. Technical report, University of Würzburg & Université Paris Sud, 2013.

[112] A. Einstein. Über einen die Erzeugung und Verwandlung des Lichtes betreffenden heuristischen Gesichtspunkt. *Ann. Phys.*, 1905.

[113] C. Bareille. *Effets d'une brisure de symétrie sur les structures électroniques d'URu$_2$Si$_2$ et de KTaO$_3$*. PhD thesis, Université Paris Sud, 2014.

[114] M. P. Seah and W. A. Dench. Quantitative electron spectroscopy of surfaces: A standard data base for electron inelastic mean free paths in solids. *Surf. Interface Anal.*, 1979.

[115] S. Hüfner. *Photoelectron spectroscopy: principles and applications.* Springer, 2003.

[116] J. Kröger, T. Greber, T. J. Kreutz, and J. Osterwalder. The photoemission Fermi edge as a sample thermometer? *J. Electron Spectros. Relat. Phenomena*, 113:241–251, 2001.

[117] C. Bareille. Structure électronique aux points X et Z de l'URu$_2$Si$_2$ autour de la transition d'ordre caché. Technical report, Université Paris-Sud, 2010.

[118] K.-J. Kim. Characteristics of synchrotron radiation. *AIP Conf. Proc.*, 184(May 2015):565–632, 1989.

[119] D. Attwood. *Soft X-rays and extreme ultraviolet radiation.* Cambridge University Press, 1999.

[120] S. Tanaka, K. Mase, and S. Nagaoka. Photostimulated ion desorption from the TiO$_2$(110) and ZnO surfaces. *Surf. Sci.*, 572(1):43–58, 2004.

[121] A. Janotti, J. B. Varley, M. Choi, and C. G. Van de Walle. Vacancies and small polarons in SrTiO$_3$. *Phys. Rev. B*, 90(8):085202, 2014.

[122] N. P. Guisinger, T. S. Santos, J. R. Guest, T.-Y. Chien, A. Bhattacharya, J. W. Freeland, and M. Bode. Nanometer-scale striped surface terminations on fractured SrTiO$_3$ surfaces. *ACS Nano*, 3(12):4132–6, 2009.

[123] Q. Fu and T. Wagner. Interaction of nanostructured metal overlayers with oxide surfaces. *Surf. Sci. Rep.*, 62(11):431–498, 2007.

[124] R. Shimizu, K. Iwaya, T. Ohsawa, S. Shiraki, T. Hasegawa, T. Hashizume, and T. Hitosugi. Effect of oxygen deficiency on SrTiO$_3$(001) surface reconstructions. *Appl. Phys. Lett.*, 100:263106, 2012.

[125] J. Goniakowski, F. Finocchi, and C. Noguera. Polarity of oxide surfaces and nanostructures. *Reports Prog. Phys.*, 71(1):016501, 2008.

[126] A. Pancotti, N. Barrett, L. F. Zagonel, and G. M. Vanacore. Multiple scattering x-ray photoelectron diffraction study of the SrTiO$_3$(100) surface. *J. Appl. Phys.*, 106(2009):034104, 2009.

[127] N. Bickel, G. Schmidt, K. Heinz, and K. Müller. Ferroelectric relaxation of the SrTiO$_3$(100) surface. *Phys. Rev. Lett.*, 62(17):2009–2011, 1989.

[128] R. Sachs, Z. Lin, and J. Shi. Ferroelectric-like $SrTiO_3$ surface dipoles probed by graphene. *Sci. Rep.*, 4:3657, 2014.

[129] M. Kawasaki, K. Takahashi, T. Maeda, R. Tsuchiya, M. Shinohara, O. Ishiyama, T. Yonezawa, M. Yoshimoto, and H. Koinuma. Atomic control of the $SrTiO_3$ crystal surface. *Science*, 266:1540, 1994.

[130] G. Koster, B. L. Kropman, Guus J. H. M. Rijnders, Dave H. A. Blank, and H. Rogalla. Influence of the surface treatment on the homoepitaxial growth of $SrTiO_3$. *Mater. Sci. Eng. B*, 56:209–212, 1998.

[131] G. Lee. Realization of ultrasmooth surface with atomic scale step structure on $LiNbO_3$ and $LiTaO_3$ substrates. *Opt. Express*, 10(13):556–60, 2002.

[132] S. Woo, H. Jeong, S. A. Lee, H. Seo, M. Lacotte, A. David, H. Y. Kim, W. Prellier, Y. Kim, and W. S. Choi. Surface properties of atomically flat poly-crystalline $SrTiO_3$. *Sci. Rep.*, 5:8822, 2015.

[133] C. Rodenbuücher, S. Wicklein, R. Waser, and K. Szot. Insulator-to-metal transition of $SrTiO_3$:Nb single crystal surfaces induced by Ar^+ bombardment. *Appl. Phys. Lett.*, 102(10):101603, 2013.

[134] P. Pal, P. Kumar, V. Aswin, A. Dogra, and A. G. Joshi. Chemical potential shift and gap-state formation in $SrTiO_3$- revealed by photoemission spectroscopy. *J. Appl. Phys.*, 116:053704, 2014.

[135] M. Kawasaki, A. Ohtomo, and T. Arakane. Atomic control of $SrTiO_3$ surface for perfect epitaxy of perovskite oxides. *Appl. Surf. Sci.*, 107:102–106, 1996.

[136] D. Hrabovsky, B. Berini, A. Fouchet, D. Aureau, N. Keller, A. Etcheberry, and Y. Dumont. Strontium titanate (100) surfaces monitoring by high temperature in-situ ellipsometry. *Appl. Surf. Sci.*, 367:307–311, 2016.

[137] M. Naito and H. Sato. Reflection high-energy electron diffraction study on the $SrTiO_3$ surface structure. *Phys. C*, 229:1–11, 1994.

[138] A. Biswas, P. B. Rossen, C.-H. Yang, W. Siemons, M.-H. Jung, I. K. Yang, R. Ramesh, and Y. H. Jeong. Universal Ti-rich termination of atomically flat $SrTiO_3$ (001), (110), and (111) surfaces. *Appl. Phys. Lett.*, 98(5):051904, 2011.

[139] J. Chang, Y.-S. Park, and S.-K. Kim. Atomically flat single-terminated $SrTiO_3$ (111) surface. *Appl. Phys. Lett.*, 92(15):152910, 2008.

[140] T. Kolodiazhnyi, M. Tachibana, H. Kawaji, J. Hwang, and E. Takayama-Muromachi. Persistence of Ferroelectricity in $BaTiO_3$ through the Insulator-Metal Transition. *Phys. Rev. Lett.*, 104:147602, 2010.

[141] J. E. Rault, J. Dionot, C. Mathieu, V. Feyer, C. M. Schneider, G. Geneste, and N. Barrett. Polarization Sensitive Surface Band Structure of Doped $BaTiO_3$(001). *Phys. Rev. Lett.*, 111:127602, 2013.

[142] M. Setvín, B. Daniel, V. Mansfeldova, L. Kavan, P. Scheiber, M. Fidler, M. Schmid, and U. Diebold. Surface preparation of TiO_2 anatase (101): Pitfalls and how to avoid them. *Surf. Sci.*, 626:61–67, 2014.

[143] A. N. Mariano and R. E. Hanneman. Crystallographic Polarity of ZnO Crystals. *J. Appl. Phys.*, 34(1963):384–388, 1963.

[144] O. Dulub, L. A. Boatner, and U. Diebold. STM study of the geometric and electronic structure of ZnO(0001)-Zn, (0001)-O, (1010), and (1120) surfaces. *Surf. Sci.*, 519:201–217, 2002.

[145] R. Di Capua, M. Radovic, G. M. De Luca, I. Maggio-Aprile, F. Miletto Granozio, N. C. Plumb, Z. Ristic, U. Scotti di Uccio, R. Vaglio, and M. Salluzzo. Observation of a two-dimensional electron gas at the surface of annealed $SrTiO_3$ single crystals by scanning tunneling spectroscopy. *Phys. Rev. B*, 86(15):155425, 2012.

[146] V. N. Ageev. Desorption induced by electronic transitions. *Prog. Surf. Sci.*, 68(25):3737–3740, jun 1994.

[147] T. Tachibana, T. Hirayama, and Y. Nagashima. Positron-annihilation-induced ion desorption from TiO_2(110). *Phys. Rev. B*, 89(20):201409, 2014.

[148] R.D. Ramsier and J.T. Yates. Electron-stimulated desorption: Principles and applications. *Surf. Sci. Rep.*, 12(6-8):246–378, 1991.

[149] M. L. Knotek and P. J. Feibelman. Ion desorption by core-hole Auger decay. *Phys. Rev. Lett.*, 40(April):964, 1978.

[150] O. Dulub, M. Batzilln, S. Solovev, E. Loginova, A. Alchagirov, T. E. Madey, and U. Diebold. Electron-induced oxygen desorption from the TiO_2(011)-2x1 surface leads to self-organized vacancies. *Science*, 317(5841):1052–6, 2007.

[151] C. M. Yim, C. L. Pang, and G. Thornton. Oxygen Vacancy Origin of the Surface Band-Gap State of TiO_2(110). *Phys. Rev. Lett.*, 104(3):036806, 2010.

[152] A. Hirata, K. Saiki, A. Koma, and A. Ando. Electronic structure of a SrO-terminated $SrTiO_3$(100) surface. *Surf. Sci.*, 319:267–271, 1994.

[153] K. Takeyasu, K. Fukada, M. Matsumoto, and K. Fukutani. Control of the surface electronic structure of $SrTiO_3$(001) by modulation of the density of oxygen vacancies. *J. Phys. Condens. Matter*, 25(16):162202, 2013.

[154] A. Locatelli, T. Pabisiak, A. Pavloska, T. O. Mentes, L. Aballe, A. Kiejna, and E. Bauer. One-dimensional Au on TiO_2. *J. Phys. Condens. Matter*, 19:082202, 2007.

[155] A. N. Shultz, W. Jang, W. M. III Hetherington, D. R. Baer, L.-Q. Wang, and M. H. Engelhard. Comparative second harmonic generation and X-ray photoelectron spectroscopy studies of the UV creation and O_2 healing of Ti^{3+} defects on (110) rutile TiO_2 surfaces. *Surf. Sci.*, 339:114–124, 1995.

[156] J. Shen, H. Lee, R. Valentí, and H. Jeschke. Ab initio study of the two-dimensional metallic state at the surface of $SrTiO_3$: Importance of oxygen vacancies. *Phys. Rev. B*, 86(19):195119, 2012.

[157] H. O. Jeschke, J. Shen, and R. Valenti. Localized versus itinerant states created by multiple oxygen vacancies in $SrTiO_3$. *New J. Phys.*, 17:023034, 2015.

[158] A. R. Silva and G. M. Dalpian. Oxygen vacancies at the surface of $SrTiO_3$ thin films. *J. Appl. Phys.*, 115(3):033710, 2014.

[159] H. L. Zhuang, P. Ganesh, V. R. Cooper, H. Xu, and P. R. C. Kent. Understanding the interactions between oxygen vacancies at $SrTiO_3$ (001) surfaces. *Phys. Rev. B*, 90(6):064106, 2014.

[160] C. Lin and A. A. Demkov. Electron Correlation in Oxygen Vacancy in $SrTiO_3$. *Phys. Rev. Lett.*, 111(21):217601, 2013.

[161] M. Choi, F. Oba, Y. Kumagai, and I. Tanaka. Anti-ferrodistortive-like oxygen-octahedron rotation induced by the oxygen vacancy in cubic $SrTiO_3$. *Adv. Mater.*, 25(1):86–90, 2013.

[162] C. Lin, C. Mitra, and A. A. Demkov. Orbital ordering under reduced symmetry in transition metal perovskites: Oxygen vacancy in $SrTiO_3$. *Phys. Rev. B*, 86(16):161102, 2012.

[163] N. Pavlenko, T. Kopp, E. Tsymbal, J. Mannhart, and G. Sawatzky. Oxygen vacancies at titanate interfaces: Two-dimensional magnetism and orbital reconstruction. *Phys. Rev. B*, 86:064431, 2012.

[164] P. Krüger, S. Bourgeois, B. Domenichini, H. Magnan, D. Chandesris, P. Le Fèvre, A. Flank, J. Jupille, L. Floreano, A. Cossaro, A. Verdini, and A. Morgante. Defect States at the TiO_2(110) Surface Probed by Resonant Photoelectron Diffraction. *Phys. Rev. Lett.*, 100(5):055501, 2008.

[165] M. Setvin, M. Schmid, and U. Diebold. Aggregation and electronically induced migration of oxygen vacancies in TiO_2 anatase. *Phys. Rev. B*, 91(19):195403, 2015.

[166] E. Di Gennaro, U. Coscia, G. Ambrosone, A. Khare, F. M. Granozio, and U. S. di Uccio. Photoresponse dynamics in amorphous-$LaAlO_3$/$SrTiO_3$ interfaces. *Sci. Rep.*, 5:8393, 2015.

[167] Y. Aiura, I. Hase, H. Bando, T. Yasue, T. Saitoh, and D.S. Dessau. Photoemission study of the metallic state of lightly electron-doped $SrTiO_3$. *Surf. Sci.*, 515:61–74, 2002.

[168] A. Thomas, W. Flavell, A. Kumarasinghe, A. Mallick, D. Tsoutsou, G. Smith, R. Stockbauer, S. Patel, M. Grätzel, and R. Hengerer. Resonant photoemission of anatase TiO_2 (101) and (001) single crystals. *Phys. Rev. B*, 67(3):035110, 2003.

[169] S. A. Chambers, T. C. Droubay, C. Capan, and G. Y. Sun. Unintentional F doping of $SrTiO_3$(001) etched in HF acid-structure and electronic properties. *Surf. Sci.*, 606:554–558, 2012.

[170] R. C. Hatch, K. D. Fredrickson, M. Choi, C. Lin, H. Seo, A. B. Posadas, and A. A. Demkov. Surface electronic structure for various surface preparations of Nb-doped $SrTiO_3$(001). *J. Appl. Phys.*, 114(10):103710, 2013.

[171] Y. Ishida. Private communications. Technical report, Institute of Solid State Physics - University of Tokyo, 2014.

[172] A. Thomas, W. Flavell, A. Mallick, A. Kumarasinghe, D. Tsoutsou, N. Khan, C. Chatwin, S. Rayner, G. Smith, R. Stockbauer, S. Warren, T. Johal, S. Patel, D. Holland, A. Taleb, and F. Wiame. Comparison of the electronic structure of anatase and rutile TiO_2 single-crystal surfaces using resonant photoemission and x-ray absorption spectroscopy. *Phys. Rev. B*, 75(3):035105, 2007.

[173] X. Hao, Z. Wang, M. Schmid, U. Diebold, and C. Franchini. Coexistence of trapped and free excess electrons in $SrTiO_3$. *Phys. Rev. B*, 91:085205, 2015.

[174] C. D. Valentin, G. Pacchioni, and A. Selloni. Reduced and n-type doped TiO_2: nature of Ti^{3+} species. *J. Phys. Chem. C*, 113:20543–20552, 2009.

[175] C. Sánchez-Sánchez, M.G. Garnier, P. Aebi, M. Blanco-Rey, P.L. de Andres, J.a. Martín-Gago, and M.F. López. Valence band electronic structure characterization of the rutile TiO_2 (110)-(1×2) reconstructed surface. *Surf. Sci.*, 608:92–96, 2013.

[176] M. Emori, M. Sugita, K. Ozawa, and H. Sakama. Electronic structure of epitaxial anatase TiO_2 films: Angle-resolved photoelectron spectroscopy study. *Phys. Rev. B*, 85(3):035129, 2012.

[177] H. A. Huy, B. Aradi, T. Frauenheim, and P. Deák. Calculation of carrier-concentration-dependent effective mass in Nb-doped anatase crystals of TiO_2. *Phys. Rev. B*, 83(15):155201, 2011.

[178] H. Kamisaka, T. Hitosugi, T. Suenaga, T. Hasegawa, and K. Yamashita. Density functional theory based first-principle calculation of Nb-doped anatase TiO_2 and its interactions with oxygen vacancies and interstitial oxygen. *J. Chem. Phys.*, 131(3):034702, 2009.

[179] Y. Hirose, N. Yamada, S. Nakao, T. Hitosugi, T. Shimada, and T. Hasegawa. Large electron mass anisotropy in a d-electron-based transparent conducting oxide: Nb-doped anatase TiO_2 epitaxial films. *Phys. Rev. B*, 79(16):165108, 2009.

[180] G. Berner, M. Sing, H. Fujiwara, A. Yasui, Y. Saitoh, A. Yamasaki, Y. Nishitani, A. Sekiyama, N. Pavlenko, T. Kopp, C. Richter, J. Mannhart, S. Suga, and R. Claessen. Direct k-space mapping of the electronic structure in an oxide-oxide interface. *Phys. Rev. Lett.*, 110(24):247601, 2013.

[181] W. Schottky. Zur Halbleitertheorie der Sperrschicht-und Spitzengleichrichter. *Zeitschrift für Phys.*, pages 367–414, 1939.

[182] N. F. Mott. Note on the contact between a metal and an insulator or semi-conductor. *Math. Proc. Cambridge Philos. Soc.*, 34(04):568, 1938.

[183] Y. Z. Chen, N. Pryds, J. E. Kleibeuker, G. Koster, J. Sun, E. Stamate, B. Shen, G. Rijnders, and S. Linderoth. Metallic and insulating interfaces of amorphous $SrTiO_3$-based oxide heterostructures. *Nano Lett.*, 11(9):3774–8, 2011.

[184] J. Delahaye and T. Grenet. Metallicity of the $SrTiO_3$ surface induced by room temperature evaporation of alumina. *J. Phys. D. Appl. Phys.*, 45(31):315301, 2012.

[185] E. Lesne, N. Reyren, D. Doennig, R. Mattana, H. Jaffrès, V. Cros, F. Petroff, F. Choueikani, P. Ohresser, R. Pentcheva, A. Barthélémy, and M. Bibes. Suppression of the critical thickness threshold for conductivity at the $LaAlO_3/SrTiO_3$ interface. *Nat. Commun.*, 5:4291, 2014.

[186] Q. Fu and T. Wagner. Metal/oxide interfacial reactions: Oxidation of metals on $SrTiO_3(100)$ and $TiO_2(110)$. *J. Phys. Chem. B*, 109:11697–11705, 2005.

[187] S. Y. Moon, C. W. Moon, H. J. Chang, T. Kim, C.-Y. Kang, H.-J. Choi, J.-S. Kim, S.-H. Baek, and H. W. Jang. Thermal stability of 2DEG at amorphous $LaAlO_3$/crystalline $SrTiO_3$ heterointerfaces. *Nano Converg.*, 3:7, 2016.

[188] N. Cai, G. Zhou, K. Müller, and D. E. Starr. Tuning the limiting thickness of a thin oxide layer on Al(111) with oxygen gas pressure. *Phys. Rev. Lett.*, 107(3):035502, 2011.

[189] S. Goswami, E. Mulazimoglu, L. M. K. Vandersypen, and A. D. Caviglia. Nanoscale Electrostatic Control of Oxide Interfaces. *Nano Lett.*, 15(4):2627–2632, 2015.

[190] K. Ozawa and K. Mase. Metallization of ZnO(1010) by adsorption of hydrogen, methanol, and water: Angle-resolved photoelectron spectroscopy. *Phys. Rev. B*, 81:205322, 2010.

[191] K. Ozawa and K. Mase. Comparison of the surface electronic structures of H-adsorbed ZnO surfaces: An angle-resolved photoelectron spectroscopy study. *Phys. Rev. B*, 83:125406, 2011.

[192] L. F. J. Piper, A. R. H. Preston, A. Fedorov, S. W. Cho, A. DeMasi, and K. E. Smith. Direct evidence of metallicity at ZnO $(000\bar{1}) - (1 \times 1)$ surfaces from angle-resolved photoemission spectroscopy. *Phys. Rev. B*, 81:233305, 2010.

[193] A. Janotti and C. G. Van De Walle. Oxygen vacancies in ZnO. *Appl. Phys. Lett.*, 87:122102, 2005.

[194] Y.-S. Kim and C. H. Park. Rich variety of defects in ZnO via an attractive interaction between O vacancies and Zn interstitials: Origin of n-type doping. *Phys. Rev. Lett.*, 102(8):086403, 2009.

[195] S. Lany and A. Zunger. Many-body GW calculation of the oxygen vacancy in ZnO. *Phys. Rev. B*, 81(11):113201, 2010.

[196] B. K. Meyer, H. Alves, D. M. Hofmann, W. Kriegseis, D. Forster, F. Bertram, J. Christen, A. Hoffmann, M. Straßburg, M. Dworzak, U. Haboeck, and A. V. Rodina. Bound exciton and donor-acceptor pair recombinations in ZnO. *Phys. Status Solidi Basic Res.*, 241(2):231–260, 2004.

[197] M. A. Hossain, J. D. F. Mottershead, D. Fournier, A. Bostwick, J. L. McChesney, E. Rotenberg, R. Liang, W. N. Hardy, G. A. Sawatzky, I. S. Elfimov, D. A. Bonn, and A. Damascelli. In situ doping control of the surface of high-temperature superconductors. *Nat. Phys.*, 4:527–531, 2008.

[198] M.-Y. Yao, L. Miao, N. L. Wang, J. H. Dil, M. Z. Hasan, D. D. Guan, C. L. Gao, C. Liu, D. Qian, and J. Jia. Surface states in lightly hole-doped sodium cobaltate $Na_{1-y}CoO_2$. *Phys. Rev. B*, 91:161411(R), 2015.

[199] P. J. Hardman, R. Casanova, K. Prabhakaran, C. A. Muryn, P. L. Wincott, and G. Thornton. Electronic-Structure Effects of Potassium Adsorption on $TiO_2(100)$. *Surf. Sci.*, 269:677–681, 1992.

[200] K. Prabhakaran, D. Purdie, R. Casanova, C. A. Muryn, P. J. Hardman, P. L. Wincott, and G. Thornton. Alkali-metal-to-substrate charge transfer in $TiO_2(100)$ c (2×2) K. *Phys. Rev. B*, 45(12):6969, 1992.

[201] B.E. Hayden and G.P. Nicholson. An ellipsometric study of potassium adsorption on $TiO_2(110)$. *Surf. Sci.*, 274(110):277–286, 1992.

[202] R.J. Lad and L. S. Dake. Electronic and structural properties of interfaces created by potassium deposited on $TiO_2(110)$ surfaces. *Mat. Res. Soc. Symp. Proc.*, 238:823, 1992.

[203] E. E. Mori and M. Kamaratos. Adsorption Kinetics of Potassium on $SrTiO_3(001)$. *Surf. Rev. Lett.*, 13:681, 2006.

[204] A. W. Grant and C. T. Campbell. Cesium adsorption on $TiO_2(110)$. *Phys. Rev. B*, 55(3):1844–1851, 1997.

[205] K. Akikubo, I. Matsuda, D. Schmaus, G. Marcaud, R.-Y. Liu, M. G. Silly, F. Sirotti, and M. D'Angelo. Observation of an e_g-derived Metallic Band at the Cs/$SrTiO_3$ Interface

by Polarization-dependent Photoemission Spectroscopy. *Thin Solid Films*, 603:149–153, 2016.

[206] J. Lee, C. Lin, and A. A. Demkov. Metal-induced charge transfer, structural distortion, and orbital order in $SrTiO_3$ thin films. *Phys. Rev. B*, 87(16):165103, 2013.

[207] G. Herranz, F. Sánchez, N. Dix, M. Scigaj, and J. Fontcuberta. High mobility conduction at (110) and (111) $LaAlO_3/SrTiO_3$ interfaces. *Sci. Rep.*, 2(110):758, 2012.

[208] A. Annadi, X. Wang, K. Gopinadhan, W. M. Lü, A. Roy Barman, Z. Q. Liu, A. Srivastava, S. Saha, Y. L. Zhao, S. W. Zeng, S. Dhar, N. Tuzla, E. Olsson, Q. Zhang, B. Gu, S. Yunoki, S. Maekawa, H. Hilgenkamp, T. Venkatesan, and Ariando. Anisotropic two-dimensional electron gas at the $LaAlO_3/SrTiO_3$ (110) interface. *Nat. Commun.*, 4:1838, 2013.

[209] G. Herranz, G. Singh, N. Bergeal, A. Jouan, J. Lesueur, J. Gázquez, M. Varela, M. Scigaj, N. Dix, F. Sánchez, and J. Fontcuberta. Engineering two-dimensional superconductivity and Rashba spin-orbit coupling in $LaAlO_3/SrTiO_3$ quantum wells by selective orbital occupancy. *Nat Commun*, 6:6028, 2015.

[210] D. Xiao, W. Zhu, Y. Ran, N. Nagaosa, and S. Okamoto. Interface engineering of quantum Hall effects in digital transition metal oxide heterostructures. *Nat. Commun.*, 2:596, 2011.

[211] K.-Y. Yang, W. Zhu, D. Xiao, S. Okamoto, Z. Wang, and Y. Ran. Possible interaction-driven topological phases in (111) bilayers of $LaNiO_3$. *Phys. Rev. B*, 84(20):201104, 2011.

[212] A. Rüegg and G. A. Fiete. Topological insulators from complex orbital order in transition-metal oxides heterostructures. *Phys. Rev. B*, 84(20):201103, 2011.

[213] D. Doennig, W. E. Pickett, and R. Pentcheva. Massive symmetry breaking in $LaAlO_3/SrTiO_3$(111) quantum wells: A three-orbital strongly correlated generalization of graphene. *Phys. Rev. Lett.*, 111:126804, 2013.

[214] J. C. Slater and G. F. Koster. Simplified LCAO method for the periodic potential problem. *Phys. Rev.*, 94(6):1498, 1954.

[215] G. Khalsa and A. H. MacDonald. Theory of the $SrTiO_3$ surface state two-dimensional electron gas. *Phys. Rev. B*, 86:125121, 2012.

[216] Z. Zhong, A. Tóth, and K. Held. Theory of spin-orbit coupling at $LaAlO_3/SrTiO_3$ interfaces and $SrTiO_3$ surfaces. *Phys. Rev. B*, 87:161102(R), 2013.

[217] J.-M. Carter. *Interplay between spin-orbit coupling, electronic correlations and lattice distortions in perovskite iridates.* PhD thesis, University of Toronto, 2013.

[218] Y. Wu, C. Won, E. Rotenberg, H. Zhao, F. Toyoma, N. Smith, and Z. Qiu. Dispersion of quantum well states in Cu/Co/Cu(001). *Phys. Rev. B*, 66(24):245418, 2002.

[219] K. Yoshimatsu, K. Horiba, H. Kumigashira, T. Yoshida, A. Fujimori, and M. Oshima. Metallic Quantum Well States in Artificial Structures of Strongly Correlated Oxide. *Science*, 333:319–322, 2011.

[220] A. Mugarza, J. Ortega, A. Mascaraque, E. Michel, K. Altmann, and F. Himpsel. Periodicity and thickness effects in the cross section of quantum well states. *Phys. Rev. B*, 62(19):12672–12675, 2000.

[221] E. D. Hansen, T. Miller, and T. C. Chiang. Quantum-well or bulklike behaviour of Cu layers on Co. *J. Phys. Condens. Matter*, 9:L435–L440, 1997.

[222] T. Yamamoto, S. Suzuki, K. Kawaguchi, and K. Takahashi. Temperature Dependence of the Ideality Factor of $Ba_{1-x}K_xBiO_3$/Nb-doped $SrTiO_3$ All-Oxide- Type Schottky Junctions. *Jpn. J. Appl. Phys.*, 37:4737, 1998.

[223] K. X. Jin, B. C. Luo, Y. F. Li, C. L. Chen, and T. Wu. Photoinduced phase transition and relaxation in bare $SrTiO_3$ single crystals. *J. Appl. Phys.*, 114:033509, 2013.

[224] T. Hasegawa, S. Mouri, Y. Yamada, and K. Tanaka. Giant Photo-Induced Dielectricity in $SrTiO_3$. *J. Phys. Soc. Japan*, 72(1):41–44, 2003.

[225] V. V. Lemanov, A. V. Sotnikov, E. P. Smirnova, M. Weihnacht, and R. Kunze. Perovskite $CaTiO_3$ as an incipient ferroelectric. *Solid State Commun.*, 110:611–614, 1999.

[226] J. H. Barrett. Dielectric constant in perovskite type crystals. *Phys. Rev.*, 86(1):1950–1952, 1952.

[227] M. I. Marqués, C. Arago, and J. A. Gonzalo. Quantum paraelectric behavior of $SrTiO_3$: Relevance of the structural phase transition temperature. *Phys. Rev. B*, 72:092103, 2005.

[228] G. A. Samara and P. S. Peercy. Pressure and Temperature Dependence of the Static Dielectric Constants and Raman Spectra of TiO_2 (Rutile). *Phys. Rev. B*, 7(3):1131, 1973.

[229] R. A. Parker. Static Dielectric Constant of Rutile (TiO_2), 1.6-1060°K. *Phys. Rev.*, 124(6):1719, 1961.

[230] A. Spinelli, M. A. Torija, C. Liu, C. Jan, and C. Leighton. Electronic transport in doped $SrTiO_3$: Conduction mechanisms and potential applications. *Phys. Rev. B*, 81(15):155110, 2010.

[231] N. F. Mott. Metal-insulator transitions. *Rev. Mod. Phys.*, 40(4):667, 1968.

[232] H. Zhang, L. Yan, and H.-U. Habermeier. Unusual ultraviolet photoconductivity in single crystalline $SrTiO_3$. *J. physics. Condens. matter*, 25(3):035802, 2013.

[233] M. C. Tarun, F. A. Selim, and M. D. McCluskey. Persistent Photoconductivity in Strontium Titanate. *Phys. Rev. Lett.*, 111(18):187403, 2013.

[234] Y. Kozuka, Y. Hikita, T. Susaki, and H. Hwang. Optically tuned dimensionality crossover in photocarrier-doped $SrTiO_3$: Onset of weak localization. *Phys. Rev. B*, 76(8):085129, 2007.

[235] K. V. Reich, M. Schecter, and B. I. Shklovskii. Accumulation, inversion and depletion layers in $SrTiO_3$. *Phys. Rev. B*, 91:115303, 2015.

[236] H. Uwe and T. Sakudo. Stress-induced ferroelectricity and soft phonon modes in $SrTiO_3$. *Phys. Rev. B*, 13(1):271, 1976.

[237] H. Uwe and T. Sakudo. Raman-scattering study of stress-induced ferroelectricity in $KTaO_3$. *Phys. Rev. B*, 15(1):337, 1977.

[238] Y. S. Kim, D. J. Kim, T. H. Kim, T. W. Noh, J. S. Choi, B. H. Park, and J.-G. Yoon. Observation of room-temperature ferroelectricity in tetragonal strontium titanate thin films on $SrTiO_3$ (001) substrates. *Appl. Phys. Lett.*, 91(4):042908, 2007.

[239] J.G. Bednorz and K.A Müller. $Sr_{1-x}Ca_xTiO_3$: An XY Quantum Ferroelectric with Transition to Randomness. *Phys. Rev. Lett.*, 52(25):2289–2292, 1984.

[240] T. Wei, C. Zhu, K. F. Wang, and H. L. Cai. Influence of A-site codoping on ferroelectricity of quantum paraelectric $SrTiO_3$. *J. Appl. Phys.*, 103:124104, 2008.

[241] M. Itoh, R. Wang, Y. Inaguma, T. Yamaguchi, and T. Nakamura. Ferroelectricity Induced by Oxygen Isotope Exchange in Strontium Titanate Perovskite. *Phys. Rev. Lett.*, 82(17):3540–43, 1999.

[242] P. A. Fleury and J. M. Worlock. Electric-Field-Induced Raman Scattering in $SrTiO_3$ and $KTaO_3$. *Phys. Rev.*, 174(2):613, 1968.

[243] E. K. H. Salje, O. Aktas, M. Carpenter, V. Laguta, and J. Scott. Domains within Domains and Walls within Walls: Evidence for Polar Domains in Cryogenic $SrTiO_3$. *Phys. Rev. Lett.*, 111(24):247603, 2013.

[244] L. Goncalves-Ferreira, S. Redfern, E. Artacho, and E. K. H. Salje. Ferrielectric Twin Walls in $CaTiO_3$. *Phys. Rev. Lett.*, 101(9):097602, 2008.

[245] E. K. H. Salje. Multiferroic domain boundaries as active memory devices: trajectories towards domain boundary engineering. *Chemphyschem*, 11(5):940–50, 2010.

[246] S. Van Aert, S. Turner, R. Delville, D. Schryvers, G. Van Tendeloo, and E. K. H. Salje. Direct observation of ferrielectricity at ferroelastic domain boundaries in $CaTiO_3$ by electron microscopy. *Adv. Mater.*, 24(4):523–7, 2012.

[247] I. Katayama, Y. Ichikawa, and K. Tanaka. Critical behaviors of photoinduced giant permittivity in potassium tantalate. *Phys. Rev. B*, 67(10):100102, 2003.

[248] M. Takesada, T. Yagi, M. Itoh, and S. Koshihara. A Gigantic Photoinduced Dielectric Constant of Quantum Paraelectric Perovskite Oxides Observed under a Weak DC Electric Field. *J. Phys. Soc. Japan*, 72(1):37–40, 2003.

[249] S. Kawakami, N. Nakajima, T. Takigawa, M. Nakatake, H. Maruyama, Y. Tezuka, and T. Iwazumi. UV-Induced Change in the Electronic Structure of $SrTiO_3$ at Low Temperature Probed by Resonant X-ray Emission Spectroscopy. *J. Phys. Soc. Japan*, 82:053701, 2013.

[250] S. Nozawa, T. Iwazumi, and H. Osawa. Direct observation of the quantum fluctuation controlled by ultraviolet irradiation in $SrTiO_3$. *Phys. Rev. B*, 72:121101(R), 2005.

[251] N. A. Pertsev, A. G. Zembilgotov, and A. K. Tagantsev. Effect of Mechanical Boundary Conditions on Phase Diagrams of Epitaxial Ferroelectric Thin Films. *Phys. Rev. Lett.*, 80(9):1988–1991, 1998.

[252] K. J. Choi, M. Biegalski, Y. L. Li, A. Sharan, J. Schubert, R. Uecker, P. Reiche, Y. B. Chen, X. Q. Pan, V. Gopalan, L.-Q. Chen, D. G. Schlom, and C. B. Eom. Enhancement of ferroelectricity in strained $BaTiO_3$ thin films. *Science*, 306:1005–1009, 2004.

[253] J. Chen, Y. Luo, X. Ou, G. Yuan, Y. Wang, Y. Yang, J. Yin, and Z. Liu. Upward ferroelectric self-polarization induced by compressive epitaxial strain in (001) $BaTiO_3$ films. *J. Appl. Phys.*, 113:204105, 2013.

[254] S.-I. Kim, D.-H. Kim, Y. Kim, S. Y. Moon, M.-G. Kang, J. K. Choi, H. W. Jang, S. K. Kim, J.-W. Choi, S.-J. Yoon, H. J. Chang, C.-Y. Kang, S. Lee, S.-H. Hong, J.-S. Kim, and S.-H. Baek. Non-volatile control of 2DEG conductivity at oxide interfaces. *Adv. Mater.*, 25(33):4612–4617, 2013.

[255] V. T. Tra, J.-W. Chen, P.-C. Huang, B.-C. Huang, Y. Cao, C.-H. Yeh, H.-J. Liu, E. A. Eliseev, A. N. Morozovska, J.-Y. Lin, Y.-C. Chen, M.-W. Chu, P.-W. Chiu, Y.-P. Chiu, L.-Q. Chen, C.-L. Wu, and Y.-H. Chu. Ferroelectric control of the conduction at the $LaAlO_3/SrTiO_3$ heterointerface. *Adv. Mater.*, 25(24):3357–3364, 2013.

[256] N. Ganguli and P. J. Kelly. Tuning Ferromagnetism at Interfaces between Insulating Perovskite Oxides. *Phys. Rev. Lett.*, 113:127201, 2014.

[257] Z. Zhong and P. J. Kelly. Electronic-structure–induced reconstruction and magnetic ordering at the $LaAlO_3|SrTiO_3$ interface. *Europhys. Lett.*, 84:27001, 2008.

[258] C. L. Jia, S. B. Mi, M. Faley, U. Poppe, J. Schubert, and K. Urban. Oxygen octahedron reconstruction in the $SrTiO_3/LaAlO_3$ heterointerfaces investigated using aberration-corrected ultrahigh-resolution transmission electron microscopy. *Phys. Rev. B*, 79(8):081405, 2009.

[259] A. Rubano, C. Aruta, U. Scotti Di Uccio, F. Miletto Granozio, L. Marrucci, T. Günter, T. Fink, M. Fiebig, and D. Paparo. Electronic states at polar/nonpolar interfaces grown on $SrTiO_3$ studied by optical second harmonic generation. *Phys. Rev. B*, 88(24):245434, 2013.

[260] A. Joshua, S. Pecker, J. Ruhman, E. Altman, and S. Ilani. A universal critical density underlying the physics of electrons at the $LaAlO_3/SrTiO_3$ interface. *Nat. Commun.*, 3:1129, 2012.

[261] A. Joshua, J. Ruhman, S. Pecker, E. Altman, and S. Ilani. Gate-tunable polarized phase of two-dimensional electrons at the $LaAlO_3/SrTiO_3$ interface. *Proc. Natl. Acad. Sci.*, 110(24):9633, 2013.

[262] H. Lu, C.-W. Bark, D. Esque de los Ojos, J. Alcala, C. B. Eom, G. Catalan, and A. Gruverman. Mechanical Writing of Ferroelectric Polarization. *Science*, 336(6077):59–61, 2012.

[263] A. Manchon, H. C. Koo, J. Nitta, S. M. Frolov, and R. A. Duine. New perspectives for Rashba spin - orbit coupling. *Nat. Mater.*, 14:871–882, 2015.

[264] M. Hasan and C. Kane. Colloquium: Topological insulators. *Rev. Mod. Phys.*, 82(4):3045–3067, 2010.

[265] I. Žutić, J. Fabian, and S. Das Sarma. Spintronics: Fundamentals and applications. *Rev. Mod. Phys.*, 76:323–386, 2004.

[266] R. Janisch, P. Gopal, and N. A. Spaldin. Transition metal-doped TiO_2 and ZnO - present status of the field. *J. Phys. Condens. Matter*, 17(27):R657–R689, 2005.

[267] C. Liu, F. Yun, and H. Morkoc. Ferromagnetism of ZnO and GaN: A review. *J. Mater. Sci. Mater. Electron.*, 6:555–597, 2005.

[268] F. Pan, C. Song, X.J. Liu, Y.C. Yang, and F. Zeng. Ferromagnetism and possible application in spintronics of transition-metal-doped ZnO films. *Mater. Sci. Eng. R*, 62:1–35, 2008.

[269] S. B. Ogale. Dilute doping, defects, and ferromagnetism in metal oxide systems. *Adv. Mater.*, 22(29):3125–3155, 2010.

[270] Z. Yang. A perspective of recent progress in ZnO diluted magnetic semiconductors. *Appl. Phys. A Mater. Sci. Process.*, 112(2):241–254, 2013.

[271] M. Opel, S. T. B. Goennenwein, M. Althammer, K. W. Nielsen, E. M. Karrer-Müller, S. Bauer, K. Senn, C. Schwark, C. Weier, G. Güntherodt, B. Beschoten, and R. Gross. Zinc oxide -From dilute magnetic doping to spin transport. *Phys. Status Solidi Basic Res.*, 1709(9):1700–1709, 2014.

[272] J. I. Hong, J. Choi, S. S. Jang, J. Gu, Y. Chang, G. Wortman, R. L. Snyder, and Z. L. Wang. Magnetism in dopant-free ZnO nanoplates. *Nano Lett.*, 12(2):576–581, 2012.

[273] B. Choudhury and A. Choudhury. Room temperature ferromagnetism in defective TiO_2 nanoparticles: Role of surface and grain boundary oxygen vacancies. *J. Appl. Phys.*, 114(20):203906, 2013.

[274] G. Xing, D. Wang, J. Yi, L. Yang, M. Gao, M. He, J. Yang, J. Ding, T. C. Sum, and T. Wu. Correlated d^0 ferromagnetism and photoluminescence in undoped ZnO nanowires. *Appl. Phys. Lett.*, 96(11):112511, 2010.

[275] B. B. Straumal, A. A. Mazilkin, S. G. Protasova, A. A. Myatiev, P. B. Straumal, G. Schütz, P. A. Van Aken, E. Goering, and B. Baretzky. Magnetization study of nanograined pure and Mn-doped ZnO films: Formation of a ferromagnetic grain-boundary foam. *Phys. Rev. B*, 79:205206, 2009.

[276] J. M. D. Coey, Jerome T. Mlack, M. Venkatesan, and P. Stamenov. Magnetization Process in Dilute Magnetic Oxides. *IEEE Trans. Magn.*, 46(6):2501–2503, 2010.

[277] J. Zhang, L. Yu, Q. Song, and Y. Du. Tunable surface and/or interface ferromagnetism of ZnO nanoparticles. *Ann. Phys. (N. Y).*, 358:159–171, 2015.

[278] S.-Y. Choi, S.-D. Kim, M. Choi, H.-S. Lee, J. Ryu, N. Shibata, T. Mizoguchi, E. Tochigi, T. Yamamoto, S.-J. L. Kang, and Y. Ikuhara. Assessment of Strain-Generated Oxygen Vacancies Using $SrTiO_3$ Bicrystals. *Nano Lett.*, 15:4129–4134, 2015.

[279] D. Marrocchelli, L. Sun, and B. Yildiz. Dislocations in $SrTiO_3$: easy to reduce but not so fast for oxygen transport. *J. Am. Chem. Soc.*, 137:4735–4748, 2015.

[280] T. Dietl. A ten-year perspective on dilute magnetic semiconductors and oxides. *Nat. Mater.*, 9(12):965–974, 2010.

[281] M. Venkatesan, C. B. Fitzgerald, and J. M. D. Coey. Unexpected magnetism in a dielectric oxide. *Nature*, 430:630, 2004.

[282] J. Coey, M. Venkatesan, P. Stamenov, C. Fitzgerald, and L. Dorneles. Magnetism in hafnium dioxide. *Phys. Rev. B*, 72(2):024450, 2005.

[283] D. W. Abraham, M. M. Frank, and S. Guha. Absence of magnetism in hafnium oxide films. *Appl. Phys. Lett.*, 87(25):252502, 2005.

[284] N. Hoa Hong, J. Sakai, N. Poirot, and V. Brizé. Room-temperature ferromagnetism observed in undoped semiconducting and insulating oxide thin films. *Phys. Rev. B*, 73(13):132404, 2006.

[285] S. Dae Yoon, Y. Chen, A. Yang, T. L. Goodrich, X. Zuo, K. Ziemer, C. Vittoria, and V. G. Harris. Magnetic semiconducting anatase TiO_2 grown on (100) $LaAlO_3$ having magnetic order up to 880K. *J. Magn. Magn. Mater.*, 309:171–175, 2007.

[286] A. K. Rumaiz, B. Ali, A. Ceylan, M. Boggs, T. Beebe, and S. Ismat Shah. Experimental studies on vacancy induced ferromagnetism in undoped TiO_2. *Solid State Commun.*, 144:334–338, 2007.

[287] F. Golmar, A. M. Mudarra Navarro, C. E. Rodriguez Torres, F. H. Sanchez, F. D. Saccone, P. C. dos Santos Claro, G. A. Benitez, and P. L. Schilardi. Extrinsic origin of ferromagnetism in single crystalline $LaAlO_3$ substrates and oxide films. *Appl. Phys. Lett.*, 92(26):262503, 2008.

[288] K. Potzger, J. Osten, A. A. Levin, A. Shalimov, G. Talut, H. Reuther, S. Arpaci, D. Bürger, H. Schmidt, T. Nestler, and D.C. Meyer. Defect-induced ferromagnetism in crystalline $SrTiO_3$. *J. Magn. Magn. Mater.*, 323(11):1551–1562, 2011.

[289] D. A. Crandles, B. DesRoches, and F. S. Razavi. A search for defect related ferromagnetism in $SrTiO_3$. *J. Appl. Phys.*, 108(5):053908, 2010.

[290] M. Khalid, A. Setzer, M. Ziese, P. Esquinazi, D. Spemann, A. Pöppl, and E. Goering. Ubiquity of ferromagnetic signals in common diamagnetic oxide crystals. *Phys. Rev. B*, 81(21):214414, 2010.

[291] J.M.D. Coey, M. Venkatesan, and P. Stamenov. Surface magnetism of strontium titanate. *arXiv Prepr.*, page 1606.09422, 2016.

[292] J.M.D. Coey and S.A. Chambers. Oxide Dilute Magnetic Semiconductors –Fact or Fiction? *MRS Bull.*, 33(11):1053–1058, 2008.

[293] Q. Xu, H. Schmidt, S. Zhou, K. Potzger, M. Helm, H. Hochmuth, M. Lorenz, A. Setzer, P. Esquinazi, C. Meinecke, and M. Grundmann. Room temperature ferromagnetism in ZnO films due to defects. *Appl. Phys. Lett.*, 92:082508, 2008.

[294] W. Liu, W. Li, Z. Hu, Z. Tang, and X. Tang. Effect of oxygen defects on ferromagnetic of undoped ZnO. *J. Appl. Phys.*, 110:013901, 2011.

[295] S. Mal, T. H. Yang, C. Jin, S. Nori, J. Narayan, and J. T. Prater. d^0 Ferromagnetism in undoped ZnO thin films: Effect of thickness, interface and oxygen annealing. *Scr. Mater.*, 65(12):1061–1064, 2011.

[296] X. Hou, H. Liu, H. Sun, L. Liu, and X. Jia. Significant room-temperature ferromagnetism in porous ZnO films: The role of oxygen vacancies. *Mater. Sci. Eng. B*, 200:22–27, 2015.

[297] A. Sundaresan, R. Bhargavi, N. Rangarajan, U. Siddesh, and C. Rao. Ferromagnetism as a universal feature of nanoparticles of the otherwise nonmagnetic oxides. *Phys. Rev. B*, 74(16):161306, 2006.

[298] F. Lechermann, L. Boehnke, D. Grieger, and C. Piefke. Electron correlation and magnetism at the $LaAlO_3/SrTiO_3$ interface: A DFT+DMFT inverstigation. *Phys. Rev. B*, 90:085125, 2014.

[299] F. Lechermann, H. O. Jeschke, A. J. Kim, S. Backes, and R. Valenti. Electron dichotomy on the $SrTiO_3$ defect surface augmented by many-body effects. *Phys. Rev. B*, 93:121103(R), 2016.

[300] A. Lopez-Bezanilla, P. Ganesh, and P. B. Littlewood. Magnetism and metal-insulator transition in oxygen-deficient $SrTiO_3$. *Phys. Rev. B*, 92(11):115112, 2015.

[301] A. Lopez-Bezanilla, P. Ganesh, and P. B. Littlewood. Research Update: Plentiful magnetic moments in oxygen deficient $SrTiO_3$. *APL Mater.*, 3:100701, 2015.

[302] M. Altmeyer, H. O. Jeschke, O. Hijano-Cubelos, C. Martins, F. Lechermann, Klaus Koepernik, A. F. Santander-Syro, M. J. Rozenberg, R. Valenti, and M. Gabay. Magnetism, spin texture, and in-gap states: Atomic specialization at the surface of oxygen-deficient $SrTiO_3$. *Phys. Rev. Lett.*, 116:157203, 2016.

[303] N. Pavlenko, T. Kopp, and J. Mannhart. Emerging magnetism and electronic phase separation at titanate interfaces. *Phys. Rev. B*, 88(20):201104(R), 2013.

[304] J. C. Li, J. I. Beltran, and M. C. Munoz. Multiorbital structure of the two-dimensional electron gas in $LaAlO_3/SrTiO_3$ heterostructures: The formation of a d_{xy} ferromagnetic sheet. *Phys. Rev. B*, 87(7):075411, 2013.

[305] B. Kalisky, J. A. Bert, B. B. Klopfer, C. Bell, H. K. Sato, M. Hosoda, Y. Hikita, H. Y. Hwang, and K. A. Moler. Critical thickness for ferromagnetism in $LaAlO_3/SrTiO_3$ heterostructures. *Nat. Commun.*, 3:922, 2012.

[306] F. Bi, M. Huang, S. Ryu, H. Lee, C.-W. Bark, C.-B. Eom, P. Irvin, and J. Levy. Room-temperature electronically-controlled ferromagnetism at the $LaAlO_3/SrTiO_3$ interface. *Nat. Commun.*, 5:5019, 2014.

[307] T. Taniuchi, Y. Motoyui, K. Morozumi, T.C. Rödel, F. Fortuna, A.F. Santander-Syro, and S. Shin. Imaging of room-temperature ferromagnetic nano-domains at the surface of a non-magnetic oxide. *Nat. Commun.*, 7:11781, 2016.

[308] S. Cho, S. Choi, S. C. Hong, Y. Kim, J.B. Ketterson, B.-J. Kim, Y.C. Kim, and J.-H. Jung. Ferromagnetism in Mn-doped Ge. *Phys. Rev. B*, 66:033303, 2002.

[309] Y.-J. Zhao, T. Shishidou, and A. J. Freeman. Ruderman-Kittel-Kasuya-Yosida-like Ferromagnetism in Mn_xGe_{1-x}. *Phys. Rev. Lett.*, 90:047204, 2003.

[310] J. H. Dil. Spin and angle resolved photoemission on non-magnetic low-dimensional systems. *J. Phys. Condens. Matter*, 21(40):403001, 2009.

[311] T. Okuda and A. Kimura. Spin- and Angle-Resolved Photoemission of Strongly Spin - Orbit Coupled Systems. *J. Phys. Soc. Japan*, 82:021002, 2013.

[312] C. Jozwiak, C.-H. Park, K. Gotlieb, C. Hwang, D.-H. Lee, S. G. Louie, J. D. Denlinger, C. R. Rotundu, R. J. Birgeneau, Z. Hussain, and A. Lanzara. Photoelectron spin-flipping and texture manipulation in a topological insulator. *Nat. Phys.*, 9(5):293–298, 2013.

[313] J. Sánchez-Barriga, A. Varykhalov, J. Braun, S. Y. Xu, N. Alidoust, O. Kornilov, J. Minár, K. Hummer, G. Springholz, G. Bauer, R. Schumann, L. V. Yashina, H. Ebert, M. Z. Hasan, and O. Rader. Photoemission of Bi_2Se_3 with circularly polarized light: Probe of spin polarization or means for spin manipulation? *Phys. Rev. X*, 4:011046, 2014.

[314] T. Okuda, K. Miyamaoto, H. Miyahara, K. Kuroda, A. Kimura, H. Namatame, and M. Taniguchi. Efficient spin resolved spectroscopy observation machine at Hiroshima Synchrotron Radiation Center. *Rev. Sci. Instrum.*, 82(10):103302, 2011.

[315] J-S Lee, Y W Xie, H K Sato, C Bell, Y Hikita, H Y Hwang, and C-C Kao. Titanium d_{xy} ferromagnetism at the $LaAlO_3/SrTiO_3$ interface. *Nat. Mater.*, 12(8):703–6, 2013.

[316] S. L. Tomarken, A. F. Young, S. W. Lee, R. G. Gordon, and R. C. Ashoori. Torque magnetometry of an amorphous-alumina/strontium titanate interface. *Phys. Rev. B*, 90:201113(R), 2014.

[317] A. D. Caviglia, M. Gabay, S. Gariglio, N. Reyren, C. Cancellieri, and J. M. Triscone. Tunable Rashba Spin-Orbit Interaction at Oxide Interfaces. *Phys. Rev. Lett.*, 104(12):126803, 2010.

[318] H. Nakamura, T. Koga, and T. Kimura. Experimental evidence of cubic Rashba effect in an inversion-symmetric oxide. *Phys. Rev. Lett.*, 108(20):206601, 2012.

[319] K. V. Shanavas. Theoretical study of the cubic Rashba effect at the $SrTiO_3(001)$ surfaces. *Phys. Rev. B*, 93(4):045108, 2016.

[320] G. Bihlmayer, Y. M. Koroteev, P. M. Echenique, E. V. Chulkov, and S. Blügel. The Rashba-effect at metallic surfaces. *Surf. Sci.*, 600(18):3888–3891, 2006.

[321] M. Nagano, A. Kodama, T. Shishidou, and T. Oguchi. A first-principles study on the Rashba effect in surface systems. *J. Phys. Condens. Matter*, 21(6):064239, 2009.

[322] I. Gierz, B. Stadtmüller, J. Vuorinen, M. Lindroos, F. Meier, J. H. Dil, K. Kern, and C. R. Ast. Structural influence on the Rashba-type spin splitting in surface alloys. *Phys. Rev. B*, 81(24):245430, 2010.

[323] S. McKeown Walker, S. Riccò, F. Y. Bruno, A. de la Torre, A. Tamai, E. Golias, A. Varykhalov, D. Marchenko, M. Hoesch, M. S. Bahramy, P. D. C. King, J. Sánchez-Barriga, and F. Baumberger. Absence of Giant Spin Splitting in the Two-Dimensional Electron Liquid at the Surface of $SrTiO_3$ (001). *arXiv Prepr.*, page 1603.00181v1, 2016.

[324] A. C. Garcia-Castro, M. G. Vergniory, E. Bousquet, and A. H. Romero. Spin-texture induced by oxygen vacancies in Strontium perovskites (001) surfaces: A theoretical comparison between $SrTiO_3$ and $SrHfO_3$. *Phys. Rev. B*, 93:045405, 2016.

[325] S. S. Ghosh and E. Manousakis. Structure and ferromagnetic instability of the oxygen-deficient $SrTiO_3$ surface. *arXiv Prepr.*, page 1511.07495v1, 2015.

[326] S. S. Rao, Y. F. Lee, J. T. Prater, A. I. Smirnov, and J. Narayan. Laser annealing induced ferromagnetism in $SrTiO_3$ single crystal. *Appl. Phys. Lett.*, 105(4):042403, 2014.

[327] P. Hofmann, I .Y. Sklyadneva, E. D. L. Rienks, and E. V. Chulkov. Electron-phonon coupling at surfaces and interfaces. *New J. Phys.*, 11(12):125005, 2009.

[328] T. Holstein. Studies of polaron motion: Part I. The Molcular-Crystal Model. *Ann. Phys. (N. Y).*, 8:325–342, 1959.

[329] F. Giustino. Electron-phonon interactions from first principles. *arXiv Prepr.*, page 1603.06965v1, 2016.

[330] J. E. Gayone, C. Kirkegaard, J. W. Wells, S. V. Hoffmann, Z. Li, and P. Hofmann. Determining the electron-phonon mass enhancement parameter λ on metal surfaces. *Appl. Phys. A Mater. Sci. Process.*, 80(5):943–949, 2005.

[331] P. M. Echenique, R. Berndt, E. V. Chulkov, T. Fauster, A. Goldmann, and U. Höfer. Decay of electronic excitations at metal surfaces. *Surf. Sci. Rep.*, 52:219–317, 2004.

[332] S. Curnoe and P. C. E. Stamp. Spectral Function Analysis of Fermi Liquids and of Composite Fermions in a Finite Magnetic Field: Renormalised Gaps. *Int. J. Mod. Phys. B*, 11(12):1477, 1997.

[333] C. N. Veenstra, G. L. Goodvin, M. Berciu, and A. Damascelli. Elusive electron-phonon coupling in quantitative analyses of the spectral function. *Phys. Rev. B*, 82(1):012504, 2010.

[334] R. Yukawa, K. Ozawa, S. Yamamoto, H. Iwasawa, K. Shimada, E. F. Schwier, K. Yoshimatsu, H. Kumigashira, H. Namatame, M. Taniguchi, and I. Matsuda. Phonon-Dressed Two-Dimensional Carriers on the ZnO Surface. *arXiv*, page 1604.05523v1, 2016.

[335] D. Gryaznov, E. Blokhin, A. Sorokine, E. A. Kotomin, R. A. Evarestov, A. Bussmann-Holder, and J. Maier. A Comparative Ab Initio Thermodynamic Study of Oxygen Vacancies in ZnO and $SrTiO_3$: Emphasis on Phonon Contribution. *J. Phys. Chem. B*, 117:13776, 2013.

[336] N. Choudhury, E. Walter, A. Kolesnikov, and C.-K. Loong. Large phonon band gap in $SrTiO_3$ and the vibrational signatures of ferroelectricity in $ATiO_3$ perovskites: First-principles lattice dynamics and inelastic neutron scattering. *Phys. Rev. B*, 77(13):134111, 2008.

[337] E. Shojaee and M. R. Mohammadizadeh. First-principles elastic and thermal properties of TiO_2: a phonon approach. *J. physics. Condens. matter*, 22(1):015401, 2010.

[338] M. Mikami, S. Nakumura, O. Kitao, and H. Arakawa. Lattice dynamics and dielectric properties of TiO_2 anatase: A first-principles study. *Phys. Rev. B*, 65(22):224112, 2002.

[339] J. Wróbel, K. J. Kurzydłowski, K. Hummer, G. Kresse, and J. Piechota. Calculations of ZnO properties using the Heyd-Scuseria-Ernzerhof screened hybrid density functional. *Phys. Rev. B*, 80(15):155124, 2009.

[340] J. Kröger. Electron–phonon coupling at metal surfaces. *Reports Prog. Phys.*, 69:899–969, 2006.

[341] C. Kirkegaard, T. K. Kim, and Ph Hofmann. Self-energy determination and electron-phonon coupling on Bi(110). *New J. Phys.*, 7:99, 2005.

[342] H. Boschker, C. Richter, E. Fillis-Tsirakis, C.W. Schneider, and J. Mannhart. Electron–phonon Coupling and the Superconducting Phase Diagram of the $LaAlO_3$–$SrTiO_3$ Interface. *Sci. Rep.*, 5:12309, 2015.

[343] K. H. L. Zhang, R. G. Egdell, F. Offi, S. Iacobucci, L. Petaccia, S. Gorovikov, and P. D. C. King. Microscopic Origin of Electron Accumulation in In_2O_3. *Phys. Rev. Lett.*, 110:056803, 2013.

[344] P. D. C. King and T. D. Veal. Conductivity in transparent oxide semiconductors. *J. physics. Condens. matter*, 23:334214, 2011.

[345] L. F. J. Piper, L. Colakerol, P. D C King, A. Schleife, J. Zúniga-Pérez, P.-A. Glans, T. Learmonth, A. Federov, T. D. Veal, F. Fuchs, V. Munoz-Sanjosé, F. Bechstedt, C. F. McConville, and K. E. Smith. Observation of quantized subband states and evidence for surface electron accumulation in CdO from angle-resolved photoemission spectroscopy. *Phys. Rev. B*, 78:165127, 2008.

[346] S. Backes, T. C. Rödel, F. Fortuna, E. Frantzeskakis, P. Le Fèvre, F. Bertran, M. Kobayashi, R. Yukawa, T. Mitsuhashi, M. Kitamura, K. Horiba, H. Kumigashira, R. Saint-Martin, A. Fouchet, B. Berini, Y. Dumont, A. J. Kim, F. Lechermann, H. O. Jeschke, M. J. Rozenberg, R. Valentí, and A. F. Santander-Syro. Hubbard band or oxygen vacancy states in the correlated electron metal $SrVO_3$? *arXiv Prepr.*, page 1602.06909v1, 2016.

[347] Z. Q. Liu, C. J. Li, W. M. Lü, X. H. Huang, Z. Huang, S. W. Zeng, X. P. Qiu, L. S. Huang, A. Annadi, J. S. Chen, J. M. D. Coey, and T. Venkatesan. Origin of the Two-Dimensional Electron Gas at $LaAlO_3/SrTiO_3$ Interfaces: The Role of Oxygen Vacancies and Electronic Reconstruction. *Phys. Rev. X*, 3:021010, 2013.

Synthèse en Français

Dans le cadre de cette thèse, j'ai travaillé dans l'équipe de "Strongly Correlated Systems and New Electronic States of Matter" au CSNSM à Orsay, dans l'équipe de "Oxide growth, magnetism and transport" à l'IEF à Orsay et dans l'équipe de la ligne de lumière Cassiopée au synchrotron Soleil. J'ai étudié des gaz d'électrons bidimensionnel (2DEG) à la surface des oxydes de métaux de transition (TMOs), principalement des isolants de bande, des titanates, par un dopage local de la région de surface avec des lacunes d'oxygène. Leur structure électronique a été caractérisée par la spectroscopie photoélectronique résolue en angle (ARPES). Depuis la découverte du 2DEG à la surface de $SrTiO_3$ en 2011 [1, 2], il y a eu 17 études d'ARPES sur les 2DEGs à la surface des oxydes de métaux de transition (TMO): [3–19]

Résumé

Des nombreux oxydes de métaux de transition (TMOs) possèdent des propriétés physiques complexes (ferroélectricité, magnétisme, supraconductivité à haute T_c ou magnétorésistance colossale). Les différents degrés de liberté (le réseau, la charge, le spin ou l'ordre orbitalaire) interagissent pour donner des phases différentes, très proches en énergie, qui vont former une grande variété d'états fondamentaux accessibles. La possibilité de fabriquer des hétérostructures de TMOs a encore accru la complexité de ces systèmes, de nouveaux phénomènes apparaissant aux interfaces. Un exemple typique est le gaz d'électrons bidimensionnel (2DEG) créé à l'interface entre deux oxydes isolants, $LaAlO_3$ et $SrTiO_3$, qui montre une transition métal-isolant, du magnétisme ou de la supraconductivité (contrôlée par une tension de grille). Le point de départ de cette thèse a été la découverte d'un 2DEG similaire à la surface nue de $SrTiO_3$ fracturée sous vide, rendant possible l'étude de sa structure électronique par photoémission angulaire.

Dans cette thèse, l'étude de surfaces préparées, plutôt que de petites facettes fracturées, a permis l'obtention de données spectroscopiques possédant des largeurs de raie proches des valeurs intrinsèques. Il est alors possible d'étudier les effets à N corps comme la renormalisation de la self-énergie due à l'interaction électron-phonon.

Ces recherches sur la structure électronique du 2DEG à la surface de SrTiO3 ont pris un tour nouveau lorsqu'une texture de spin complexe y a été mesurée par photoémission résolue en spin. Nous présentons des résultats qui contredisent ces conclusions et nous discutons des raisons pouvant expliquer ce désaccord.

Une des motivations de cette thèse était de savoir si la structure électronique et les propriétés

du 2DEG pouvaient être contrôlées. L'étude du 2DEG sur des surfaces (110) et (111) de $SrTiO_3$ révèle que sa structure de bandes (ordre orbitalaire, symétrie de la surface de Fermi, masses effectives) peut être ajustée en confinant les électrons sur des surfaces de différentes orientations du même matériau.

Un succès majeure est la mise en évidence de 2DEGs à la surface de nombreux autres TMOs (TiO_2-anatase, $CaTiO_3$, $BaTiO_3$) ou d'oxydes plus simples utilisés dans les applications (ZnO). Dans tous ces oxydes, nous avons identifié les lacunes en oxygène comme étant à l'origine de la création des 2DEGs.

Dans l'anatase, ou d'autres TMOs en configuration électronique initiale d^0, les lacunes en oxygène produisent à la fois des électrons localisés ou itinérants (le 2DEG). Il peut être subtile de prévoir quel est le cas est le plus favorable énergétiquement comme le démontre l'étude de deux polymorphes de TiO_2, anatase et rutile. Dans $CaTiO_3$, l'octaèdre formé par les atomes d'oxygène autour du Ti est incliné. Cette rupture de symétrie provoque un mélange des orbitales d et modifie le 2DEG. Dans $BaTiO_3$, la création d'un 2DEG entraîne la coexistence de deux phénomènes normalement incompatibles, la ferroélectricité et la métallicité, dans deux zones spatialement distinctes du même matériau. Ce travail démontre qu'un 2DEG existe aussi à la surface de ZnO qui est, contrairement aux oxydes à base de Ti, plutôt un semiconducteur conventionnel, le caractère des orbitales pour les électrons itinérants étant alors de type s et non de type d.

Le principal résultat est la mise au point d'une méthode simple et versatile pour la création de 2DEGs en évaporant de l'aluminium sur des surfaces d'oxydes. Une réaction d'oxydo-réduction entre le métal et l'oxyde permet de créer un 2DEG à l'interface entre le métal oxydé et l'oxyde réduit. Dans cette thèse, les 2DEGs ont été étudiés uniquement par photoémission sous ultravide. Cette méthode ouvre la possibilité d'étudier ces 2DEGs dans des conditions de pression ambiante en utilisant, par exemple, des techniques de transport, un pas important vers la production de masse et à bas coûts de 2DEGs dans les oxydes pour de futures applications.

Motivation

1. Vers une connaissance microscopique de la structure de bande électronique

La recherche sur les 2DEGs dans des systèmes basées sur des oxydes de métaux de transition est devenue très populaire après la découverte d'une interface métallique 2D à l'interface entre deux oxydes isolants: $LaAlO_3$ et $SrTiO_3$. [20] La physique du système $LaAlO_3/SrTiO_3$ est très variée et va des transitions isolant-supraconducteur contrôlées par un champ à grille [21], au magnétisme [22] en passant par la coexistence de la supraconductivité et le magnétisme [23–25]. De plus, plusieurs origines pour expliquer l'existence du 2DEG sont possibles: la reconstruction électronique en raison de la catastrophe polaire [26], des lacunes d'oxygène [27] ou un mélange des cations à l'interface [28]. Une physique complexe associée à une origine controversée conduisent à des efforts de recherche intense au cours de la dernière décennie.

Une grande partie des études sur $LaAlO_3/SrTiO_3$ sont des mesures de transport électrique. Pour mieux comprendre ces mesures macroscopiques, la connaissance de la structure de bande électronique, qui est une propriété microscopique, est essentielle. La découverte et l'étude du 2DEG à la surface de $SrTiO_3$ a contribué à ce domaine parce que la structure des bandes électronique peut être mesurée directement par l'ARPES. [1] En utilisant cette technique, les bandes des trois orbitales de types t_{2g} composant le 2DEG peuvent être caractérisées : les masses de bande, l'ordre énergétique des orbitales, la dédoublement énergétique des bandes, la forme et taille de la surface de Fermi et la densité des électrons mobiles à la surface. En outre, l'influence des différentes configurations du réseau crystalin (par exemple le type d'empilement ou les rotations des octaèdres d'oxygène) sur la structure électronique peut être déterminée par l'étude de matériaux similaires (par exemple TiO_2 ou $CaTiO_3$) ou d'autres orientations de surface. C'est l'approche choisie dans cette thèse.

2. Etude des surfaces: une approche "bottom-up" à la physique des interfaces dans des oxydes de métaux de transition

Plus généralement, la physique des oxydes de métaux de transition (TMOs) couplés avec des effets d'interface dans des hétérostructures d'oxyde entraînent l'existence des propriétés diveres à l'interface qui n'existent pas nécessairement dans le bulk. [29] Dans ce contexte, on peut voir les hétérostructures d'oxyde comme une version évoluée des hétérostructures basées sur des semi-conducteurs qui sont connues par exemple pour la découverte de l'effet Hall quantique fractionnaire [30] ou les transistors à effet de champ à grille qui se trouvent partout dans la microélectronique [31].

Les TMOs ont une physique très variée: une des raisons pour cette diversité est le caractère d des orbitales des électrons de valence au lieu du caractère p dans les semi-conducteurs classiques. Par conséquence, divers états fondamentaux existent (ferroélectricité, ferromagnétisme, supraconductivité, ...) qui n'existent pas dans les semi-conducteurs classiques. En plus, il y a souvent un couplage fort entre des degrés de liberté différents (réseau, spin, charge, orbital). Donc, la combinaison des oxydes différents dans des hétérostructures est un terrain de jeu immense pour les scientifiques des matériaux et les physiciens. [32–34]

Dans ce contexte, l'étude de la surface peut être considérée comme une approche bottom-up aux problèmes plus complexes aux interfaces d'oxydes. Après tout, l'interface vide/surface est une interface comparablement simple. On peut se demander si les propriétés exotiques des hétérostructures de $LaAlO_3/SrTiO_3$ sont exclusives à cette interface particulière ou si, au contraire, elles ressortent plus généralement pour des interfaces basées sur $SrTiO_3$ dopé avec des électrons. Par conséquence, la connaissance de la physique de l'interface vide/surface peut aider à mieux comprendre les interfaces liées aux hétérostructures d'oxydes et à démêler l'origine des différentes propriétés émergentes à l'interface des systèmes plus complexes.

3. L'importance et l'ingénierie des lacunes d'oxygène

Une autre motivation de ce travail est le contrôle des défauts, c'est-à-dire des lacunes d'oxygène. La lacune d'oxygène est un défaut ponctuel qui est omniprésent et très commun dans les oxydes. [35] Les propriétés des TMOs changent souvent d'une façon spectaculaire en raison de la présence ou de la distribution (défauts ponctuels distribués d'une façon homogène, au hasard, par cluster, ou dans des couches) de lacunes d'oxygène. Habituellement, les lacunes d'oxygène agissent comme les donneurs d'électrons et peuvent induire des transitions métal-isolant dans les TMOs qui sont normalement isolants (comme par exemple dans $SrTiO_3$). L'ingénierie des lacunes d'oxygène peut entraîner des transitions métal-isolant locales [15, 36], des champs électriques peuvent induire la diffusion des lacunes qui, à son tour, peut influencer le "resistive switching" des memristors [37–39], l'existence du ferromagnétisme a été liée aux lacunes d'oxygène [40, 41] et la (photo)chimie ou des propriétés (photo)catalytiques dépendent également de la distribution des lacunes [42–45]. La création locale des lacunes d'oxygène à la surface ou à l'interface d'oxydes et le contrôle de leur concentration sont indispensables pour étudier et contrôler les propriétés des 2DEGs dans des oxydes de métaux de transition.

Création du 2DEG à la surface de $SrTiO_3$

Le 2DEG à la surface de $SrTiO_3$ est créé par la génération des lacunes d'oxygène à la surface. Il y a deux possibilités pour cette création locale de lacunes d'oxygène:

- en utilisant le faisceau intense des photons UV crée par un synchrotron
- en utilisant une réaction redox entre $SrTiO_3$ et une couche ultra-mince d'aluminium

Pour mieux comprendre comment cette distribution locale des lacunes d'oxygène influence la structure électronique des oxydes on va utiliser un modèle pédagogique d'un puits quantique triangulaire.

Puits quantique triangulaire

On suppose que des lacunes d'oxygène sont distribuées d'une façon homogène dans une couche d'épaisseur d à la surface (approximation de Schottky). De plus, on suppose qu'une lacune donne deux électrons et est donc, chargée doublement positive. Basé sur ces hypothèses, le potentiel qui confine les électrons et qui est créé par des lacunes avec une densité N_{V_o} est donné par l'équation de Poisson à une dimension:

$$\frac{\partial^2 V_{conf}(z)}{\partial z^2} = -\frac{\rho}{\epsilon_r \epsilon_0}. \tag{9.1}$$

ϵ_0 est la permittivité du vide, ϵ_r la permittivité relative et ρ est la densité de porteur:

$$\rho = \begin{cases} 2eN_{V_o}, & \text{for } 0 \leq z \leq d, \\ 0, & \text{for } z > d \end{cases}$$

e est la charge élémentaire et la surface est située à $z = 0$. L'équation de Poisson mène à un champ électrique de confinement $F(z)$:

$$F(z) = \frac{2eN_{V_o}}{\epsilon_r \epsilon_0}(z - d), \quad \text{for } 0 \leq z \leq d \tag{9.2}$$

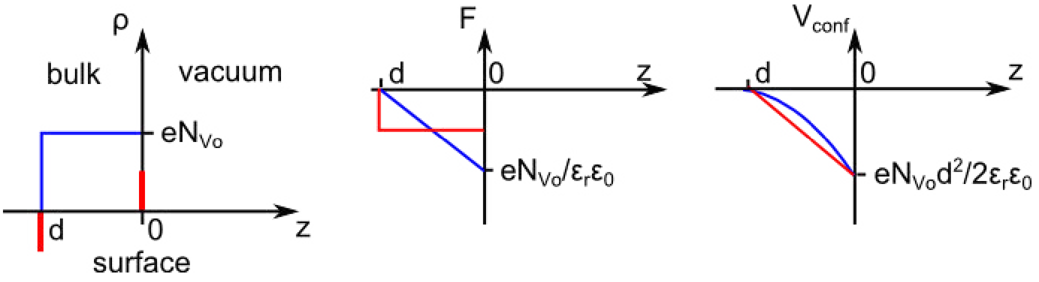

Figure 9.3: La densité des porteurs de charge ρ, le champ électrique de confinement $F(z)$ et le potentiel de confinement $V_{conf}(z)$ du model de Schottky (courbe bleu) et sa approximation (rouge).

et un potentiel de confinement $V(z)$ de

$$V_{conf}(z) = -\frac{eN_{V_o}}{\epsilon_r\epsilon_0}(z-d)^2, \quad \text{for } 0 \le z \le d. \tag{9.3}$$

L'offset de bande à la surface est $V_{conf}(0) = -(eN_{V_o}d^2)/(\epsilon_r\epsilon_0)$.
L'Hamiltonian 1D des électrons non-interagissant dans ce puits quantique est:

$$H(z)\Phi(z) = \frac{p_z^2}{2m_z^*}\Phi(z) + V_{conf}(z)\Phi(z) = E_n\Phi(z).$$

m_z^* est la masse effective dans la direction de confinement qui dépend aussi de la symétrie des orbitales d concernées. L'approximation qui facilite la solution analytique de Hamiltonian H est la dépendance linéaire du potentiel du confinement en fonction de z (c'est-à-dire un puits quantique triangulaire):

$$V_{conf}(z) \approx (z-d)F$$

avec un champ électrique constant $F = (eN_{V_o}d)/(\epsilon_r\epsilon_0)$ qui correspond à un condensateur avec deux plaques en parallèles séparées par la distance d et ayant une densité des porteurs de charge à la surface de $eN_{V_o}/2$. La densité des porteurs de charge ρ, le champ électrique de confinement $F(z)$ et le potentiel de confinement $V_{conf}(z)$ du model de Schottky et son approximation sont montrés dans la figure 9.3.

En utilisant la transformation de variable $z-d = \left(\frac{\hbar^2e^2F^2}{2m_z^*}\right)^{\frac{1}{3}}/(eF-E_n)\zeta$, on obtient l'équation d'Airy de Hamiltonian:

$$\frac{d^2}{d\zeta^2}\Phi(\zeta) - \zeta\Phi(\zeta) = 0.$$

Les vecteurs propres $\Phi(\zeta)$ sont des fonctions d'Airy. Les valeurs propres E_n sont: [100]

$$E_n = V_{conf}(0) + \left(\frac{\hbar^2}{2m_z^*}\right)^{\frac{1}{3}}\left[\left(\frac{3\pi}{2}\right)\left(n-\frac{1}{4}\right)eF\right]^{\frac{2}{3}} \tag{9.4}$$

Plus tard, on va utiliser les valeurs propres E_n pour estimer l'extension des états électroniques confinés à la surface. La différence énergétique entre deux bandes $\Delta E \equiv E_2 - E_1$ peut être utilisé pour calculer le champ de confinement:

$$F = \left(\frac{\hbar^2}{2m_z^*}\right)^{-\frac{1}{3}} \left(\frac{3\pi}{2}e\right)^{-\frac{2}{3}} \left[\left(\frac{7}{4}\right)^{\frac{2}{3}} - \left(\frac{3}{4}\right)^{\frac{2}{3}}\right]^{-1} \Delta E. \tag{9.5}$$

En résumée, le confinement à la surface cause une dédoublement des bandes qui sont uniques dans le massif. Ces bandes ont des nombres quantiques n différents. Les valeurs propres d'énergie E_n dépendent de ces nombres quantiques n mais aussi de la masse effective dans la direction de confinement m_z^* qui est différente pour des types d'orbitales différentes.

2DEG mesuré par ARPES

La motivation principale de cette thèse a été la découverte du gaz d'électrons bidimensionnel (2DEG) à la surface de cristaux fracturés de $SrTiO_3$. Les résultats sont brièvement résumés dans la figure 9.4 à la page 196. Cette découverte est tout à fait surprenante car $SrTiO_3$ est un oxyde isolant et la présence d'un état métallique confiné à la surface de cet isolant est loin d'être intuitif. La technique utilisée pour observer le 2DEG était la spectroscopie de photoélectrons. En utilisant cette technique, les photoélectrons sont excités par des photons UV et cette excitation éjecte les électrons hors du solide dans le vide. Ensuite, l'énergie et l'angle d'émission des photoélectrons sont analysés pour obtenir la structure de bande électronique. Comme présenté dans la figure 9.4(f), trois bandes paraboliques qui correspondent aux orbitales t_{2g} ont été observées et attribuées aux états 2D confinés dans un puits de potentiel.

Changement et brisure de symétrie de réseau de perovskite cubique

Une question majeure de cette thèse était de savoir si et comment les propriétés du 2DEG peuvent être modifiées. Des idées de modification des propriétés différentes sont montrées dans la figure 9.5 à la page 197 et sont basées sur un changement de réseau dans lequel le 2DEG est confiné.

Confinement du 2DEG aux différentes surfaces de $SrTiO_3$

De nouveaux types de 2DEGs peuvent être créer aux surfaces (110) et (111) de $SrTiO_3$. [10] En utilisant l'ARPES, on caractérise leur structure électronique. Comme montré dans la figure 9.6 à la page 198, les surfaces de Fermi, les masses effectives des sous-bandes, et l'ordre des orbitales sont différents de ceux du 2DEG à la surface (001) de $SrTiO_3$ [1, 2] et de ceux prévus dans le massif. Ces propriétés sont donc sensibles à la direction cristallographique de confinement. Cela se produit parce que les symétries cristallographiques des couches de surface et les masses effectives des électrons dans la direction du confinement ont une influence sur la symétrie de la structure électronique et l'ordre des orbitales t_{2g}.

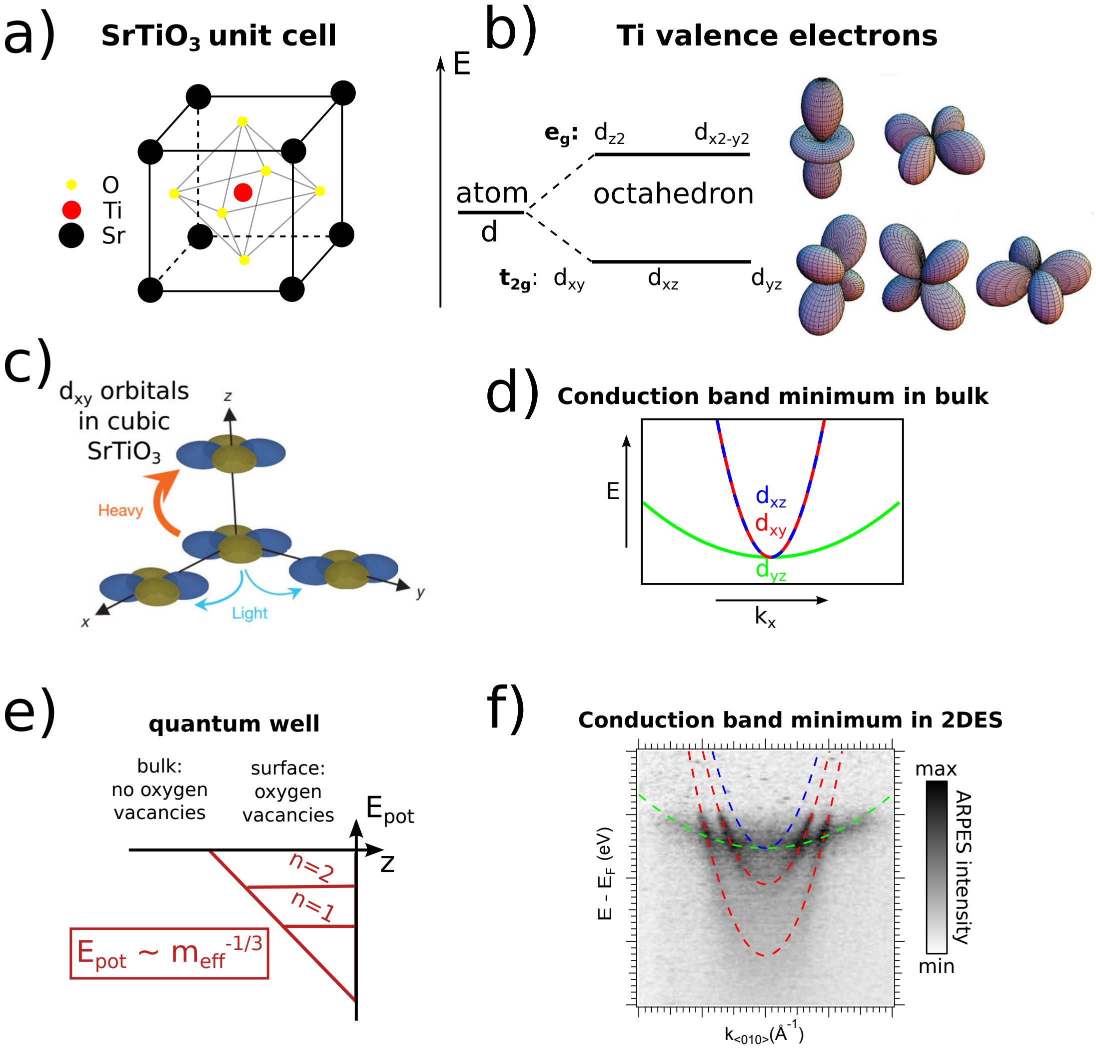

Figure 9.4: (a) Maille élémentaire d'un réseau perovskite cubique ($SrTiO_3$). Les anions oxygène (sphères jaunes) forment un octaèdre (lignes grises) autour du cation Ti (sphère rouge). Les cations Sr (sphères noires) sont situés aux coins de la maille élémentaire. (b) La dégénérescence des orbitales d d'un atome est brisée en raison du champ cristallin de symétrie octaédrique dans les perovskites. Les énergies propres des états d sont divisées en des états t_{2g} et e_g. Les amplitudes de probabilité des fonctions d'onde des orbitales d sont indiquées en (b) (Référence [32]). (c) Orbitales d_{xy} dans le réseau de $SrTiO_3$. Le recouvrement des orbitales est grand dans les directions x ou y mais petit dans la direction z (Référence [1]). (d) Par conséquent, le minimum de la bande de conduction (CBM) est constitué de bandes légères et lourdes. Par exemple, dans la direction x, les orbitales d_{xy} et d_{xz} forment des bandes légères et l'orbitale d_{yz} une bande lourde. (e) Comme discuté auparavant le confinement des électrons dans un puits de potentiel triangulaire entraîne la quantification des énergies propres. (f) L'effet du confinement sur la structure électronique du matériau massif conduit à un changement de l'ordre des orbitales dans le 2DEG à la surface du $SrTiO_3$ qui est montré dans le graphique d'intensité mesurée par ARPES. La présence des deux sous-bandes d_{xy} correspond aux énergies propres E_n avec $n = 1$ et $n = 2$. Les couleurs correspondent à l'intensité mesurée par l'ARPES où le blanc correspond à une intensité faible et le noir à une intensité élevée. Les lignes en pointillés correspondent aux fits des bandes mesurées.

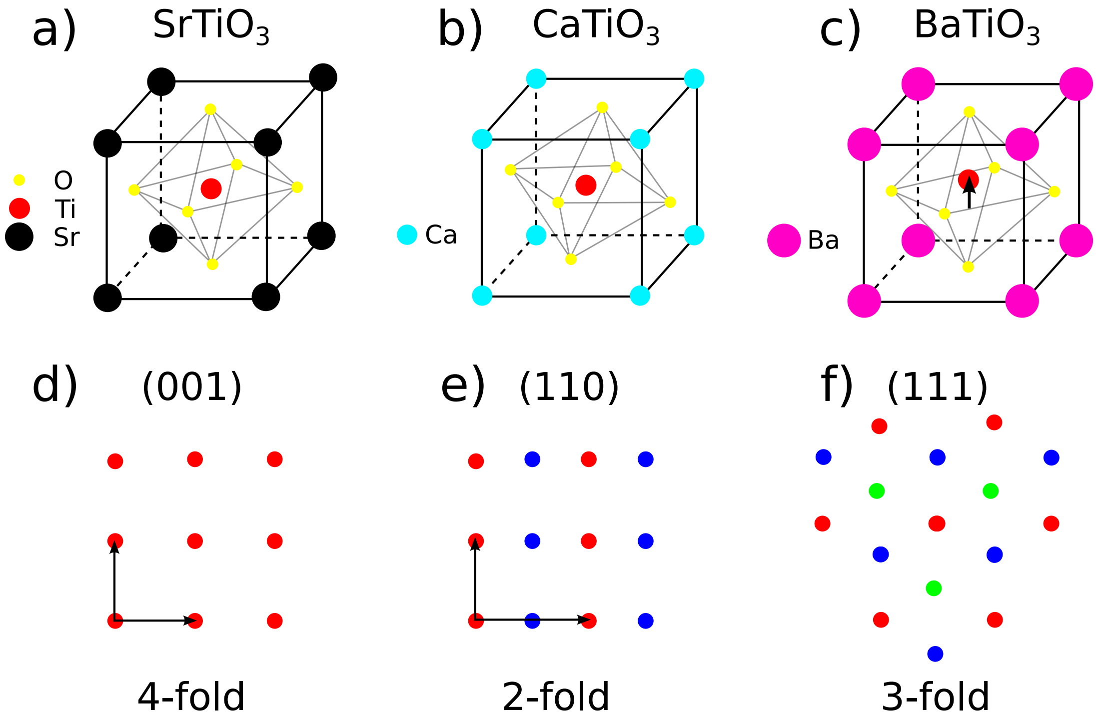

Figure 9.5: Modification des propriétés du 2DEG par brisure de la symétrie du réseau perovskite cubique. (a) Dans $SrTiO_3$ les tailles des ions (Sr^{2+}, Ti^{4+} et O^{2-}) ont le bon rapport pour former la phase perovskite cubique. (b) L'ion Ca^{2+} est plus petit que l'ion Sr^{2+}. Par conséquent, un ordre antiferrodistortif est observé dans $CaTiO_3$: les octaèdres d'oxygène sont inclinées et forment un réseau orthorhombique. (c) L'ion Ba^{2+} est plus grand que l'ion Sr^{2+}. Par conséquent, l'ion Ti^{4+} bouge hors du centre de l'octaèdre d'oxygène dans $BaTiO_3$ qui forme ainsi un réseau quadratique. La brisure de symétrie centrale dans le réseau quadratique entraine la ferroélectricité de $BaTiO_3$.
Une façon de changer la symétrie apparente est d'observer le 2DEG suivant des orientations de surface différentes. (d) La projection du réseau de $SrTiO_3$ sur la surface (001) montrant seulement des ions Ti^{4+}. (e) Surface (110). (f) Surface (111). Les couleurs différentes des ions Ti^{4+} correspondent à des ions situés dans des couches différentes. Le symétrie de rotation des surfaces différentes est indiqué (symétrie d'ordre quatre, deux ou trois).

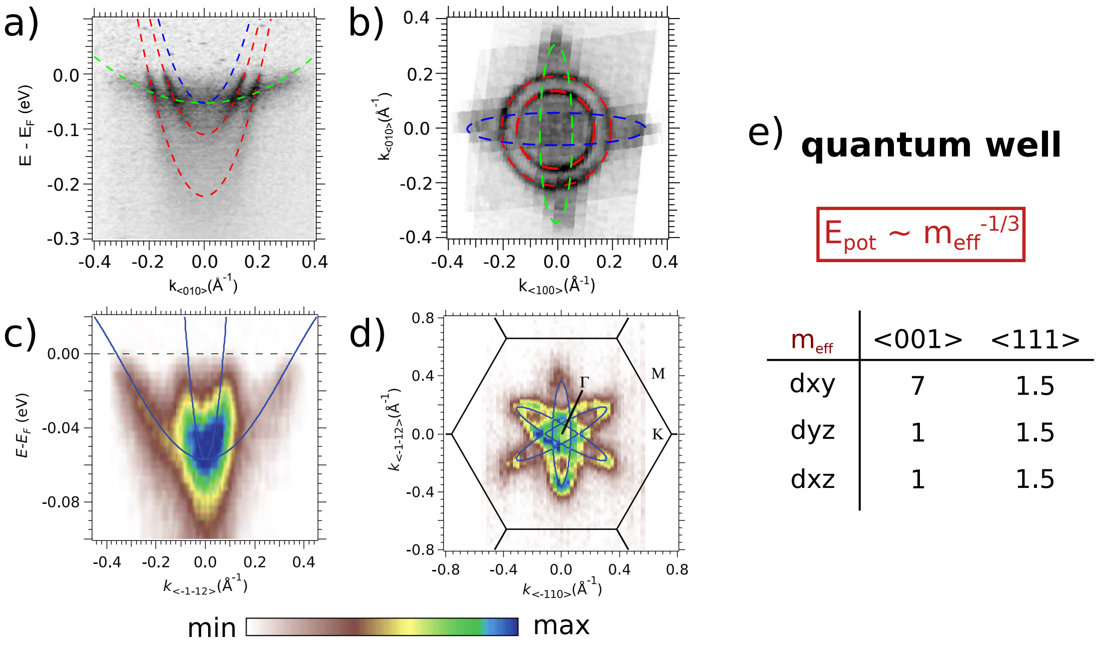

m$_{eff}$	<001>	<111>
dxy	7	1.5
dyz	1	1.5
dxz	1	1.5

Figure 9.6: (a) Carte d'intensité ARPES $E - k$ et (b) surface de Fermi à la surface (001) de SrTiO$_3$. La carte $E - k$ et la surface de Fermi sont obtenues par superposition de mesures effectuées aux énergies de photons $h\upsilon_1 = 47$ eV et $h\upsilon_2 = 90$ eV. Les couleurs des courbes (rouge, vert, bleu) correspondent à des caractères différents des orbitales et sont basés sur des fits parabolique des données d'ARPES. (c) Carte d'intensité ARPES $E - k$ et (d) surface de Fermi mesurées à $h\upsilon = 110$ eV à la surface (111) de SrTiO$_3$. (d) Les lignes noires indiquent les bords de zone de Brillouin autour de Γ_{222}. Les courbes bleus sont les fits basés sur un modèle de liasions fortes. (e) Dans un puits quantique triangulaire l'ordre des orbitales est déterminé par les valeurs propres d'énergie qui sont proportionnels aux masses effectives des électrons dans la direction de confinement $E_n \propto (m_z^*)^{-\frac{1}{3}}$ (c.f. eq(9.4)). La différence observée dans (a) et (c) sur l'ordre des orbitales peut être expliqué par des masses effectives différentes des orbitales dans les direction <001> et <111> présentées dans ce tableau.

2DEG aux surfaces de ATiO$_3$ (A=Ca,Sr,Ba)

Une autre façon d'obtenir des 2DEGs avec des propriétés différentes est de changer la géométrie du réseau en remplaçant le cation sur le site A des pérovskites ATiO$_3$. On utilise le 2DEG à la surface de SrTiO$_3$(001) qui a été présenté auparavant comme un système de référence pour comprendre les changements induits dans les 2DEGs à la surface de CaTiO$_3$ et BaTiO$_3$. Le bloc central pour construire le réseau pérovskite ATiO$_3$ est l'octaèdre d'oxygènes autour du cation Ti. Dans SrTiO$_3$, les octaèdres ne sont pas déformés et ne subissent aucune rotation, le réseau est ainsi cubique.

Cependant, dans BaTiO$_3$, le mouvement du cation Ti en dehors du centre de l'octaèdre brise la symétrie centrale du réseau et crée une phase quadratique qui est ferroélectrique. Normalement, un solide ne peut pas être ferroélectrique et en même temps métallique parce que les porteurs de charge mobiles masquent les interactions coulombiennes entre les dipôles électriques. Mais les deux phénomènes peuvent coexister dans le même matériau s'ils sont séparés spatialement comme dans le cas d'un dopage local de la surface (création d'un 2DEG). La polarisation ferroélectrique crée un champ électrique qui se superpose au champ électrique qui confine les électrons du 2DEG. Donc, la densité de porteurs est deux fois plus élevée dans BaTiO$_3$ que dans SrTiO$_3$.

Dans CaTiO$_3$, les rotations des octaèdres induisent un réseau orthorhombique. Cette rupture de symétrie entraîne une hybridation des différents orbitales d (d_{xz} et d_{yz}) qui n'est pas observée dans SrTiO$_3$. Cette hybridation change la forme de la surface de Fermi, les masses effectives des électrons et donc, aussi l'ordre des orbitales.

Les résultats d'ARPES sont regroupés dans la figure 9.7 à la page 200.

2DEG aux surfaces des non-perovskites: ZnO et TiO$_2$ anatase

Des 2DEGs peuvent aussi être créés dans d'autres oxydes que des perovskites. Figure 9.8, page 201, présente des 2DEGs à la surface de ZnO(000$\bar{1}$) et TiO$_2$ anatase(001) qui sont composés de deux bandes légères qui forment des surfaces de Fermi circulaires. ZnO est différent des autres systèmes parce que le matériau présente plutôt des propriétés d'un semi-conducteur conventionnel. La raison est que la bande de conduction de ZnO est composé des orbitales s et non pas d. Les surfaces de TiO$_2$ ont été enormément étudiées dans un effort de comprehension de leurs propriétés photocatalytiques. [43, 80–82]. Le 2DEG est seulement formé des bandes d_{xy} parce que le champ cristallin du réseau quadratique montré figure 9.8(d) lève la dégénérescence des bandes t_{2g}. Contrairement à l'anatase, on n'a pas trouvé de 2DEG à la surface de la phase rutile - un autre polymorphe de TiO$_2$. Le réseau rutile est aussi formé d'octaèdres d'oxygènes mais l'ordre de l'empilement de ces octaèdres est différent de celui de l'anatase. Cette différence montre que la question de savoir si l'excès d'électrons dû aux lacunes d'oxygène sont mobiles ou localisés depend de différences subtiles du réseau.

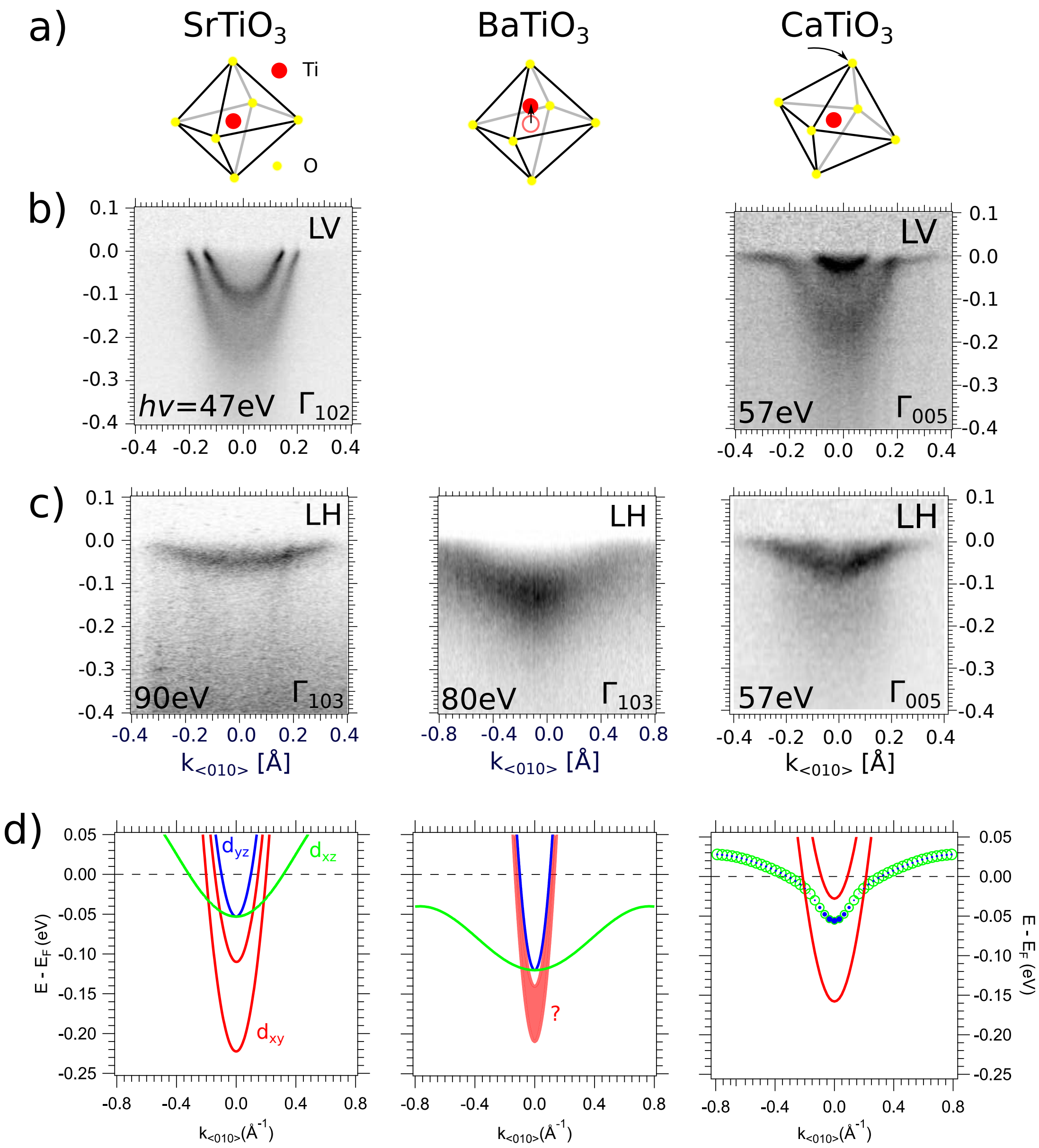

Figure 9.7: (a) Les octaèdres d'oxygènes dans des pérovskites $ATiO_3$ (A = Sr, Ba, Ca), (b,c) les cartes d'intensité ARPES $E-k$ et (d) les schémas de dispersion des bandes observées dans le 2DEGs. (b,c) Des polarisations de lumière différentes ont été utilisé lors des mesures ARPES: (b) linéaire verticale (LV) et (c) linéaire horizontale (LH). Les énergies de photons utilisées pour les mesures et la position des mesures dans l'espace réciproque sont également indiquées sur les graphiques. (d) Car la dispersion de la bande d_{xy} n'a pas pu être déterminée précisément dans le cas de $BaTiO_3$, une large bande rouge et un point d'interrogation indiquent la meilleure estimation. La taille des marqueurs pleins et vides dans le cas de $CaTiO_3$ représentent la fraction de d_{xz} (vert) et de d_{yz} (bleu) dans la dispersion de la bande qui a été obtenu en utilisant un modèle de liaisons fortes.

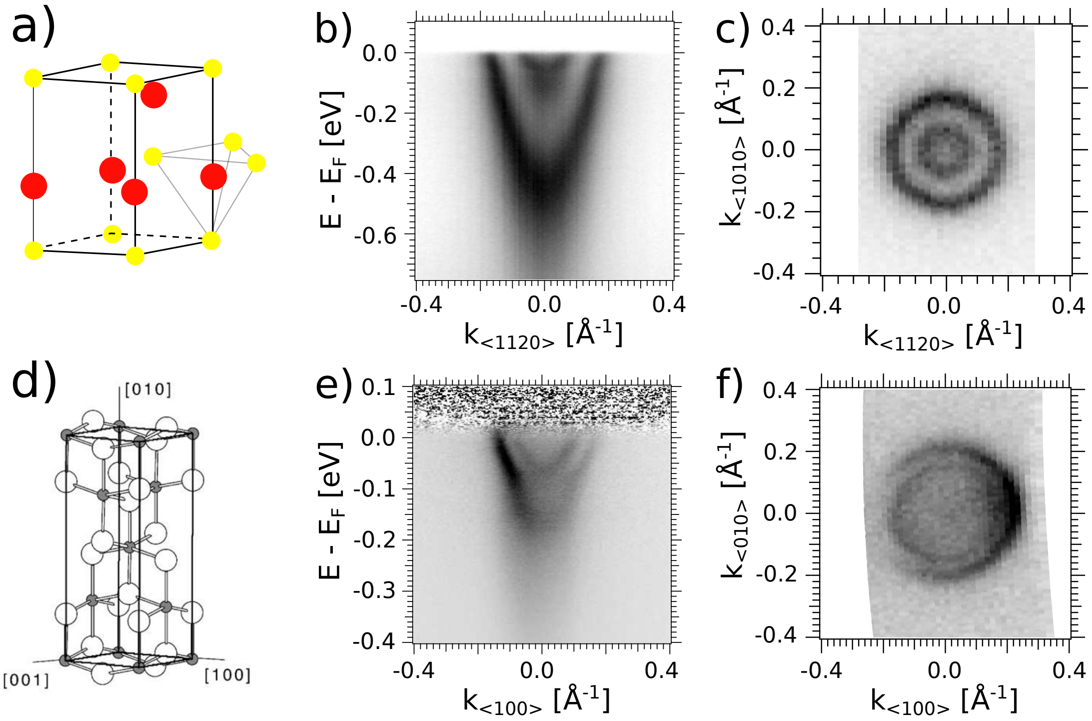

Figure 9.8: (a) Maille élémentaire d'un réseau wurzite (ZnO). Contrairement aux perovskites, les anions d'oxygène forment un tétraèdre autour du métal de transition Zn et la bande de conduction est formée par les orbitales s. (b) Carte d'intensité ARPES $E-k$ et (b) surface de Fermi à la surface $(000\bar{1})$ de ZnO mesurées aux énergies de photons $hv_1 = 25$ eV (b) et $hv_2 = 88$ eV (c). (d) Maille élémentaire du réseau quadratique d'anatase (TiO_2) (référence [80]). (e) Carte d'intensité ARPES $E-k$ et (e) surface de Fermi à la surface (001) d'anatase mesurées à $hv = 47$ eV. Le 2DEG dans l'anatase est composé de deux sous-bandes de type d_{xy}. Contrairement aux perovskites, les bandes lourdes ne forment pas le 2DEG parce que le champ cristallin du réseau quadratique présentée en (d) lève la dégénérescence des bandes t_{2g}.

Effets à N corps: couplage électron-phonon

En ARPES, l'analyse de la fonction spectrale $A(\vec{k}, E)$ peut être utilisé pour caractériser des effets à N corps. La fonction spectrale décrit la probabilité avec laquelle un électron peut être ajouté ou enlevé d'un système électronique dans son état fondamental. Dans un système avec des interactions à N corps, les valeurs propres d'énergie E sont renormalisée par rapport à celles d'un système sans interactions $E^0(\vec{k})$. La durée de vie du photoélectron dans un système à électrons libres est infinie, mais finie s'il y des interactions avec d'autres électrons, des défauts, des phonons,... . Ceci est exprimé par la fonction spectrale $A(\vec{k}, E)$ [115]:

$$A(\vec{k}, E) = \frac{1}{\pi} \frac{\Sigma_2(\vec{k}, E)}{(E - E^0(\vec{k}) - \Sigma_1(\vec{k}, E))^2 + (\Sigma_2(\vec{k}, E))^2}.$$

La function complexe $\Sigma = \Sigma_1 + i\Sigma_2$ est la self énergie. La partie réelle de la self énergie décrit la renormalisation de l'énergie à cause des interactions et la partie imaginaire la durée de vie finie. Les partie réelles et imaginaires sont reliées par une relation de Kramers-Kronig/ transformée de Hilbert. La figure 9.9 à la page 203 montre l'analyse de la self énergie du 2DEG à la surface (001) de $SrTiO_3$. Figure 9.9(a) montre la carte d'intensité d'ARPES $E - k$ qui montre les deux sous-bandes d_{xy} à la surface de $SrTiO_3$. Figure 9.9(b) montre des données simulées sur la base de l'analyse de la self énergie de la figure 9.9(d, e). Ce modèle utilise un couplage d'électrons avec des phonons d'Einstein et la fonction spectrale résultante est ensuite convoluée avec une gaussienne dont la largeur est donnée par la résolution énergetique expérimentale. Les largeurs et les positions de bandes dans (a) sont déterminées en fittant les données d'intensité ARPES 1D à énergie constante et vecteur d'onde constant. Les positions de pic utilisés pour les fits sont montrées dans (c) avec la dispersion de bandes sans interaction $E^0(\vec{k})$.
Enfin, les panneaux (d, e) montrent les self énergies des différentes branches des bandes. Les marqueurs rouges correspondent aux self énergies obtenues à partir des fits des données, tandis que les courbes noires sont les transformations Kramers-Kronig. L'analyse permet d'obtenir la fréquence de phonon, le paramètre $E^0(\vec{k})$ et également l'amplitude de couplage électron-phonon.

Creation du 2DEG par une couche ultra-mince d'aluminium

Le système de 2DEG de $SrTiO_3$ le plus étudié est l'hétérostructure $LaAlO_3$-$SrTiO_3$. Le 2DEG est crée à l'interface pour des couches de $LaAlO_3$ d'une épaisseur supérieure à 15 Å. [26] La croissance de cette hétérostructure nécessite des techniques de dépôt complexes et coûteuses (par exemple l'ablation laser pulsé). De plus, les propriétés de l'hétérostructure dépendent largement des paramètres de croissance. [347] La complexité de cette croissance empêche la production de masse de dispositifs électroniques à base d'oxyde. La découverte du 2DEG à la surface nue de $SrTiO_3$ n'a pas répondu à tous ces défis. Même si l'absence d'une surcouche facilite l'utilisation des techniques de spectroscopie sensibles à la surface, cette absence rend impossible la fabrication de dispositifs parce qu'il n'y a pas de passivation dans des conditions ambiantes.

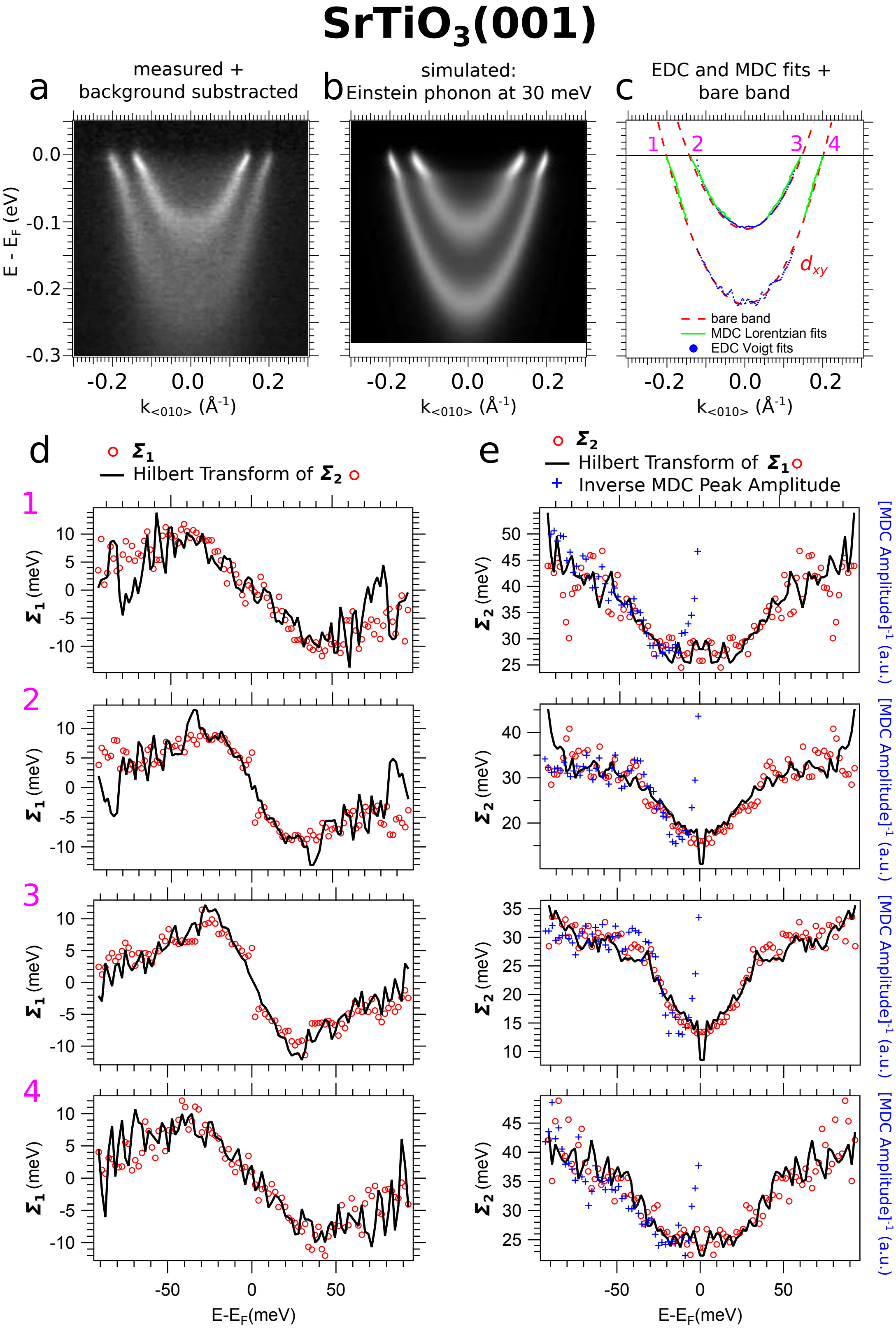

Figure 9.9: c.f. texte

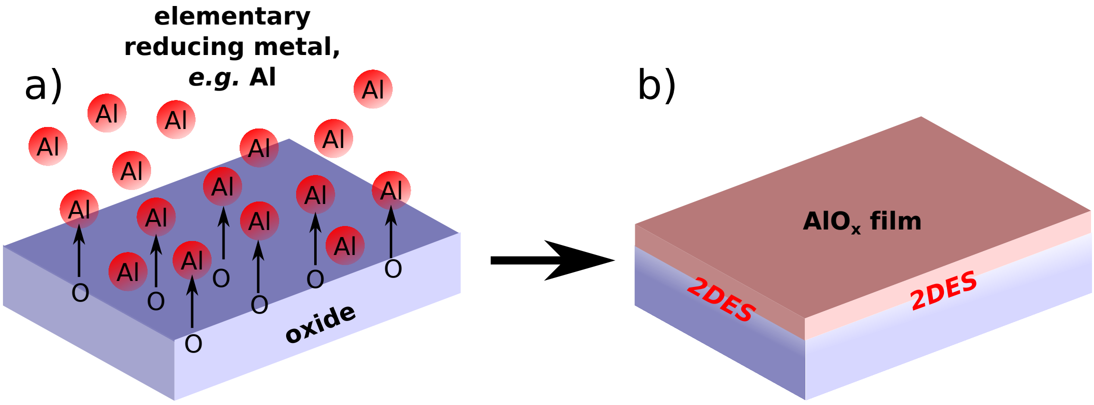

Figure 9.10: (a) Le dépôt d'un métal élémentaire qui provoque une réaction d'oxydoréduction avec un oxyde. Cette réaction crée des lacunes d'oxygène dans l'oxyde. (b) Pour une couche d'Al avec une épaisseur de ≈ 2 Å , la couche est complètement oxydée. A l'interface entre le film d'Al oxydé et l'oxyde la création d'un 2DEG est possible.

Une possibilité pour surmonter ces défis d'une manière très simple est la fabrication de 2DEGs dans des TMO par un dépôt d'aluminium à température ambiante. Grace à une réaction redox, l'aluminium pompe l'oxygène du substrat TMO et s'oxyde ainsi en AlO_x isolant. Les lacunes d'oxygène dans le TMO et à l'interface avec AlO_x créent le 2DEG comme discuté auparavant. Dans cette thèse, j'ai démontré la faisabilité de cette approche qui est montrée schématiquement figure 9.10, page 204. [19]